Università degli Studi di Catania
Dottorato di Ricerca in Ingegneria Elettronica, Automatica e del controllo di sistemi complessi

XIII CICLO

Placido Maria Montalto

INSIGHTS INTO MT. ETNA VOLCANO DYNAMICS BY SEISMIC AND INFRASONIC SIGNALS

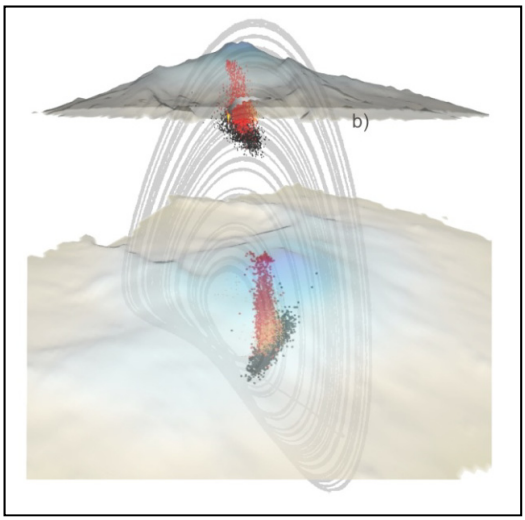

INGV

Tutor: Prof. G. Nunnari
Dr. D. Patanè
Coordinatore: Prof. L. Fortuna

INSIGHTS INTO MT. ETNA VOLCANO DYNAMICS BY SEISMIC AND INFRASONIC SIGNALS

Università degli Studi di Catania
Dottorato di Ricerca in Ingegneria Elettronica, Automatica e del controllo di sistemi complessi

XIII CICLO

Placido Maria Montalto

INSIGHTS INTO MT. ETNA VOLCANO DYNAMICS BY SEISMIC AND INFRASONIC SIGNALS

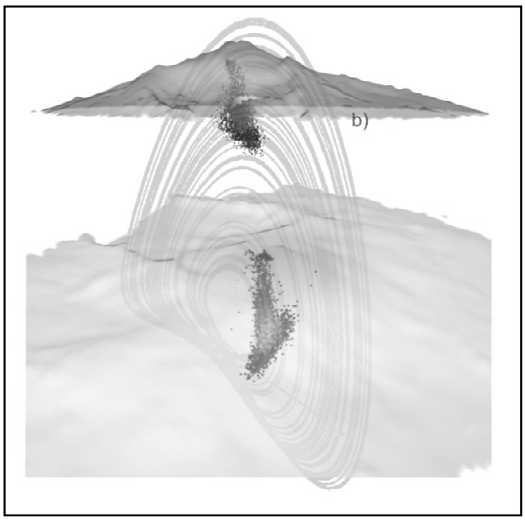

INGV

Tutor: Prof. G. Nunnari
Dr. D. Patanè
Coordinatore: Prof. L. Fortuna

Physical concepts are free creations of the human mind, and are not, however it may seem, uniquely determined by the external world.

Albert Einstein

Preface

Active volcanoes are one of the most severe natural hazards in the world. Volcanoes are geologic manifestations of highly dynamic and complexly coupled physical and chemical processes in the interior of the Earth. They are complex dynamical systems that produce distinctive patterns. Volcanic eruptions are the culmination of a complex ensemble of processes that occur on a broad range of time scale, from tens or hundreds of years (e.g. magma rise and differentiation) to fractions of seconds (e.g. fragmentation). About 550 volcanoes have erupted in historical times. Reconstruction of the eruptive history of many volcanoes has shown that inactive periods of thousands of year are not uncommon (Scarpa and Gasparini, 1996). Historical data indicate that eruptions are almost always preceded and accompanied by "volcanic unrest" manifested by physical and/or geochemical changes in the state of the volcano (Tilling, 2008). Detection of precursory phenomena (e.g., seismic, geodetic, gravity signals, gas emission) is the main aim of volcano monitoring which provides parameters for early warning systems. Systematic collection and analysis of huge amount of data recorded on active volcanoes are performed for both research and monitoring purposes. The fact that strongly different precursory patterns can be observed for different eruptions at the same volcano means that there exists no universal sets of empirical parameters relating precursor to eruptions. However, data from volcano monitoring constitute the only scientific basis for short-term forecast of imminent eruption or changes in the volcano behavior. Most active volcanoes are routinely monitored

observing the pattern of the seismic activity and ground deformations. During the last years a key role in volcano monitoring is played by time series analysis methods and pattern recognition techniques, both in time and time-frequency domain, in order to detect and analyze different eruptive patterns. The aim of this thesis is the study of seismic and infrasonic signals generated by volcanoes using signal processing techniques and novel approaches based on nonlinear time series analysis and pattern recognition (PR) techniques. Chapter 1 is an overview on the state of the art of volcano monitoring. The description of methods applied to analyse different kinds of signal will be given in chapter 2. Chapter 3 deals with pattern recognition techniques largely applied on infrasonic signal treatment at Mt.Etna. In chapter 4 the methods used for seismo-volcano signal analysis will be described. In chapter 5, practical applications of the techniques depicted in chapters 2, 3, and 4 will be shown with the aim of investigating the infrasonic signals at Mt. Etna and their relationship with eruptive activity. While seismo-volcanic transients have been treated in literature using PR approaches (e.g. Del Pezzo et al., 2003; Scarpetta et al., 2005; Benitez et al., 2007), infrasonic signals characterization by PR techniques is brand new. Since infrasonic signals exhibit very suitable descriptive features, one of the most important topics that will be treated in this thesis, is the robust PR approach for infrasonic signals characterization and classification. In chapter 6 Mt. Etna volcano dynamics will be investigated from a seismo-volcanic point of view. In particular, in the second half of the chapter, a novel technique based on the multi station coherence will be used to highlight lava fountain precursor phenomena. Finally, in chapter 7 conclusions will be reported.

Acknowledgment

I would like to thank my scientific colleagues for their fundamental cooperation. In particular the following people deserve special mention: Dr. S. Alparone, Dr. Ferruccio Ferrari, Dr. G. Di Grazia and Dr. E. Privitera. A special acknowledgment goes to my colleagues and friends Dr. Andrea Cannata, Dr. Marco Aliotta and Dr. Ing. Michele Prestifilippo for their fundamental support in my scientific and personal growth.

Many thanks to my tutors Prof. G. Nunnari and Dr. D Patanè for their constant guidance and encouragement, without their help this thesis would not have been possible. I am also very grateful to my family for their support. A special thought goes to my wife Elisabetta that made me a better person.

Chapter 1

Volcano monitoring

Monitoring of active volcano uses a wide range of techniques and instrumentations. Its aim is the interpretation of data in order to discover pattern in geophysical and/or geochemical parameters before, during and after eruptions. Monitoring provides the means to answer questions of vital interest to communities affected by impending eruptions such as when and where will the volcano erupt? Which areas are safe or dangerous? When will the eruptions cease? (McNutt et al., 2000). The answers come from an optimal interpretations of data and give information for forecast purpose. Unfortunately, the capability to answer these questions depends on the adequate scientific understanding of complex volcano dynamics both in general and for each specific volcano. A primary role in volcano monitoring is to establish the level of background or baseline activity of each monitored parameter, against which anomalous activity can be measured (McGuire, 1991). Well-equipped and well-staffed volcanological observatories are located only close to 20 of the potentially eruptive volcanoes and some geophysical instruments (most seismometers and benchmarks of geodetical networs) are installed on about 150 volcanoes in the world (Scarpa and Gasparini, 1996). Changes in geophysical and geochemical pattern are indicative of possible eruptive reactivation and include

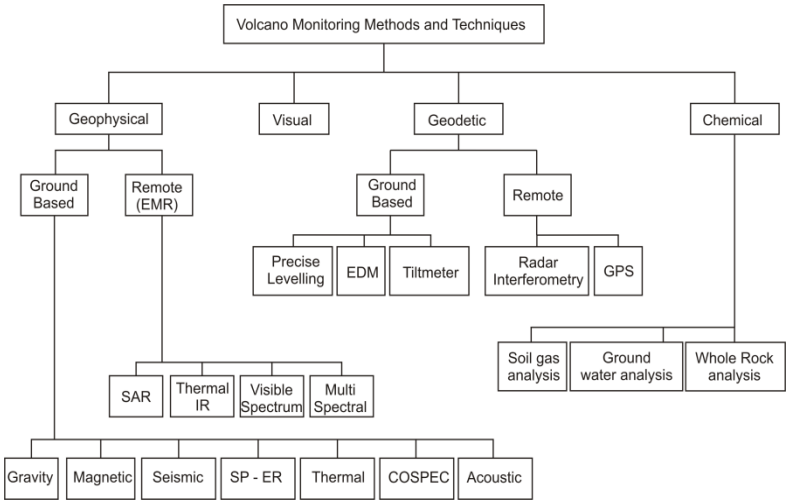

Figure 1: Techniques for volcano monitoring (modified from McGuire, 1991). Acronyms: EMR: electro-magnetic radiation; EDM: electronic distance measurement; GPS: global positioning system; SAR: synthetic aperture radar; IR: infrared; SP: self-potential; ER: electrical resistivity; COSPEC: correlation spectrometer.

changes in seismicity, ground deformations, physical-chemical changes in fumaroles, emission rates of volcanic gases, anomaly in gravity and magnetic fields. When combined with geological mapping and dating studies to reconstruct comprehensive eruptive histories of high-risk volcanoes, these geoindicators can help to reduce eruption-related hazards to life and property. Different techniques are used to monitor these parameters (figure 1). Each type of data provides information related to process which may be related to movement of molten rock or other precursory phenomena. Seismic activity is considered one of the best indicator of the evolution of volcanic activity and is one of the most common surveillance tool for active volcano.

The seismology gives useful information about the location of magma bodies/hydrothermal fluids in depth, their dynamics and composition and the plumbing system geometry (e.g. Kumagai and Chouet, 1999; Chouet et al., 2003; Patanè et al., 2006). Moreover, most volcanic eruptions have been preceded by increases in earthquake activity beneath or near the volcano (McNutt, 1996). Once the background seismicity has been characterized for a particular volcano, changes in the "steady state" may be related to changes in the volcano activity. Ground deformation study is another technique for volcano monitoring. Generally, the movement of subsurface material precedes volcanic eruptions and the increasing pressure results in ground deformation (Van der Laat, 1996). It is possible to model deformation caused by change of volume at a certain depth and modeling magma reservoirs, cracks and conduits (e.g. Van der Laat, 1996; Linde et al., 1993). GPS is the most suitable technique to measure ground deformations. However, it provides spot data, i.e. they refer to network vertices whose number rarely exceeds the order of tens in areas of hundreds, often thousands, of square kilometers (Palano et al., 2008). Remote sensing is a growing field in volcano monitoring and provides the only practical monitoring tools for many volcanic areas that are in relatively isolated regions. As defined in Francis et al. (1996), remote sensing consists of detection by a sensor of electromagnetic energy reflected, radiated or scattered from the surface of volcano or its airborne erupted material. For volcanoes already monitored by conventional techniques, this technique not only provides complementary observations but also offers new approaches (e.g. monitoring of ground deformation using InSAR techniques). Electromagnetic variations, preceding eruptive or seismic activity, are sometimes observed in volcanic areas (e.g. Johnston et al., 1981). Microgravity studies, involving the measurement of small changes with time in the value of gravity at a network of stations with

respect to a fixed base, are a valuable tool for mapping out the subsurface mass redistributions that are associated to volcanic activity (Rymer, 1996). Volcanic gas analysis and temperature measurements are also commonly performed. While geophysical precursors may yield different patterns related to the particular volcanic system, tectonic setting and physicochemical properties of the magma, geochemical precursory mostly depends on changing rates of magma degassing and interactions with shallow aquifers (Martini, 1996). Significant variations have been observed prior to some eruptions but often the changes occurred with the onset of the eruption (McNutt et al., 2000). Although these techniques have been successfully applied to forecast eruptive events on different volcanoes, during the last years new insights into explosive volcanic processes have been achieved by studying infrasonic signals (e.g. Vergniolle and Brandeis, 1994; Ripepe et al., 1996, 2001a). This kind of signal, together with seismic signal related to volcanic processes, constitutes an useful tool able to significantly contribute to volcano activity monitoring.

1.1 Volcano seismology

Seismic sources at volcanoes are highly complex and involve gases, melts and solids interaction (McNutt et al., 2000). Volcano seismology is a field of volcanology in which seismological techniques are employed to understanding physical conditions and dynamic states of volcanic edifices and volcanic fluid systems (Kawakatsu and Yamamoto, 2007). The main goal of volcanic seismology is to understand the nature and dynamics of seismic sources associated with the injection and transport of magma and related hydrothermal fluids (Chouet, 2003). Active volcanoes are the sources of a great variety of seismic signals. Traditionally, seismo-volcanic signals have been classified into six different types: high-frequency (HF) and low-frequency (LF) events, Very Long Period (VLP) events, volcanic tremor, hybrid events and volcanic explosions (figure 2) (e.g. Minakami, 1974; Lahr et al., 1994; McNutt, 1996; Zobin, 2003; Ibanez et al., 2003):

HF events: high-frequency events, also called Volcano Tectonic events (VT), manifest clear onset of P- and S-wave arrivals. In general, they are subdivided into two classes: deep VT events (VT-A), located below about 2 km, that manifest high frequency content (> 5 Hz); VT of type B (VT-B) that show much more emergent P-wave onset and sometimes any clear S-wave arrival and their spectral bands are shifted to lower frequencies (< 5 Hz) (Wassermann, 2009). High frequency may be generated at the source, but is not recorded because of instrumental limitations or high local attenuation (McNutt, 1996). HF events have been attributed to regional tectonic forces, gravitational loading, pore pressure effects and hydrofracturing, thermal and volumetric forces associated with magma intrusion withdrawal, cooling, or some combinations of any or all of these

(McNutt, 2005). This kind of events differ from their tectonic counterpart only in their patterns of occurrence, which, at volcanoes, are typically in swarm rather than mainshock-aftershock sequences (McNutt, 1996). HF events are useful at volcanoes to determine stress orientation via study of focal mechanisms and stress tensor inversion (e.g. Moran, 2003; Sanchez et al., 2004; Waite and Smith, 2004). The greatest progress in study VT events has been the implementation of new techniques for defining the volcanic structures; in particular, high-resolution tomography is a powerful method for determining subsurface volcanic structure (e.g. Dawson et al., 1999; Patanè et al., 2006).

LF events: Low-frequency events (LF), also called long period events (LP) (figure 2b), commonly observed on many volcanoes worldwide, are believed to be caused by fluids moving in volcanic conduits, heat and gas supply (Chouet, 1996a; Almendros et al., 2002a) and considered precursory phenomenon for eruptive activity. LP signals show no S-wave arrivals and very emergent signal onset. LP sources are often shallow (< 2 km) and their frequency content is mostly restricted in a narrow band between 0.5-5 Hz. LP activity originates in particular locations within the magma plexus where disturbances in the flow are encountered (Chouet, 1996a). Despite the ambiguity regarding the source, many authors have studied these events, focusing on particular features such as spectral content, rates, or relation to eruptions (McNutt, 2005). Injection of water into hot dry rock has been found to produce seismic signal similar to LF volcanic signal and support the idea of a source that involves the opening of tensile cracks caused by excess fluid pressure (Bame and Fehler 1986; Konstantinou, 2002). The associated source models range from an opening and resonating crack (Chouet, 1996a; Wassermann, 2009) to existence of pressure transients within the fluid-gas mixture

causing resonance phenomena within the magma itself (Wassermann, 2009; Seidl et al., 1981). Since LF events exhibit no emergent onset, phase picks are difficult to determine, thereafter it is impossible to apply standard location algorithm based on travel time inversion. Recently, LF events are located using semblance location techniques from particle motions recorded on a broad-band seismometer network (Kawakatsu et al., 2000).

Hybrid events: Some seismo-volcanic signals show characteristics of both LF and HF events and are called Hybrids (figure 2d). They are considered a subset of LF earthquakes, characterized by high-frequency onsets. Signals of this class begin with high-frequency phase followed by monochromatic signal which may reflect a possible mixture of source mechanisms. Spectral analysis reveals the different properties of these two distinct phases. The initial high-frequency portion has a broad spectrum, extending up to frequencies of 40 Hz. In contrast, the LP segment is quasi-monochromatic and peaks at low frequencies (1-6 Hz) (Ibanez et al., 2003). These events are thought to represent the failure of brittle rock which is accompanied by the excitation of nearby magmatic fluids. Some studies suggest that the onsets represent a separate trigger that initiates conduit resonance (Neuberg, 2006). Events of this sort have been observed at different volcanoes such as Montserrat, Redoubt, and Deception Island (Lahr et al., 1994; Miller et al., 1998; Neuberg et al., 2000; Ibanez et al., 2003).

Explosion quakes (ExQ): This signal class accompanies Strombolian or other explosive eruptions (figure 2e). Most of these signals can be identified by the occurrence of an air-shock phase caused by the sonic boost during an explosion (Wasserman, 2009). Some LF events show the same

frequency-time characteristics but lack an air phase (McNutt, 1986) reflecting a common source mechanism of deeper situated LF and shallow produced explosion. They have been studied by using calibrated infrasonic microphones or infrasonic pressure sensors. Key issues include the depth, ground-air energy coupling and seismic or acoustic efficiency (McNutt, 2005). The infrasonic signal (figure 2f) for short distances travels in an almost homogenous atmosphere without structures that may scatter, attenuate or reflect acoustic waves. Then, unlike the seismic signal whose wavefield is strongly affected by topography (Neuberg and Pointer, 2000) and path effects (Gordeev, 1993), the infrasonic signal maintains its features almost unchanged during propagation, allowing obtaining information concerning source dynamics. This can be explained by the simpler Green's functions for a fluid atmosphere than those for a complex, heterogeneous volcanic edifice, which supports compressional, shear, and surface waves (Johnson, 2005). Thus acoustic data give a more direct view of some explosive and eruptive processes (McNutt, 2005). The source mechanism of the sound radiated during eruptions is still open to debate. According to some studies, this signal can be related to the acoustic resonance of magma in the conduit, triggered by explosive sources, implying propagation of sound waves in the magma and atmosphere through an open vent (Buckingham and Garces, 1996; Garces and McNutt, 1997; Hagerty et al., 2000; Cannata et al., 2009a). Other theories relate the source of sound to eruption dynamics, such as a sudden uncorking of the volcano (Johnson et al., 1998; Johnson and Lees, 2000), local coalescence within a foam (Vergniolle and Caplan-Auerbach, 2004) and Strombolian bubble vibration (Vergniolle and Brandeis, 1994, 1996; Vergniolle et al., 1996, 2004). Methods to estimate relative elastic energy partitioning during Strombolian eruptions were developed and show variations related to changing vent conditions (Johnson and Aster, 2005).

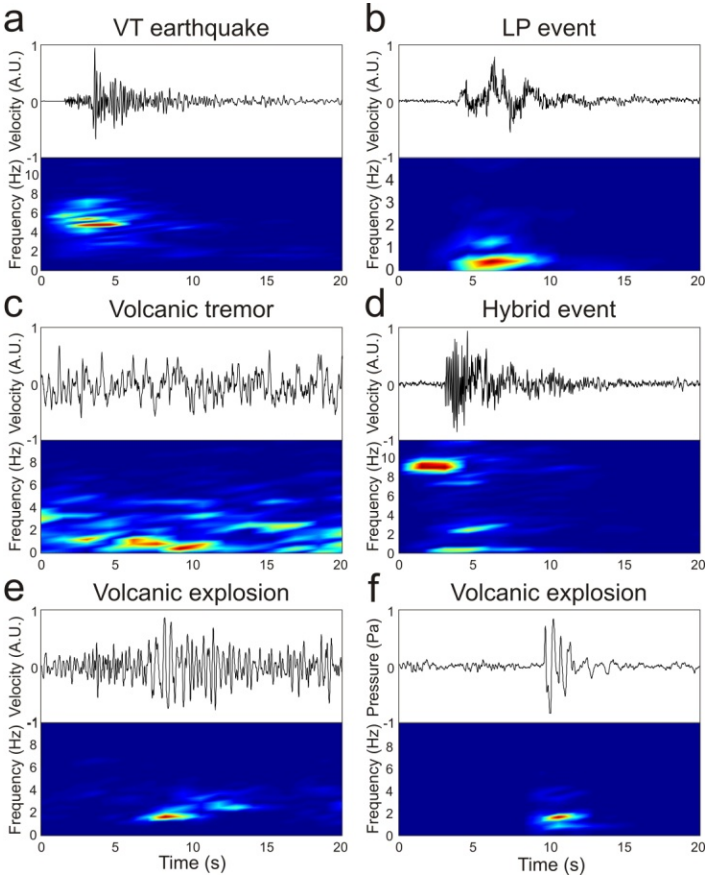

Figure 2: waveforms with the associated spectrograms for: (a) VT earthquake (VT); (b) long period event (LP); (c) volcanic tremor; (d) hybrid event (Hyb); (e) explosion quake (EXQ); (f) infrasonic signal.

Very Long Period Events: the use of broadband seismometers in the past decade has allowed to record a new class of seismo-volcanic signals called Very Long Period (VLP) events. VLP events with dominant periods in the range 2–100s (Neuberg et al., 1994; Ohminato et al., 1998) are assumed to be linked to mass movements, and to represent inertial forces resulting from perturbations in the flow of magma and gases through conduits (Uhira and Takeo, 1994; Kaneshima et al., 1996; Chouet, 1996b; Cannata et al., 2009c). This class of signals has been observed at several volcanoes such as Aso Volcano (Kawakatsu et al., 1994; Kaneshima et al., 1996; Yamamoto et al., 1999), Stromboli (Neuberg et al., 1994; Chouet et al., 2003), Kilauea (Ohminato et al., 1998), Etna (Cannata et al., 2009c; Patanè et al., 2008).

Volcanic tremor: volcanic tremor is a persistent ground vibration recorded near active volcanoes (figure 2e). In figure 3 is shown a location of volcanoes where the tremor occurrences were recorded (Konstantinou and Schlindwein, 2002). This signal is the most favored parameter in volcano early eruption warnings. At Mt. Etna (Italy), strong fluctuations of volcanic tremor amplitude are associated with lava fountaining or with opening of a flank fissure (Cosentino et al., 1989). Tremor is generally characterized by narrow frequency range and long duration compared with earthquakes and other seismo-volcanic signals (figure 2e). Although spectra of tremor usually contain a series of narrow peaks suggesting the modes of oscillation of a resonant system, commonly tremor signal is complicated and chaotic in appearance (Julian, 1994). Seismo-volcanic earthquakes like LP and explosion quakes events have spectra similar to tremor and probably are closely related to it. Observations made at different volcanoes suggest the involvement of gas/fluid interaction.

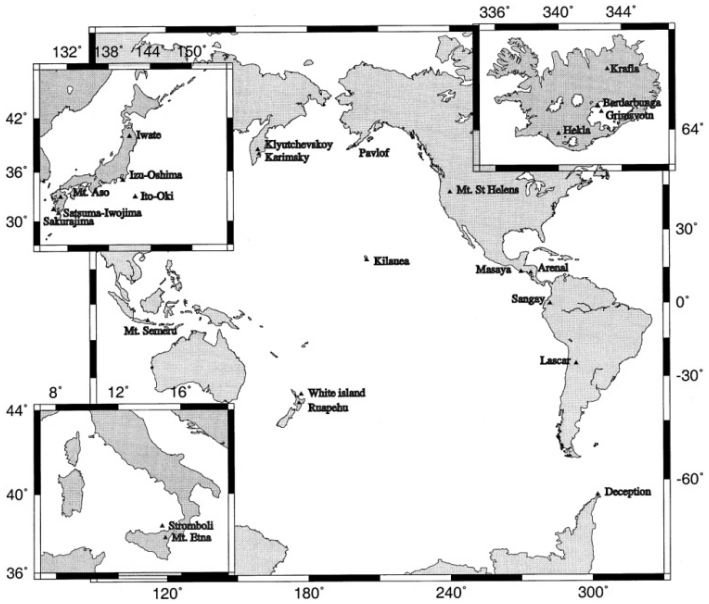

Figure 3: Location of volcanoes that present tremor occurrence (from Konstantinou and Schlindwein, 2002)

The content spectra similarity with LP and ExQ signals suggests a similar source process. Flow instability plays an important role in the excitation of volcanic tremor in multi phase flow pattern (Seidl et al., 1981; Schick, 1988) and associate LP and ExQ are seen as a transient within the same physical process (Wasserman, 2009). The physical mechanism of the tremor source has proved to be very difficult. Complexity arises from the fact that a volcano represents the place of interaction between material of different physical properties: magmatic fluids, surrounding bedrock and gases (Konstantinou and Schlindwein, 2002). It is well known that very different physical processes in a volcano may produce quite similar results (Schick, 1992). This has been confirmed by theoretical modeling in the frequency domain of tremor and low frequency seis-

mo-volcanic events and was found that many physical mechanisms could explain them equally well (Nishimura et al., 1995). Also, many authors support the fact that the tremor source is not unique and may differ from a volcano to another. Harmonic tremor and spasmodic tremor are two special cases of more general volcanic tremor.

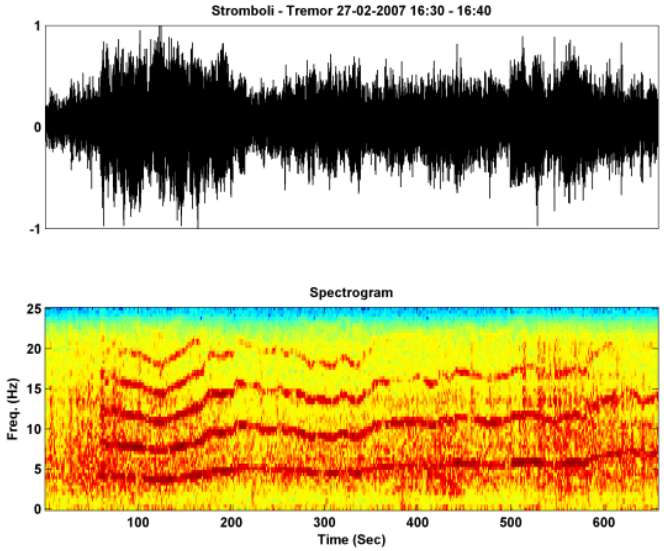

Figure 4: Tremor gliding phenomena . The changing frequency content with time is related to conduit physical parameters changes.

The former is a low-frequency, often monotonic sinusoid with smoothly varying amplitude, the latter is a higher-frequency, pulsating and irregular signal (Finch, 1949; McNutt, 1996). A very interesting feature of tremor is referred to as gliding (figure 4), in which the frequencies of evenly spaced spectral peaks vary systematically with time. Also in the case of the volcanic tremor, the standard location techniques based on travel time inversion cannot be used because of the non-impulsive signature of tremor. Therefore, new methods based on the space distribution of the seismic amplitude were developed and used for the signals coming from classical seismic networks (different techniques are used for the seismic arrays) (Battaglia and Aki, 2003; Di Grazia et al., 2006). A large number of papers showed a strict relationship between eruptive activity and variations of volcanic tremor. They consist of whether spectral and amplitude changes (Gresta et al., 1991; McNutt, 1994; Alparone et al., 2007; Cannata et al., 2008) or location source variations (Patanè et al., 2008; Di Grazia et al., 2009).

1.2 Time Series Analysis: an introduction

Time series (TS) problems arise in almost all disciplines, ranging from studying variations in biomedical measurements to variations in geophysical or in financial parameters. A time series is a finite series of observations usually collected at regular intervals. Using time series analysis it is possible to characterize, predict and model the observed system. Also, time series obtained by different disciplines (e.g. geophysics and geochemistry) can be analyzed in order to discover a possible link among them. Once the background level has been characterized, changes in the so called "steady state" may be related to changes in the activity.

From a seismo-volcanic point of view, several parameters can be extracted from recorded signals. Since they are linked to magma-gas motion inside the volcano, studies of changes in parameters like spectral content, rate, quality factor, background noise and wavefield, can be used for understanding volcano dynamic evolution and their implications for monitoring purposes. In order to accomplish this task, time series analysis (TSA) techniques provide useful tools for volcano state changes interpretation. In TSA there are three recurring main tasks (Gershenfeld, 2006). The first task is related to nature of the underlying system that produces observed time series. It provides information about the nature of the system, its degrees of freedom, its linear or nonlinear nature, noise influences and how random it is. The second task is related to forecast defined as the estimation of the next state known the current state. The last task is the TS modeling and is related to governing equations estimation and their long-term behavior.

In general, TS analysis can be articulated on the following points:

Regression analysis: Linear system theory is expressed by the Wold decomposition where a stochastic process is separated into the sum of two processes: deterministic one that is a linear function of its past values; stochastic one that is a linear function of previous values of uncorrelated random variable (Priestley, 1981; Gershenfeld, 2006). Approximation of Wold form with finite number of parameters leads to auto-regressive/moving-average (ARMA) process where the system output y is a linear function of external inputs x, its previous outputs and noise. Although linear systems are very well understood, they appear very limited in real geophysical applications where non-linearities are significant.

Stationarity: Traditional time series analysis implicitly assume that data come from a linear dynamical system with many degrees of freedom and added noise. The variation is assumed to be a superposition of sine waves and additional terms that grow or decay. The exponential terms typically lead to nonstationarity in which statistical properties of time series, such mean or standard deviation, change in time (Sprott, 2003). In time series measurement, reproducibility is closely connected to the stationarity of the underlying process (Kantz and Schreiber, 1997). The weakest stationarity requires that probably density functions (p.d.f.) remain constant for all parameters that characterize the dynamic of the system. A time series is considered to originate from a stationary process if statistical fluctuation of mean, variance and auto-covariance, does not change over time. In order to estimate the stationarity, some methods use nonlinear statistics techniques, such as the so-called cross-prediction error (Schreiber, 1997).

Non-linear analysis: Link between chaos theory and real world is the analysis of time series in terms of nonlinear dynamics. It is well known

that real processes are characterized by a number of interdependent variables. Modeling of geophysical/geochemical systems is an extremely difficult task. Data sequences are obtained from the observation rather than physical equations. For a dynamical description of such time series, linear statistical techniques are insufficient as they do not take into account nonlinear relationship (Matcharashvili et al., 2000). A nonlinear dynamical approach provides more information on complex system behavior than classical linear tools (Berge et al., 1984; Theiler, 1990; Abarbanel et al., 1993; Kantz and Shreiber, 1997). Theory of deterministic chaos is an useful tool in order to explain irregular behavior of systems that are not influenced by stochastic inputs. The dynamics of systems is described in state space, whose dimension is given by the number of the dependent variables of the model. State space describes how the behavior of a nonlinear system evolves as one or more of its parameters are bifurcating (Konstantinou and Lin, 2004). When we analyze a time series, we will almost always have only incomplete information due to the measurement on a single variable as a function of time. In this cases the state space and the dynamics of the system that generated the measures are unknown. The missing information can be recovered from time delayed copies of the available time series if certain requirements are fulfilled (Schreiber, 1998). Several geophysical systems exhibit chaotic behavior characterized by high sensitivity to initial conditions. Small changes in initial conditions or slightly different external forces produce wildly different outcomes even when the governing equation are known. Nonlinear time series analysis provides practical method for studying chaotic signals by reconstructing phase space and extracting information about the underlying process.

Time-frequency analysis: In time series analysis we can represent information in two basic ways: time and frequency representations. The former does not display spectral content while the latter shows only frequency information. Frequency representation is commonly computed using the Fourier transform that allows the retrieval of information on power content at any frequency. The widely used Fourier transform is designed for stationary signals; in classical Fourier analysis we lose the frequency location in the time domain. For the analysis of time series containing non-stationary power at many different frequencies, Short time Fourier transform (STFT) and wavelet transform (WT) are commonly applied (Daubechies, 1990). In contrast to the Fourier transform, which consists of a linear superposition of independent and nonevolving periodicities, the WT is based on the convolution of signals with a set of functions derived from the translations and dilatations of a basic function called the "mother wavelet". Unlike STFT, WT gives a more accurate time-frequency description of signals containing low and high frequency components. Taking into account STFT method, once the length of the moving window is chosen, also the frequency resolution is fixed, and the entire phase space is uniformly described by cells of fixed sizes. Conversely, WT method, based on variable-sized cells, allows the use of long time intervals to gather more precisely low-frequency information, and of shorter regions for high-frequency information (Bartosch and Seidl, 1999; Lesage et al., 2002). Some example of time-frequency representation of seimo-volcanic events are reported in figure 2 and 4.

1.3 Pattern recognition approach

The process of automatic extraction, recognition, description and classification of patterns extracted from time series plays an important role in modern volcano monitoring techniques. In particular, the ability of a certain system to recognize different volcano regimes can help the researchers to better understand the complex dynamics underlying the geophysical systems. The recognition process consists of one of the following tasks: supervised classification and clustering. Clustering and classification processes in high dimension metric space are widely applied on data analysis when more than two descriptive features are needed. For this purpose approaches based on Self Organizing Map and density based method will be illustrated. Also, the classification problem by optimal hyperplane separator using support vector machine (SVM) will be faced with the aim of classifying information provided by the clustering task. A basic pattern recognition schema is shown in figure 5 and can operate in two modes: training mode and classification mode (Jain et al., 2000).

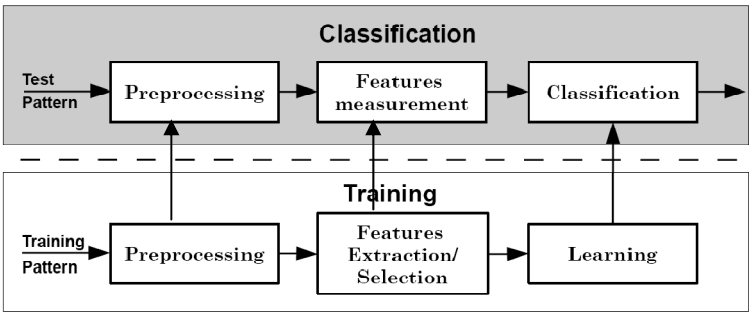

Figure 5: Basic pattern recognition model (from Jain et al., 2000).

The role of the preprocessing module is to segment and filter the pattern of interest from the background, remove noise, normalize the pattern and then comprises all the operations used to define a compact representation of the pattern. In the training mode, the features extraction block finds the descriptive features of the input patterns and then the classifier is trained to partition the features space.

Chapter 2

Time series analysis methods

In this chapter methods for time series analysis will be introduced. In particular, we will focus on the time-frequency domain signal processing and nonlinear analysis techniques. The former techniques are related to multi-scale/frequency signals representation using wavelet framework considering statistical significance with respect to a background noise. Further, a brief description of power parametric spectrum estimation will be introduced. The nonlinear techniques will be treated to investigate time series from a dynamical point of view. In particular, various methods for determinism and nonlinearity detection will be applied in order to characterize different kinds of signals. A very important topic will be the chaotic behaviour detection and phase space reconstruction from a single time series. This methodology has been widely applied since the available data are generally in form of time series and the underlying dynamical system in unknown. All of these techniques will be applied in the next chapters with the aim to investigate different volcano activity regimes at Mt. Etna volcano.

2.1 Time-Frequency analysis

Information content of a physical quantity can be represented either as a function of time (time domain) or as a spectrum (frequency domain). A function of time does not show spectral content while representation by Fourier spectrum cannot represent the temporal variation of the signal. The Fourier transform give information about the spectral content of a signal using a linear superposition of independent and non-evolving periodicities. This technique implicitly assumes that the underlying process is stationary and gives no information about the location of these frequency in time. This treatment is not well suited for data which involves transient process and frequency content changes in time. Fourier analysis presents limitation if applied on signals including intermittent burst processes or intermittent processes (Labat, 2005). To overcome this problem methods based on sub-sections or moving-windows of the data are used in order to detect abrupt regime changes in statistical property of the signal. Common approaches in time-frequency analysis are the Windowed Fourier Transform (WFT), also known as Short Time Fourier Transform (STFT), and Continuous Wavelet Transform (CWT). These representations give a very clear picture of the non-stationarity nature of the signal in a time-frequency domain. STFT provides this representation by transforming short windows of data. In this case a Fourier spectrum is computed over time by a fixed-size window shifted along the time axis. This has the problem that a fixed size moving window limits the detection of cycles at wavelengths that are longer than windows itself, and nonstationarity in short wavelength are smoothed (Prokoph and Patterson, 2004; Gershenfeld, 1999). The use of CWT solves this problem because it uses wide windows at low frequencies and narrow window at high frequencies providing a multi-scale representation of the signal.

2.1.1 Short Time Fourier Transform

STFT is defined as a convolution between a signal *f(t)* and a sliding window *w(t-t')*:

$$S(t,\omega) = \int_{-\infty}^{\infty} f(t')w^*(t-t')e^{-j\omega t'}dt' \tag{2.1}$$

where *w*(t-t')* is the window function centered on t, commonly a Hann or Gaussian window (Bartosch and Seidl, 1999; Lesage et al., 2002). STFT can be seen as a local spectrum of *f(t')* around the analysis time *t,* whose position indicate the approximate time for which the spectrum is valid. STFT of a sequence *f(n)* is defined as:

$$F(\omega,m) = \sum_{n=-\infty}^{\infty} f(n)w(m-n)e^{-j\omega n} \tag{2.2}$$

where the sequence *f(n)w(m-n)* is called short-time section of the sequence *f(n)* at time *m*. The windowing process introduces leakage effects and frequency resolution strongly depends on the choice of the window function. In particular, time-frequency resolution can be adjusted by the window length t_w. A good time resolution requires a narrow window in time, while a good frequency resolution requires a large window in time (corresponding to a narrow filter in frequency domain). Once the window size is chosen, both time and frequency resolutions are fixed and the entire phase space is described by cells of fixed size (figure 1).

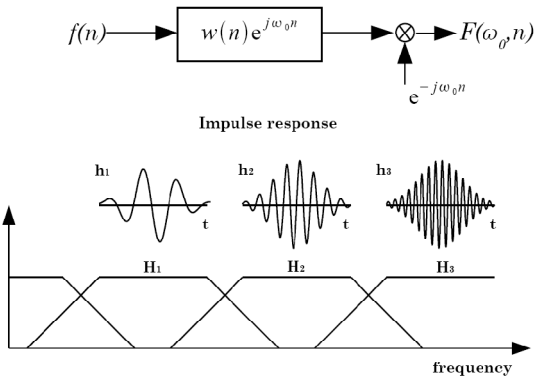

Fig. 1: Filtering view of STFT at frequency ω_0.

This is related to Heisenberg's uncertainty principle that prohibits the existence of a window with arbitrary small duration and bandwidth.
Once the windows size t_w is chosen, the smallest measurable frequency is determined as $f_w=1/t_w$ (Lesage et al., 2002; Bartosch and Seidl, 1999). Equation (2.1) can be interpreted as a convolution between the signal *f(t)* and the window function *w(t)* also called analysis filter. The last definition is justified on the basis of the fact that STFT can be interpreted as the output of an infinite channel of filter bank where the window *w(n)* plays the role of the filter input response (Nawab and Quatieri, 1988). Fixing $\omega=\omega_0$ equation (2.2) can be rewritten as:

$$F(\omega_0,m)=\sum_{m=-\infty}^{\infty}\left[f(n)e^{-j\omega_0 m}\right]w(m-n) \tag{2.3}$$

Using the convolution operator * equation (2.3) can be rearranged as:

$$F(\omega_0,m)=\left[f(n)e^{-j\omega_0 m}\right]*w(m-n) \tag{2.4}$$

The term $f(n)e^{-j\omega_0 n}$ can be interpreted as modulation of *f(n)* up to the frequency ω_0.

In the light of it equation (2.4) can be rewritten in the following form:

$$F(\omega_0, n) = e^{-j\omega_0 n}\left[f(n) * w(n)e^{j\omega_0 n}\right] \tag{2.5}$$

Time variation of STFT for a fixed frequency ω_0 can be represented using a block diagram as shown in figure 2 (Nawab and Quatieri, 1988; Bartosch and Seidl, 1999). Considering a finite number of frequencies the STFT can be viewed as the output of the filter bank shown in figure 2 where each filter is a bandpass filter centered around its selected frequency ω_i (i=0..N-1).

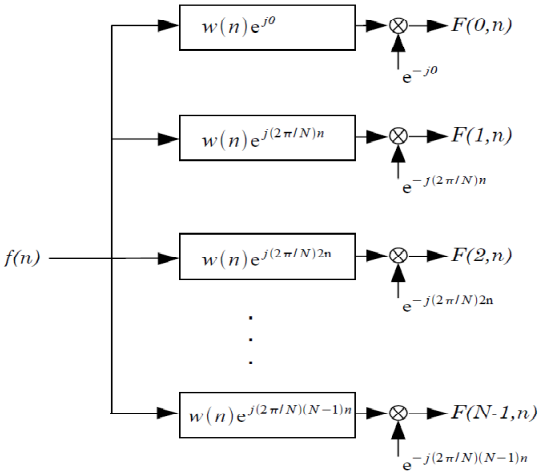

Figure 2: STFT as the output of a bandpass filter bank.

2.1.2 Continuous Wavelet Transform

As aforementioned, STFT has the drawback of fixed resolution in time-frequency domain. In general it is very difficult to find a good trade-off between frequency and time resolution. The continuous wavelet transform (CWT) solves this problem because it combines high temporal resolution with good frequency resolution offering a reasonable balance between these two parameters. For this reason CWT is an useful tool when signals are characterized by localized high frequency or scale-variable process and allows tracking time evolution at different scales (Labat, 2005; Leasage et al., 2002). The CWT transforms the signal in a time-scale plane called *scalogram*. From a mathematical point of view it is defined as:

$$W(t,a) = \frac{1}{\sqrt{a}} \int_{-\infty}^{\infty} f(t') \Psi^* \left(\frac{t - t'}{a} \right) dt' \tag{2.6}$$

where ψ is a real or complex function called analyzing wavelet, a is the dilatation parameter which controls the time duration of the wavelet and t is the translation parameter. The analyzing wavelet fulfills the admissibility condition:

$$0 < \int \frac{|\Psi(\omega)|^2}{|\omega|} d\omega < \infty \tag{2.7}$$

where

$$\hat{\Psi}(\omega) = \int_{-\infty}^{\infty} \Psi(t) e^{-j\omega t} dt \tag{2.8}$$

is the Fourier transform of $\psi(t)$ (Daubechies, 1992; Bartosch and Seidl, 1999). Let a discrete sequence $x(n)$ (n=1,..,N), the CWT can be defined as:

$$W(n,a) = \sum_{n'=0}^{N} x(n')\Psi^* \left[(n-n')\frac{\delta t}{a} \right] \tag{2.9}$$

where δt is the uniform time step, * indicates complex conjugate, a is the wavelet scale and N is the number of points in the time series. By translating the time index n and varying the scale a we obtain a picture showing amplitude at any scales and its variation with time. The convolution in equation (2.9) can be computed faster in the Fourier space. The DFT (Discrete Fourier Transform) of the sequence $x(n)$ is defined as:

$$X_K = \frac{1}{N}\sum_{n=0}^{N-1} x(n) e^{-2\pi i k n / N} \tag{2.10}$$

with frequency index $k=0...N-1$. Using the convolution theorem, wavelet transform can be viewed as the inverse Fourier transform of the product:

$$W(n,a) = \sum_{k=0}^{N-1} X_k \hat{\psi}^*(a\omega_k) e^{i\omega_k n \delta t} \tag{2.11}$$

where the angular frequency is defined as:

$$\omega_k = \begin{cases} \dfrac{2\pi k}{N\delta t}: & k \le \dfrac{N}{2} \\ -\dfrac{2\pi k}{N\delta t}: & k > \dfrac{N}{2} \end{cases} \tag{2.12}$$

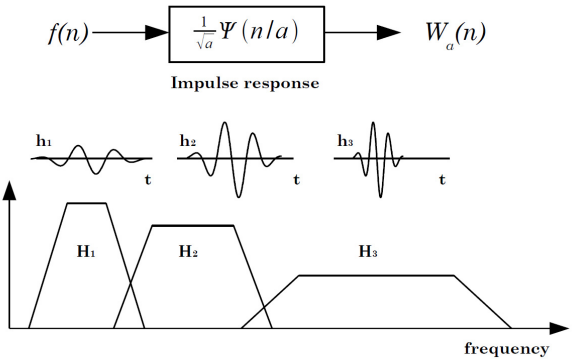

Figure 3: CWT as non-uniform infinite channel filter bank.

and $\widehat{\Psi}(a\omega)$ is the Fourier transform of the wavelet function $\Psi(t/a)$. The choice of wavelet function (also called mother wavelet) is a critical aspect of the CWT and it is related to the particular features that we want to consider in our analysis (Torrence and Compo, 1998; Farge, 1992). One particular wavelet, used in time series feature extraction, is the Morlet wavelet that provides a Gaussian modulation of the time-scale plane:

$$\psi_0(\eta) = \pi^{-1/4} e^{j\omega_0\eta} e^{-\frac{1}{2}\eta^2} \tag{2.13}$$

where ω_0 and η are the dimensionless frequency and time respectively (Grinsted et al., 2004). In order to provide a good balance between time and frequency and satisfy the admissibility condition ω_0 must be 6 (Farge, 1992). It is noteworthy that for Morlet wavelet (with $\omega_{0=6}$) the Fourier period T is almost equal to the scale ($T \sim 1.03a$). In order to

normalize the CWT that is to have unit energy, equation (2.9) can be written as:

$$W(n,a) = \sqrt{\frac{\delta t}{a}} \sum_{n'=1}^{N} x(n') \Psi^* \left[(n - n') \frac{\delta t}{a} \right] \tag{2.14}$$

Similar to STFT (section 2.1.1), the CWT can be investigated as a non-uniform infinite channel filter bank (figure 3). In this case impulse response is derived by dilatation of prototype band pass impulse response Ψ(n) whose duration depends on the scale parameter *a* (Bartosch and Seidl, 1999). Transferring concepts of classical Fourier analysis to wavelet domain, a wavelet power can be defined as the transformation of the autocorrelation function. Since the wavelet function *Ψ(n)* is in general complex the *W(n,a)* is also complex. The transform can be divided into real part *R{W(n,a)}* and imaginary part *I{W(n,a)}* and amplitude $|W(n,a)|$, and phase, $tan^{-1}[I\{W(n,a)\}/R\{W(n,a)\}]$. The Wiener-Khinchin theorem can be defined as the expectation value of *W(n,a)* multiplied by its conjugate:

$$\left|W(n,a)\right|^2 = \left\langle W(n,a) W^*(n,a) \right\rangle \tag{2.15}$$

If wavelet is centered close to the beginning or to the end of the time series, edge artifacts occur. For this reason it is useful to introduce the so called Cone of Influence (COI) in which edge effect become important and the results should be interpreted carefully. COI can be defined as the area in which the wavelet power caused by a discontinuity at the edge has dropped by a factor e^{-2} of the value at the edge itself (Torrence and Compo, 1998; Grinsted et al, 2004; Maraun and Kurths, 2004).

2.1.3 Comparison between STFT and CWT

Both time-frequency methods can be interpreted as the inner product of the signal *f(t)* and a function *F(t,f)*. In the case of STFT the *F(t,f)* takes the form:

$$\psi(t,f) = g(t'-t)e^{-2i\pi ft'} \tag{2.16}$$

while, in wavelet transform, it becomes:

$$\psi(t,f) = g\left(\frac{t-t'}{a}\right) \tag{2.17}$$

Both techniques have the same time-frequency resolution limitations. While STFT resolution do not depend on the investigated frequency (the window size is fixed a priori) the CWT is a multi-resolution approach with better time resolution at high frequency and better frequency resolution at low frequency. The *tilling* of the time-frequency plane is different for both STFT and CWT and is characterized by duration T and bandwidth B. In the former these two parameters are constant (T=const, B=const) and the tiled time-frequency plane can be represented as in figure 4a. In the latter case the parameters T and B are related to the scale parameter a (T=a, $B=B_{a=1}/a$) and lead to a non uniform tile time-frequency plane (figure 4b). An example of time-frequency representation of a signal with added spike and noise using STFT and CWT is shown in figure 5.

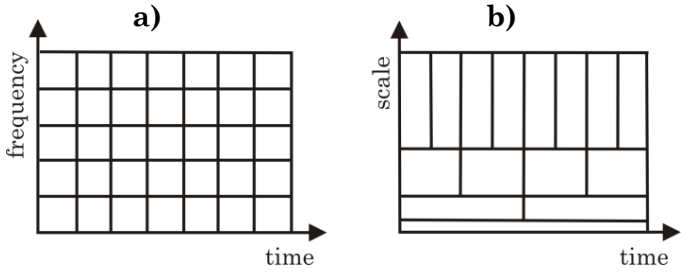

Figure 4: Tilling of time-frequency plane of a) STFT and b) CWT.

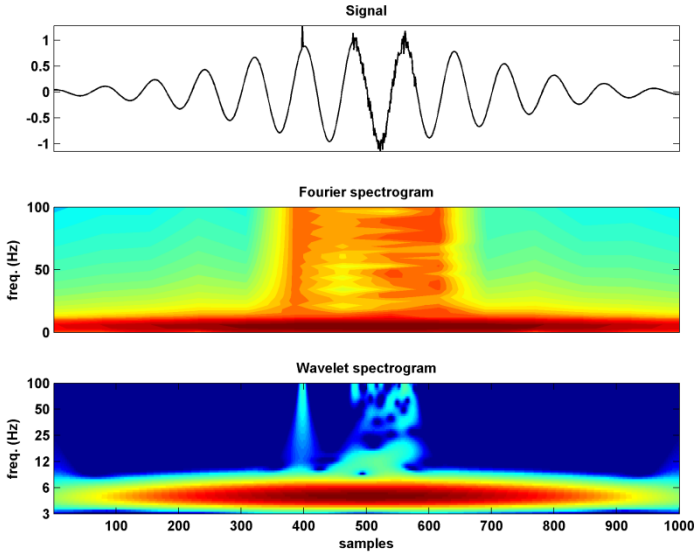

Figure 5: STFT (middle plot) and CWT (bottom plot) of a synthetic signal (top plot) of Gaussian windowed 5 Hz harmonic signal with added spike and noise. The spike and the beginning of the high frequency noise is well resolved in time by CWT than STFT. This picture clearly shows the advantages of CWT respect to classical spectrogram based on Fourier transform.

2.1.4 Statistical significance

In order to estimate the reliability of the power spectrum a statistical significance level is required. To accomplish this task one firstly needs an appropriate hypothesis about background spectrum.

Statistical significance of power spectrum is based on the assumption that the investigated signal is generated by a stationary process with a given background power spectrum. This assumption is known as the *null hypothesis*. Hypothesis about an appropriate background spectrum is closely related to the considered system. For many geophysical phenomena background spectrum can be white noise (flat Fourier power spectrum) or red noise (increasing power with decreasing frequency). The last one reflects the fact that a sort of memory is presented in the process that generates the measured signal. A simple method for red noise modeling is an AR1 (auto-regressive model of first order) process with lag-1 autocorrelation α:

$$x_n = \alpha x_{n-1} + z_n \tag{2.18}$$

with $x_0 = 0$, and zn is taken from Gaussian white noise (Torrence and Compo, 1998). Fourier power spectrum of (18) is given by (e.g. Allen and Smith, 1996):

$$P_k = \frac{1-\alpha^2}{\left|1-\alpha e^{-2i\pi k}\right|^2} \tag{2.19}$$

where k is the Fourier frequency index. Let a time series and a background spectrum hypothesis, the estimated power spectrum peak above background spectrum can be assumed to be a true feature with a certain percent confidence. Peaks in the time series power spectrum are assumed

significant if they exceed the 95% confidence spectrum computed based on the hypothesis of white or red background noise. For definition the '*95% confidence'* level is equivalent to '*significant at the 5%'* and *'95% confidence interval'* is related to the range of confidence about a given value. If a time series x_n is normally distributed, both real and imaginary part of the DFT coefficients X_k are normally distributed (Chatfield, 1989). Since the square of normally distributed variable is *chi-square* distributed with one degree of freedom then $|X_k|^2$ is *chi-square* distributed with two degree of freedom denoted by χ_2^2 (Jenkins and Watts 1968). For instance, to obtain 95% confidence level, the background spectrum given by equation (2.19) must be multiplied by the *95Th* percentile value for χ_2^2 (Gilman et al., 1963; Torrence and Compo, 1998). Under the assumption of a background noise given by equation (2.19), the distribution of normalized Fourier power spectrum can be expressed as:

$$Dist\left(\frac{N\left|\hat{X}_k\right|^2}{\sigma^2}\right)=\frac{1}{2}P_k\chi_2^2 \tag{2.20}$$

The corresponding relation in wavelet domain at each scale a and time n is:

$$Dist\left(\frac{\left|W_X(n,a)\right|^2}{\sigma_X^2}\right)=\frac{1}{2}P_k\chi_\nu^2 \tag{2.21}$$

These relations are correct assuming that the underlying distribution of the original time series is Gaussian. The choice of the mother wavelet is very important in the definition of wavelet power. As explained in Ge (2007) the wavelet power has a χ_2^2 distribution only when a wavelet fam-

ily used is the Morlet wavelet. In practice, for many time series an analytical expression of the significance level against red-noise null hypothesis is not available. In this case the significance level can be obtained empirically through Monte Carlo simulations (e.g. Torrence and Compo, 1998; Grinsted et al., 2004). More details about wavelet significance test can be found in Ge (2007,2008).

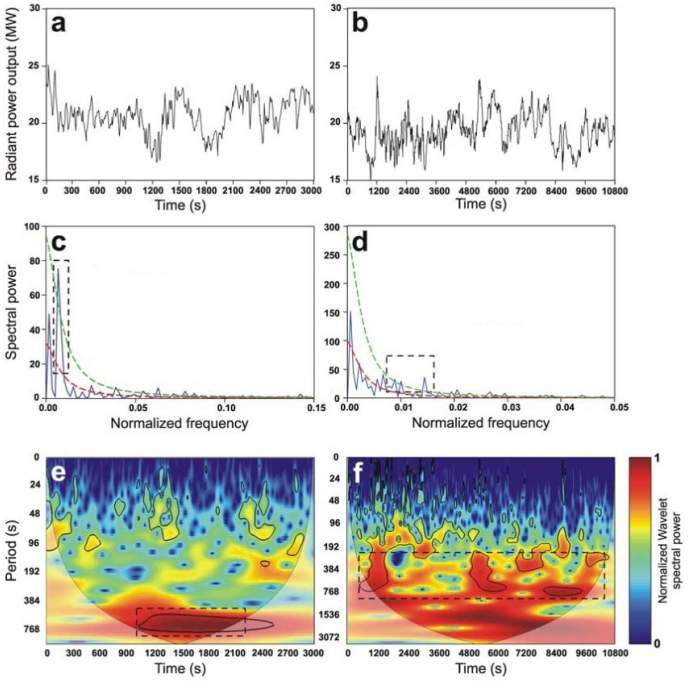

Figure 6: (a and b) Time series of the radiant power output of thermal camera; (c and d) power spectra computed via periodogram normalized by standard deviation of the time series shown in Figures 6a and 6b; (e and f) Wavelet transform, computed using a Matlab code provided by Grinsted et al., 2004, of the two time series.

Methods described in this section have been widely applied on different scientific research areas, such as geophysics, volcanology and seismology. In figure 6 an application of Fourier and Wavelet power spectrum estimation together with the confidence level is shown. The two time series reported in figure 6a and 6b, were obtained from thermal image (Spampinato et al., 2008). Both time series were normalized with 0 mean and unit standard deviation before wavelet spectrum computation. In order to investigate the most energetic periods, classical Fourier transform (figure 6c and 6d) and wavelet transform (figure 6e and 6f) were applied. Peaks in power spectrum are assumed significant if they exceed the 95% confidence spectrum computed based on the hypothesis of red background noise. Peaks found using periodogram (figure 6c and 6d) are consistent with the wavelet transform results (figure 6e and 6f), which show significant spectral power (highlighted by the solid contour at 95% confidence interval). Also the cone of influence (COI) discussed in section 2.1.2 is shown in figure 6e and 6f.

2.1.5 Cross-spectrum and coherence

Let *x(t)* and *y(t)* two ergodic and stationary processes, the cross-correlation can be considered as a quantitative measure of the relatedness of two signals. The Fourier cross-spectrum can be defined as (Labat, 2005):

$$S_{XY}(f) = \int_{-\infty}^{\infty} R_{XY}(\tau) \exp(-i2\pi f\tau) d\tau \qquad (2.22)$$

where $R_{XY}(\tau)$ is the cross-correlation between the signals x and y. S_{XY} is called cross-spectral density or cross spectrum and S_{XX} and S_{YY} are the

autospectra of the two signals X and Y respectively. Coherence is an extension to Pearson's correlation coefficient and can provides a measure of the linear relationship between two signals at various frequency (Saab et al., 2005; Caviness et al., 2003). In the light of it, spectral coherence can be defined as:

$$C_{XY}(f) = \frac{|S_{XY}(f)|}{\sqrt{|S_{XX}(f)S_{YY}(f)|}} \tag{2.23}$$

Using Schwarz inequality we observe that $C_{XY}(f)$ takes values between 0 and 1. The aforementioned Coherence measure assumes stationary of the signals and, similarly to Fourier transform, is insensitive to changes over time. To overcome this problem, a STFT (see section 2.1.1) approach is applied to produce the *coherogram*. In practice, while with Fourier coherence it is possible to isolate frequency bands in which two time series are covarying, with coherence computations using a moving window approach it is possible to identify both frequency band and time intervals in which the two time series are covarying. This can be produced by calculating the coherence using a moving window providing coherence in time-frequency space. Similar to STFT, this process is constrained by the uncertainty principle and requires definition of several parameters such as window length and overlapping.

2.1.6 Cross wavelet spectrum and wavelet coherence

Wavelet analysis has been defined for a single signal *x(t)*. As defined for Fourier transform, it is possible to calculate the cross-wavelet spectrum from two signal *x(t)* and *y(t)* extending the idea of coherogram from a time-frequency to time-scale space. The cross wavelet transform can be defined as the expectation value of the product of the $W_X(n,a)$ and $W_Y(n,a)$ respectively:

$$W_{XY}(n,a) = \left\langle W_X(n,a) W_Y^*(n,a) \right\rangle \tag{2.24}$$

Cross wavelet spectrum (CWS) is complex (analogous to Fourier cross-spectrum) and can be decomposed in amplitude $|W_{XY}|$ and phase $\Phi(n,a)$:

$$W_{XY}(n,a) = \left|W_{XY}(n,a)\right| e^{i\phi(n,a)} \tag{2.25}$$

The phase describes the delay between the two time series at time n and on scale a (Maraun and Kurths, 2004; Torrence an Compo, 1998; Torrence and Webster, 1999). As Fourier and Wavelet spectrum, it is possible to define a confidence level for wavelet cross-spectrum. It can be derived from the probability density function defined by the square root of the product of two chi-square distributed (Jenkins and Watts, 1968; Torrence and Compo, 1998; Grinsted et al., 2004). Let two spectra χ^2 distributed with ν degrees of freedom, the probability distribution can be expressed as:

$$f_\nu(z) = \frac{2^{2-\nu}}{\Gamma^2\left(\frac{\nu}{2}\right)} z^{\nu-1} K_0(z) \tag{26}$$

where z is a random variable, Γ is gamma function, $K_0(z)$ is modified Bessel function of zero order. From (22) the cumulative distribution function is given by:

$$p = \int_0^{Z_\nu(p)} f_\nu(z)dz \tag{2.27}$$

with $Z_\nu(p)$ confidence level associated with the probability p. Given a probability p, inversion of integral (23) provides the confidence level $Z_\nu(p)$. Let X and Y two time series with background power and P_k^X P_k^Y, theoretical distribution of cross-wavelet power is given by (Torrence and Compo, 1998):

$$Dist\left(\frac{W_X(n,a)W_Y^*(n,a)}{\sigma_X\sigma_Y} < p\right) = \frac{Z_\upsilon(p)}{\nu}\sqrt{P_k^X P_k^Y} \tag{2.28}$$

where σ_X and σ_Y are the respective standard deviations. CWS reveals areas with high common power of two signals without normalization. This can lead to misleading results due to the fact that the CWS is basically a product of the CWT of two time series. For example, if one spectrum is flat in band and the other spectrum exhibits strong peaks, the CWS can produce peaks in cross-spectrum that are not related to effective coupling between the signals. For this reason CWS is not suitable for significance testing relations between two signals (Maraun and Kurths, 2004). This problem can be avoided by normalizing to the single CWT leading to the concept of wavelet coherence (WC) that provides a measure of how coherent the CWT is in time-scale/time-frequency space. This measure can find significant coherence also in intervals where CWS shows low common power. Also in this case, it is possible to estimate the confidence levels against background red noise.

Similarly to Fourier coherence, wavelet coherence can be defined as the square of the cross-spectrum normalized by the individual power spectrum:

$$C^2(n,a) = \frac{\left| W_{XY}(n,a) \right|^2}{W_{XX}(n,a) W_{YY}(n,a)} \tag{2.29}$$

The equation (2.29) gives a quantity between 0 and 1. A value of 1 means a linear relationship between the two time series *X* and *Y* around time n and on scale a. A value of 0 means a vanishing correlation. As reported in Liu, 1994, the equation (2.29) is identically one at all times and scale. To overcome this problem, equation (2.29) is modified by introducing a smoothing operator:

$$C^2(n,a) = \frac{\left| \left\langle a^{-1} \left| W_{XY}(n,a) \right| \right\rangle \right|^2}{\left\langle a^{-1} \left| W_X(n,a) \right|^2 \right\rangle \left\langle a^{-1} \left| W_Y(n,a) \right|^2 \right\rangle} \tag{2.30}$$

Where the factor a^{-1} is used to convert to an energy density and the symbol $\langle \cdot \rangle$ indicates a smoothing operation in both time and scale. The wavelet-coherency phase difference is given by:

$$\phi(n,a) = \tan^{-1}\left(\frac{\Im\{\langle s^{-1} W_{XY}(n,a) \rangle\}}{\Re\{\langle s^{-1} W_{XY}(n,a) \rangle\}} \right) \tag{2.31}$$

In general, smoothing operator can be defined as:

$$\langle W \rangle = \left\langle \langle Wn, a \rangle_{time} \right\rangle_{scale} \tag{2.32}$$

The choice of smoothing operator is related to the mother wavelet used in the analysis. For a Morlet wavelet a suitable time smoothing operation is performed by the following convolution in time (Torrence and Webster, 1999; Jevrejeva et al., 2003):

$$\left\langle W \right\rangle_{time} = \left(W(n,a) * c_1 e^{-t^2/2a^2} \right)\Big|_{scale} \tag{2.33}$$

and in scale:

$$\left\langle W \right\rangle_{scale} = \left(W(n,a) * c_2 \, \Pi(0.6a) \right)\Big|_{time} \tag{2.34}$$

where c_1 and c_2 are normalization constants and Π is the *rectangle* function. The value 0.6 is empirically determinate in Torrence and Compo, 1998.

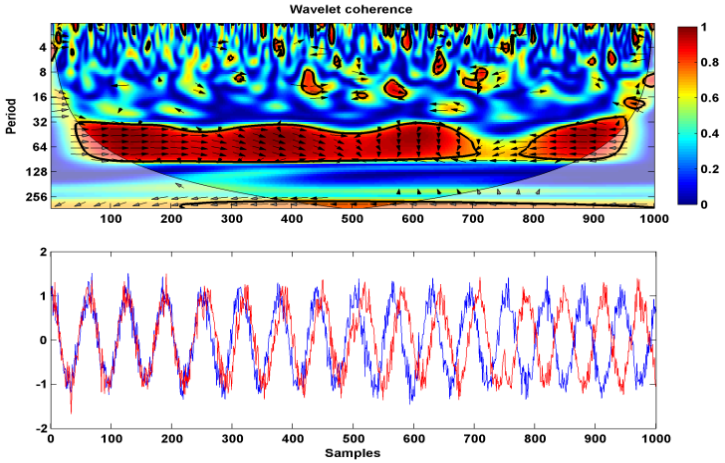

Figure 7: Simple wavelet coherogram of two synthetic signals with growing phase difference. The relative phase relationships are plotted using arrows.

As aforementioned, wavelet cross-spectrum and wavelet coherence are complex and can be expressed in terms of absolute value and phase. As argued in Grinsted et al., 2004, an useful way to see the phase evolution in time-scale space is the overlay plotting of the phase angle on the coherogram (figure 7). The relative phase relationship can be plotted using arrows with in-phase plotting right, anti-phase plotting left and 90° pointing straight down while the 5% significance level against red noise is shown as a thick contour. In figure 8 an example of wavelet coherence is shown (Cannata et al., 2010). In particular, the relationship between amplitude of continuous background seismic signal (figure 8a**)** and soil CO_2 flux (figure 8b) both recorded at Mt. Etna during the period 2003-2005, was investigated using cross-wavelet spectrum (figure 8c) and wavelet coherence (figure 8d). As explained before, the vectors indicate the phase difference between CO_2 flux and tremor amplitude time series. Horizontal arrow pointing from left to right signifies in phase and an arrow pointing vertically upward means the first series lags the second one by 90°. The 5% significance level against red noise is shown as a thick contour and the COI, where the edge effects might distort the picture (see section 2.1.2), is shown as a lighter shade.

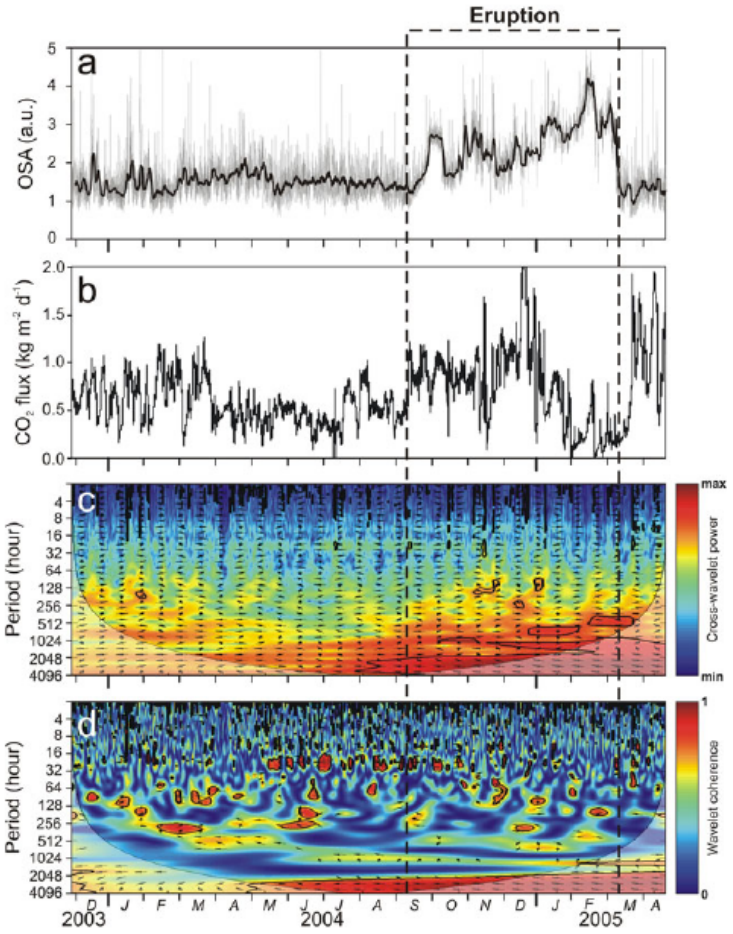

Figure 8: a) tremor amplitude; b) CO_2 flux; C) cross-wavelet spectrum and d) wavelet coherence between the time series in a) and b) (both time series were standardize before cross-wavelet spectrum and wallet coherence computation). The 5% significance level against red noise is shown as a thick contour. The black dashed lines indicate the onset and the end of the eruption.

2.2 Time series power spectrum estimation

The problem of estimating the power spectral density (PSD) of a time series can be brought back to the PSD function $X(w)$ of a signal from a finite number of observations. This task cannot be performed in a consistent manner. To overcome this problem there are two main strategies. The first considers the digital signal as the output y_n of a stationary linear filter excited by an input x_n. This approach leads to the parametric or model-based methods where the estimation of the PSD is reduced to the problem of estimating a number of parameters m, much smaller than the length data N, of a generating model with known functional form. The second approach are in general known as nonparametric methods and are generally implemented using the Fast Fourier Transform (FFT). Two common power spectral estimators are known as periodogram and correlogram. In general these estimators are poor spectral estimators because their variance is high and does not decrease with the increase of data length. This motivates the development of other methods, such as Bartlett or Welch methods, that present lower variance at a cost of reduced resolution (Stoica and Moses, 1997). To increase the resolution other methods, known as filter bank methods (e.g. Capon, 1969; Lacos, 1971; Benesty et al., 2005), were developed. In particular, these methods come from a filter bank interpretation of the periodogram,

In the next sections two kinds of power spectrum estimators, parametric and nonparametric, will be presented. In particular, in section 2.2.1 the Sompi method (Kumazawa et al., 1990), widely applied in geophysical time series analysis, will be explained. In section 2.2.2 the minimum variance distortionless response (MVDR) method, both for PSD and cross-PSD estimation, will be introduced.

2.2.1 Parametric power spectrum estimation: the Sompi Method

Time series modelling consists of estimating the governing dynamics of the hypothetical linear dynamic system that has yielded the given time series data (Kumazawa et al., 1990). In these approaches, a signal is considered as the impulse response of an AR (autoregressive) or an ARMA filter (autoregressive moving average). ARMA filter is a discrete-time system that takes an input sequence x_n and produces an output sequence y_n. This kind of system can be described by a linear-constant difference equation:

$$x_n = \sum_{k=1}^{p} a_k x_{n-k} - \sum_{k=1}^{q} b_k y_{n-k} \tag{2.35}$$

where $\{a_k\}$ and $\{b_k\}$ are the system coefficients, p and q are the order of the AR and MA parts of the filter, respectively. The coefficients of the AR filter can be obtained by solving the modified Yule-Walker equation (Marple, 1987) and the coefficients of the MA filter can be estimated using the Durbin method (Kay, 1981; Mars et al., 2004). As argued in Lesage (2008), this process is affected by numerical instabilities and long computation time. Furthermore, the deconvolution of the AR part alone gives good estimation of the duration and spectral content of the considered signals (Lesage, 2008). In order to estimate the AR coefficients, Sompi method (Kumazawa et al., 1990) can be implemented. Unlike the traditional spectral estimators in real frequency space, this method yields a line-shaped spectrum in complex frequency space. The basic concepts of the AR model and the formulation based on the maximum likelihood principle lead to a model estimation algorithm different from other AR methods (Fukao and Suda, 1989; Kumazawa et al., 1990). By Sompi

analysis, a time series is deconvoluted into a linear combination of coherent oscillation with decaying amplitude and additional noise. Let $\{x_n\}$ time series that can be considered the sum of signal $\{u_n\}$ and Gaussian white noise $\{e_n\}$:

$$x_n = u_n + e_n \tag{2.36}$$

where u_n is described as a set of decaying sinusoids (Fukao and Suda,1989):

$$u_n = \sum_k \{C_k (z_k)^i + C_k^* (z_k^*)^i\} \tag{2.37}$$

and z_k is defined as:

$$z_k = \exp(2\pi(g_k + jf_k)\Delta t) \tag{2.38}$$

where Δt is the sampling step and the symbol * represents the complex conjugate. In equation (2.37) C_k represents the complex amplitude of the kth sinusoid at the complex frequency given by f_k-jg_k and j is $\sqrt{-1}$. The time series $\{u_i\}$ is defined as the sequence satisfying the AR equation:

$$\sum_{j=-m}^{m} a_j u_{i-j} = 0 \tag{2.39}$$

where $\{a_j\}$ (j=0,1,….,m) are real AR coefficients. An exhaustive treatment about a_j coefficients estimations is reported in Hori et al. (1989), Fukao and Suda (1989) and Kumazawa et al. (1990). Briefly, a way to compute the coefficients a_j that satisfy equation (2.39) is the minimization of the functional S:

$$S = \sum_{i=-N+m}^{N-m} \left(\sum_{j=-m}^{m} a_j x_{i-j} \right)^2 \tag{2.40}$$

under the condition:

$$\sum_{j=-m}^{m} a_j^2 = 1 \tag{2.41}$$

This minimization problem leads to an eigenvalue problem where coefficients a_j are the eigenvectors corresponding to minimum eigenvalues. Now, once the a_j are calculated, the Sompi characteristic equation is defined as:

$$\sum_{j=-m}^{m} a_j z^{-j} = 0 \tag{2.42}$$

The roots z_k of equation (2.42) give the complex frequencies expressed in equation (2.38). Let $\{x_i\}$ a time series, Sompi method extracts m wave elements characterized by a complex frequency f_k-jg_k where f_k is the frequency, g_k is the growth rate. Each wave element can be represented as a point in a frequency-growth rate domain. The quality factor Q is then given by $-f_k/2g_k$. An example of frequency-growth rate domain is reported in figure 9. In particular, clusters of points in figure 9b were obtained considering AR model with order spanning from 2 to 60. The obtained point clusters indicate dominant spectral components of the signal and scattered points represent noise.

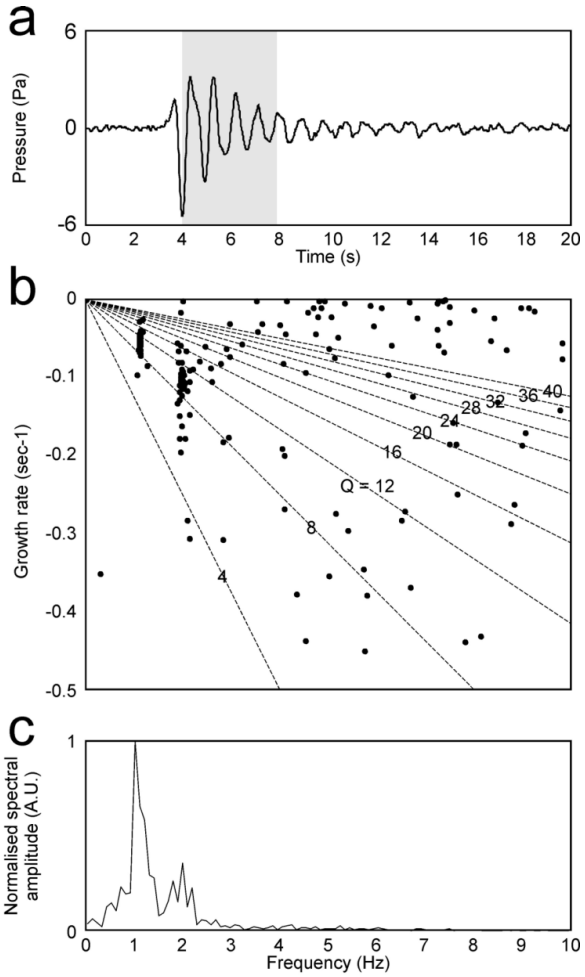

Figure 9: (a) Waveform of infrasound event recorded at Mt. Etna, and corresponding (b) frequency-growth rate plot (AR order 2-60) and (c) amplitude spectrum. The grey area in (a) represents the window used to calculate the frequency-growth rate plot in (b). The dashed lines in (b) represent lines along which the quality factor (Q) is constant. Clusters of points in (b) indicate dominant spectral components of the signal; scattered points represent noise.

2.2.2 High resolution power spectrum estimation

One of the best known nonparametric power spectrum estimation approach is the Capon's method, also known as minimum variance distortionless response (MVDR) (Capon, 1969; Lacoss; 1971), which consists of measuring the signal power by using a band-pass filters bank. The MVDR method can be interpreted as the output of a bank of filters, with each filter centered at one of the analysis frequencies (Benesty et al., 2005). While the periodogram-based approach can be viewed as a band-pass filters both data and frequency independent, the bandpass filters in the MVDR approach are both data and frequency dependent (Stoica and Moses, 1997; Stoica et al., 1998; Benesty et al., 2005). The filter must respect two conditions: 1) for a given frequency fk the frequency response is unity; 2) the influence of the other spectral components of the signal is minimized. This minimization under constrain leads to the following spectrum definition (Lesage et al., 2002):

$$P(f_k) = \frac{1}{S_k^H R_X^{-1} S_k} \tag{2.43}$$

where R_x is the correlation matrix of the signal, $S_k^T = [1, s_k, s_k^2, \dots, s_k^p]$, with $s_k = e^{2i\pi f_k \Delta t}$, p is the filter order, T and H denote the transpose and the conjugate transpose, Δt is the sampling interval.

Assuming *x(n)* and *y(n)* two zero mean stationary random signals with respective spectra P_x and P_y, the cross-spectrum can be generalized from equation (2.43) as:

$$P_{xy}(f_k) = \frac{S_k^H R_{xx}^{-1} R_{xy} R_{yy}^{-1} S_k}{\left[S_k^H R_{xx}^{-1} S_k\right]\left[S_k^H R_{yy}^{-1} S_k\right]} \tag{2.44}$$

where R_{xy} is the cross-correlation matrix between *x(n)* and *y(n)*, R_{xx} and R_{yy} are the cross-covariance matrices (for more details see Benesty et al., 2005). From equation (2.44) the coherence between the signals *x(n)* and *y(n)* can be expressed as (see section 2.1.5):

$$C_{xy}^2(f_k) = \frac{\left|P_{xy}(f_k)\right|^2}{P_{xx}(f_k)P_{yy}(f_k)} \tag{2.45}$$

In figure 10 a comparison between classical Welch method and MVDR method is shown. In particular, a coherence function is computed considering two sinusoidal signals:

$$x = \cos(2\pi f_1 t) + \cos(2\pi f_2 t) + \cos(2\pi f_3 t)\omega_1(t) \tag{2.46}$$

$$y = \cos(2\pi f_1 t + \phi_1) + \cos(2\pi f_2 t + \phi_2) + \cos(2\pi f_3 t + \phi_3) + \omega_2(t) \tag{2.47}$$

where $\omega_1(t)$ and $\omega_2(t)$ are two white Gaussian processes (figure 10a), the phases Φ_1, Φ_2 and Φ_3 are random, f_1=0.03, f_2=0.04 and f_2=0.05. The results show that high resolution methods like MVDR provide a more reliable result with respect to the classical Welch's method (figure 10b). For these reasons, the MVDR approach will be applied in the next chapters (see chapter 4) together with time-frequency approaches (see section 2.1.5) in order to build a high resolution coherogram for geophysical time series comparison (see chapter 4).

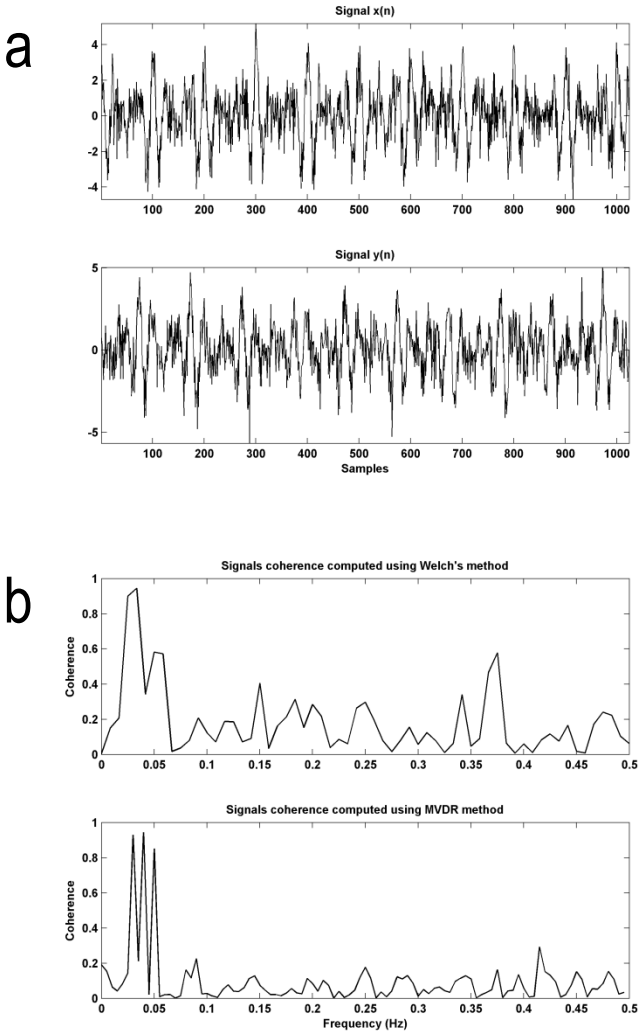

Figure 10: (a) Two signals *x(t)* and *y(t)* obtained as superposition of cosinusoidal function with added white Gaussian noise. (b) Coherence estimated by Welch method (top plot) and MVDR (bottom plot).

2.3 Nonlinear analysis

Real world processes comprise linear and nonlinear components, together with deterministic and stochastic ones. Figure 11 shows real world signal spanned by the properties of linearity and stochasticity. Signal from real world phenomena are related to processes that are located in the region denoted by (a), (b), (c) and (?). This is a consequence of nonlinearity, uncertainty and noise that constitute the process. In terms of time series modelling only linear stochastic autoregressive moving average model (ARMA) and nonlinear deterministic models (NARMA) are well understood (Mandic et al., 2008). In order to characterize a time series from a dynamical point of view, it is necessary to verify the presence of an underlying linear or nonlinear dynamics.

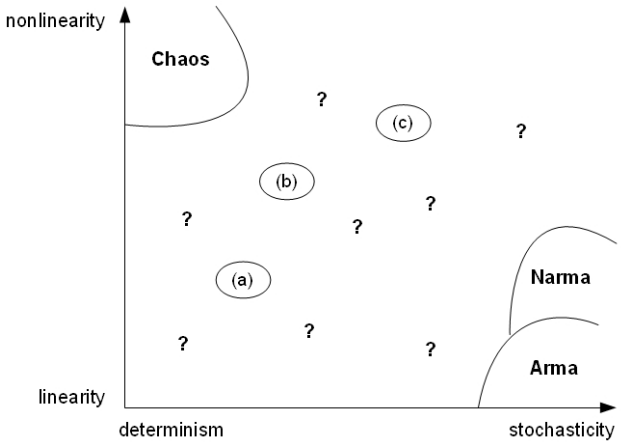

Figure 11: Real world signals grouped in classes spanning from nonlinearity to stochasticity. The areas where the analysis method are readily, such as chaos and ARMA, are highlighted (redraw from Mandic et al., 2008).

While for many systems the assumption of nonlinearity may be correct in principle, real world signals are subject to uncertainty and noise, so it is impossible to distinguish between nonlinear dynamics and linear dynamics that involve stochastic components. In addition, time series comes from discrete measures on continuous dynamical systems. In this case the sampling space can influence the nature of observed data. For these reasons, the rejection of the null hypothesis of linearity is an important tool for time series analysis (e.g. Schreiber ans Schmits, 2000; Timmer, 2000, Mandic et al., 2008; Hou and Li, 2010).

2.3.1 Nonlinear methods

In order to study temporal evolution of a dynamic system, phase space is used. Phase space is a representation of the state vector X of the system at any given time by a point in an n-dimensional space $\Re^n$. Dynamic systems can be described by using a set of n first-order differential equations with initial condition $X(0)$:

$$\frac{d}{dt}X(t) = f(t, X(t)) \tag{2.48}$$

$X(t)$ solving the equation (2.48) is called trajectory of the dynamic system. The trajectory in the phase space evolves in time from initial conditions onto a geometrical object called attractor. Attractors can be divided into three categories: fixed point, limit cycle and the so-called strange attractor. Fixed point is the simplest attractor where, after a transient time, the system settles to a stationary state; a limit cycle is an isolated close trajectory, and in this case the system approaches a periodic motion; an attractor with aperiodic trajectories is called strange. In this case trajec-

tories in phase space approach each other without intersection and orbits that are initially close diverge exponentially from each other due to sensitivity conditions. This kind of attractor presents specific topological shape displaying infinite complexity in a bounded structure. There are two important parameters that characterize a dynamic system: the number of degrees of freedom, given by the fractal dimension of the attractor, and the degree of chaoticity, given by an estimation of the largest Lyapunov exponent (e.g., Kostantinou and Lin, 2004). As aforementioned, the property of sensitive dependence on initial conditions is characterized by an exponential divergence of nearby trajectories in the phase space. The averaged exponent of this increase is called the Lyapunov exponent. Chaotic systems are characterized by at least one positive Lyapunov exponent and a low-dimensional fractal attractor in the phase space. In recent years, with the developments of nonlinear dynamic theory, many investigations have shown that time series can be considered as outputs of nonlinear dynamic systems and can provide information about the pertinent variables that characterize the dynamics of the source processes. In this view, a n-dimensional vector characterizing state of the system is estimated by the analysis of available time series data. The basic idea is that we cannot obtain the original phase space but rather we reconstruct a pseudo-phase space that maintains the topological characteristics of the original space from a given time series. The most common method for phase space reconstruction is known as Delay Embedding Theorem (e.g., Takens, 1981). The reconstructed trajectory is expressed in matrix form:

$$Y = [X_1, \ldots, X_M] \tag{2.49}$$

where X_i (with i=1,…,M) represents the state of the system at time i. Considering a N-point time series $\{x_i,\ldots,x_N\}$, the state vector X_i is defined as:

$$X_i = [x_i, x_{i+j}, \ldots, x_{i+(m-1)j}] \tag{2.50}$$

where j and m are called reconstructed delay time and embedding dimension, respectively. The vector X_i, also called delay vector, has a corresponding target, namely the next sample x_i (e.g. Guatama et al., 2003). Therefore, in order to reconstruct the phase space, it is necessary to estimate j and m. Delay time is chosen such that the two values x_i and x_{i+j} are dynamically independent. There are two techniques able to estimate the delay time: autocorrelation function and the average mutual information. The first technique selects j as the first zero value of the autocorrelation function. This method has a drawback: autocorrelation function is a linear statistic and does not account for nonlinear correlation (Abarbanel, 1996). To overcome this limitation a nonlinear autocorrelation function called mutual information is used (e.g., Fraser and Swinney, 1986). It is a measure of the amount of knowledge of x_{i+j} known the value x_i and can be defined as:

$$I(\Delta t) = \sum_h \sum_k P_{hk}(\Delta t) \ln P_{hk}(\Delta t) - 2\sum_h P_h \ln P_h \tag{2.51}$$

where P_h is the probability that value x_i is in the bin h and P_{hk} is the (joint) probability that value x_i is in bin h and x_{i+j} in bin k. Using this method, time delay j is chosen as the first minimum value of mutual information and provides time when x_{i+j} adds maximum information to the knowledge that comes from x_i. In order to estimate the embedding dimension m, considered as the sufficient dimension for phase space recon-

struction and strictly related to the number of equations of the system, Cao's method (Cao, 1997) can be applied. This algorithm provides a minimum embedding estimation without any external parameters except for the delay time. Moreover, the considered method does not strongly depend on the number of samples of the investigated time series. Similarly to the false nearest neighbour method (Kennel et al., 1992), the quantity $a(i,m)$ is defined as:

$$a(i,m) = \frac{\left\| X_i(m+1) - X_{n(i,m)}(m+1) \right\|}{\left\| X_i(m) - X_{n(i,m)}(m) \right\|} \qquad i = 1, 2, ..., N - mj \tag{2.52}$$

where $\| \ \|$ is the Euclidean distance and $n(i,m) \in [1,\ N - mj]$ is an integer such that $X_{n(i,m)}(m)$ is the nearest neighbour of $X_i(m)$ in the m-dimensional reconstructed phase space (Cao, 1997). The mean value of all $a(i,m)$ is defined as:

$$E(m) = \frac{1}{N - jm} \sum_{i=1}^{N-jm} a(i,m) \tag{2.53}$$

To estimate the variation from m to m+1, the parameter $E1(m)$ is defined as:

$$E1(m) = \frac{E(m+1)}{E(m)} \tag{2.54}$$

If the time series X comes from an attractor, $E1(m)$ stops changing when m is greater than a quantity m_0. Then, the value m_0+1 is the

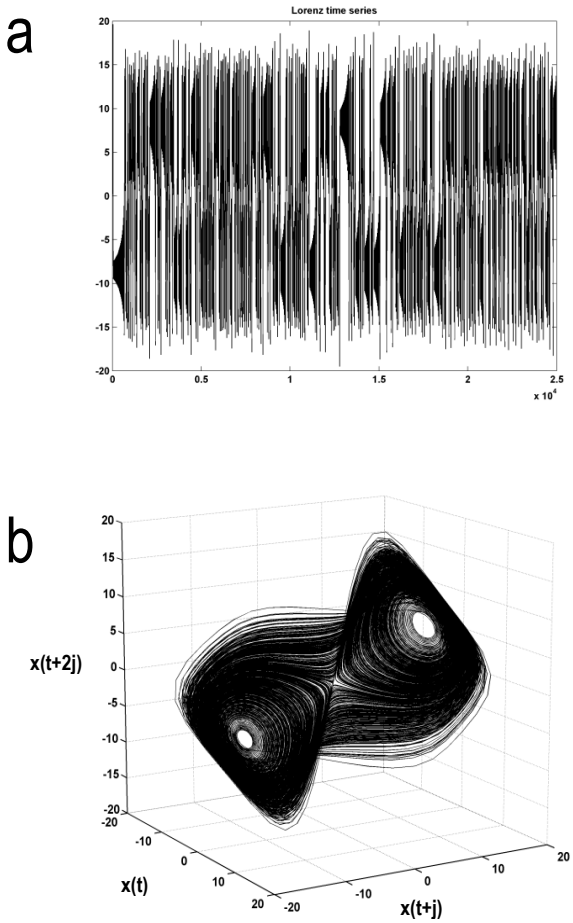

Figure 12: (a) Lorenz time series. (b) Reconstructed strange attractor.

minimum embedding dimension. In order to distinguish deterministic data from random data, Cao's method introduces a new quantity $E2$:

$$E2(m) = \frac{E^*(m+1)}{E^*(m)} \tag{2.55}$$

where

$$E^*(m) = \frac{1}{N - jm} \sum_{i=1}^{N-jm} \left| x_{i+jm} - x_{n(i,m)+jm} \right| \tag{2.56}$$

For random data the value of $E2(m)$ will be equal to 1 for any m while, for deterministic data, there will exist some values of m such that $E2(m) \neq 1$. Once delay time j and embedding dimension m are known, the phase space can be reconstructed. An example of reconstructed phase space that preserves the invariant characteristics of the original one is shown in figure 12, where the attractor (figure 12b) is reconstructed from data series (figure 12a) with a time delay j=7, estimated using mutual information (figure 13a), and an embedding dimension m=3 estimated as the first kink in the E1 and E2 plots (figure 13b). As aforementioned, exponential divergence of nearby orbits in phase space is recognized as the hallmark of chaotic behaviour (Drazin, 1994).

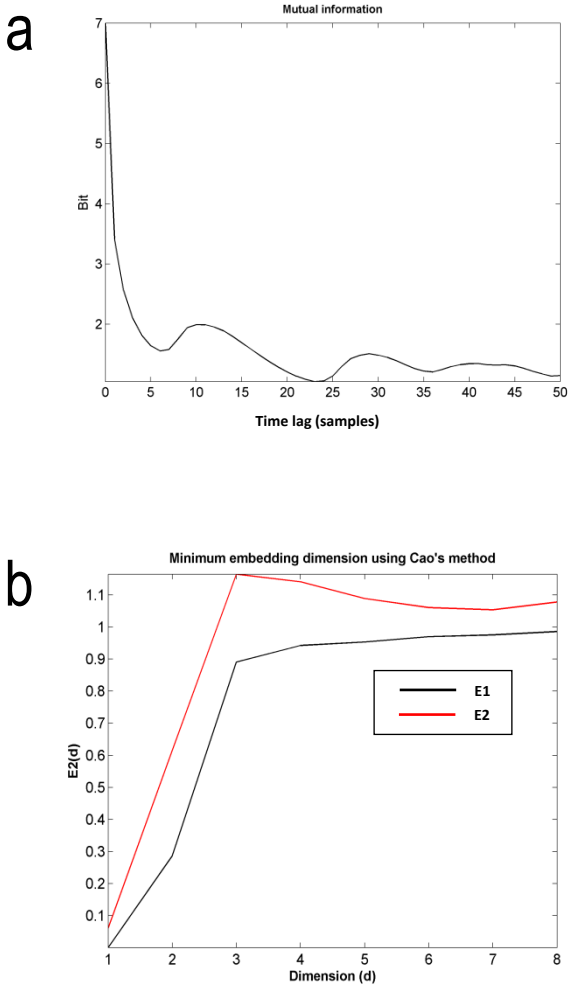

Figure 13: (a) Mutual information related to Lorenz time series. (b) Values of E1 and E2 for Lorenz time series.

Given two points in the phase space X_{n1} and X_{n2}, their distance δ_0 can be defined as $\|X_{n1} - X_{n2}\| = \delta_0$.After a time t the new distance δ will be equal to $\delta = \delta_0 exp(\lambda_1 t)$, where λ_1 is the largest Lyapunov exponent. There are several techniques for λ_1 estimation. The average exponential divergence between nearby trajectories can be studied using the prediction error:

$$p(k) = \frac{1}{Mt_s} \sum_{n=1}^{M} \log_2 \left(\frac{\left\| X_{n+k} - X_{nn+k} \right\|}{\left\| X_n - X_{nn} \right\|} \right) \tag{2.57}$$

where t_s is the sampling time, X_{nn} is the nearest neighbour of X_n, and k is the time step. For sufficient time steps k, the largest Lyapunov exponent λ_1 can be estimated by the slope of the linear segment in $p(k)$ vs k diagram. As reported in Parlitz (1998), this method provides not only the estimation of λ_1 but also a direct measure of exponential growth of distances to distinguish deterministic chaos from stochastic process.

2.3.2 Surrogate data analysis

Usual methods widely applied in chaos theory, such as saturation of correlation dimension and the existence of positive Lyapunov exponent, alone do not provide sufficient evidence of the presence of deterministic chaos in the observed time series (Govindan et al., 1998; Mitschke and Dämmig, 1993). The method of surrogate data analysis was developed for the first time by Theiler et al., 1992, to detect the presence of nonlinearity in time series. Since one of the necessary hypothesis for chaotic dynamics is nonlinearity, the technique has been widely applied to rule out the null hypothesis of linear stochastic process in an observed time series (e.g. Theiler et al., 1992; Fell et al., 1996). The surrogate time series method test a specified null hypothesis about the underlying dynamics of a given time-series. In order to accomplish this task, a group of surrogate time series are constructed from the original in such a way that the surrogates have all statistical properties included in the null hypothesis in common with the original, but are otherwise random (Kunhimangalam et al., 2008). As reported in Govindan et al., (1998), errors associated with the acquisition of data like bad choice of the sampling frequency, noise and digitization can lead to uncertainties in the estimation of correlation dimension. Moreover, correlation dimension estimated from uncorrelated random data converges at a value $(-2\log N)/\log\varepsilon$, where N is the number of points and ε is the length scale at which the slope of the correlation integral is calculated (Eckmann and Ruelle, 1992). In an experimental time series of limited length and finite precision, it may be impossible to distinguish nonlinear dynamics from linear dynamics involving stochastic component. For this reason, the only convergence of the correlation dimension is insufficient to confidently take the system behaviour as chaotic. In section 2.3.1 the Lyapunov exponent, λ_{max}, was de-

fined as the exponential rate of divergence of two neighboring trajectories in the phase space. However, the existence of positive Lyapunov exponent is also true for stochastic dynamical systems ande the estimation of the largest Lyapunov exponent can be problematic in presence of noise. Therefore, similarly to the correlation dimension, the λ_{max} cannot be used to brand a time series as chaotic since both the chaotic and stochastic system have a positive λ_{max} (Mitschke and Dämmig, 1993). The surrogate analysis, together with correlation dimension and positive Lyapunov exponent can provide more consistent hypotheses about the chaotic behaviour of the underlying time series process. It is important to highlight the fact that if there is nonlinearity in the data., chaos has not been proven, but only a necessary condition has been established. There are two main types of null hypothesis: simple and composite. The former asserts that the data are generated by a specific and known linear process, the latter asserts that the unknown underlying process is a member of a certain family process (Schreiber and Schmitz, 2000; Mandic et al., 2008). In order to improve the simple null hypothesis, one possible composite null hypothesis would be that the observed time series is generated by a linear stochastic process driven by Gaussian white noise constrained to produce a time series with an autocorrelation function identical to the original time series. Owing to the Wiener-Khintchin theorem, this constrain is equivalent to say that the original and surrogate time series have identical power spectrum. Let Q a discriminating statistic (for instance correlation dimension, Lyapunov exponents, entropy etc..), the null hypothesis is rejected if the observed value of Q for the data is very unlikely when the null hypothesis is true (Hou and Li, 2010). If many realizations of the experimental data are available the distribution of Q for the observed and surrogated data can be compared directly using conventional statistical test (t-test, Mann-Whitney U-test,

etc.). If the available knowledge regards only an experimental time series, surrogate data can be generated from the observed time series and the z-score Z estimated as (Stam et al., 1998; Govindan et al., 1998):

$$Z = \frac{\left| Q_d - \langle Q_s \rangle \right|}{\sigma_s} \tag{2.58}$$

where Q_d is the value of Q for the experimental data, Q_s is the value of Q for the surrogate time series, $\langle Q_s \rangle$ is the expected value of Q_s and σ_s is the standard deviation of Q_s. The value of Z provides a measure of many standard deviation *sigmas* of Q for the experimental data deviates from the expectation value of the surrogates data. Assuming the normal distribution of metric Q, the null hypothesis can be rejected for two-sided testing at a significance level of $p < 0.05$ when $Z > 1.96$ (Hou and Li, 2010). This method is general and many discriminating statistic deemed appropriate.

Various approaches have been proposed in literature for generating surrogate time series (e.g. Schreiber and Schmitz, 2000). Since the null hypothesis of linear Gaussian process implies that time series information are contained in its autocorrelation function and power spectrum, a suitable method for surrogate construction is the *random phase surrogate approach*. This kind of surrogate time series preserves the signal distribution and amplitude spectrum of the original one.

The *random phase surrogate approach* can be summarized as follow:

- Let $z(n)$ $n=1,..,N$ a general complex time series:

  $$z(n) = s(n) + iy(n) \tag{2.59}$$

  where, for real data, $y(n) = 0$, $n=1,..,N$;

- Compute the DFT of the series z(n):

$$Z(m)= S(m)+iY(m)=\frac{1}{N}\sum_{n=1}^{N} z_n e^{-2\pi i(m-1)(n-1)/N} \tag{2.60}$$

- Compute random phase set:

$$\phi_m \in [0,\pi] \qquad m=2,3,\ldots,N/2$$

- Phase randomization of the Fourier transformed data:

$$Z(m)'=\begin{cases} Z(m) \\ |Z(m)|e^{i\phi m} \\ |Z(N-m+2)|e^{-i\phi_{N-m+2}} \end{cases} \tag{2.61}$$

- Surrogate construction by Inverse Fourier Transform of $Z(m)'$:

$$z(n)'= s(n)'+iy(n)'=\frac{1}{N}\sum_{n=1}^{N} Z_m^{'} e^{2\pi i(m-1)(n-1)/N} \tag{2.62}$$

An example of *random phase surrogate* time series is shown in plot figure 14a, where nonlinear nature of Lorenz time series is investigated. Lorenz signal is produced with a sample rate of 10Hz by:

$$\begin{cases} \dfrac{dx}{dt}=a(y-x) \\ \dfrac{dy}{dt}=bx-y-xz \\ \dfrac{dz}{dt}=-cz+xy \end{cases} \qquad a=10;\ b=28;\ c=8/3 \tag{2.63}$$

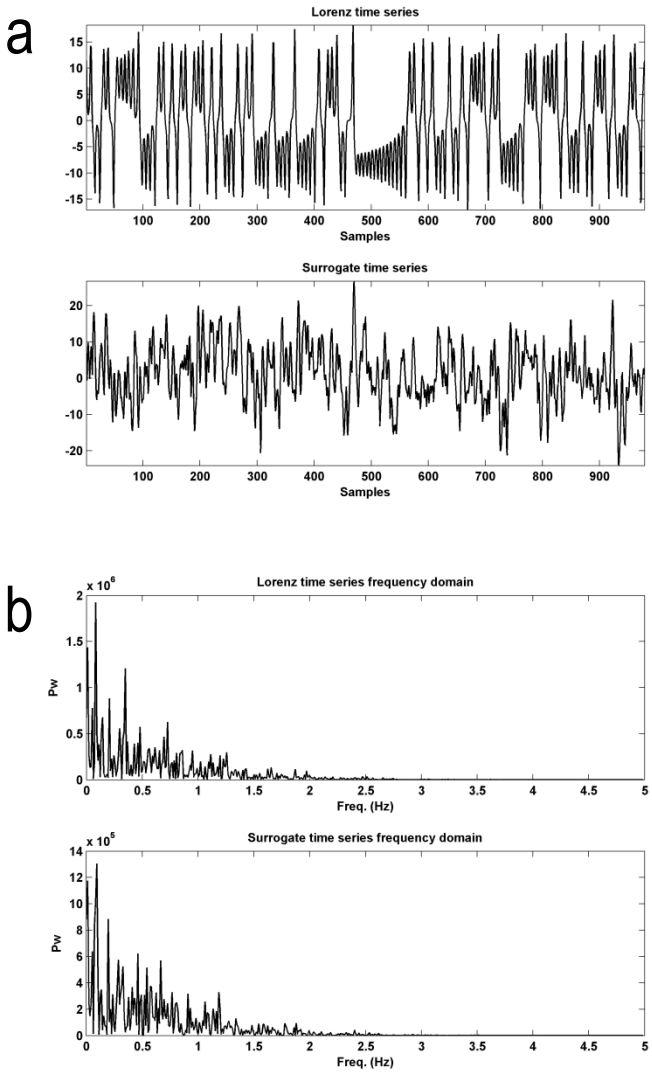

Figure 14: (a) Lorenz time series (top plot) and random phase surrogate (bottom plot.). (b) Power spectrum of Lorenz time series (top plot) and its random phase surrogate (bottom plot).

As aforementioned, the random phase approaches maintains the information related to the original time series as shown in the power spectrum reported in figure 14b.

2.3.3 Hypothesis testing

In order to detect the nonlinear nature of the investigated time series, a null hypothesis is that the original time series is generated by a Gaussian linear stochastic process (Kantz and Schreiber, 1997); it is rejected if the associate test statistic is not conform with the null hypothesis. Since the analytical form of the probability distribution of the metrics (nonlinearity measure) is not known, a nonparametric rank-based test may be used (Theiler & Prichard, 1996). From the original time series, Ns = 99 surrogate are generated; a statistic test for the original time series t_o and for the surrogates $t_{s,i}$ (i=1…Ns) is computed. The series $\{t_o\ t_{s,i}\}$ is sorted and the rank, defined as the position index r of t_o, is determined. A right-tiled (left-tiled) test rejects the null hypothesis if rank r of the original time series exceeds 90, and two-tiled test is rejected if rank r is greater than 95 or less than or equal to 5. For the analyses, it is convenient to define the symmetrical rank r_{symm} for the right-tiled tests as:

$$r_{sym} = \frac{r}{Ns+1} \tag{2.64}$$

for the left-tailed tests as:

$$r_{sym} = \frac{Ns+2-r}{Ns+1} \tag{2.65}$$

finally, for the two-tiled tests:

$$r_{sym} = \frac{\left| \frac{(Ns+1)}{2} - r \right|}{\frac{Ns+1}{2}} \tag{2.66}$$

Any of the described tests (left, right or two-tiled) are rejected if r_{symm}> 90% (Guatama et al., 2003; Mandic et al., 2008).

2.3.4 Nonlinearity metrics

As explained in section 2.3.1, nonlinearity analysis methods are based on the time-delay embedding representation of a time series in a phase space by a set of delay vector $X_i = [x_i, x_{i+j}, \ldots, x_{i+(m-1)j}]$, where j analysis can be performed by computing a statistic for a certain number of surrogates. In order to accomplish this task a nonlinearity measure is required in combination to surrogate data approach.

Traditional nonlinearity metrics used for nonlinearity measurement are the third-order autocovariance (C3) and the asymmetry due to time reversal (REV) (Schreiber and Schmitz, 1997). The former is a high-order extension of the traditional autocovariance and can be expressed as:

$$\beta_{C3}(\tau) = \langle x_k x_{k-\tau} x_{k-2\tau} \rangle \tag{2.67}$$

where τ is a time lag. A time series is said to be reversible if its probability properties are invariant with respect to time reversal (Guatama et al., 2003; Mandic et al., 2008).

Time reversal is preserved by a static transform and can be expressed as:

$$\beta_{rev}(\tau) = \left\langle \left(x_k - x_{k-\tau}\right)^3 \right\rangle \tag{2.68}$$

For a time series generated by a linear process, the expected value of $\beta_{rev} \approx 0$. In contrast, time series generated by a nonlinear dynamics is asymmetrical in time and may yield values of $\beta_{rev} > 0$ or $\beta_{rev} < 0$ (Hou and Lin, 2010). It has been shown in Schreiber and Schmitz, 1997, that in combination with the surrogate data approach, C3 and REV measures yield two-tiled tests for nonlinearity.

2.3.5 The δ-ε method

The δ-ε was used for model-free examination of the degree of predictability of a time series (Kaplan, 1994; Kaplan, 1997). Let time delay vectors Xi and Xj, the $\delta_{i,j}$ Euclidean distance is computed. Then, distance between the corresponding targets x_i and x_j is computed and denoted as $\varepsilon_{i,j}$. Let $\varepsilon(r)$ averaged ε-values conditional to $r \leq \delta_{j,k} \leq r+\Delta r$, where Δr is the width of the 'bind' used for averaging $\varepsilon_{j,k}$. Then, the smallest value for $\varepsilon(r)$ denoted as $\lim_{r\to 0} \varepsilon(r)$ is a measure of predictability of the time series. A Heuristic way for determining E value is the Y-intercept of the linear regression of $N_\delta(\delta,\varepsilon)$-pairs with smallest δ (Mandic et al., 2008).

2.3.6 Deterministic versus stochastic plots

Deterministic versus stochastic plots (DVS) method was introduced by Casdagli, 1991, and is based on the averaged prediction error *E(n)* for local linear models of a given embedding dimension *m* as a function of the number of data points within the local linear model. The degree of locality is controlled by the number of nearest delay vectors (DVs) of the given embedding dimension. A complete set of DVs is then divided into a test set V_{test} and training set V_{train}. For every DV X_k in the test set, a subset Ω_k is generated by grouping the DV in the training set nearest to X_k. The prediction error *E(n)* can be computed as:

$$E(n) = \left\langle \left| x_k - \hat{x}_k \right| \right\rangle_{X_k \in Vtest} \tag{2.69}$$

where $\hat{x}_k$ is the output of local linear model whose parameters are computed using the set Ω_k and X_k as input (Guatama et al., 2004). The prediction error computed as a function of the degree of locality, defined as the number *n* of DVs in the set Ω_k, provides information about the nonlinearity nature of the time series. The DVS plots represent *E* as a function of the number of false neighbours *n*. The position of the minimum in the DVS plot is used as an indicator of the nature of the investigated time series. The left-hand side is referred as 'local linear extreme' and a minimum near to it indicates a deterministic nature. The right-hand side is referred as 'global linear extreme' and a minimum of E indicates a linear and stochastic nature. Minima occurring between two extremes are an indication of nonlinearity (Casdagli, 1991; Guatama et al., 2004; Mandic et al., 2008).

2.3.7 Delay vector variance method

Delay vector variance method (DVV) is an approach related to the δ-ε method, DVS (Casdagli, 1991) and false nearest neighbors (Kennel et al., 1992). For a given embedding dimension m, DVV approach can be summarized as follows (Gutama et al., 2003; Guatama et al., 2004; Mandic et al., 2008; Hou and Li, 2010):

- Construct the delay vectors X_k and compute the mean μ_d and standard deviation σ_d for all pairwise Euclidean distances between the DVs: $\|X_i - X_j\|_{i \neq j}$;
- The set Ω_k (k=1,..,N) are generated considering all DVs that lie closer to X_k than a threshold distance r_d, where $\Omega_k(r_d) = \{X_i \| X_k - X_i\| \leq r_d\}$. The distance rd is taken from the interval $[max\{0,\mu_d-\eta_d\sigma_d\}; \mu_d+\eta_d\sigma_d]$ uniformly spaced where η_d is a parameter controlling the span over which to perform the DVV analysis;
- For every set Ω_k the variance of the corresponding target $\sigma_k^2(r_d)$ is computed. The target variance $\sigma^{*2}(r_d)$ is computed by averaging over all set Ω_k the variance $\sigma_k^2(r_d)$ and normalizing by the variance of the time series σ_x^2:

$$\sigma^{*2}(r_d) = \frac{\frac{1}{N}\sum_{k=1}^{N}\sigma_k^2(r_d)}{\sigma_x^2} \tag{2.70}$$

The variance measurement is considered valid if the set $\Omega_k(r_d)$ contains at least N_o=30 DVs. When the time series exhibit some kinds of structure and the embedding dimension and time lag are correctly determined, similar delay vectors (in term of Euclidean distance) have similar targets

(Kaplan, 1994). In this case, the target variance conveys information regarding the predictability of the time series. The DVV-plots are obtained by plotting the target variance $\sigma^{*2}(r_d)$ as a function of the standardized distance (in statistical sense) defined as $(r_d - \mu_d)/\sigma_d$. The minimal target variance $\sigma^{*2}_{min} = min_{r_d}(\sigma^{*2}(r_d))$ is a measure of the amount of noise, that represents the stochastic component in the analyzed time series. To illustrate the DVV approach, the nonlinear nature of Lorenz time series is investigated. In particular, the DVV analysis is performed on both the original and a 99 surrogate time series. In figure 15 the target variance versus standardized distanced is shown for both original time series and the mean of target variance of the surrogate. The difference between target variance of the original and surrogate, suggests the nonlinear nature of the investigated time series.

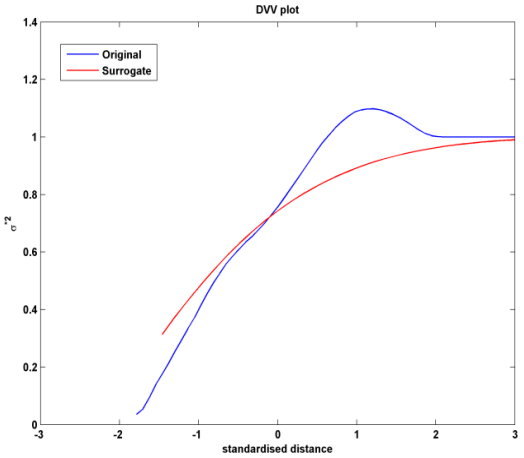

Figure 15: Plots of the target variance as a function of standardized distance.

A more reliable plot can be obtained by using a *DVV scatter diagram* plotting the target variance of the original time series against the mean

of the target variances of the surrogate data. If the DVV plots of the surrogate and original time series are similar to each other, then the DVV scatter diagram coincides with the bisector line. In this case, the original time series is judged to be linear. Conversely, when the DVV scatter diagram shows a deviation from the bisector line, the original time series can be judged nonlinear. In figure 16 the DVV scatter diagram for Lorenz time series is shown; the deviation from the bisector line is an indication of the nonlinear nature of the observed time series.

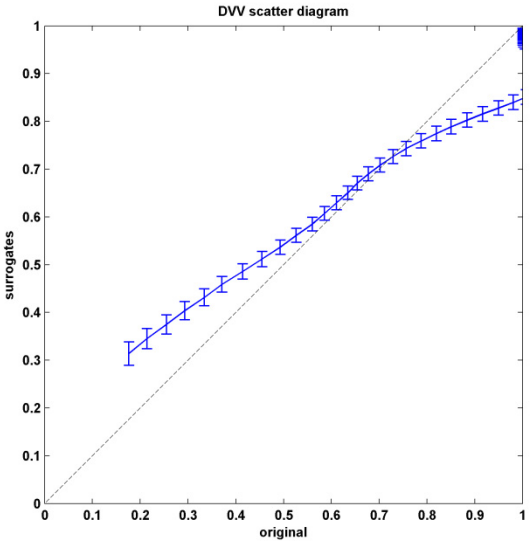

Figure 16: DVV scatter diagram obtained by plotting the target variance of the original Lorenz time series against the mean of the target variance of the surrogate data.

The degree of nonlinearity can be quantified by measuring the deviation of the DVV scatter diagram from the bisector line. This task is very useful for statistical testing and can be performed by computing the root

mean square error (RMSE) between the target variance σ^{*2} of the original time series and the averaged target variance of the surrogate time series (Mandic et al., 2008):

$$t^{DVV} = \sqrt{\left\langle \left(\sigma^{*2}(r_d) - \frac{\sum_{i=1}^{N_s} \sigma_{s,i}^{*2}(r_d)}{N_s} \right)^2 \right\rangle} \tag{2.71}$$

Since the DVV plot represents a test statistic, a traditional right-tailed surrogate testing can be performed. In order to improve the performance of the DVV method, the nonlinear nature of Lorenz time series (figure 14a) is tested using traditional nonlinear metric as C3 and REV (see section 2.4) and 99 surrogate time series.

For DVV method, a right-tailed test is rejected if rank r exceeds 90 while, for C3 and REV, a two-tailed test is rejected if the rank r is less than or equal to 5 or greater than 95. As explained in section 2.3.3, by using the quantity r_{symm} the described tests (right or two-tailed) are rejected if r_{symm}>90% (i.e. significant rejection of the null hypothesis at level α = 0.10). The comparison results of the three aforementioned methods (DVV, C3 and REV) are shown in table 1. In particular, for the considered simulation, REV method does not detect the nonlinear nature of the Lorenz time series. Other two simulations are computed on AR model (table 2) and Henon time series (table 3). According to test statistic, DVV approach yields more consistent results with respect to the other two methods.

Table 1: result of the rank test for the Lorenz time series

C3	REV	DVV
1	32	100
nonlinear	**linear**	**nonlinear**

Table 2: result of the rank test for the AR time series

C3	REV	DVV
2	64	38
nonlinear	**linear**	**linear**

Table 3: result of the rank test for the Henon time series

C3	REV	DVV
100	1	100
nonlinear	**nonlinear**	**nonlinear**

Other simulations about the robustness of DVV method can be found in literature (e.g. Guatama et al., 2003; Guatama et al., 2004; Mandic et al., 2008; Hou and Li, 2010).

Chapter 3

Pattern recognition analysis methods

Automatic extraction, recognition, description and classification of patterns extracted from images and signals are the most important tasks in several scientific disciplines. In the last years pattern recognition techniques together with time series analysis constitute a novel research field in active volcano modelling and can provide useful information for monitoring purposes. There are many definitions of pattern recognition (hereafter referred to as PR). Fukunaga (1990) defined PR as the problem of estimating density functions in a high-dimensional space and dividing the space into regions of categories of classes. Duda and Hart (1973) defined PR as a field concerning machine recognition of meaningful regularities in noisy or complex environments. Gonzalez and Thomas (1978) defined PR as the process of classifying input data via extraction of significant features from a set of noise data. Other definitions of the term pattern are given by several authors. Pavlidis (1977) refers the word pattern to the root of word *patron* that is used to indicate something which is set up as a perfect example to be imitated. The main aspect of PR is the definition of a set of peculiar features or descriptive elements of the analyzed objects. Given a pattern, the recognition process consists of one of the following tasks: i) supervised classification in which the patterns are classified on the basis of a known learning rule; ii) clustering that is the process of grouping sets of objects into classes called clusters with no

a priori knowledge. In the first case the classifier design can be implemented by several techniques, implying the definition of a metric based on template matching or the minimum distance between pattern and class prototype. There are different methods for metric definition, such as vector quantization and learning vector quantization (Oehler and Gray, 1995; Xie et al., 1993). For instance, in statistical pattern recognition classification process is based on probabilistic approaches: the pattern-class association is computed on the basis of a probability density function. The optimal Bayes decision rules assign a pattern to a class with the maximum posterior probability (Jain et al., 2000). Other classification techniques are based on geometric approaches. These kinds of classifiers are based on a training procedure that minimizes an error (such as the mean square error, MSE) computed comparing classification output and target value. Typical examples are Fisher's linear discriminant (LDA) and single layer perceptron (SLP). The former minimizes the MSE between the classifier output and the desired label, the latter iteratively updates the decision surface in the form of hyperplane between classes. Fisher's discriminant can be extended in non-linear classification where original observations are mapped into a higher dimensional non-linear space. Applying linear classification on this higher dimensional space is equivalent to non-linear classification in the original space. The most commonly used technique is the kernel Fisher discriminant (Mika et al., 1999). The nonlinear extension of SLP is the Multi Layer Perceptron (MPL) that allows nonlinear decision boundaries and overcomes many of the limitations of single layer perceptron. A powerful method in classifier design is the Support Vector Machine (SVM) introduced by Vapnik (1998). This algorithm is different from other hyperplane-based classifiers such as SLP. The problem of estimating hyperplane separating two classes is not unique. The SVM algorithm is able to find the optimal hy-

perplane that separates the classes. Beyond supervised classification, the other important task in PR is the clustering problem, that, as aforementioned, is the process of grouping data without any a priori information.

3.1 Clustering: an overview

Objects belonging to the same cluster will be more similar than objects belonging to different clusters with respect to some given similarity measures. An object could be referred to a physical object or, in general, to a physical recording, such as a waveform, on which a set of quantitative descriptive elements can be identified. A pattern is a set of features describing an object and generally is represented as a vector. In the light of it, a set of patterns is represented by a *pattern matrix*. The problem of clustering arises in many different scientific fields, and, thus, a vast amount of literature has been produced on the subject. The clustering methods exist can be broadly divided into hierarchical and partitioning (Berkhin, 2002). Hierarchical algorithms gradually (dis)assemble objects into clusters. On the other hand, partitioning algorithms learn clusters directly trying to discover clusters either by iteratively relocating points between subsets or by identifying areas heavily populated with data. This second type of partitioning algorithms attempts to discover dense connected components of data. Examples of algorithms belonging to such a category are: DBSCAN, OPTICS, DENCLUE (Berkhin, 2002).

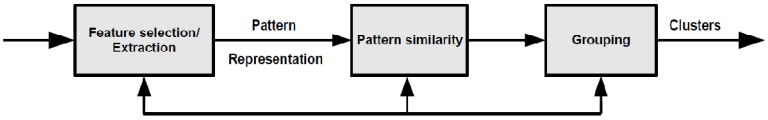

Figure 1: Clustering stages.

In figure 1 a general clustering task is shown (Jain and Dubes,, 1988). It can be synthesized as follow:

- pattern representation;
- definition of pattern proximity measure appropriate to the data domain;
- clustering algorithm;
- data abstraction (if needed);
- assessment of clustering result.

As reported in Jain et al., 1999, the pattern representation refers to the number of classes, number of available patterns, and number, type and scale of the features available for the clustering algorithm. While the *feature selections* task identifies the most effective features for discriminating available patterns, the *features extraction* can be defined as the process transforming the available features into new features with the purpose to better describe characteristics usable in the clustering process. For instance, considering a simply decaying waveform, the descriptive characteristics may be the frequency peak, a measure of decay and the amplitude. *Pattern proximity* is usually evaluated by a distance function defined on pairs of patterns. Given a set of n patterns with d features the pattern set can be expressed in matrix form using an $n \times d$ matrix. The jth feature of the generic ith pattern is x_{ij}. Using this notation, the ith pattern is described by the column vector $x_i = [x_{i1} x_{i2} \dots x_{id}]^T$.

The clustering process requires proximity indices between all pairs of patterns (Dubes, 1993). A possible distance index is the Minkowski metric defined as:

$$d(p,q)=\left(\sum_{j=1}^{d}\left|x_{qj}-x_{rj}\right|^{m}\right)^{1/m}=\left\|X_q-X_r\right\|_m \tag{3.1}$$

where q and r are pattern matrix indices. For m=2 the Minkowski metric produces the Euclidean distance between two patterns, while for m=1 results in the Manhattan distance (e.g. Aldridge, 2006; Jain et al., 1999). In particular, the Euclidean distance is commonly used to evaluate proximity of objects in two or three-dimensional space and it is a good choice when the data set has compact or isolated clusters (Mao and Jain, 1996). To avoid features of large degree dominate the others, normalization process of the feature is required. A simple normalization can be performed by a mapping process of the original feature space into the range [0,1] by dividing the distance for each feature by the feature's range. The features distance measures can be distorted by the presence of a linear correlation. To overcome this problem a whitening process of the data can be applied or the squared Mahalanobis distance can be used:

$$d_M\left(X_q-X_r\right)=\left(X_q-X_r\right)\Sigma^{-1}\left(X_q-X_r\right)^T \tag{3.2}$$

where the patterns X_q and X_r are row vectors, $\sum$ is the covariance matrix. This distance definition assigns different weights to different features based on their variances and pairwise linear correlation (Jain, 1999). It is noteworthy that distances computation between pairs of patterns exhibiting some or all noncontinuous features, may be problematic. In order to overcome this problem, a proximity measure for heterogeneous types of

pattern should be used. For instance, Wilson and Martinez (1997) have proposed a combination of a modified Minkowski metric for continuous features and a distance based measure for nominal attributes. A variety of other metrics can be found in Diday and Simon (1976) and Ichino and Yaguchi (1994). Another way of representing patterns is by using string or tree structures (Knuth, 1973). In particular, patterns string representation is commonly used in syntactic clustering (e.g. Fu and Lu 1977). Several measures of similarity between strings can be found in Baeza-Yates (1995), while similarity measures between trees are reported in Zhang (1995). Once the indices of dissimilarity or similarity have been computed, the outliers can be identified based on high distances from other patterns. Depending on the data domain and the intended goal of the clustering process, such outliers may be removed prior to applying a clustering algorithm. However, outliers sometimes provide useful information that would otherwise be lost if removed prematurely (Aldridge, 2006).

3.1.1 Hierarchical versus patitional algorithms

Hierarchical clustering builds a cluster hierarchy or a tree of clusters, also known as a dendrogram. Each node in the dendrogram represents a cluster. The root of the dendrogram is a cluster that includes all objects, while each child contains a sub-cluster of its parent node. Hierarchical clustering methods are categorized into agglomerative (bottom-up) and divisive (top-down) (Jain and Dubes, 1988; Kaufman and Rousseeuw, 1990). The agglomerative clustering process starts with one-point clusters, called singleton, and recursively merge two or more of the most similar clusters. A divisive hierarchical clustering, by beginning with the root node, starts with a single cluster containing all data points and recursively splits the most appropriate clusters. The process continues until a stopping criterion (for example the requested number k of clusters) is achieved. The height of each node is proportional to the measure of similarity or dissimilarity between its sub-clusters. Typically, the leaf nodes in the dendrogram represent individual patterns. The hierarchical clustering approach allows data exploration on different levels of granularity (figure 2).

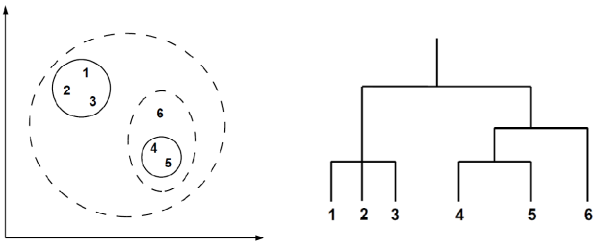

Figure 2: a) A possible set of clusters for six patterns. B) Dendrogram corresponding to the clusters of a).

The creation of a hierarchical clustering may involve excessive time and space constraints, because the algorithm used must make an iteration for each level in the hierarchy (Dunham, 2003).

Another clustering approach is the partitional clustering algorithm producing a single partition of the patterns. This kind of clustering process requires less time and space than hierarchical clustering. However, partitional methods require the user to choose a specific number k of clusters, in general known a priori, to be created. Additionally, while a partitional method produces only one final set of clusters, the algorithm may create the final set iteratively, in the form of iterative optimization, beginning each time with a different starting configuration and choosing the best result from all the runs (e.g. Jain et al., 1999). Unlike traditional hierarchical methods, in which clusters are not revisited after being constructed, relocation algorithms can gradually improve clusters. With appropriate data, this results in high quality data (Berkhin, 2002). Another kind of partitioning algorithm is the *Density-Based Partitioning*. As the name suggests these clustering approaches rely on a density-based notion of clustering and are capable of discerning clusters of arbitrary shape in spatial database with noise. One of the best known density based clustering approach is the Density-Based Spatial Clustering of Applications with Noise (DBSCAN).

3.1.2 Cluster assessment

Process of cluster assessment is multi-faceted. Indeed, this process can be involved in the assessment of data domain itself or as a validation of clustering results. The former should be verified if the data set contains a reasonable number of clusters prior to performing cluster analysis. In this process the assessment procedure should be used to estimate if the data set has a low cluster tendency, meaning there is or no a benefit in attempting to perform clustering. In this case, data which do not contain clusters should not be processed by a clustering algorithm. (e.g. Jain et al., 1999; Aldridge, 2006).

Assessment process as validation task is the goodness estimation of the clustering algorithm results. Let K_m as cluster of N points $\{t_{m1},t_{m2},...,t_{mN}\}$, three typical measurements are proposed in Dunham (2003) and are *centroid*, *radius* and *diameter* respectively. The *centroid* can be viewed as the middle of the cluster and may not coincide with a point of cluster itself. It can be expressed as:

$$C_m = \frac{\sum_{i=1}^{N} t_{mi}}{N} \tag{3.3}$$

Alternatively, a *medoid* can be defined as the centrally located point of the cluster. The *radius* represents the averaged mean squared distance from any point to the cluster's centroid. It is defined as :

$$R_m = \sqrt{\frac{\sum_{i=1}^{N} (t_{mi} - C_m)^2}{N}} \tag{3.4}$$

The diameter is defined as the square root of the averaged mean squared distance between all pairs of points in the cluster. The diameter of a cluster m is then defined as:

$$D_m = \sqrt{\frac{\sum_{i=1}^{N}\sum_{j=1}^{N}\left(t_{mi} - t_{mj}\right)^2}{N(N-1)}} \tag{3.5}$$

Common clustering evaluation involves the clusters distance by utilizing the centroid of cluster. In Dubes (1993) three types of validation studies are reported. In particular, an *external* assessment of validity compares the recovered structure to an *a priori* structure and attempts to quantify match between the two. An *internal* examination of validity tries to determine if the clustering structure is intrinsically appropriate for the data. This assessment considers whether a given cluster is unusually compact or isolated compared to other clusters of the same size in random data (Aldridge, 2006). A *relative* test compares two structures and measures their relative merit (Jain et al., 1999). Indices used for this comparison are discussed in detail in Jain and Dubes (1988) and Dubes (1993). An internal cluster validation measure is the Davies-Bouldin (*DB*) index (Davies and Bouldin, 1979). Such an index is function of the number of clusters, the inter-cluster and within-cluster distances. Formally it is defined as follows:

$$DB = \frac{1}{n}\sum_{i=1}^{N}\max_{i\neq j}\left\{\frac{S_n(Q_i) + S_n(Q_j)}{S_n(Q_i, Q_j)}\right\} \tag{3.6}$$

where S_n is the average distance of all cluster objects to their cluster centers, $S(Q_i, Q_j)$ is the distance between clusters centers. Small values of *DB* correspond to compact clusters whose centres are far away from each

other. In the light of it, the number of clusters that minimizes *DB* is taken as the optimal number of clusters.

3.1.3 Squared error clustering and k-means algorithm

Partitional clustering algorithms perform a subdivision of data set into clusters based on some distance metrics. The most common used criterion function is the squared error criterion, which tends to work well with isolated and compact clusters. This kind of methods is iterative and the clustering process terminates when a stopping criterion is met. For example, a common stopping criterion is met when squared error between successive iterations ceases to decrease significantly. Let a cluster C of size k and a pattern set X, the squared error is defined as:

$$e^2(X,C)=\sum_{j=1}^{k}\sum_{i=1}^{n_j}\left\|x_i^{(j)}-c_j\right\|^2 \tag{3.7}$$

where j represents the cluster number, n_j denotes the number of elements, $x_i^{(j)}$ represents the ith pattern of cluster j and c_j is the centroid of jth cluster (Jain et al., 1999). General squared error clustering can be summarized as follows: 1) Set an initial partition of the data into k clusters and calculate initial k cluster centers. 2) Assign each pattern to its closest cluster center and compute the new cluster centers based on the new cluster assignments; compute the squared error; repeat this step until a stopping criterion is not met (i.e., until the cluster membership is stable). 3) Merge and split clusters based on some heuristic information, optionally repeating step 2. The most common square error clustering method is the k-means clustering algorithm (McQueen, 1967). It differs from the general squared error clustering method only in the initializa-

tion phase where k cluster means are chosen and patterns are assigned to its closest mean. In this case the cluster mean is defined as:

$$c_j = \frac{1}{n_j} \sum_{i=1}^{n_j} x_i^{(j)} \tag{3.8}$$

The k-means algorithm is easy to implement, and its time complexity is $O(n)$, where n is the total number of patterns. This algorithm converges to a locally but not globally optimal solution and depends on the choice of the initial cluster means. K-means algorithm can be summarized as follows (Jain et al., 1999): 1) Choose k cluster centers to coincide with k randomly-chosen patterns or k randomly defined points inside the hypervolume containing the data set. 2) Assign each pattern to the closest cluster center. 3) Recompute the cluster centers using the current cluster memberships. 4) If a convergence criterion is not met, repeat step 2. Typical convergence criteria are: no (or minimal) reassignment of patterns to new cluster centers, or minimal decrease in squared error. Since k-means algorithm is based on the concept of *centroid*, it is sensitive to noise and outlayer and a data filtering procedure is required. One solution is the use of feature weighting and a distortion measure to produce a partition that will minimize average within-cluster variance while simultaneously maximize the average between cluster distances (Modha and Spangler, 2002). Several variants (Anderberg, 1973) of the k-means algorithm have been reported in the literature.

For instance, another distance measure may be (Wu et al., 2004):

$$d(x, y) = 1 - e^{-\beta \|x-y\|^2} \tag{3.9}$$

β is a positive constant. The measure provided by equation (3.9) is robust to data outlayer and noise. Other methods are based on the idea of downweight data outlayer respect to its cluster centroid (Wu and Yang, 2002). As aforementioned, k-means algorithm assumes that the number k of clusters is known a priori. In practical applications the optimal value of k is, in general, not known. To overcome this limitation, many k-means clustering algorithms are executed with many values of k. The best k value is then determined on the basis of some cluster assessment criterions (section 3.2.). A possible approach may be the use of validity algorithms such as Davies-Bouldin (DB) index. As explained in section 3.2., the number of clusters that minimizes DB is taken as the optimal number. An example of 3-class k-means together with DB index is shown in figure 3. In particular, figure 3a shows the best 3-clustering structure of the data set, while figure 3b shows the value of DB index for increasing value of k. The best cluster number is chosen on the basis of minimum value of DB index. As aforementioned, k-means algorithm is very sensitive to the choice of the initial partition leading to a locally optimal solution instead of a globally optimum. To alleviate this problem, different initialization strategy have been proposed. One of the common initialization method is the Random Approach (RA) where the initial partitioning is computed in random way. Other methods that apply different strategy can be found in Pena et al., (1999) and Likas et al. (2003).

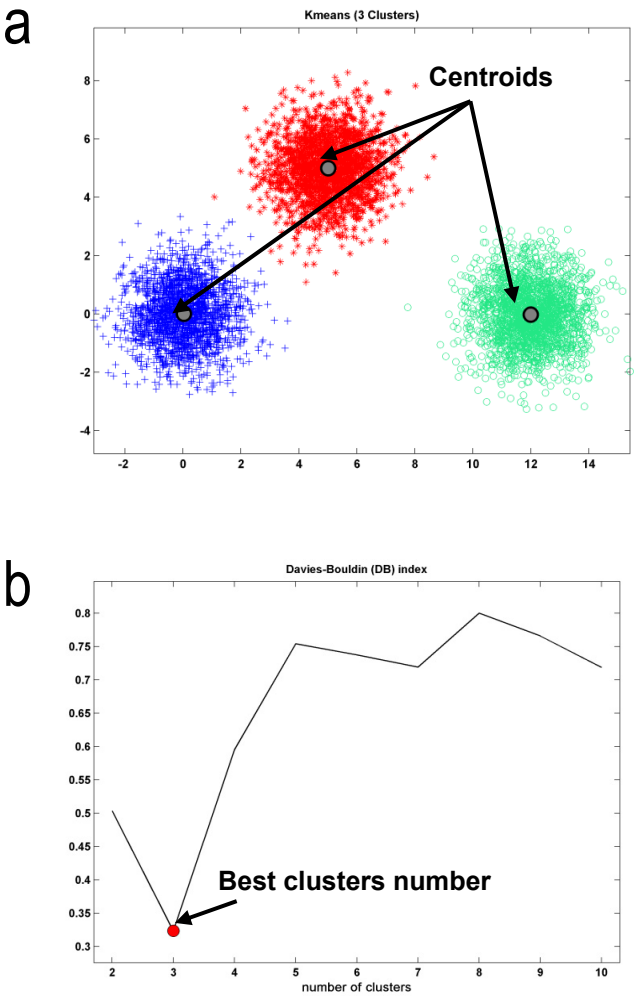

Figure 3: a) A features plane with three clusters; b) best clustering structure computed on the features plane using Davies-Bouldin index.

3.1.4 Clustering algorithm based on DBSCAN

DBSCAN (Density-Based Spatial Clustering of Applications with Noise; Ester et al., 1995) is a density-based clustering algorithm able to discover clusters of arbitrary shape in spatial databases with noise (figure 4). Clusters are defined as maximal sets of density-connected points. Usually DBSCAN runs on datasets drawn from multidimensional or metric spaces and uses a distance function to compare objects. Given a dataset D of objects DBSCAN makes use of the following structures and definitions: i) *ε-neighbourhood*, ii) *core point*, iii) *directly density-reachable*, iv) *density-reachable* and v) *density-connected*. The *ε-neighbourhood* of a point p, denoted by $N_\varepsilon(p)$, is a subset of points q in D, such that a distance measure $dist(p,q)$ (such as the Euclidean distance) is lower than ε. The point p is called *core point* or *core object* if its *ε-neighbourhood* has cardinality above a minimum threshold called *MinPts*. Each point q which lies in the *ε-neighbourhood* of a point p is called *directly density-reachable* from p (figure 5a). A point q is *density-reachable* from a point p with respect to ε and *MinPts* if there is a chain of points $q_1,...,q_n$ such that $q_1=p$, $q_n=q$ and q_{i+1} is *directly density-reachable* from q_i for each I (figure 5b). A point q is *density-connected* to a point p with respect to ε and *MinPts* if there is

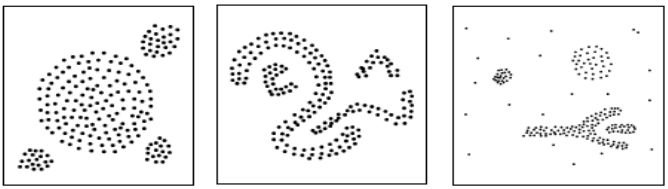

Figure 4: Different clusters shape.

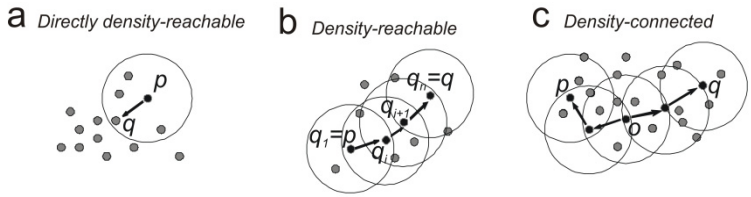

Figure 5: Examples of (a) directly density-reachable, (b) density-reachable, (c) density connected in density-based clustering.

a point *o* such that both *p* and *q* are *density reachable* from *o* with respect to *ε* and *MinPts* (figure 5c). Given *D*, *ε* and *MinPts* as input parameters, DBSCAN clusters *D* by checking the *ε-neighbourhood* of each object in *D*. If the *ε-neighbourhood* of an object *p* contains more than *MinPts*, a new cluster with *p* as *core object* is created. DBSCAN iteratively collects *directly density-reachable* objects from these *core objects*. The process terminates when no new objects can be added to any cluster. In such a case the algorithm will return the set of clusters and a special cluster containing outliers.

3.1.5 Self Organizing Maps (SOM)

Self-Organizing Map (SOM), also known as Kohonen map (Kohonen, 1989), is a popular neural network approach based on unsupervised learning, that represents a general paradigm for knowledge extraction from a large and heterogeneous amount of data. Self-organization refers to the ability of a biological or technical system to adapt its internal organization to structures sensed in the input of the system. In the context of knowledge discovery, in which the dimension, complexity or the amount of data has so far been prohibitively large for human observation

alone, SOMs represent a useful tool in data exploration and visualization. The SOM consists basically of two layers of so called units or neurons. The input layer consists of N elementary computational units or neurons corresponding to the real-valued input data vector X of dimension N. These units are connected to a second layer of neurons U. SOM maps high-dimensional input data vectors $\in \mathcal{R}^n$ onto two-dimensional grid of prototype vectors that are easier to visualize and explore than the original data. A reference weight vector, also called prototype vectors, $m_i = [m_{i1}, m_{i2}, \ldots, m_{iN}] \in \mathcal{R}^n$, are associated with each neuron in the map and N is the dimensionality of the input data. By means of lateral connections, the neurons in U form a lattice structure of dimensionality M which is typically much smaller than N (Utlsch, 2000). The fundamentals of SOM are the competition between nodes in the output layer.

The basic algorithm is " winner takes all" where not only one node (the winner) but also its neighbours are updated. When an input data vector is presented to the network, it responds with a unit in the output layer closest to the presented input. This unit is called best-matching unit. From a mathematical point of view, at each iteration, the distance among prototype vector and the input space X are calculated. The best matching unit b represents the neuron with prototype vector closest to X satisfying the equation:

$$\|X - m_b\| = \min_i \{\|X - m_i\|\} \tag{3.10}$$

The prototype vector of each neuron i is updated following the rule:

$$m_i(t+1) = m_i(t) + \alpha(t)\, h_{bi}(t)\left[X - m_i(t)\right] \tag{3.11}$$

where t is the time, α(t) is the learning rate, h_{bi} is a neighbour function between neuron i and best matching unit b. Both the learning rate and the neighbour function decrease monotonically over time. In particular, assuming h_{bi} to be Gaussian, it can be expressed as:

$$h_{bi}(t) = e^{-\|r_b - r_i\|^2 / \left(2\sigma^2(t)\right)} \tag{3.12}$$

where r_b and r_i are the position of neuron i and b respectively, $\sigma(t)$ is the standard deviation of the Gaussian. As a result of learning process, the presentation of all input vectors and the adaptation of weight vectors generate a mapping from input space onto the lattice output layer (figure 6) with the property that topological relationships in input space are preserved (Ritter and Schulten, 1986; Kohonen, 1989).

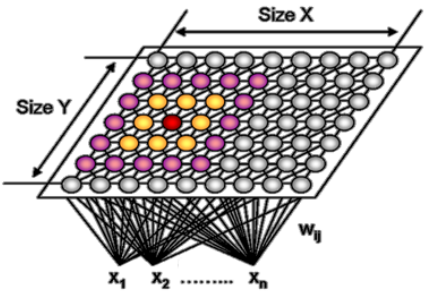

Figure 6: SOM lattice structure.

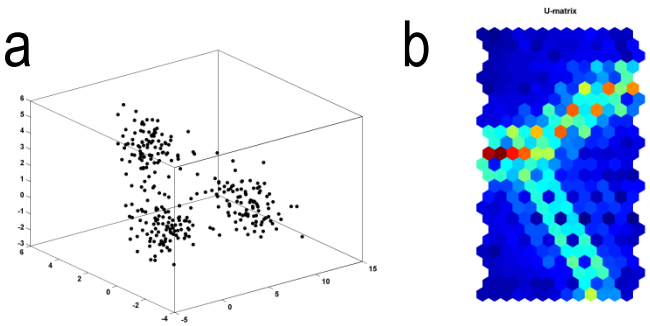

Figure 7: a) 3D feature space with three clusters; b) U-Matrix after learning. The blue regions are related to neuron that are near to each other underling the existence of clusters.

As aforementioned, the aim of visualization is to present large amount of detailed information in order to give a qualitative idea of data properties (Vesanto, 2000). Typically the number of properties that need to be visualized is much higher than the number of usable visual dimensions. The low-dimensional map obtained by SOM algorithm provides a 2D projection of the high dimensional data that can be visually inspected. A common way to visualize the presence of clusters after SOM learning process is the so called unified distance matrix (U-matrix). In order to calculate the U-Matrix the averaged distances between each neuron and its neighbours are computed. This method provides a colour matrix representing distances between neighbouring map units, and thus shows the cluster structure of the map: high values of U-matrix indicate a cluster border while uniform areas of low values indicate clusters themselves (Ultsch, 1993). A simple example of clustering data in 3D space is reported in figure 7. More in detail, figure 7a shows the 3D data structure while figure 7b shows the SOM U-Matrix after training process. The existence of three clusters is clearly visible in the U-Matrix by the blue re-

gions. While the use of U-matrix leads to a visual inspection of the clusters, automatic clustering of SOM grid can be used to quantify the number of discovered clusters (Vesanto and Alhoniemi, 2000). By studying the final U-Matrix map, and the underlying features planes of the map, a number of cluster can be identified by k-means algorithm (see section 3.3.) (McQueen, 1967; Dubes and Jain, 1976). Figure 8a shows the Davies-Bouldin index applied on the prototype vector obtained by the SOM trained on the 3D dataset shown in figure 7a. As expected, the best clustering corresponds to a number of three clusters. The best clustering is then projected onto the SOM obtaining the new component plane shown in figure 8b. Two-level clustering process is summarized in figure 9.

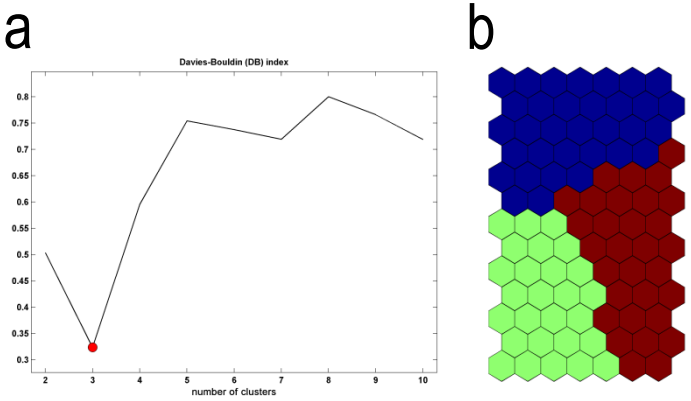

Figure 8: a) Davies-Bouldin index; b) Best clustering structure of SOM.

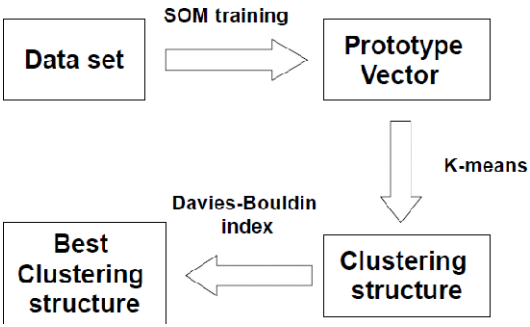

Figure 9: Two level clustering approach.

3.2 Classification task

Classification process can be defined as the task in which objects are classified on the basis of inference rules acting on a set of knowledge patterns (Joswig, 1990). The main difference between clustering and classification process is the unsupervised nature of the clustering. While the clustering process attempts to derive meaningful classes directly from the data, the traditional classification methods involve a special input training set of classes in which known objects are placed. The choice of classification algorithm is strictly related to the data structure and is guided by the prediction performance obtained by the chosen model. In particular, in the following section, the support vector machines (SVM), that are a new generation of algorithms used for regression and classification task, will be treated (Vapnik, 1995; Vapnik, 1998). SVM minimizes simultaneously the empirical classification error and maximizes the inter-class geometric margin leading to a unique solution (Burges,

1998; Cristianini and Shave-Taylor, 2000). One of the major features of this kind of algorithm is that it can work in a kernel-induced feature space allowing nonlinear modelling (Devos et a., 2009). It has been reported that the obtained classification models are robust and less subject to the curse of dimensionality and over-fitting (Belousov et al., 2002). Also, a good generalization performance can be obtained with a relatively small data set (Vapnik, 1995).

3.2.1 Support Vector Machine

Support Vector Machines (SVMs) are a popular machine learning method for solving problems in classification and regression, able to guarantee high classification quality (Burges, 1998). In recent years, novel applications of SVM have been performed in several research areas such as biology (e.g. Noble, 2004) and volcano seismology (e.g. Masotti et al., 2008; Langer et al., 2009). The SVM algorithm can be summarized as follows. It first uses a non-linear mapping to transform the original dataset into a higher dimension space. Next, it identifies a hyperplane able to maximize the *margin* of separation among the classes of the training set. Such a hyperplane is called Maximum Marginal Hyperplane (MMH). The margin in SVMs denotes the distance from the boundary to the closest data in the feature space (figure 10). With appropriate mapping, data from two classes can always be separated by a hyperplane.

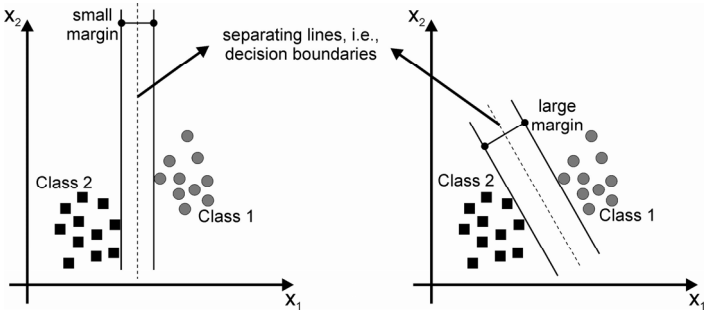

Figure 10: Two-features planes each of which with two classes of data (black squares and grey circles) and a separating line (dashed lines): the left one shows a small margin between clusters, the right one a larger margin (redrawn from Kecman, 2001).

The problem of computing the MMH can be formulated in terms of quadratic programming in the following way (Hwanjo et al., 2003):
minimize:

$$W(\alpha) = -\sum_{i=1}^{l} \alpha_i + \frac{1}{2}\sum_{i=1}^{l}\sum_{j=1}^{l} y_i y_j \alpha_i \alpha_j k(x_i, x_j) \tag{3.13}$$

subject to:

$$\begin{aligned} & W(\alpha) = \sum_{i=1}^{l} y_i \alpha_i = 0 \\ & \forall i : 0 \le \alpha_i \le C \end{aligned} \tag{3.14}$$

The number of training data is denoted by l, a is a vector of l variables, where each component a_i corresponds to a training data (x_i, y_i). C is the soft margin parameter controlling the influence of the outliers (or noise) in training data. The kernel for linear boundary function is $x_i \cdot y_i$, a scalar product of two data points. The nonlinear transformation of the feature space is performed by replacing $k(x_i, y_i)$

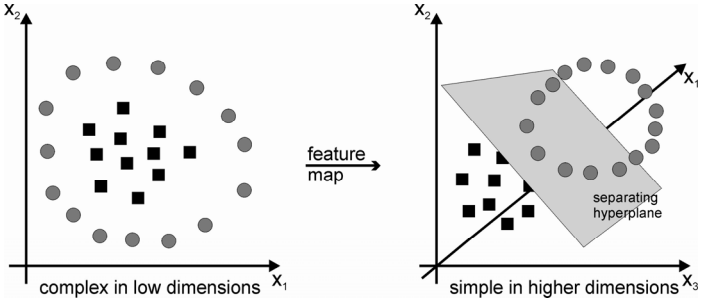

Figure 11: Two classes of data in the original 2D space (left) and in a higher-dimensional feature space (right).

with an advanced kernel φ, such as polynomial kernel $(x^T x_i + 1)^p$ or a radial basis function kernel $exp\left(-\frac{1}{2\sigma^2}\|x - x_i\|^2\right)$. The use of an advanced kernel is an attractive computational short-cut which avoids the expensive creation of a complicated feature space. An advanced kernel is a function that operates on the input data but has the effect of computing the scalar product of their images in a usually much higher-dimensional feature space (or even an infinite-dimensional space), which allows working implicitly with hyperplanes in such highly complex spaces (figure 11). The extension of SVM to multiclass problems can be performed using two different methods called one-against-one and one-against-all. The former constructs $k(k-1)/2$ classifier where each one is trained on data from two classes. The latter constructs k SVM classifier. In this last case, the ith SVM is trained using all training patterns belonging to ith class with positive labels and the others with negative labels. A point is assigned to the class for which the distance from margin is maximal. Finally, the output of one-against-all method is the class corresponding to SVM with highest output value (Weston and Watkins, 1999; Hsu and Lin, 2002).

3.3 Model selection

Typically our model will have a set of tuning parameters α that varies the complexity of our model, and we wish to find the set of α that minimizes error, that is, produces the minimum of the average test error. As mentioned the choice of such parameters is a key step in model learning because their values determine classification performance. It is important to note that there are two separate goals in a classification modeling: 1) model selection that is the task of estimating the performance of different models in order to choose the best one; 2) model assessment: having chosen a final model, estimating its predic-tion error (generalization error) on new data. As a consequence, model selection is applied with the aim of finding the best set of parameters that minimizes the error rate estimated as the ratio between misclassified and hit patterns. More in detail, in a data-rich situation, the best approach for both problems is to randomly divide the dataset into three parts: a training set, a validation set, and a test set (figure 12). The first set is used to fit the models; the second set is used to estimate prediction error for model selection; the third set is used for assessment of the generalization error of the final chosen model (Hastie et al., 2002). In practical application it is difficult to give a general rule on how to choose the number of observations in each of the three parts. In particular, it depends on the signal-to-noise ratio and the training sample size.

Figure 12: Subdivision of data set: training, validation and test.

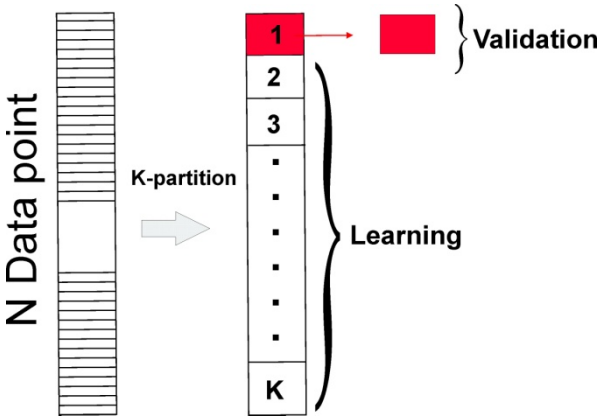

Figure 13: Basic scheme of K-Fold Cross-Validation.

A typical split might be 50% for training, and 25% each for validation and testing. In order to overcome this limitation, model parameters can be chosen using a *cross-validation* (CV) approach, which is a statistical method for learning algorithms evaluation and model selection. In particular, in *K-fold* CV the available dataset is partitioned into K subsets or "folds": K-1 folds are used for classifier learning purpose, and the remaining fold for model validation. Thus, K iteration of learning and validation are performed and for each *i*th iteration the training process is carried out using K-1 folds and the *i*th fold for validation (figure 13). The model selection procedure can be summarized as follows: 1) for each set of tuning parameters a mean error rate is computed averaging the error rate values obtained by the K classifiers $\{C_1, C_2, .., C_k\}$; 2) the set of parameter a with the minimum error rate are selected; 3) such parameters set is used to train the final classifier with the whole dataset, comprising all the K folds. The model selection scheme is shown in figure 14.

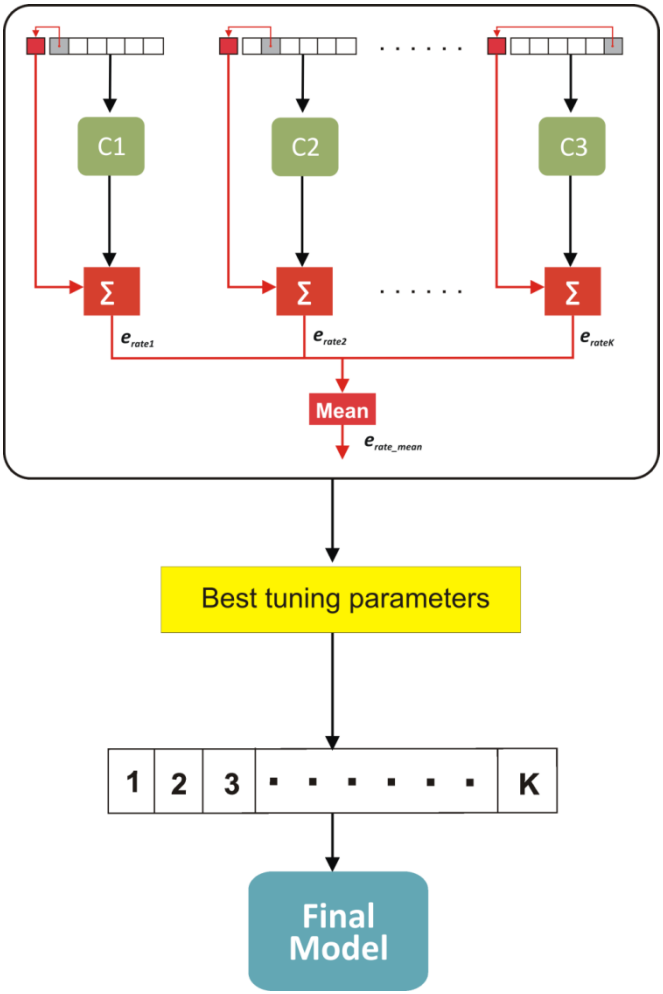

Figure 14: Best model selection using K-Fold cross-validation.

Chapter 4

Seismo-volcanic analysis methods

In this chapter the basic techniques applied in seismo-volcanic analysis will be briefly reported. While methods of spectral estimation have been treated in chapter 2, method for multi sensors and multi component signals analysis will be explained here. In particular, the detection of multi channel coherence, widely applied in biomedical signals, will be adapted here in order to provide a measure of signal coupling on active volcano environment. Moreover, a novel triggering procedure able to extract waveform transients from continuous signal recording will be introduced. This is a very important task since it constitutes the first step in events analysis. Also algorithm for seismo-volcanic events and tremor source location will be described. Once that events are extracted, algorithm for waveform classification are used in order to discover similarity among analyzed waveforms. For this purpose a methods based on waveform cross-correlation will be introduced. All the methods described in this section, together with methods described in chapters 2 and 3, provide the basic knowledge for the data analysis that will presented in the next chapters.

4.1 Spectral analysis

Estimation of frequency content is one of the primary tools for signal investigation. As reported in chapter 1, most of the waveform classification are based on time-frequency characteristics. An example of basic distinctive spectral features among the seismo-volcanic signals introduced in section 1.2 is shown in figure 1. The different power spectrum content, computed using a periodogram (see section 2.2), is the first tool for an preliminary analysis of the recorded events. This approach is also applied on infrasonic signals. As will be explained in chapters 5 and 6, the spectral content of these signals is very useful to classify them.

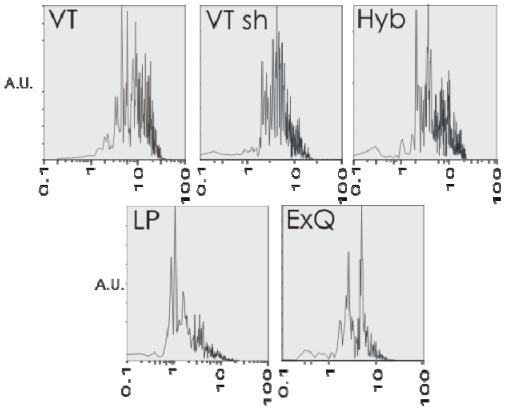

Figure 1: Power spectrum of seismo-volcanic events: VT earthquake (VT); shallow VT (VT sh); hybrid event (Hyb), long period event (LP) and an explosion quake (EXQ).

In the analysis that will be shown in the next chapters, parametric power spectrum estimation methods described in section 2.2.1 are widely applied. This choice is justified by the fact that the seismo-volcanic and infrasonic waveform can be approximate using an auto regressive (AR) model (Lesage, 2008). Another important technique applied on the aforementioned signals is the time-frequency analysis that allows the time localization of the frequencies. This approach can be applied on continuous volcanic tremor and seismo-volcanic events by using Short Time Fourier Transform (STFT) or Continuous Wavelet Transform (CWT), both reported in sections 2.1.1 and 2.1.2 In particular, these technique are applied for the long-term analysis of volcanic tremor, a kind of signal that lasts for long periods and exhibits strong temporal variations in amplitude and frequency content (see section 1.2). These parameters are very important because they are used for source modeling and eruption forecasting. Together with time-frequency representation of a signal, the Root Mean Square (RMS) time series, computed using a time moving window on the signal, provide the temporal variation of the tremor amplitude. This parameter is widely used in volcano eruption forecast since it provides information about how "energetic" is volcanic tremor. It is generally evaluated after filtering the observed signals in a frequency band of interest. In figure 2 a time-frequency representation of volcanic tremor together with its RMS series is shown. By simply having a look at the figure, evident tremor amplitude changes occurred at the end of April 2008 (figure 2a) with a strong variation at the same time as the lava fountain episode on 10 May 2008, and before the occurrence of the eruption on 13 may 2008. It is noteworthy that also the STFT (figure 2b) changed its features during the same time intervals.

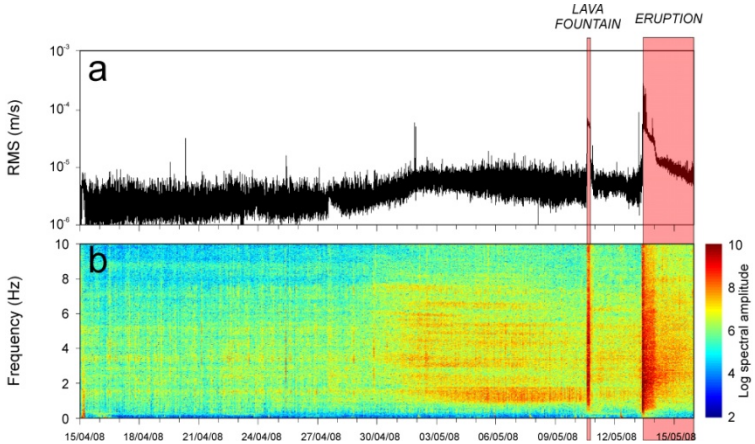

Figure 2: (a) RMS of tremor signal recorded at Mt Etna from 15 April to 15 May 2008.

4.2 Events triggering

In order to automatically trigger transients placed inside a signal several techniques were developed. Some methods are applied on the signal in time domain, others in frequency domain, and others are based on the wavefield features such as rectilinearity and planarity. One of the widely used method is STA/LTA (short time average/long time average) algorithm that evaluates the ratio of short- to long-term energy density (squared data). The optimal window lengths depend on the frequency content of the investigated seismic signal. Withers, 1997, and Withers et al., 1998, showed that the lengths of short and long windows equal to 3 and 27 times the centre period of the detected frequency band can be considered a reasonable compromise between

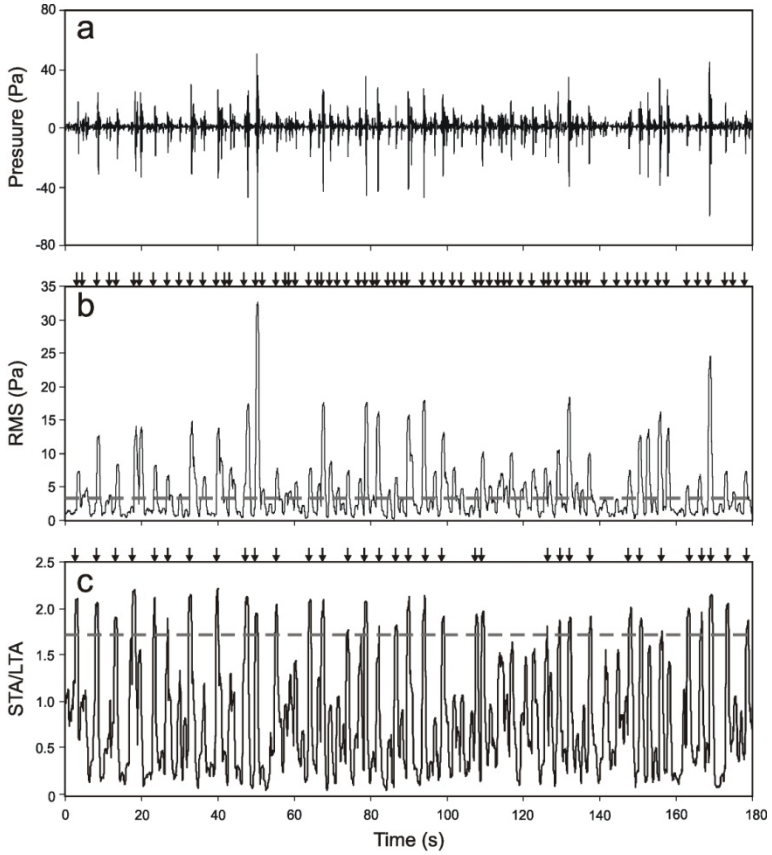

Figure 3: (a) Three-minute-long infrasound signal recorded, (b) corresponding RMS envelope (black line) calculated by using a moving window of 0.7 s and (c) STA/LTA values. The horizontal grey dashed line in (b) indicates the detection threshold calculated by the 5th percentile multiplied by a constant value α=5. The horizontal grey dashed line in (c) indicates the detection threshold calculated fixed at 2. The arrows at top of (b,c) indicate the onset time of the detected events.

sensitivity and noise reduction. A novel triggering algorithm used for transients detection is here after reported. The root mean square (RMS) envelope of the recordings (seismic or infrasound signals) is calculated by a moving window of fixed length. Successively, the percentile envelope on moving windows of RMS envelope is computed. For a given time series, the *p-th* percentile can be defined as the value such that at most (100**p*)% of the measurements are less than this value and 100*(1-*p*)% are greater. In the light of this, the estimation of percentile enables efficiently detecting amplitude transients and estimating background signal level. The percentage threshold should be chosen on the basis of both the amount of transients in the signal that have to be included or excluded in calculations and the signal to noise ratio. The performance of this method is compared with the STA/LTA (short time average / long time average) technique (e.g. Withers, 1997; Withers et al., 1998). As shown in **figure 3**, the trigger results obtained by the two methods were similar; nevertheless, the technique based on percentile was also able to detect transients very close to each other. This is a very important feature for seismo-volcanic and infrasound transients detection, especially when events swarm took place before or during a volcanic eruption. This method can be used both to find transients within a signal (necessary task to automatically count LP events, infrasonic transients, etc…) and to estimate background noise level. Triggering techniques routinely applied on active volcanoes provide useful information about the occurrence rate of a certain type of seismo-volcanic or infrasonic events. As will be shown in the next chapters, change of this parameter can be related to volcano regime variations that may lead to a volcanic eruption. Events occurrence rate estimation, together with spectral feature changes, is an useful tool for active volcano monitoring and constitutes the first step in volcano early warning systems. As introduced in the previous section,

RMS amplitude change and variation in the spectral content of the signals are related to different volcano regimes. In figure 4, the rate of seismo-volcanic long period events (see section 1.2) together with tremor RMS and its STFT, recorded at Mt. Etna Volcano during the period April-May 2008, is shown. It is clear that seismo-volcanic events rate, RMS and spectral content of tremor changed after the onset of the eruption (figure 4).

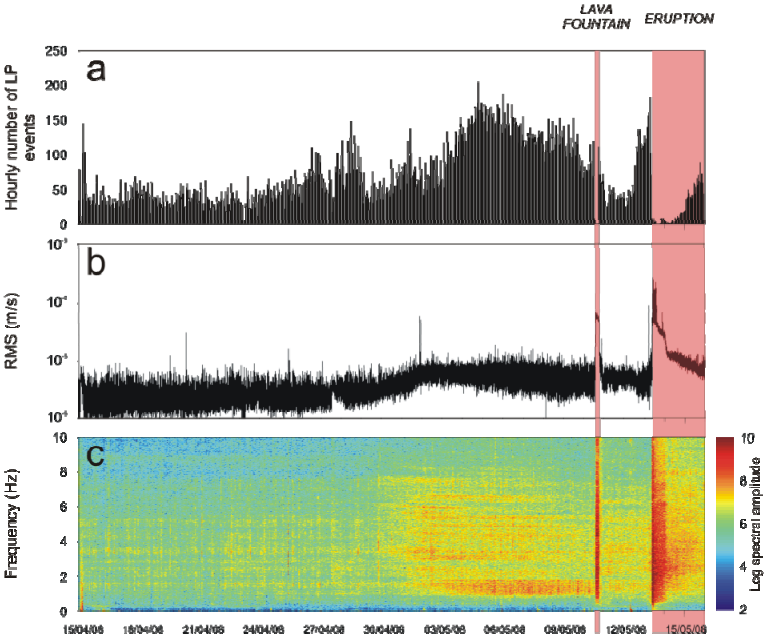

Figure 4: Seismo-volcanic features at Stromboli volcano during the time period October 2006 - April 2007. (a) occurrence rate of LP events; (b) RMS of volcanic tremor; (c) averaged STFT of triggered events. The red vertical line indicates the onset of the eruption.

4.3 Averaged multi-channel coherence

In this section an approach to measure averaged coupling or synchrony among signals simultaneously recorded at different stations is presented. The aim of this analysis is to highlight significant bursts of coherence among summit stations over time. Although the source mechanism producing these coherence time changes is still not known, in the investigated time intervals high summit coherence seems to precede periods of intense volcano activity. In particular, during the periods that will be investigated in the next chapter, high summit coherence among signals appears before lava fountains or effusive eruptions. As explained in section 2.1.5 the coherence is a metric providing a measure of linear relationship between signals at various frequencies widely used in the studies of biomedical signals as EEG (e.g. Saab et al., 2005). An extension of the coherence in a time-frequency space leads to the concept of coherogram. Here, the term *averaged coherence* refers as to the high resolution coherence (see section 2.2.2) computed between all pairs of stations and then averaged. Let n the number of stations, the value $m=n(n-1)/2$ represents the number of all possible pairs on which the coherence is computed over time. In figure 5 a hourly averaged coherogram, computed at Mt Etna summit stations, is shown together with the RMS time series and the hourly rate of the triggered LP events. The red rectangle indicates a period of high coherence (figure 5c), taking place at the same time as an increase of tremor amplitude (figure 5b) and followed by an increase of the LP rate (figure 5a). All the time series described so far, will be used in the analysis of both non-eruptive and eruptive periods at Mt Etna with the aim of better understanding the processes leading to a critical state of the volcano system.

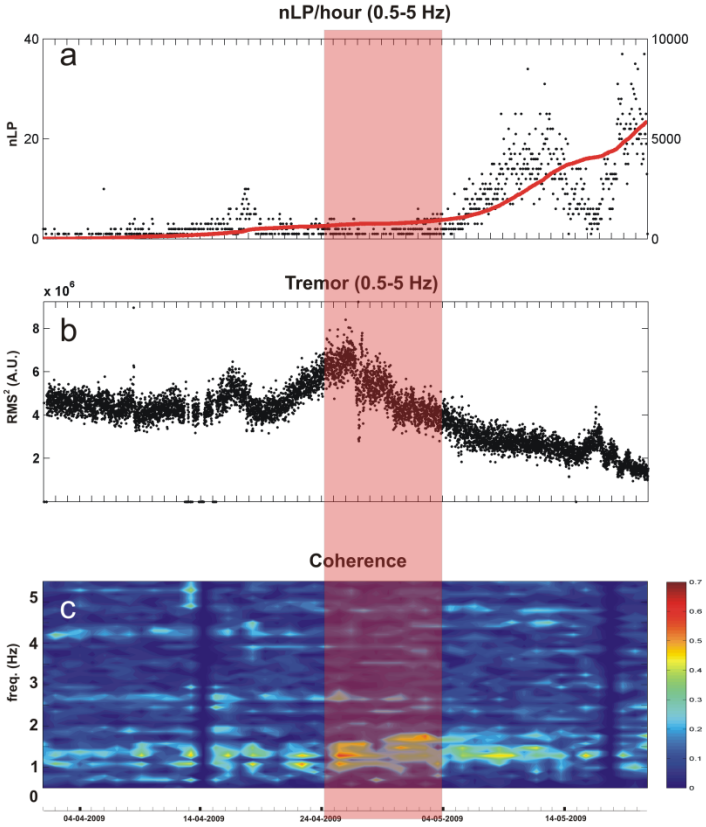

Figure 5: (a) hourly rate of triggered LP events from 01-04-2009 to 20-05-2009; (b) Tremor RMS amplitude; (c) coherogram computed by averaging coherence at summit Mt Etna stations over time.

4.4 Seismo-volcanic events source location

Many of the analyses treated in this thesis are related to infrasound and seismo-volcanic signals whose onset is usually not clearly identified on the traces. For this reason, conventional approaches of event location by picking first arrivals cannot be applied. Therefore, different techniques, generally based on grid searching procedures, were developed. One of the most widely applied location approach is the semblance method (Neidell and Taner, 1971), based on the semblance function, that is a measure of similarity of multichannel data. Considering traces U acquired by a certain number of sensors N, the semblance is defined as (Neidell and Taner, 1971):

$$S_0 = \frac{\sum_{j=1}^{M}\left(\sum_{i=1}^{N} U_i(\tau_i + j\Delta t)\right)^2}{N\sum_{j=1}^{M}\sum_{i=1}^{N} U_i(\tau_i + j\Delta t)^2} \tag{4.1}$$

where Δt is the sampling interval, τ_i is the origin time of the window sampling the i-th trace, $U_i(\tau_i + j\Delta t)$ is the j-th time sample of the trace i-th U, and M represents the number of samples in the window. S_0 is a number between 0 and 1. The value 1 is only reached when the signals are identical, not only in waveform but also in amplitude. If the traces are normalized, and then the semblance values only depend on the shape of the signals, it can be demonstrated that the definition of semblance is equivalent to an averaging of the correlation coefficients of all the possible trace pairs (Almendros and Chouet, 2003). The semblance method consists in finding a set of arrival times (τ_i, $i = 1,\ldots, N$), that yields a maximum semblance for the N-channel data. The procedure is composed of several steps. First of all, a broad enough region of interest has to be de-

termined to include the actual source. A start time t_s is fixed as the time of first arrival at a reference station (generally chosen on the basis of the highest signal to noise ratio) by visual inspection or triggering algorithm (see section 4.2). The source is assumed to be in each node of the grid, and for each node the origin time t_o is calculated, assuming a certain value of propagation velocity of the infrasonic or seismic waves, as follows:

$$t_o = t_s - r/v \tag{4.2}$$

where r is the distance between the reference station and the node of the grid assumed as source location. Successively, the theoretical travel times are calculated at all the sensors t_i (i = 1,…, N, number of stations):

$$t_i = r_i/v \tag{4.3}$$

where r_i is the distance between the station i-th and the node of the grid assumed as source location. Then, by these theoretical travel times and the origin time, signals at the different stations are delayed and compared by the semblance function. Signal windows containing between one and two cycles of the dominant period are generally used to calculate the semblance value because they provide the best performance (Almendros and Chouet, 2003). Therefore, the semblance function is assumed representative of the probability that a node has to be the source location. The source is finally located in the node where the delayed signals show the largest semblance value. In order to estimate the error of the location, the method described in Almendros and Chouet (2003) is followed. Firstly, the signal to noise ratio (hereafter called *SNR*) for each event is compute by the following equation (Almendros and Chouet, 2003):

$$SNR = \frac{1}{N}\sum_{i=1}^{N}\frac{\max\left|\vec{U}_i\right| - \sigma_i^n}{\sigma_i^n} \tag{4.4}$$

where $\left|\vec{U_i}\right|$is the modulus of the velocity recorded at the *i*-th station and σ_i^nrepresents the RMS of the seismogram within a window containing only noise. Successively, in order to define an error region, a semblance level, equal to $(1 - dS)S_{max}$ is fixed for each event on the basis of its *SNR* and of the following equation (Almendros and Chouet, 2003):

$$dS = 0.062\ SNR^{-1.54} \tag{4.5}$$

Finally, the extension of this region can be calculated in the three space directions (longitude, latitude and altitude). The semblance method is used in several works to locate LP and VLP events, as well as infrasound events recorded by sensors arranged in both sparse networks and array configurations (e.g. Ripepe and Marchetti, 2002; Gresta et al., 2004; Patanè et al., 2008, Cannata et al., 2009a,b; Montalto et al., 2010). The main difference concerns the grid: a 3D grid is used for LP and VLP events, while a 2D grid coinciding with the topography for infrasound events. Indeed, the vent radiating infrasound can be reasonably considered a source point located on the topographical surface. This location procedure can be also performed in near real-time. In this case computational time has to be shorter than the analysed period. Therefore, if the event rate is high and then not all the detected events can be located, only the "best" transients must be analysed. The choice is based on both the signal to noise ratio at all the available stations and the peak-to-peak amplitude of the events at the reference station. Finally, the number of events that can be located depends on the used space grid and on the available computational power. For instance, by this location technique

three different infrasonic sources, coinciding with North-East crater, South-East crater and the 2008 eruptive fissure have been found active during 2007-2008.

In figure 6 three examples of semblance distribution and infrasound traces are reported. It is worth noting that, as infrasonic signals are sinusoidal, semblance space distribution is roughly sinusoidal too. The wavelength of such sinusoidal semblance function strictly depends on the wavelength of the infrasonic event. The higher the frequency of the infrasound event, the shorter the wavelength of the semblance function. In order to estimate the location error, the equation 4.5. can be followed. In this case the SNR is computed as:

$$SNR = \frac{1}{N}\sum_{i=1}^{N}\frac{\sigma_i^s - \sigma_i^n}{\sigma_i^n} \tag{4.6}$$

where N is the number of stations, σ_i^s and σ_i^n are RMS of the infrasound signal windows at the i-th station containing the event and only noise preceding the event, respectively.

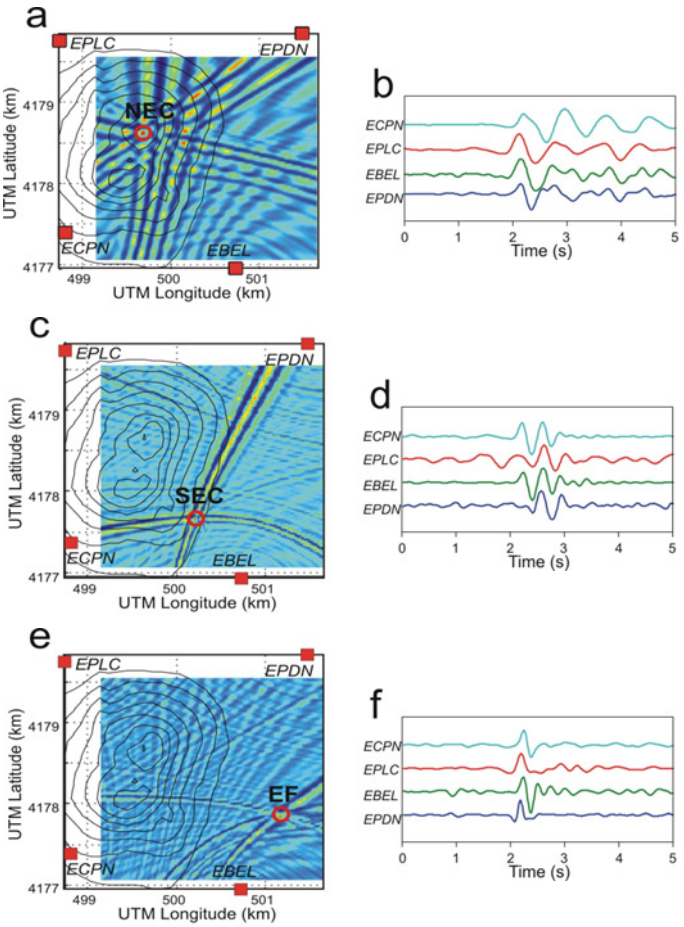

Figure 6: (a, c, e) Examples of space distribution of semblance values calculated by locating three infrasonic events at Mt. Etna and (b, d, f) corresponding infrasonic signals at four different stations shifted by the time delay that allows obtaining the maximum semblance. The red squares and circles in (a, c, e) indicate four station sites and the nodes with the maximum semblance value, respectively. The black lines in (a, c, e) are the altitude contour lines from 3 to 3.3 km a.s.l.

4.5 Volcanic tremor location and errors estimate

Tremor source location is estimated by using a grid-search approach, assuming the propagation in a homogenous medium and a seismic amplitude decay with the distance (Gottschammer and Surono, 2000, Battaglia et al., 2005; Di Grazia et al., 2006), according to the general law:

$$A(f,s) = A_0(f)s^{-b}e^{-\alpha s}, \alpha = \frac{\pi f}{Qc} \tag{4.7}$$

where f is the frequency, c the velocity and b the exponent which takes values of 0.5 or 1 for the cases of surface and body waves, respectively. Q represents the ray-path-averaged quality factor. The equation (4.7) can be linearized taking the logarithm on both sides as:

$$\ln A_i + \alpha s_i = \ln A_0 - b \ln s_i \tag{4.8}$$

where A_i is the RMS amplitude measured at the ith station, α is the frequency-dependent absorption coefficient and s_i is the corresponding source-to-receiver distance. In this form $\ln A_0$ and b represent the intercept and the slope of the linear equation, respectively. The location process considers the RMS amplitudes of the 25th percentile instead of average values. This leads to efficiently remove undesired transients in the signal and consider continuous recordings (Di Grazia et al., 2006). Furthermore, tremor locations were retrieved considering two different frequency bands (0.5-2.5 Hz and 0.5-5.0 Hz). Though most of the tremor energy at Mt.Etna is radiated in the 0.5-5.0 Hz frequency band, seismic signals above 2.5 Hz are generally due to superficial activity, such as degassing and/or strombolian activity

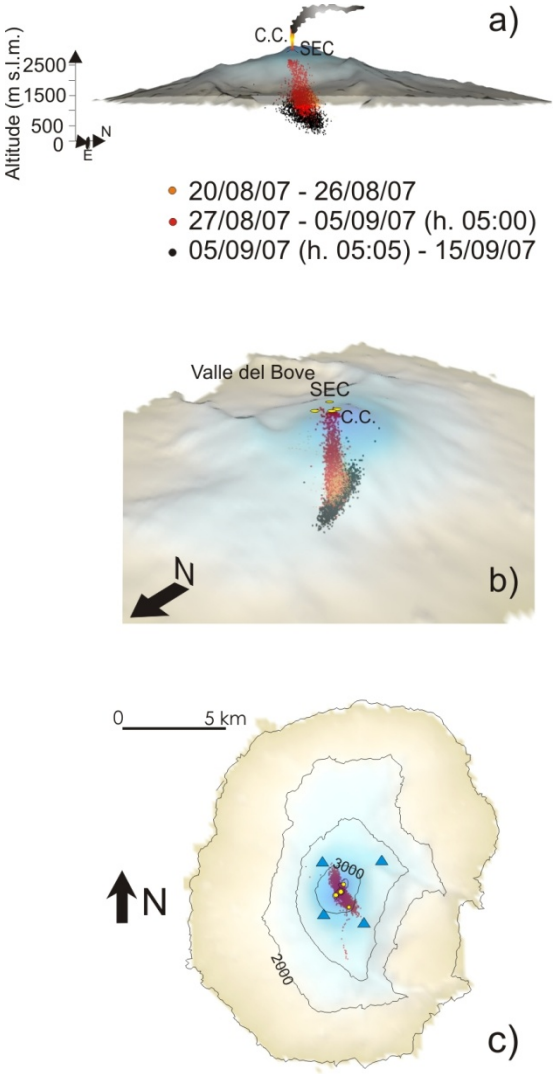

Figure 7: (a,b) 3-D images of the volcanic edifice reporting volcanic tremor locations computed between 20 August and 15 September 2007. (c) 3-D source centroids of volcanic tremor locations computed between October 2006 and December 2007, separated into twoclasses of depth (black dots ≤1000 m and red dots >1000 m a.s.l.).

at summit craters. By using also the 0.5-2.5 Hz frequency band the deeper portion of tremor source volume is highlighted. The observed difference in the tremor locations in the two frequency bands suggests that close portions of the same source volume can be active. The source location of tremor is found on the basis of the goodness of the fit (R^2) obtained for each point of a 3D grid with centre underneath the craters. With the 3D grid search, the most probable source location is identified as the point where the measured amplitudes best fit the amplitude decay law for body of surface waves (see eq. 4.8). The centroid position of all 3D grid points whose R^2 do not differ more than 1% of the maximum R^2 is assumed as source location (Di Grazia et al., 2006).

In order to assess the stability of source location a Jackknife technique was employed (Efron, 1982). The procedure is especially useful to reduce bias when extreme scores are present in the data set and/or the statistical distribution of the underlying population is unknown. For each source location in the Jackknife procedure, also called "leave one out", n (number of stations) estimates of an unknown parameter P (latitude, longitude and depth) are computed by leaving one station out at a time. The expected value of P is:

$$\overline{P} = \frac{1}{n}\sum_{i=1}^{n} P_i \tag{4.9}$$

where P_i is the parameter computed by omitting the ith station. Let define the ith so called "pseudo-value" as:

$$J_i = n\hat{P} - (n-1)P_i \tag{4.10}$$

where $\hat{P}$ is the parameter computed by considering all the stations. Finally, the Jackknife estimator of parameter P is given by:

$$J(\hat{P}) = \frac{1}{n}\sum_{i=1}^{n} J_i = n\hat{P} - (n-1)\overline{P} \tag{4.11}$$

If the original estimate of parameter $\hat{P}$ is biased then part of the bias is removed by the Jackknife procedure. Further, an estimate of the standard error of the Jackknife estimate, $J(\hat{P})$, is given by:

$$\delta_{J(\hat{P})} = \sqrt{\frac{1}{n(n-1)}\sum_{i=1}^{n}(J_i - J(\hat{P}))^2} \tag{4.12}$$

For instance, in the Tables 1 and 2, the *25*th, *50*th and *75*th percentile of the standard error for the computed Jackknife locations during during 20 August - 15 September 2007 at Mt. Etna are reported. An example of tremor source location related to the time period 2006 – 2007 is shown in figure 7 (Patanè et al., 2008).

Table 1: Standard Error for Latitude, Longitude and Depth of the Jackknife Estimation (0.5-5.5 Hz)

	25th percentile	50th percentile	75th percentile
Latitude (m)	415	476	555
Longitude (m)	492	563	637
Depth (m)	668	785	889

Table 2: Standard Error for Latitude, Longitude and Depth of the Jackknife Estimation (0.5-2.5 Hz)

	25th percentile	50th percentile	75th percentile
Latitude (m)	442	491	573
Longitude (m)	508	586	649
Depth (m)	685	802	918

4.6 Three component sensor analysis

In order to extract features from wavefield of seismic, seismo-volcanic events and volcanic tremor, a multi component approach is needed. Although, several algorithms are used in frequency domain, in this section an algorithm based on three component covariance is carried out in the time domain (Jurkevics, 1988). Three-component seismic signals are bandpass filtered into narrow frequency bands. The frequency and the time resolution depends on the considered application. For the frequency band of interest a series of overlapped and tapered time window is extracted for each component. For each window the polarization is estimated as follows. Considering the data matrix in each window $X = [x_{ij}]$; $i = 1,\ldots, N$; $j = 1,\ldots, 3$, where x_{ij} is the ith sample of component j and N is the number of samples. Also, the mean of each component of matrix X is assumed to be zero. Then, the covariance matrix S is evaluated as follows:

$$S_{jk} = \frac{X_j^T X_k}{N} = \frac{1}{N}\sum_{i=1}^{N} x_{ij}\, x_{ik} \tag{4.13}$$

where T denotes transpose. The covariance matrix is 3×3, real and symmetric. Explicitly, the terms of S are the auto- and cross-variances of the three components of motion:

$$S = \begin{pmatrix} S_{zz} & S_{zn} & S_{ze} \\ S_{zn} & S_{nn} & S_{ne} \\ S_{ze} & S_{ne} & S_{ee} \end{pmatrix} \tag{4.14}$$

where z,n,e denote the vertical, north-south, east-west components respectively. S is a positive semidefinite matrix of coefficients for a quad-

ratic form which is an ellipsoid called *polarization ellipsoid* (Jurkevics, 1988). The principal axis orientation of the polarization ellipsoid and their length can be obtained from the solution of the algebraic eigenproblem for S. This involves eigenvalues ($\lambda_1, \lambda_2, \lambda_3$) and eigenvector ($u_1, u_2, u_3$) which are solution of the algebraic equation:

$$(S - \lambda^2 I)u = 0 \tag{4.15}$$

where I is the 3×3 identity matrix. The eigenvector are chosen to be orthogonal and unit length. The direction of the principal axes of the ellipsoid are given by the eigenvectors u_j, whereas the axes lengths are specified by the eigenvalues λ_j. The eigenvalues are ordered such that $\lambda_m > \lambda_n$ for m < n. It is noteworthy that in practical application the three eigenvalue are nonzero and different to each other, this leads to a polarization that is ellipsoidal. Information that describe features of ground motion are computed from the principal axes. In order to obtain a measure of what kind of motion prevails in the time window on which the analysis is performed, the rectilinearity and planarity are used. The rectilinearity coefficient *rect*, quantifying the degree of linearity of particle motion (i.e. the relative elongation of the ellipsoid in one direction) can be calculated by the following equation (Benhama et al., 1988):

$$rect = \sqrt{\frac{\left(1 - \frac{\lambda_2}{\lambda_1}\right)^2 + \left(1 - \frac{\lambda_3}{\lambda_1}\right)^2 + \left(\frac{\lambda_2}{\lambda_1} - \frac{\lambda_3}{\lambda_1}\right)^2}{2\left(1 + \frac{\lambda_2}{\lambda_1} + \frac{\lambda_3}{\lambda_1}\right)^2}} \tag{4.16}$$

For linear polarization, as theoretically expected for body waves, *rect* is equal to 1 while, for particle motion with no preferred direction ($\lambda_1 = \lambda_2 = \lambda_3$), *rect* is equal to 0. Pure Rayleigh-wave motion is elliptical and the particle motion is confined to a plane. A measure of the degree of "planarity" is given by the planarity *plan* and is defined as (Benhama et al., 1988):

$$plan = \frac{\sqrt{\lambda_1} + \sqrt{\lambda_2} - 2\sqrt{\lambda_3}}{\sqrt{\lambda_1} + \sqrt{\lambda_2} + \sqrt{\lambda_3}} \tag{4.17}$$

Also the values of *plan* lie in the interval [0,1], indicating no preferred polarization and polarization in a plane, respectively. The estimate of azimuth and incidence angles depends on the assumed wave. Assuming P-wave propagation, the azimuth φ can be estimated from the horizontal orientation of rectilinear motion given by eigenvector u_1 related to the largest eigenvalue:

$$\varphi = \arctan\left(\frac{u_{21}\ sign(u_{11})}{u_{31}\ sign(u_{11})}\right) \tag{4.18}$$

Finally, the incidence angle of a P-wave is obtained by:

$$\psi = \arccos|u_{11}| \tag{4.19}$$

An example of polarization analysis parameters computed on one day of continuous recording of volcanic tremor signal is shown in figure 8.

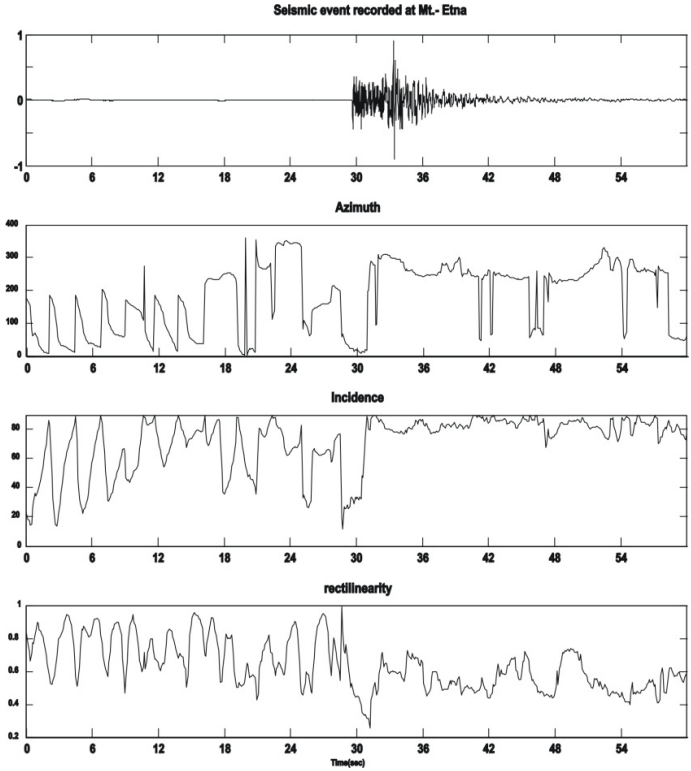

Figure 8: Example of polarization parameters calculated by using 4-second-long moving windows slid every 0.1 s on a seismic event recorded at Mt. Etna.

4.7 Waveform similarity detection

On a active volcano there are a wide range of seismic and infrasonic signals related to fluids movement inside it. As reported in section 1.2 each type of signal can be distinguished by its temporal signature and frequency content. In literature there are two different groups of waveform classification: methods based on frequency content and methods based on a similarity measure of the whole waveform. The former, generally used to distinguish hybrid, LP, VLP events and so on, divides the events into groups on the basis of how much of the signal power is concentrated in certain frequency bands (e.g. Power et al., 1994; Miller et al., 1998). In contrast to frequency feature of a signal, waveforms morphology provides detailed information on the path that the signals has taken from the source to the sensor. A classification method based on waveform similarities allows signals to be grouped into classes with distinct physical meaning. Most of the methods of waveform classification use cross-correlation techniques to quantify event similarity (e.g. Stephens and Chouet, 2001). Similarity between events is defined using the cross correlation function (Green and Neuberg, 2006):

$$r_{xy}(i,i-l)=\frac{\sum_{i=1}^{n}\left(x_i-\bar{x}\right)\left(y_{i-1}-\bar{y}\right)}{\sqrt{\sum_{i=1}^{n}\left(x_i-\bar{x}\right)^2}\sqrt{\sum_{i=1}^{n}\left(y_{i-1}-\bar{y}\right)^2}} \tag{4.20}$$

where n is the number of sample, x_i is the i-th sample of the signal x, y_{i-l} is the $(i\text{-}l)$th sample of the signal y, the index l is the lag between the two signals and the overbar represents the mean value of the signal. It is noteworthy that the correlation function r_{xy} provides only the relative similarity of two waveforms and does not depend on the amplitude of the

signals. Using a trigger procedure (see section 4.2) n events are isolated from the continuous recording and each one is then cross-correlated with every other event. A maximum correlation coefficient matrix $m \in \boldsymbol{\mathcal{R}^{n \times n}}$ is constructed where each element m_{xy} represents the maximum correlation coefficient between waveform x and y. In order to subdivide events into families a correlation coefficient threshold ψ is needed. As reported in Green and Neuberg, (2006), the choice of this value is a trade-off between classification accuracy and event detection: low values of ψ lead to wrong classification of waveform; high values of ψ lead to discharge events with low signal to noise ratio. In order to sort the correlation matrix m into families, a master event is chosen as the event with the largest number of cross correlation values above ψ. Then, an average waveform of the family is found by stacking all events well correlated with the master event. This stack waveform is cross-correlated with the original records, and all events with a cross correlation coefficient greater than the threshold are grouped into a waveform family. Once an event is assigned to a given family, it is removed from the correlation matrix. The same process is applied until the entire matrix is classified into distinct families (e.g. Green and Neuberg, 2006). Although different methods based on sophisticated pattern recognition techniques (see chapter 3) were developed in the last years, the method reported here constitutes the state of art about seismo-volcanic event classification. This method can work also online. Once that a new event is triggered, its family class is then determined using a cross-correlation procedures between the new event and a stacking event of each family. The new waveform is then classified when cross-correlation is greater than the fixed threshold ψ. However, it is noteworthy that in a volcano environment, whose characteristics change in time, this approach can be weak since new families born and other families disappear. As will be explained in chapter 6,

infrasound waveforms maintain more stable features over time. For this reason a more robust classification system, based on pattern recognition processes, was developed with the aim to provide a novel method for infrasonic waveform clustering.

Chapter 5

Infrasonic signals on active volcanoes

Volcanic unrest is often evidenced by time variations of some physical and geochemical parameters. The geophysical surveillance of volcanoes is routinely performed mainly by observing the patterns of seismic activity and ground deformations (Scarpa and Gasparini, 1996). In recent years, new insights into explosive volcanic processes have been made by studying infrasonic signals (e.g., Vergniolle and Brandeis, 1994; Ripepe et al., 1996; 2001a). Indeed, infrasonic activity on volcanoes is generally evidence of open conduit conditions and can provide important indications on the dynamics of the explosive processes. Unlike the seismic signal, whose wavefield can be strongly affected by topography (Neuberg and Pointer, 2000) and path effects (Gordeev, 1993), the infrasonic signal keeps its features almost unchanged during propagation. In fact, for short distances the infrasonic signal travels in an almost homogeneous atmosphere with no structures that can scatter, attenuate or reflect acoustic waves, providing information about the source. This can be explained by the simpler Green's functions for a fluid atmosphere than those for a complex, heterogeneous volcanic edifice, which supports compressional, shear, and surface waves (Johnson, 2005). However, the source mechanism of the sound radiated during eruptions is still open to debate. Several phenomena are able to generate infrasound signals such as rockfalls or pyroclastic flows (e.g., Moran et al., 2008; Oshima and

Maekawa, 2001). Nevertheless, in most cases these signals are related to internal magma dynamics, like the acoustic resonance of fluids in the conduit, triggered by explosive sources; this implies propagation of sound waves in both magma and atmosphere (Garces and McNutt, 1997). According to some authors (e.g., Ferrick et al., 1982; Julian, 1994; Seidl and Hellweg, 2003), seismic and acoustic wave generation in volcanoes can be caused by nonlinear processes. Unlike linear models, nonlinear ones allow the harmonic frequencies to be not proportional to a geometric length scale, which for example may explain why tremor frequencies are similar at volcanoes of vastly different size (Hagerty and Benites, 2003). Another attraction of nonlinear models is that they are able to produce a large range of complex behaviors for relatively small changes in some control parameters (Hagerty and Benites, 2003). Recent studies relate the source of sound to the sudden uncorking of the volcano (Johnson and Lees, 2000), opening of "valves" sealing fluid-filled cracks (Matoza et al., 2009), local coalescence within a magma foam (Vergniolle and Caplan-Auerbach, 2004) and Strombolian bubble vibration (Vergniolle and Brandeis, 1996; Vergniolle et al., 2004). The location of the source of the infrasonic signals, generally coinciding with active vents, is of great importance for volcanic monitoring. Therefore, some techniques, based on signals recorded by infrasound arrays or networks, were developed to locate the source of this signal (e.g., Ripepe and Marchetti, 2002; Garces et al., 2003; Johnson, 2005; Matoza et al., 2007; Jones et al., 2008). At multivent systems, as Stromboli (Ripepe and Marchetti, 2002), Kilauea (Garces et al., 2003) and Mt. Etna (Cannata et al., 2009a, b), methods based on the comparison of the infrasonic signals by cross-correlation or semblance functions have enabled monitoring and discriminating of the explosive activity of distinct craters. Recently, joint analysis of seismic, infrasonic and thermal signals has proved very useful to investigate ex-

plosive processes and distinguish the different eruptive styles and dynamics in various volcanoes, such as Stromboli (Ripepe et al., 2002), Santiaguito (Sahetapy-Engel et al., 2008), Villarica and Fuego (Marchetti et al., 2009). Moreover, recent multiparametric approaches, based on the investigation of infrasound, several different types of seismic signals, such as earthquakes and seismo-volcanic signals, ground deformation and so on, have allowed tracking the evolution of activity in both deep and shallow parts of volcanoes (e.g., Sherrod et al., 2008; Di Grazia et al., 2009; Peltier et al., 2009). For several years, the surveillance of Mt. Etna volcano (Italy) has been performed by using permanent seismic, GPS, tilt and video camera networks. However, information provided by these networks is sometimes insufficient to characterize and well locate very shallow phenomena such as explosive activity episodes, especially when the visibility of the volcano summit is poor. In the light of this, the staff of Istituto Nazionale di Geofisica e Vulcanologia (INGV) section of Catania has recently started recording and studying the infrasound signal, strictly related to the volcano shallowest dynamics, with the aim of integrating the information provided by the aforementioned networks. The summit area of Mount Etna volcano is currently characterized by four active craters: Voragine, Bocca Nuova, southeast crater, and northeast crater (hereafter referred to as VOR, BN, SEC, and NEC, respectively; see figure 1). These craters are characterized by persistent activity that can be of varying nature and sometimes involve different types simultaneously: degassing, lava filling or collapses, low rate lava emissions, phreatic, phreatomagmatic or Strombolian explosions, and lava fountains (Cristofolini et al., 1988).

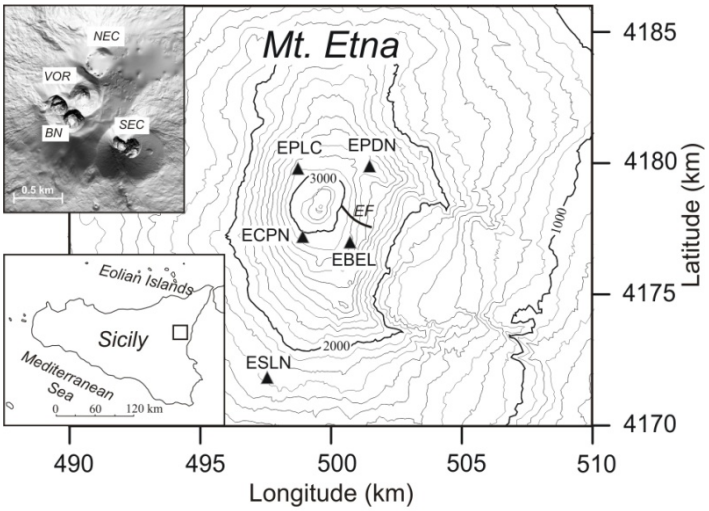

Figure 1: Sketch map of Mount Etna with location of the five infrasonic sensors (triangles) composing the permanent infrasonic network. In top left inset the distribution of the four summit craters (VOR, Voragine; BN, Bocca Nuova; SEC, southeast crater; NEC, northeast crater) is reported.

The greatest risk for the villages located around the volcano is linked to flank eruptions that take place from fractures cutting the slope of the edifice. During the second half of the 20th century, Mt. Etna was characterized by an unusually high level of eruptive activity, with a clear increase in effusive rates and in the frequency of summit and flank eruptions observed in recent decades (Behncke and Neri, 2003). A remarkable increase in the frequency of short-lived, but violent eruptive episodes at the summit craters has also been observed. Between 1900 and 1970 about 30 paroxysmal eruptive episodes occurred at the summit craters, while there have been more than 180 since then (Behncke and Neri, 2003). The location and characterization of the source of the infrasonic activity are of great importance for the monitoring of the explosive activity of the volcano. The first infrasound investigations at Mt. Etna were

performed by temporary experiments (e.g., Ripepe et al., 2001b; Gresta et al., 2004). Since 2006 a permanent infrasound network has been deployed and has allowed to continuously record infrasounds and investigate their link with volcanic activity (Cannata et al., 2009a, b; Di Graziaet al., 2009).

5.1 Infrasound monitoring at Mt.Etna

The permanent infrasound network of Mt. Etna, run by INGV, Section of Catania, comprises five stations, located at distances ranging between 1.5 and 7 km from the center of the summit area (figure 1). The infrasonic sensors consist of Monacor condenser microphones MC-2005, with a sensitivity of 80 mV/Pa in the 1–20 Hz infrasonic band. The infrasonic signals are transmitted in real-time by radio link to the data acquisition center in Catania (Italy) where they are acquired at a sampling rate of 100 Hz.

The entire infrasound monitoring system may be described by the following parts: (1) data acquisition, (2) event detection, (3) event characterization, (4) source location and (5) modeling (figure 2) (Montalto et al., 2010). The steps (1–4) are designed for a real-time application, whereas the step (5) is for near real-time or off-line analysis. Once the infrasound signal is recorded, the signal portions of interest, which are the infrasonic events, have to be extracted. A reference station is chosen, according to the best signal-to-noise ratio. At Mt. Etna we use EBEL as reference station. Therefore, the STA/LTA (short-time average/long-time average) method is applied (see section 4.2). This method is used both to pick the onset of the events and to count them. The picking allows the location analysis to be performed (see section 4.2).

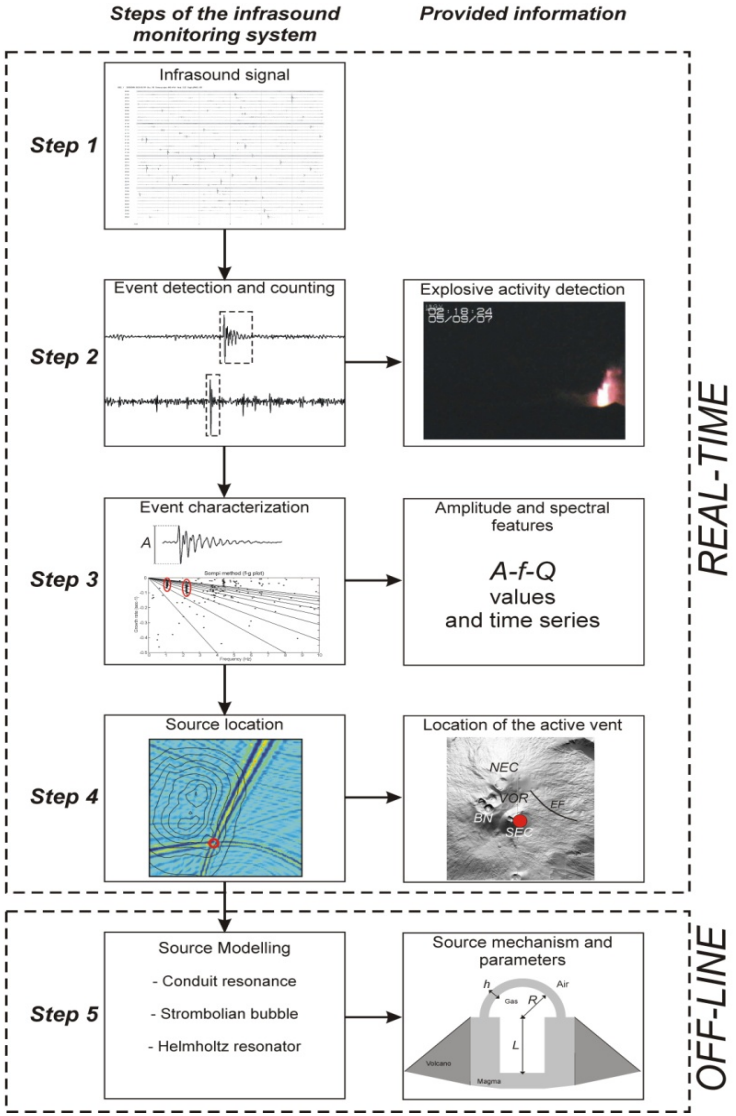

Figure 2: Scheme of the infrasound monitoring system (see text for details).

The rate of occurrence of infrasonic events is useful for monitoring explosive activity. Indeed, the occurrence rate of the events increases during the explosive activity (see figure 3). The efficiency of videocameras and thermal sensors, that visually detect changes in explosive activity (Bertagnini et al., 1999; Harris et al., 1997), is strongly reduced (or inhibited) if there are clouds, fog or gas plumes. Thus the detection and characterization of explosive activity by infrasound is very useful, especially when the visibility of the volcano summit is poor (e.g., Cannata et al., 2009a).

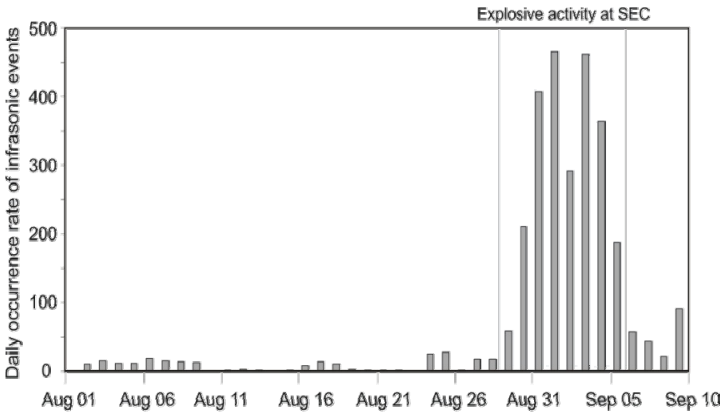

Figure 3: Histogram showing the daily number of infrasonic events from 1 August to 10 September 2007, detected at EBEL station. The light gray rectangle indicates the period characterized by explosive activity at SEC.

Nevertheless, it is worth noting that infrasonic events occurring during lava fountains are not detectable. The very high occurrence rate of events during the paroxysmal stages gives rise to an almost continuous signal (the so-called infrasonic tremor), preventing the detection of single events. On the other hand, the events also occurring during periods characterized by strong wind are not detectable because of the high noise. Recent studies performed at Mt. Etna have allowed recognizing SEC and NEC as the most active summit craters from an infrasonic point of view (Cannata et al., 2009a,b). During 2007–2008 the former was characterized by both degassing and explosive activity (strombolian activity and lava fountaining), while the latter mainly by degassing. According to Cannata et al. (2009a,b) these craters generate infrasound signals with different spectral features and duration: "NEC events", lasting up to 10 s and characterized by dominant frequency generally lower than 2.5 Hz, are related to the degassing activity of NEC and are recorded almost continuously (figure 4a); "SEC events", with a duration of about 2 s, dominant frequency mainly higher than 2.5 Hz and higher peak-to-peak amplitude than the NEC events, are recorded during explosive activity at SEC (figure 4b). Moreover, during the 2008–2009 eruption a third infrasound source, coinciding with the lowermost tip of the eruptive fissure, was active. During periods with explosive activity, this source generated signals, called "EF events", with features similar to the SEC events (figure 4c). On this basis and according to Cannata et al. (2009a, b), a simple spectral analysis of the infrasonic events recorded at a single station, together with the amplitude estimation, can give preliminary information on the ongoing volcanic activity and active craters. In particular, spectral and amplitude variations over time of such infrasound signals can be a good indicator of changes in the volcanic activity. Therefore, the third step of the automatic monitoring system consists of extracting spectral

features and the peak-to-peak amplitudes from the waveforms of the detected events (figure 2). As shown in Cannata et al. (2009b), Sompi method (see section 2.2.1; Kumazawa et al., 1990) is a useful algorithm to calculate the dominant frequency and the quality factor of the events. Similarly to the detecting step, the infrasound characterization is carried out on the signal recorded by EBEL, considered as reference station. In figure 5 the time variation of peak-to-peak amplitude, frequency and quality factor values of events, recorded during January-June 2008, is reported, together with the source location and a scheme summarising the volcanic activity. There are strict relationships between variations of the infrasound event features and changes in the eruptive activity (figure 5).

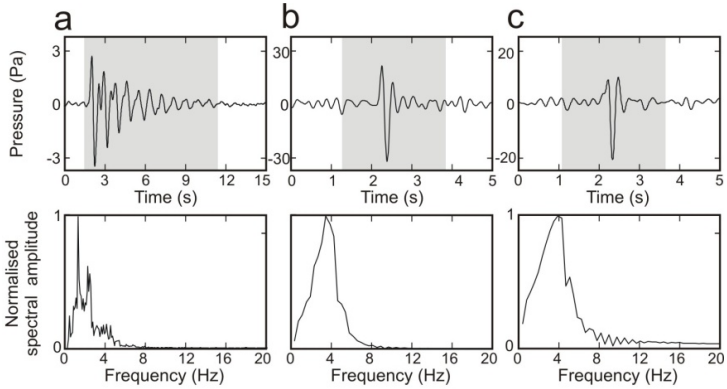

Figure 4: Infrasonic events recorded by EBEL station and corresponding spectra. The gray areas in (a), (b), (c) show the signal windows used to calculate the spectra. In particular, the events (a), (b) and (c) were generated at NEC, SEC and at the lowermost tip of EF, respectively.

For example the explosive activity at SEC, taking place on February 12, 2008, and mainly consisting in ash emission (Corsaro, 2008), was accompanied by increases in both amplitudes and frequency peak values. Similar changes in the infrasound activity occurred on May 13, 2008, at the onset of the eruption at the eruptive fissure opened on the same day in the upper part of the Valle del Bove (Di Grazia et al., 2009). The source location (fourth step in figure 2) was performed by the semblance algorithm (see section 4.4). During 2007–2008 the most active vents from the infrasonic point of view were SEC and NEC, mainly characterized by explosive and degassing activity, respectively (figure 5). Moreover, an eruptive fissure (EF in figure 6), opened on May 13, 2008, in the upper part of the Valle del Bove and characterized by both effusive and explosive activity, generated infrasound signals (figure 4).

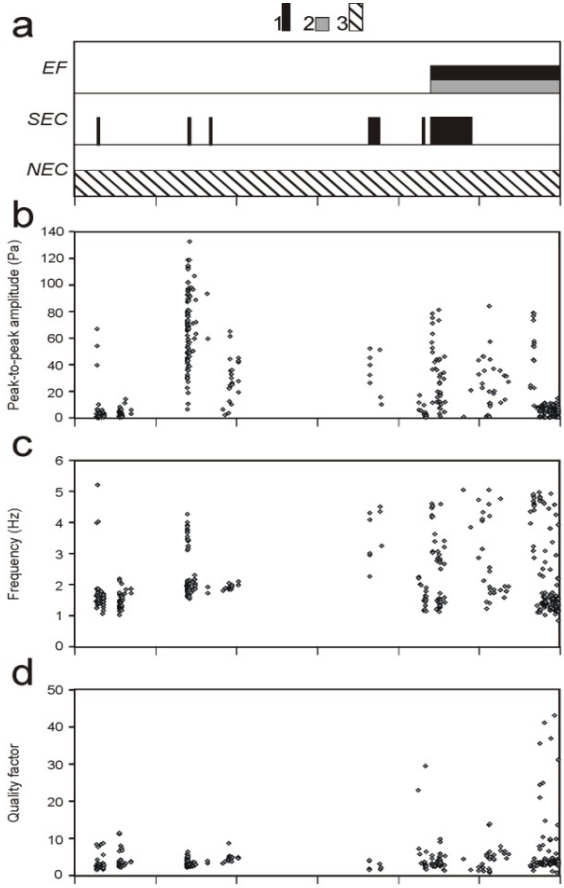

Figure 5: (a) Scheme of the volcanic activity of Mt. Etna at SEC, NEC and EF during January–June 2008 (1: explosive activity; 2: effusive activity; 3: degassing and/or deep explosive activity with no ash emission). (b) Peak-to-peak amplitude, (c) frequency, (d) quality factor and (e,f) source location of about 450 infrasonic events recorded during January–June 2008. The error bar in (e, f), calculated by using the method explained in Sect. 2.4, was multiplied by a factor of 5 to become more visible. The volcanological information in (a) was provided by the internal reports of INGV.

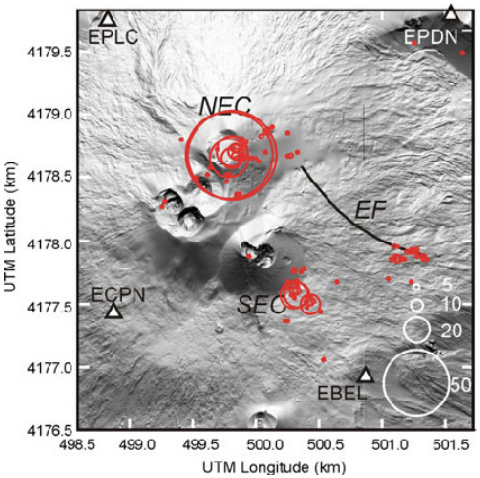

Figure 6: Digital elevation model of Mt. Etna summit with the source locations of the infrasound events, indicated by red circles, occurring during January–June 2008. The radii of the circles are proportional to the number of the locations in each grid node (see white circles and numbers reported in the lower right corner of the map). The sites of four infrasonic sensors are indicated with triangles.

5.2 Source mechanism

Following the sketch of figure 2, once the waveforms of infrasonic events have been extracted and characterized, and the source located, the source mechanism can be investigated. Since this task is not critical from the monitoring point of view, it can be performed in near real-time or even off-line. The source process of infrasound in volcanic areas is still open to debate. However, among the infrasound source models, three have been well developed and applied on observed data: (1) resonating conduit (Buckingham and Garces, 1996; Garces and McNutt, 1997; Hagerty et al., 2000); (2) Strombolian bubble vibration (Vergniolle and Brandeis, 1994, 1996; Vergniolle et al., 1996, 2004; Vergniolle and Ripepe, 2008); (3) local coalescence within a magma foam (Vergniolle and Caplan-

Auerbach, 2004). The first model is based on a pipe-like conduit, that, if affected by trigger mechanisms such as explosive processes, can resonate generating seismic and infrasonic signals, whose waveforms strictly depend on the geometrical-chemical-physical features and specific boundary conditions of the conduit. The acoustic signal, thus generated, consists in gradually decaying sinusoids with a fundamental mode and harmonics. A candidate example recorded at Mt. Etna is shown in figure 4a. On the other hand, in the Strombolian bubble vibration model the infrasound is produced by the vibration of a thin layer of magma, pushed by a variation of pressure inside a shallow metric bubble prior to bursting. The bubble shape is approximated by a hemispherical head and a cylindrical tail, as expected in slug-flow (figure 7a). The propagation of pressure waves is radial and the waveform of the resulting infrasound signal is composed of a first energetic part roughly composed of one cycle–one cycle and a half (corresponding to the bubble vibration), followed by a second part with various weaker oscillations sometimes with higher frequency (radiated during and after the bubble bursting) (e.g.,figure 4b, c). Finally, according to the Helmholtz resonator model the source of infrasound signals is the coalescence of the very shallow part of a foam building up into the conduit, which produces large gas bubbles.. In this case the gas escapes through a tiny upper hole. The shape of the bubble is similar to the Strombolian bubble model with the exception of a tiny upper hole (figure 7b). The resulting acoustic signal consists in gradually decaying monochromatic sinusoids and can be modelled by a Helmholtz resonator (Vergniolle and Caplan-Auerbach, 2004). Also this source mechanism, like the resonating conduit model, could give rise to harmonics in the signal. In fact the event in figure 4a can be interpreted as generated either by a resonating conduit or by a Helmholtz resonator. The infra-

sound events at Mt. Etna, recorded during 2007–2008, can be interpreted as generated by the aforementioned source models.

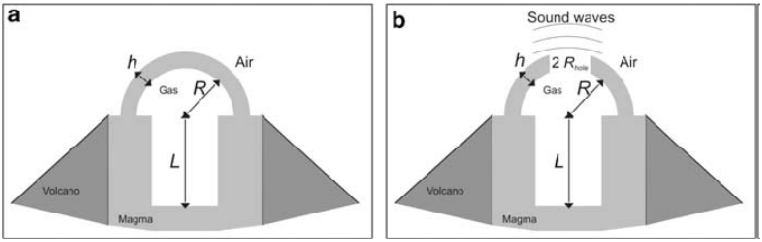

Figure 7: (a) Sketch of a vibrating bubble at the top of a magma column. R, L and h are, respectively, bubble radius and length, and thickness of the magma layer above the bubble (redrawn from Vergniolle et al., 2004). (b) The Helmholtz resonator is a rigid cavity of radius R and length L. Gas can escape through a small hole of radius Rhole with a velocity large enough to produce sound waves. h is the thickness of magma layer above bubble (redrawn from Vergniolle and Caplan-Auerbach, 2004)

5.2.1 Resonating conduit

A pipe-like conduit, if affected by trigger mechanisms such as explosive processes, can resonate generating seismic and infrasonic signals. Both these signals are characterized by spectra with a fundamental mode and harmonics. The spectral content depends on conduit geometrical-chemical-physical features.

The first characteristic influencing the frequency content of the radiated waves is the conduit length (L). The longer is the conduit, the lower is the frequency content. Moreover, also specific boundary conditions influence the resonating system. In fact, if the conduit is an open–open or closed–closed system has $n\lambda/2$ (λ = wavelength, n = 1,2,3,...) waves as longitudinal resonance modes whereas a system with one open and one closed end has $(2n-1)\ \lambda/4$ waves. Therefore, open–open or closed–closed systems produce signals with spectra characterized by evenly spaced peaks consisting of the fundamental mode, f_0, and a set of n integer harmonics which are multiples of f_0 (f_0, $f1 = 2\ f_0$, $f_2 = 3\ f_0$, …, $f_n = n\ f_0$); on the other hand spectra that have equally spaced peaks and contain only odd harmonics (f_0, $f_1 = 3f_0$, $f_2 = 5f_0$, …, $f_n = (2n-1)\ f_0$) are linked to resonant systems with one open and one closed end (De Angelis and McNutt, 2007). Finally, the frequency is also directly related to the wave velocity of the fluid in the conduit (c). The fluid could be gas or bubbly magma, that show a very wide range of variability of velocity. If air or pure hot gas are considered, their wave velocity are equal to 0.34 and 0.704 km/s (Weill et al., 1992), respectively. If we take into account bubbly magma, the wave velocity ranges from 0.3 km/s (Aki et al. 1977) to 2.5 km/s (Murase and McBirney, 1973), according to different flow conditions and magma properties (above all the gas fraction). Considering these prospective fluids filling the conduit, the lower end of the resonating system can consist in

the interface between bubbly-magma or gas and non-vesciculated magma. Because of the strong impedance contrast between the source fluid and the underlying non-vesciculated magma, this termination acts like a closed termination (De Angelis and McNutt, 2007). The upper end of the conduit can be either open to the atmosphere and act as an open termination, or obstructed by a relatively viscous plug at the vent acting as a closed boundary. In any case, the observation that the conduit is plugged at the vent (e.g. high porosity materials) does not necessary imply that it is an acoustically closed boundary (Garces and McNutt, 1997). In the light of these parameters, the fundamental mode of the generated signal is equal to (Hagerty et al., 2000):

$$f_0 = \frac{c}{2L} \tag{5.1}$$

5.2.2 Strombolian bubble vibration

In the Strombolian bubble vibration model the infrasound is produced by the vibration of a thin layer of magma, pushed by a variation of pressure inside a shallow metric bubble prior bursting. The bubble shape is approximated by a hemispherical head and a cylindrical tail, as expected in slug-flow (figure 7a). The radius of the bubble R varies around its equilibrium radius R_{eq} by (Vergniolle and Brandeis, 1996):

$$R = R_{eq}\left(1+\varepsilon\right) \tag{5.2}$$

where ε is the dimensionless radius of the bubble. The bubble volume V_g can be calculated by (Vergniolle and Brandeis, 1996):

$$V_g = \frac{2\pi R^3}{3} + \pi R_0^2 L \tag{5.3}$$

where L is the bubble length, R_0 is the initial radius. R_{eq} can be obtained by the following adiabatic law (Vergniolle and Brandeis, 1996):

$$R_{eq} = \left\{ \frac{3R_0^2}{2} \left[\left(\frac{2R_0}{3} + L \right) \left(1 + \frac{\Delta P}{p_{air}} \right)^{\frac{1}{\gamma}} - L \right] \right\}^{\frac{1}{3}} \tag{5.4}$$

where ΔP is the initial overpressure, p_{air} is the air pressure, γ is the ratio of specific heats. The Strombolian bubble vibration model is based on the general equation for the bubble vibration (Vergniolle and Brandeis, 1996):

$$\ddot{\varepsilon} + \left(\frac{12\mu}{\rho_l R_{eq}^2} \right) \dot{\varepsilon} + \frac{p_{air} \left[1 - \left(\frac{V_{eq}}{V_g} \right)^{\gamma} \right]}{\rho_l R_{eq} h} (1+\varepsilon)^2 = 0 \tag{5.5}$$

where μ is the viscosity, ρ_l is the magma density, V_{eq} is the equilibrium value of the gas volume, h is the thickness of the thin upper membrane. It is worth noting that V_g is a function of ε. The first initial condition to be specified is the initial value of the dimensionless radius ε_0. The second initial condition is the initial radial acceleration $\ddot{\varepsilon}_0$, which depends on the initial force applied to the layer of magma. Assuming that the bubble, at rest at the magma-air interface is suddenly overpressurized by an amount ΔP, this force is directly related to the bubble overpressure. Therefore the initial conditions are (Vergniolle and Brandeis, 1996):

$$\ddot{\varepsilon}_0 = \frac{\Delta P R_0^2}{\rho_l R_{eq}^3 h_{eq}} \tag{5.6}$$

$$\varepsilon_0 = \frac{R_0}{R_{eq}} - 1 \tag{5.7}$$

Ignoring viscous damping and assuming small oscillations our equation has only one physically possible solution, which is a simple oscillator. Therefore, on the basis of these assumptions the excess pressure in air is expressed as a sinusoidal function:

$$p_{ac} - p_{air} = -\rho_{air} R_{eq}^3 \frac{A\omega^2}{r} \sin(\omega t + \phi) \tag{5.8}$$

where the amplitude A, the radian frequency ω and the phase delay φ are:

$$A = \frac{\Delta P R_0^2}{3\gamma p_{air} R_{eq}^2} \left(\frac{2 + 3L/R_{eq}}{2} \right) \tag{5.9}$$

$$\omega = \left[\frac{3\gamma p_{ext}}{\rho_l R_{eq} h_{eq}} \left(\frac{2}{2 + 3L/R_{eq}} \right) \right]^{1/2} \tag{5.10}$$

$$\varphi = -\frac{\pi}{2} \tag{5.11}$$

where p_{ext} is close to the atmospheric pressure p_{air}. In general, the equation (6.5) has no analytical solution. We solved it by numerical integration using a fourth order Runge-Kutta method. Finally, in order to calcu-

late the excess pressure in air, the following equation is used (Vergniolle and Brandeis, 1996):

$$p_{ac} - p_{air} = \left[2\dot{R}^2\left(t - r/c\right) + R\left(t - r/c\right)\ddot{R}\left(t - r/c\right)\right]\frac{\rho_{air} R\left(t - r/c\right)}{r} \qquad (5.12)$$

where t is time, r is the distance source-sensor and c is the speed of sound in air, 340 m/s (Lighthill, 1978).

5.2.3 Helmholtz resonator

For a piston emitting sound in a halfspace, acoustic pressure is (Vergniolle and Caplan-Auerbach, 2004):

$$p_{ac} - p_{air} = \frac{\rho_{air}\ddot{\xi}R_{hole}^2}{2\pi r} \qquad (5.13)$$

where ξ is the displacement of air, R_{hole} is the hole radius. If the dimensions of the resonator are small compared to the wavelength, the behavior of an element of air in the neck of an undriven Helmholtz resonator is (Vergniolle and Caplan-Auerbach, 2004):

$$m_{helm}\ddot{\xi} + R_{helm}\dot{\xi} + s_{helm}\xi = 0 \qquad (5.14)$$

where m_{helm}, R_{helm} and s_{helm} are the mass, the resistance coefficient leading to damping and the stiffness coefficient of the oscillator, respectively (Vergniolle and Caplan-Auerbach, 2004):

$$m_{helm} = \rho_{air}\varepsilon S_{hole} \qquad (5.15)$$

$$R_{helm} = \frac{\rho_{air}\omega^2 S_{hole}^2}{2\pi c} \tag{5.16}$$

$$s_{helm} = \frac{\rho_{air} c^2 S_{hole}^2}{V_{helm}} \tag{5.17}$$

where ρ_{air} is the air density, S_{hole} is the hole area, V_{helm} is the volume of the resonator, ε is the effective length of the orifice (calculated as $\varepsilon = 8R_{hole}/3\pi$; Temkin, 1981). S_{hole} and V_{helm} are calculated as follows (Vergniolle and Caplan-Auerbach, 2004):

$$S_{hole} = \pi R_{hole}^2 \tag{5.18}$$

$$V_{helm} = \pi R^2 L + 2\pi R^3 / 3 \tag{5.19}$$

where R and L are radius and length of the bubble, respectively.
The air acceleration $\ddot{\xi}$ can be calculated by (Vergniolle and Caplan-Auerbach, 2004):

$$\ddot{\xi} = -\omega^2 A \exp(-t/\tau)\cos(\omega t + \varphi) \tag{5.20}$$

where ω and τ, radian frequency and relaxation time, respectively, are:

$$\omega = c\left(S_{hole} / \varepsilon V_{helm}\right)^{1/2} \tag{5.21}$$

$$\tau = \frac{2m_{helm}}{R_{helm}} \tag{5.22}$$

and, finally, A and φ are arbitrary constants for a damped harmonic solution and are calculated as follows:

$$A = -\frac{\Delta P}{\rho_{air}\varepsilon\omega^2 \cos\varphi} \tag{5.23}$$

$$\varphi = \arctan\left[\frac{-1}{\omega\tau}\right] \tag{5.24}$$

These equations of the Helmholtz resonator are not able to model harmonics, but only the fundamental mode of vibration.

5.2.4 Model inversion

The choice of the model to apply strictly depends on the waveform of the investigated signal. If the infrasound signal is composed of one cycle–one cycle and a half, followed by a second part with weaker oscillations (figure 4b, c), the Strombolian bubble model should be applied. On the other hand, if the infrasonic event is characterized by gradually decaying sinusoids with a fundamental mode and harmonics or with monochromatic spectral content (figure 4a), two different models can be applied: the resonating conduit and the Helmholtz resonator. The method to choose the model has still to be defined. We suggest using the damping features of the oscillations composing the infrasonic events as a quantitative parameter indicating the source type. For example, slow damping, that means many cycles, would be indicative either of a resonating conduit or of a Helmholtz resonator. Conversely, quick damping, and then one or two cycles, could be due to a Strombolian bubble model. Therefore, the quality factor values, computed in the third step (see sketch of figure 2) and describing the damping features of the infrasound waveforms, can be chosen as a model discriminator. If the quality factor is less than a certain threshold the Strombolian bubble model will be applied, otherwise

the Helmholtz resonator or the resonating conduit model will be considered. In the resonating conduit model, if there is information about the fluid filling the conduit, the length of the resonating portion of the conduit can be calculated by using the equation (6.1). For example assuming that the event, shown in figure 4a and generated by the NEC, is caused by a resonant conduit and that the fluid filling the conduit is gas, we infer that the length of the resonating portion of the conduit roughly ranges between 150 and 320 m, according to the air/gas conditions. However, since the ranges of variability of fluid features are very wide and the conduit resonance model oversimplified, the variations over time of the model parameters are to be taken into account rather than the exact values. In the other two models there are three unknown source parameters: radius of the bubble/ hole (Strombolian bubble and Helmholtz resonator respectively), length of the bubble and overpressure (R or R_{hole}, L and ΔP, respectively).

It is worth noting that the Helmholtz resonator model requires that the radius of the bubble, which can be inferred by the vent radius, is known. In order to constrain these unknowns, the estimation of the similarity between synthetic and observed infrasound signals is required. The synthetic signals can be calculated by using the equation (6.12) and (6.13) for the Strombolian bubble and Helmholtz resonator models, respectively. The comparison is carried out by the following equation:

$$E = \frac{\sum_{i=1}^{M} \left(U_{obs\ i} - U_{syn\ i} \right)^2}{M} \tag{5.25}$$

where E is the misfit between observed and synthetic signals, called prediction error, U_{obs} and U_{syn} are the observed and synthetic signals, and M is their number of samples. Model identification consists of two tasks.

The first task is a structural identification of the equations and the second one is an estimation of the model parameters. The optimization method chosen to look for the best fit between observed and synthetic signals is the Genetic Algorithm (GA) that applies Darwin's evolutionary theory to general optimization problems. This kind of algorithm represents a highly idealized model of a natural process and as such can be legitimately viewed as a very high level of abstraction. Biological strategies of behaviour adaptation and synthesis are used to enhance the probability of survival and propagation during their evolution (Ghoshray et al., 1995). This method is based on individuals, grouped into populations that represent the parameters searched in the estimation process. The GA method can be reassumed by the following steps: i) an initial set of candidate solutions, called initial population, are generated; ii) the evaluation of the candidate solutions is performed according to some fitness criteria; iii) on the basis of the performed evaluation some candidate solutions are kept and the others are discarded; iv) finally, certain variants are produced by using some kinds of operator on the surviving candidate solutions (Mitchell, 1996). The identification problem can be formulated as an optimization task whose aim is to find a set of parameters that minimize the prediction error between measured data and the model output (figure 8). The inversion task can be considered completed if the prediction error is lower than a fixed threshold or if a time-out condition occurs. In the former case the source parameters are stored in a database, while in the latter the event is discarded (figure 8).

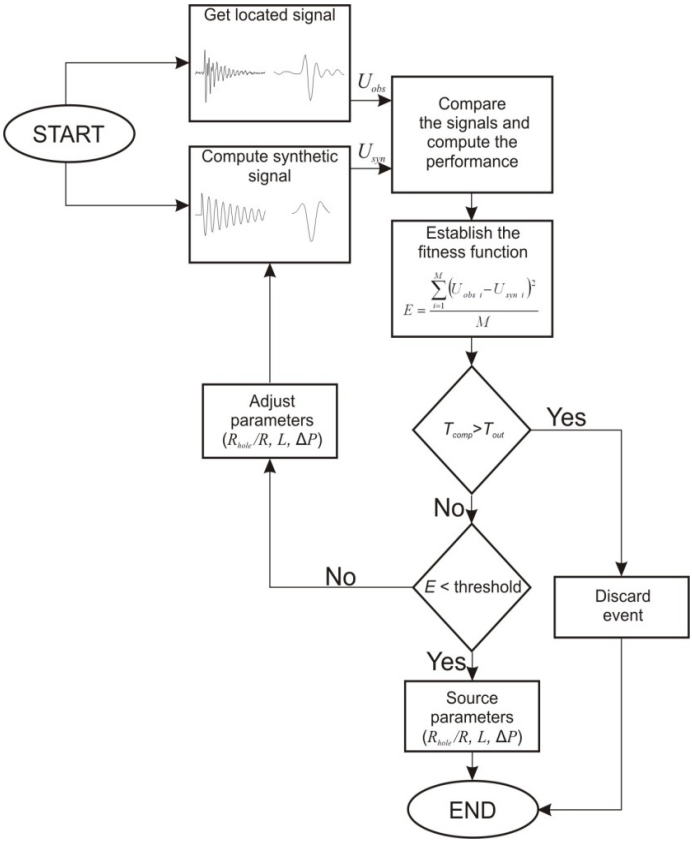

Figure 8: The principle scheme for parameter estimation by Genetic Algorithm (GA). T_{comp} and T_{out} indicate the computational time and the fixed timeout, respectively.

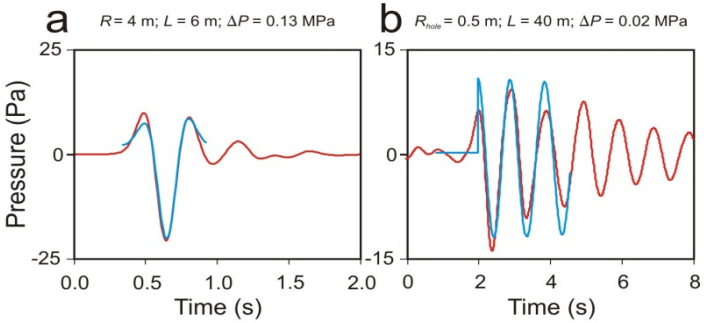

Figure 9: Comparison between the observed waveforms of infrasonic events recorded by EBEL station (red) and the synthetic ones (blue) considering Strombolian bubble vibration (a) and Helmholtz resonator (b) models. In (b) the bubble radius was fixed to 6 m. The observed waveform in(b) was low-pass filtered below 1.5 Hz, in order to remove harmonics.

Following Vergniolle and Caplan-Auerbach (2004), when the Helmholtz resonator model is applied, the fit between observed and synthetic signals should be optimised at the beginning of the oscillations in case there are other sources of damping not considered in the model. Examples of waveform inversion are reported in figure 9. By the waveform inversion of the event of figure 9a, due to Strombolian bubble vibration, the obtained radius and length of the bubble were equal to 4 m and 6 m, respectively, with an initial overpressure of 0.13 MPa. On the other hand, assuming that the event reported in figure 9b was generated by the Helmholtz resonator and fixing the bubble radius to 6 m, the obtained radius of the hole and length of the bubble would be equal to 0.5 m and 40 m, respectively, with an initial overpressure of 0.02 MPa. Similarly to the resonating conduit model, also the changes over time of the calculated source parameters of Helmholtz resonator and Strombolian bubble models can be important information to track the evolution of the volcanic activity (Vergniolle and Ripepe, 2008).

5.3 Infrasound investigation at Mt. Etna during September-November 2007 as a case of study.

A high degree of similarity of the waveforms of different infrasonic events implies the same source mechanism and locations varying roughly within one fourth of the dominant wavelength of the events (Geller and Mueller, 1980). However, the exact fraction of the wavelength depends on heterogeneity of velocity structure around the source (Nakahara, 2004). In light of these assumptions, a waveform classification is useful in order to get an initial idea about the variability of source mechanism and location. In Cannata et al. 2009b, a modified version of the method of Green and Neuberg (2006) was proposed (see section 4.7). In order to illustrate the algorithm, a set of 987 infrasonic events, recorded in the period spanning from September to November 2007 are used. The infrasonic signals, recorded in September–November 2007, contain a large number of infrasonic transients, generally short (1–4 s), characterized by impulsive compression onsets and by a spectral content in the frequency range 1–5 Hz (figure 10). The observed waveforms of these infrasonic transients are very similar to those recorded at other volcanoes: Stromboli (Ripepe et al., 1996), Klyuchevskoj (Firstov and Kravchenko, 1996), Sangay (Johnson and Lees, 2000), Karymsky (Johnson and Lees, 2000), Erebus (Rowe et al., 2000), Arenal (Hagerty et al., 2000), and Tungurahua (Ruiz et al., 2006). The method comprise the following step: (1) the 987 infrasonic events, belonging to the first data set (see section 2.1) and recorded at EBEL station are filtered in the frequency range 1–5 Hz; (2) the correlation matrix is calculated (figure 11); (3) a threshold value of cross correlation coefficient equal to 0.85 is chosen; (4) a master event was selected as the event with the largest number of correlation values above the chosen threshold; (5) an average family waveform is found by

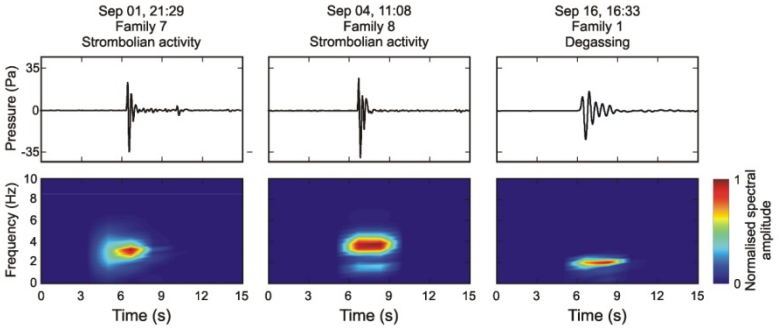

Figure 10: Examples of infrasonic events recorded by EBEL station and their short time Fourier transform, obtained by using 2.56-s-long windows overlapped by 1.28 s. The volcanic activity and the family (as explained in the text) are reported at the top.

stacking all events well correlated with the master event; (6) this stack waveform is then cross-correlated with the original infrasonic records, and all events with a correlation greater than 0.8 are grouped into a waveform family; and (7) steps 4–6 are repeated until the entire matrix was classified into distinct groups. In this procedure, overlap between clusters was not allowed; in fact, once an event was assigned to a given group, it was removed from the correlation matrix. Generally, the choice of the cross correlation threshold is a trade-off between classification accuracy and event detection. A too low threshold allows waveforms having different structure to be classified into the same group; conversely, a too high one does not allow events characterized by poor signal-to-noise ratio to be classified at all. For this reason, unlike the method of Green and Neuberg (2006), two different cross correlation thresholds are used in steps 3 and 6 are fixed: thus, this algorithm is able to achieve a reasonable number of families, each of which contains a significant quantity of events. By using this method nine families, comprising about 95% of

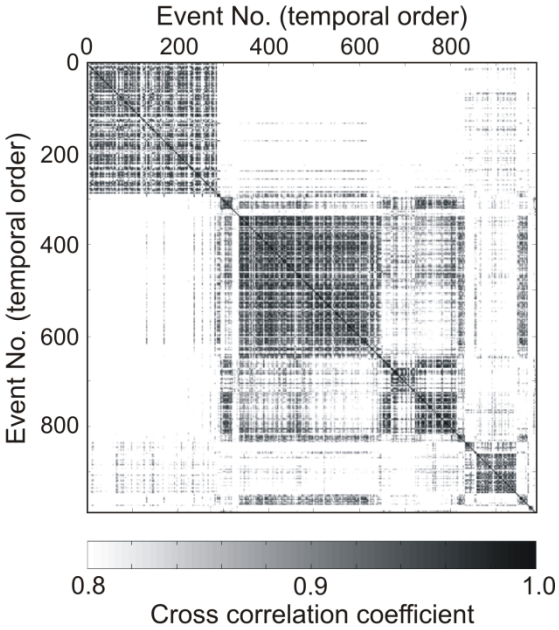

Figure 11: Correlation matrix of the 987 infrasonic events.

all the considered events, were found. This result suggests the repetitive excitation of stationary sources. The average waveforms and the time distribution of nine families are shown in figures 12 and 13, respectively. The great similitude observed among some families (figure 12) suggested the application of the cross correlation analysis described above on the stacked waveforms of the nine families. Tuning the cross correlation coefficient threshold to 0.9, three clusters were recognized. Families from 1 to 5 were grouped in cluster 1, families 6 and 7 in cluster 2, and families 8 and 9 in cluster 3. Finally, it is noteworthy that, unlike the other families that are spread out over periods of months, the events belonging to the families 8 and 9 (cluster 3) occurred during the interval 1–4 Septem-

ber. Several other analyses were performed on the 987 events belonging to the first data set to characterize the infrasonic activity at Mount Etna during the studied period. At first, the peak-to-peak amplitude of the infrasonic events that ranged from 1 to over 100 Pa was calculated. The highest values are mainly clustered at the beginning of September and are linked to the Strombolian activity at SEC (figure 14a). Successively, two different spectral analyses on the infrasonic events were performed. First, a 10-s-long window (1024 samples) for each event recorded at EBEL was used, comprising the whole waveform, and a spectrum was calculated by fast Fourier transform (FFT).

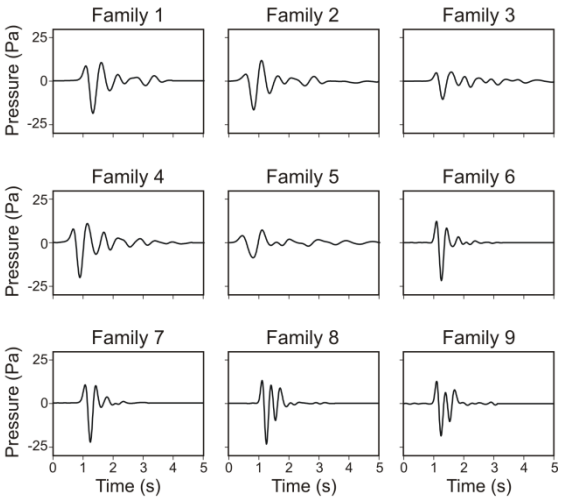

Figure 12: Waveforms obtained by stacking the events belonging to each family.

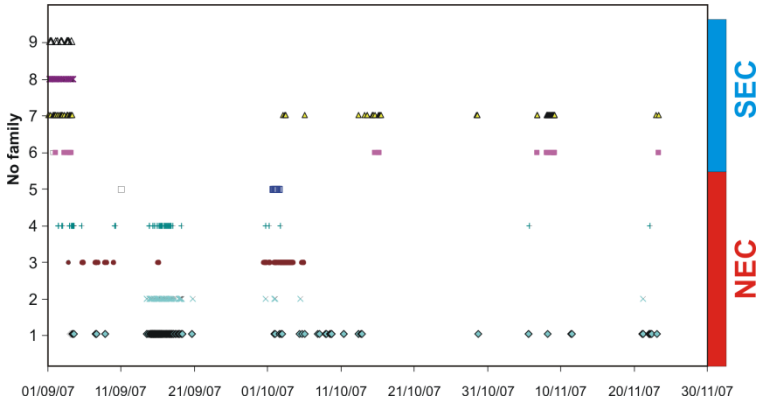

Figure 13: Time distribution of the families of the infrasonic events. These families were obtained by filtering the infrasonic signals between 1 and 5 Hz and following the method of Green and Neuberg, 2006. As explained in the text, families 1–5 are linked to activity at NEC, and families 6–9 are linked to activity at SEC.

Then, a peak frequency value was obtained for each event (figure 14b). Most of the calculated peak frequencies ranged between 1 and 4 Hz. It is also noteworthy that most of the highest frequency values (3–4 Hz) are clustered in the interval 1–4 September. Second, in order to verify the aforementioned spectral variations and to obtain information about the damping features of these infrasonic signals, the Sompi analysis (section 2.2.1; Kumazawa et al., 1990) was performed. Therefore, 2-s-long windows of infrasonic signal, recorded at EBEL and coinciding with the tails of the events, were taken into account, and frequency and quality factor were calculated for AR orders ranging between 2 and 10. The sharply monochromatic nature of the investigated signals justifies the choice of these low orders (Lesage, 2008). The results were very similar for all the used orders. As shown in figure 15a, the obtained frequency values confirmed the overall results of the FFT analysis. The quality factor values mainly ranged between 2 and 10 (figure 15b). In order to confirm the re-

sults gained with the crosscorrelation method, and try to reduce the size of information (signals, data, etc.), a parametric approach is an useful strategy able to speed up classification analyses, especially during monitoring activities.

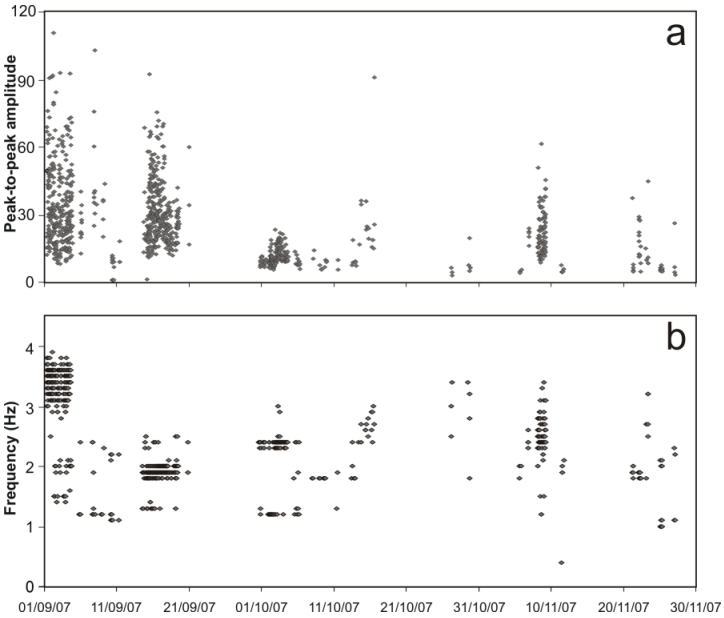

Figure 14: (a) Peak-to-peak amplitude and (b) peak frequency, calculated by FFT, of the infrasonic events at EBEL.

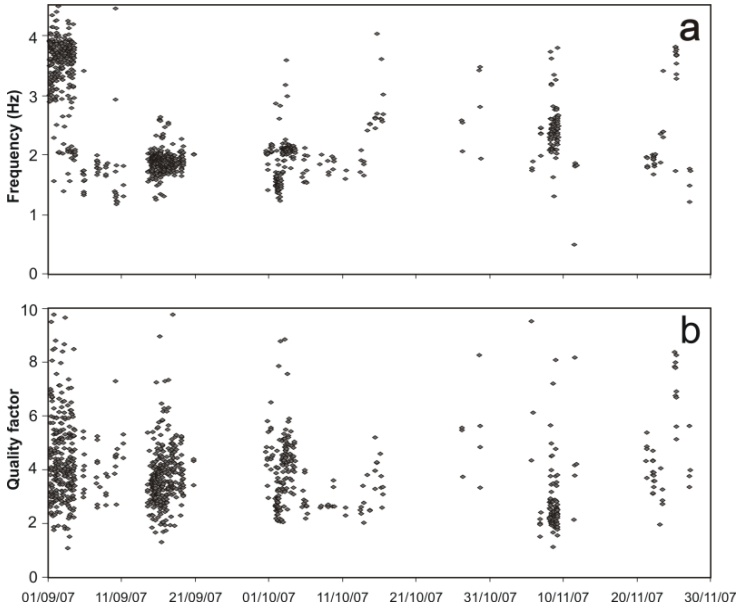

Figure 15: (a) Peak frequency and (b) quality factor at EBEL obtained by Sompi method for AR order of 2.

Generally, definition of peculiar features or properties by a "feature extractor" may be useful. In this case, the obtained spectral characteristics, computed by Sompi method (section 2.2.1), can be used as features to describe the infrasonic events. Then, in order to investigate prospective similarities or differences among these features extracted from the infrasonic signals, we plotted the frequency and the quality factor, in the x axis and y axis, respectively, and obtained the so-called "features plane'.' As shown in figure 16, the three clusters found by cross-correlation method were confirmed. Cluster 1 (containing the families 1, 2, 3, 4 and 5) showed frequency and quality factor in the range 1.2–2.2 Hz and 1.5–6.0, respectively.

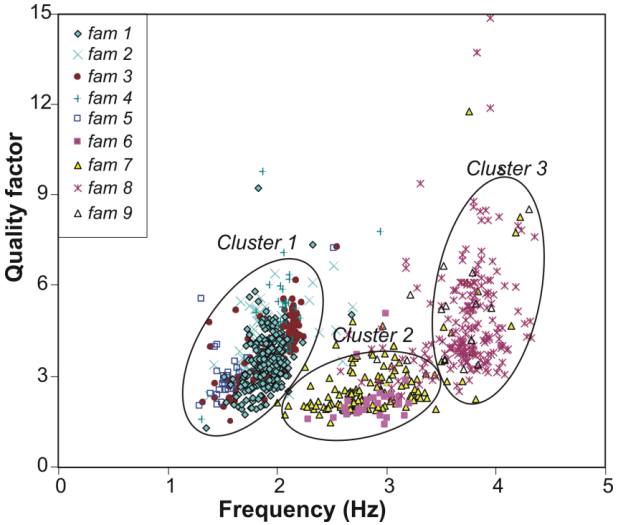

Figure 16: Peak frequency of the nine families of infrasonic events plotted versus the quality factor calculated by Sompi method (see legend).

Cluster 2 (comprising the families 6 and 7) was characterized by frequency range 2.0–3.5 Hz and quality factor 1.5–4.0. Finally, cluster 3 (composed of the remaining families 8 and 9) comprises events with frequency range 3.5–4.5 Hz and quality factor 3–9. The average waveforms of the three clusters and the respective spectra and f-g diagrams are shown in figure 17. The stacked trace of cluster 1 is characterized by the longest duration. The broadest range of quality factor of cluster 3 is due to the characteristics of this cluster. In fact, the waveforms of the events belonging to this cluster, composed of about 2.5 cycles with slow decay followed by a sharp amplitude decrease, cannot be considered as a perfect superposition of simple decaying sinusoids. Hence, the calculated quality factor values are slightly scattered.

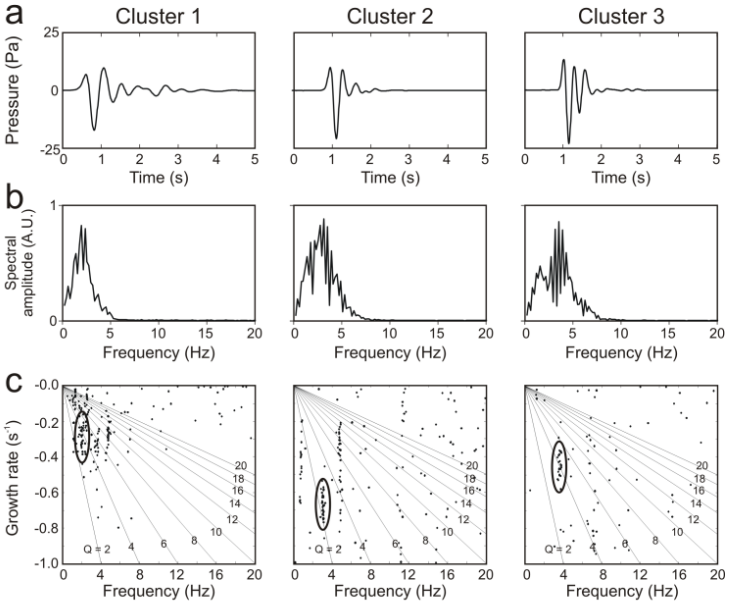

Figure 17: (a) Waveforms obtained by stacking the events belonging to the three clusters. (b) Amplitude spectra of the average waveforms, shown in (a). (c) The f-g diagrams of the average waveforms shown in (a) and obtained for all the trial AR orders (4–60). The gray lines represent lines along which the quality factor (Q) is constant. Clusters of points indicate a resolved dominant mode; scattered points represent noise. The solid ellipses encircle clusters of points representing resolved dominant mode with high spectral amplitude.

5.3.1 Source location

In order to obtain preliminary qualitative information about the source location of the infrasonic events, the differences between the arrival times of the 987 events of the first data set at the four stations were calculated (figure 18). It is noteworthy that only two different sets of time lag values were found, suggesting the existence of only two source locations. Moreover, events belonging to the same family shared the same time lag values, confirming a common source location. Successively, the location of the infrasonic source, computed using semblance method (see section 4.4), was estimated by the semblance grid searching procedure over a surface of 1.5 × 1.5 km, with spacing of 25 m, centered on the volcanic edifice and coinciding with the topographical surface. In this case, a point source and a sound speed of 340 m/s in the atmosphere is assumed. As the events of each family show both very similar waveforms and time lag values, they obviously share the same location and source mechanism. Therefore, a stacked waveforms of each family at all the stations is computed and then located. In order to calculate the stacked waveforms, all the waveforms from the two first events of the family 1 (one set of 4 signals for each event) and tried different time lags between these two sets of signals are taken into account. For each time lag value, the similarity between the events was evaluated by averaging the cross correlation coefficients calculated for each couple of corresponding signals (for example, “EBEL of event 1” and “EBEL of event 2” are two corresponding signals). The time lag value that gave the maximum average cross correlation coefficient was chosen and an average signal was obtained for each station.

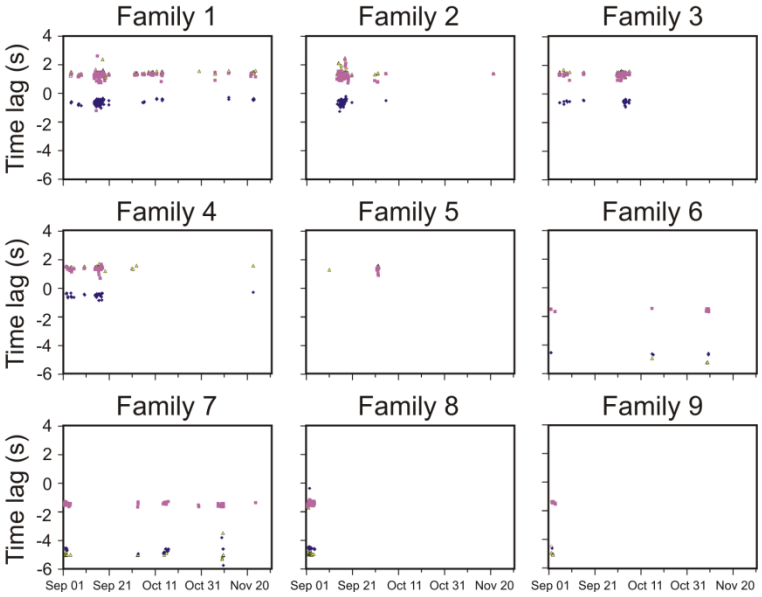

Figure 18: Difference between the arrival times of the infrasonic events at EBEL and EPDN (blue diamonds), at EBEL and ECPN (pink squares), and at EBEL and EPLC (yellow triangles).

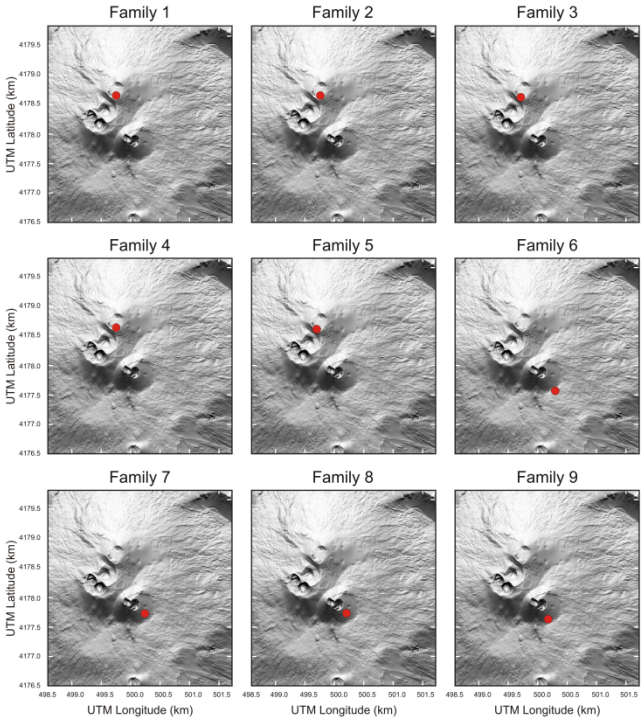

Figure 19: Location of the stacked events of the nine families recognized by the waveform classification.

The other events were compared to the average event that was "updated step by step" Thus, all the events contributed to the stacked signals representing the family (figure 12). The same procedure was followed for the other families. Then, the stacked waveforms were located (figure 19). The results of this analysis, in good agreement with the position of the most active summit craters during the studied period, confirm the existence of only 2 sources, the one coinciding with NEC and the other one with the pit crater on the eastern flank of SEC. Therefore, the families 1, 2, 3, 4 and 5 to NEC and the families 6, 7, 8 and 9 can be attributed to

SEC. Similarly, cluster 1 is related to the activity of NEC, and clusters 2 and 3 are related to the activity of SEC. Similar results were found at Stromboli by Ripepe and Marchetti, 2002, that recognized two different groups of infrasonic signals associated to two different craters. However, in other cases, different clusters of infrasonic events were found with no apparent relation to location (e.g., Ruiz et al., 2006).

5.3.2 Source mechanism

The detected infrasonic events are similar to the signals described by Vergniolle and Brandeis (1996), Ripepe and Marchetti (2002), Vergniolle (2003), and Vergniolle et al. (2004), and explained as generated by the vibration of a large gas bubble before bursting (see section 6.2). The other possible well developed models give rise to different waveforms to our recordings. For example, the local coalescence within a foam (Vergniolle and Caplan-Auerbach, 2004) produces gradually decaying sinusoids. The detected events are generally characterized by a first energetic part roughly composed of one cycle and a half, followed by a second part with various weaker oscillations. The acoustic resonance of magma/fluid in a conduit (Garces and McNutt, 1997) should produce signals with different harmonics components (a fundamental mode and overtones), whereas our recorded signals are mainly monochromatic. Therefore, in order to quantitatively investigate the source mechanism of the infrasonic events on the basis of bubble vibration model, a waveform inversion was performed. Using the equations reported in section 6.2.2, and fixing the values of density, viscosity of the magma, and thickness of magma above the vibrating bubble to 2700 kg/m3, 400 Pa s, and 0.1 m, respectively (Vergniolle, 2003; Vergniolle and Ripepe, 2008), synthetic waveforms can be calculated.

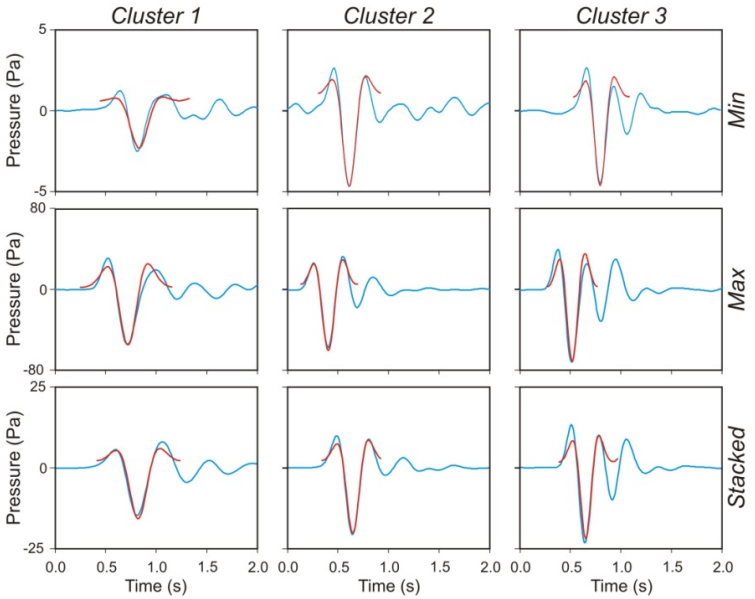

Figure 20: Comparison between the observed and stacked waveforms of the three clusters of infrasonic events (blue) and the synthetic ones (red). Min, Max, and Stacked indicate the waveforms of the events with minimum and maximum peak-to-peak amplitude and the stacked waveforms, respectively. The source parameters obtained by the waveform inversion are reported in Table 1.

Then, by the optimization algorithms described in section 6.2.4, the values of the three unknown parameters (radius, length of the bubble, and initial overpressure), that allow finding the best fit between synthetic and measured waveforms, were constrained. As described in section 6.2.4 the identification problem can be formulated as an optimization task whose aim is to find a set of parameters that minimize the prediction error between measured data and the model output. In this case, the model is represented by the vibration of a large gas bubble before bursting, mathematically described in section 6.2.2, as mentioned above, and the

measured data for each cluster consist in the waveforms of the two events with minimum and maximum values of peak-to-peak amplitude, and the stacked waveform. The comparison between synthetic and observed or stacked waveforms is reported in figure 20 and shows that the fit is good at least for the first cycle of vibration: an explanation can be that at the end of the first cycle the bubble bursts and then the model ceases to be valid. The results of the inversion (Table 1) exhibit smaller bubbles for clusters 2 and 3 (roughly radius of 3–4mand length of 2–7 m) than for cluster 1 (roughly radius of 5–7mand length of 11–16 m). Moreover, the initial overpressure is higher for clusters 2–3 (in the range 0.06–1.15 MPa) than cluster 1 (in the range 0.02–0.32 MPa). It is also worth noting that cluster 3 shows the maximum values of overpressure (up to 1.15 MPa). The obtained values of the three unknown parameters are reasonable and in good agreement with previously obtained values at Etna (Vergniolle, 2003; Vergniolle and Ripepe, 2008; Cannata et al., 2009a), at Stromboli (Vergniolle and Brandeis, 1996), and at Shishaldin (Vergniolle et al., 2004). Moreover, given that clusters 2 and 3 shared the same source crater, the similarity of the bubble radii of these clusters was expected. In fact, the bubble radius strongly depends on the size of the source vent. Finally, the lower overpressure value of cluster 1 is consistent with the longer duration of the events. Indeed, high gas overpressure produces large pressure perturbations in the atmosphere with short duration. Conversely, low regimes of gas overpressure generate long lasting explosions with small acoustic amplitude (Wilson and Head, 1981; Ripepe and Marchetti, 2002).

	R (m)	*L* (m)	*P* (MPa)
Min (Cluster 1)	6	15	0.02
Max (Cluster 1)	5	16	0.32
Stacked (Cluster 1)	7	11	0.08
Min (Cluster 2)	3	7	0.06
Max (Cluster 2)	4	2	0.56
Stacked (Cluster 2)	4	6	0.13
Min (Cluster 3)	3	5	0.08
Max (Cluster 3)	3	2	1.15
Stacked (Cluster 3)	3	4	0.23

Table 1: Strombolian bubble Parameters obtained by the waveform inversion: R, L, and P indicate radius, length of the bubble and initial overpressure, respectively. Min, Max, and Stacked indicate the waveforms of the events with minimum and maximum peak-to-peak amplitude, and the stacked waveforms, respectively.

5.3.3 Emitted gas volume

Following the method shown by Vergniolle et al., 2004, Vergniolle, 2008, and Vergniolle and Ripepe, 2008, we quantified the emitted gas volume per day for NEC and SEC. In this case the second data set, comprising the detectable events occurring during the studied period, was used. The whole data set was divided into subsets, each containing the events occurring in a day. Then, on the basis of the spectral features of the events, each subset was again divided into three subsets, containing events with similar spectral content to the ones belonging to clusters 1, 2 and 3. Therefore, assuming that events of all the three clusters occurred every day during the studied 3 months, 91 times 3 subsets should be created. However, only 103 subsets were formed because of the lack of events in some clusters during several days (especially cluster 3, taking place only during the first days of September). Successively, the number of events and the stacked waveform at EBEL station (figure 21) were calculated for each obtained subset. Then, by performing the waveform inversion, as

shown in section 2.5, the bubble volume and the overpressure were calculated for each stacked waveform. The bubble gas volume expelled in the atmosphere can then be deduced from the gas volume at the vent by using the overpressure values and the perfect gas law (Vergniolle and Ripepe, 2008). Finally, the daily emitted gas volume was calculated for each cluster by multiplying the bubble gas volume in the atmosphere with the daily number of events. The daily emitted gas volume of the NEC coincides with the total gas volume of the subset of events similar to cluster 1, whereas the one of the SEC is equal to the sum of the gas volume of the subsets of events similar to clusters 2 and 3.

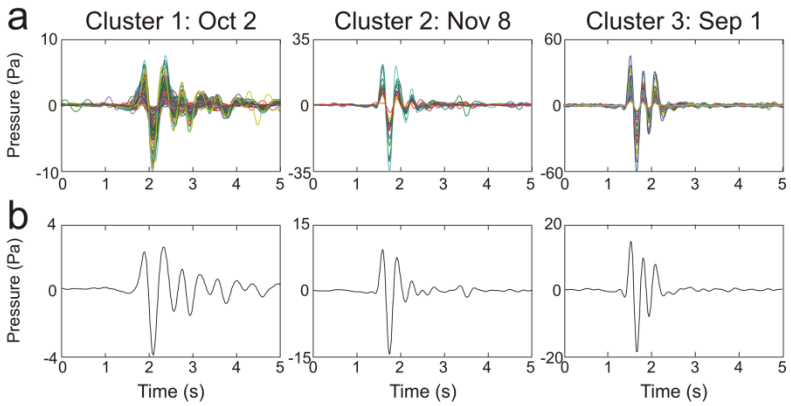

Figure 21: Examples of (a) daily subsets of infrasound events and (b) corresponding stacked waveforms (see section 6.3.3 for details).

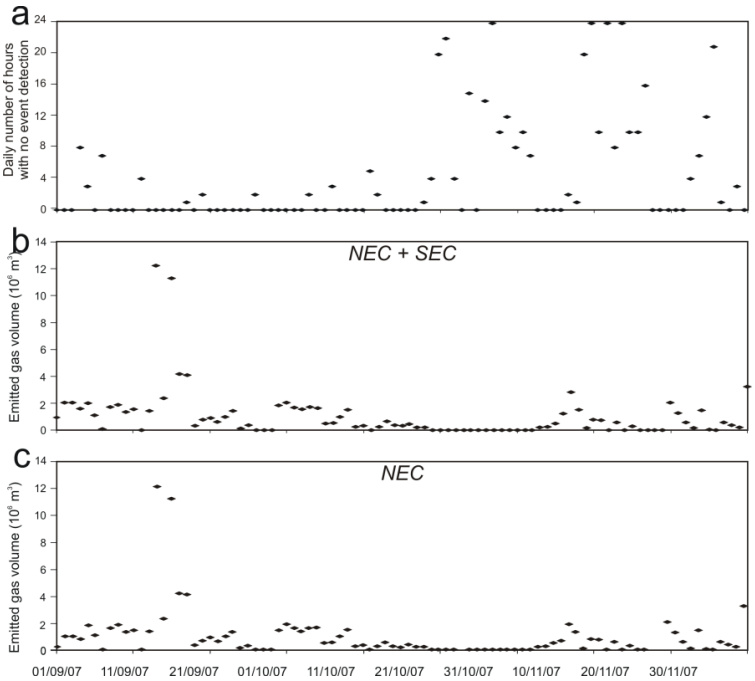

Figure 22: (a) Daily number of hours, when the detection of events was not possible because of infrasonic tremor during paroxysmal volcanic activity or noise mainly due to bad weather. (b) Total daily emitted gas volume of NEC and SEC, calculated by inversion of infrasound events (see section 6.3.3 for details). (c) Daily emitted gas volume of NEC.

Moreover, the estimation of daily duration of the time periods characterized by infrasonic tremor (recorded at the same time as the two lava fountain episodes) and bad weather, when the events could not be performed, was performed (figure 22a). Then, for the days characterized by wind and/or tremor we multiplied the estimated daily emitted gas volume by a factor calculated on the basis of the percentage of the day when the event detection was not possible. For instance, assuming that during a certain day there was a 12 h time interval of impossible event

detection, the gas volume estimated for that day would be multiplied by 2. Thus, we could correct the daily emitted gas volume taking into account also the prospective nondetectable infrasonic events during these "blind time intervals" (figures 22b, 22c, and 23a). In summary, this method enabled estimating the emitted gas volume for each active crater. The average and maximum daily emitted gas volume were equal to about 10^6 and 10^7 m^3, respectively, at NEC, and about 10^5 and 10^6 m^3, respectively, at SEC. It is worth noting that infrasound measurements can only detect bubbles with an inner overpressure and thus likely coming from depth. Surface degassing activity observed at vents results from both the bubbles coming from depth and those quasi-stagnant in the conduit, which are silent on acoustic records (Vergniolle and Ripepe, 2008).

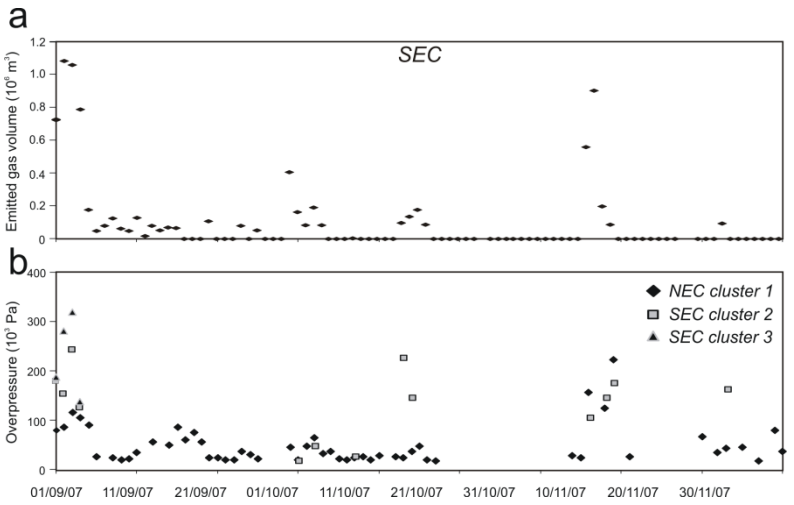

Figure 23: (a) Daily emitted gas volume of SEC. (b) Overpressure values calculated by waveform inversion of each daily stacked event related to clusters 1, 2, and 3 (see legend).

Consequently, degassing related to the former is called active, while degassing caused by the latter is passive (Vergniolle and Ripepe, 2008). Therefore, by using the aforementioned method daily active degassing per crater was estimated. This was also confirmed by the overpressure values calculated for each stacked waveform (figure 23b), much higher than the ones obtained by the coalescence of two bubbles in a conduit (Vergniolle and Caplan-Auerbach, 2004; Vergniolle and Ripepe, 2008). Finally, NEC has been the most active crater from the active degassing point of view, although most of the explosive and effusive eruptions have affected SEC during the investigated period.

5.3.4 Volcanic activity

In September–November 2007 the eruptive activity at Mount Etna volcano, described in the reports of INGV, Sezione di Catania was characterized by explosive activity and degassing at two summit craters (figure 24). In particular, SEC was affected by Strombolian activity (resumed on 15 August 2007), ash emission and two lava fountain episodes that took place on 4–5 September and 23–24 November. These two episodes lasted several hours and gave rise to lava flows on the eastern flank of the volcano. Strong degassing activity was observed at NEC. Moreover, the images recorded by a video camera located on the upper southern flank of the volcano (ca. 4 km away from SEC) to follow the eruptive activity of SEC in detail were used (see step 2 of the sketch shown in figure 2). The images of video camera are stored at a rate of 30 frames per minute. Unfortunately, only very short time periods could be analyzed because of the generally bad weather conditions at high altitude. Focusing on the time period 1–4 September, characterized by fairly good visibility of the sum-

mit area and by the occurrence of clusters 2 and 3, both linked to the activity of SEC (see section 6.3.1). It was noted that the infrasonic events generally occurred at the same time as explosions taking place at the pit crater opened on the ESE flank of the SEC during the 2004–2005 eruption. In particular, the events belonging to cluster 3 (that was present only in this time span) were coincident with "more visible" explosions than the events of cluster 2. The explosions linked to cluster 3 were characterized by a relevant presence of ash composed by lithic clasts due to moderate landslides and collapse of the inner walls of the cone (figure 25). The different features of the explosions can be due to (1) variable gas expansion velocity in the magma column; (2) changes in the depth of the bubble formation; and (3) variations in the gas volume and/or the gas mass fraction in the magma. Because explosions with different features were not separated in time but generally occurred during the same time intervals, the hypotheses

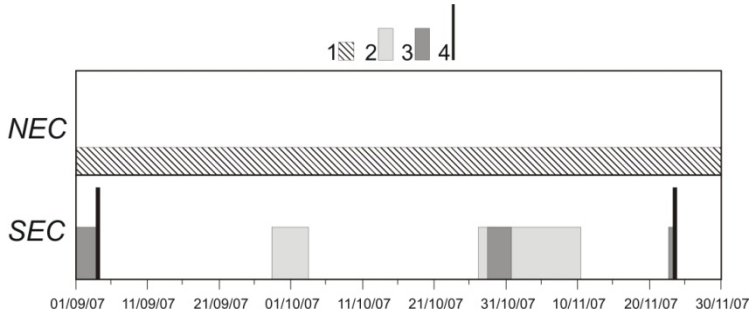

Figure 24: Eruptive activity at Mount Etna between September and November 2007 shown for two summit craters (SEC and NEC) (1, degassing; 2, ash emission; 3, Strombolian activity; 4, lava fountains). See Figure 1 for details of the summit area.

involving continuous and quick variation of the magma characteristics are not plausible. In light of this, the different intensity of events belonging to cluster 3 may be linked to the occasional occurrence of landslides, as testified by images gathered. The interpretation of an overload generated by lithic clasts accumulation that occludes the vent seems more reasonable. Moreover, the stronger intensity of the explosions accompanying the infrasonic events of cluster 3 is also supported by the higher values of overpressure of cluster 3 than cluster 2, obtained by the study of source mechanism (see section 6.3.2).

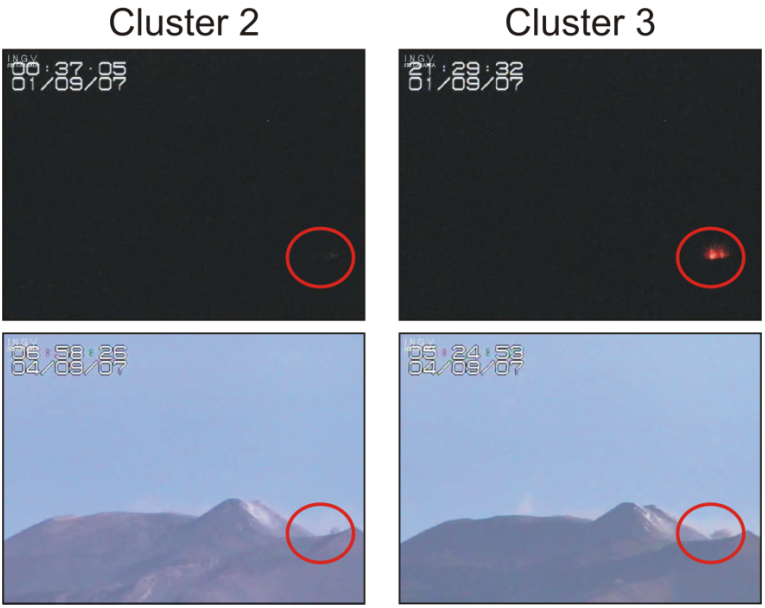

Figure 25: Video camera frames showing explosive activity at the SEC recorded at the same time as infrasonic events belonging to clusters 2 and 3.

5.4 Mt.Etna during May 2008: second case of study

In this section, the capability of infrasound monitoring at Mt. Etna is shown. In particular, the methods explained in section 6.1 and 6.2, were applied in the period May 8-16, 2008, characterised by intense and spectacular volcanic activity affecting two of the four summit craters, the NEC and the SEC, and a new eruptive fissure (EF) that opened east of the summit area (figure 26) on May 13. During the last years Mt. Etna showed a high eruption rate. From January 2008 mild Strombolian and degassing activity took place at SEC and NEC. On May 8-9, strong degassing occurred at NEC, then on May 10, Strombolian activity followed by a lava fountain, occurred at SEC. After the end of SEC eruption, NEC was the most active vent and was affected by moderate to strong degassing. On May 13 at 08:39 (all times are GMT) a seismic swarm took place under the summit area (focal depths ranging between -1.5 and 1.5 km a.s.l.). Volcanic tremor showed a significant amplitude increase at 08:52, and clinometric and GPS networks almost simultaneously evidenced remarkable ground deformations. All these phenomena highlight an intrusive process in the summit part of the volcano. Nevertheless, adverse weather conditions inhibited observations by the video-camera network on the volcano. The first detection of the eruption was made by Meteosat satellite images, whereas volcanologists climbing the volcano in the fog were only able to hear loud detonations until 13:00, when the improved weather allowed Strombolian activity at the upper part of EF to be visible. On the basis of the onset of the eruptive activity of EF, the period May 8-16, 2008 was divided into two intervals: period I, from May 8 to 13 at 09:25, and the following period II, until May 16 (figure 27a). Also in this case the infrasonic signal consisted of a few

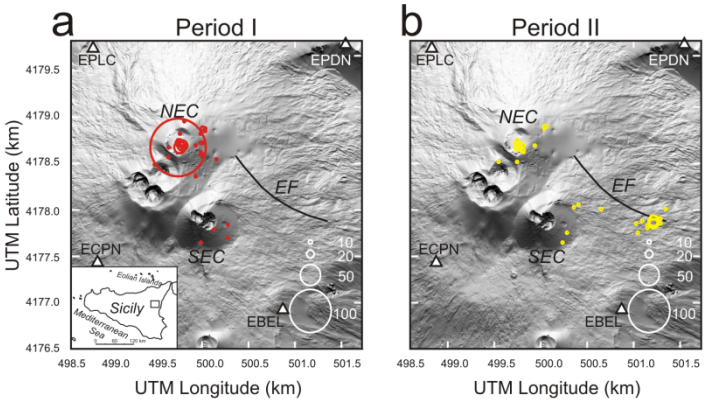

Figure 26: Digital elevation model of Mt. Etna summit. North East Crater (NEC), South East Crater (SEC) and the eruptive fissure (black line, EF), which opened on May 13, are indicated. The source locations of 400 infrasound events recorded during the periods I (a) and II (b) are indicated with red and yellow circles, respectively. The radii of the circles are proportional to the number of the locations in each grid node (see white circles and numbers reported in the lower right corner of the map). The sites of the infrasonic sensors are indicated with triangles.

seconds long transients characterised by impulsive compression onsets (figure 27b) and by sharply peaked spectra (figure 27c). During the lava fountains the increasing rate of infrasonic events gave rise to an almost continuous signal called "infrasonic tremor" (figure 27d-e). Four types of data and/or information were helpful to instrumentally follow the evolution of the eruptive activity: i) the time variation of the root mean square (RMS) amplitude of raw data; ii) the peak-to-peak amplitude and iii) the dominant frequency of the infrasound events; iv) their source location. The signal amplitude at EBEL station (chosen because marginally affected by wind noise) was obtained by calculating the RMS within non-overlapping 30-second-long windows for the whole recordings.

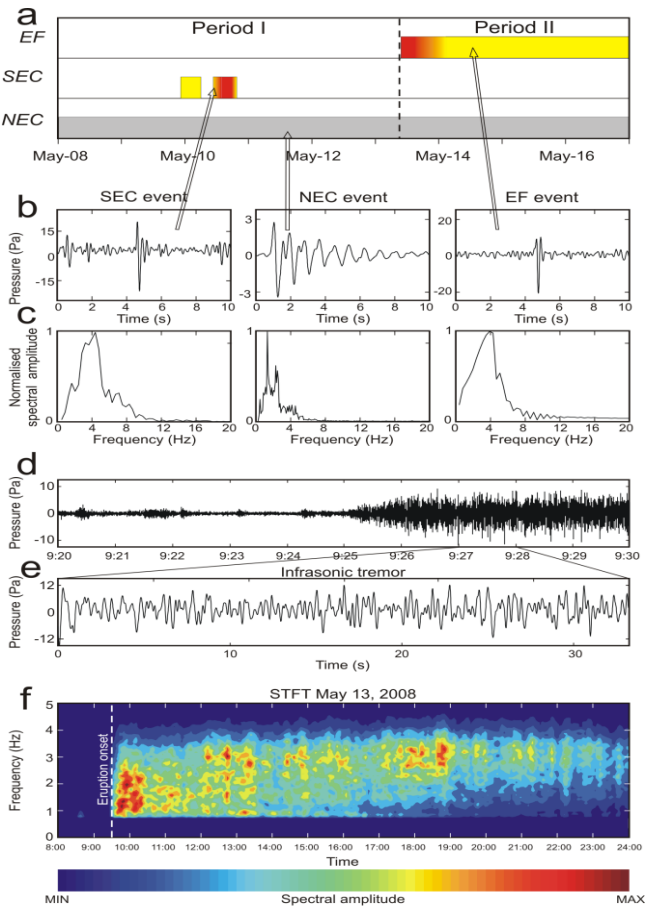

Figure 27: (a) Eruptive activity (red = lava fountain; yellow = Strombolian activity; grey = degassing activity) from May 8 to 16, 2008 shown for NEC, SEC and EF. The dashed line indicates the boundary between period I and period II (see text for details). (b) Infrasonic events related to the activity of SEC, NEC and EF and their spectra (c). (d) Infrasonic recordings at EBEL station between 9:20 and 9:30 on May 13, 2008. (e) Infrasonic tremor recorded at 9:27 on May 13, 2008 at EBEL (same time scale as in b). (f) Short Time Fourier Transform (STFT) of the infrasonic signal recorded at EBEL station on May 13, 2008, from 8:00 to 24:00. The white dashed line indicates the onset of the eruption.

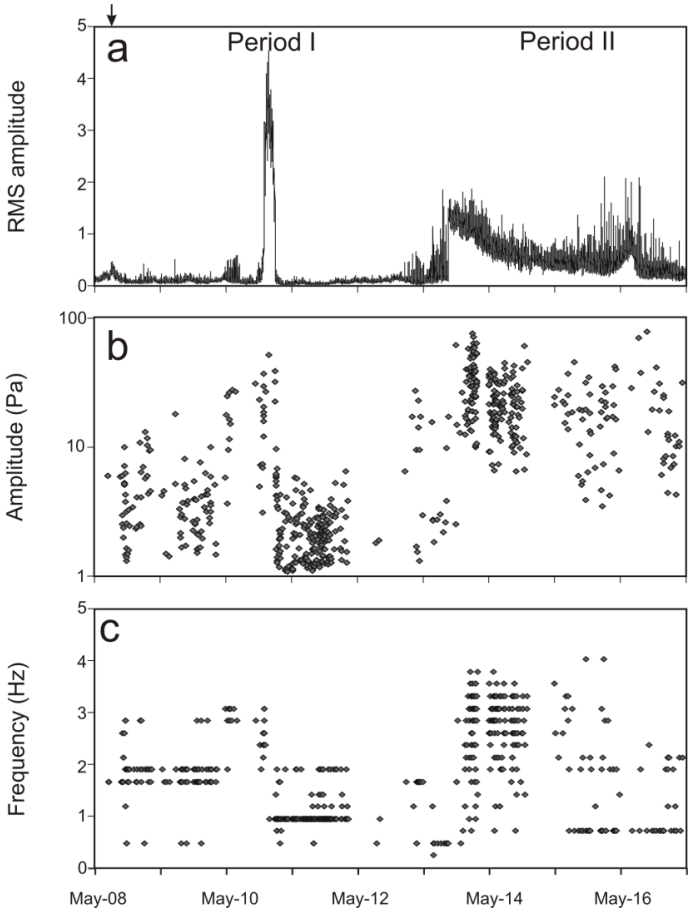

Figure 28: (a) Time variation of amplitude of the infrasonic signal, calculated as root mean square (RMS) of moving windows of the recordings at EBEL; the top arrow evidences a period characterized by strong wind affecting the RMS amplitude, nevertheless wind effect influenced other stations in a severe way also in crucial periods such as the May 10, during the lava fountain. (b) Time distribution of the peak-to-peak amplitude, and (c) of the dominant frequency of 400 infrasonic events recorded at EBEL.

The value of peak-to-peak amplitude was easily measured for each event. The dominant frequency of each event was obtained from a Fast Fourier Transform (FFT) spectrum computed on a 2.56-second-long window, starting at the onset of the event. The evolution of the three above parameters during the investigated time span is shown in figure 28a,b,c, respectively. The location of the infrasonic source was estimated by the 2D semblance algorithm over a surface grid of 1.5×1.5 km, with spacing of 25 m, covering the summit area and coinciding with the topographic surface. The location results are reported in (figure 29a-b and 26a-b). The precision of locations is impressive, especially for the events linked to the activity of NEC and of spatter-cones located at the lowermost tip of EF. The scatter in source locations for the SEC events is due to wind effects, and then to both the noise and the break of the assumption of a constant sound speed. The considered period was analyzed using the steps explained in section 6.1 In particular, during period I (figure 28a), the infrasound signal was mainly characterised by transients (recognized by means of automatic STA/LTA trigger) lasting up to 10 seconds (figure 27b), with two different frequency peaks between 1 and 2 Hz (figure 27c and 28c), low values of peak-to-peak amplitude (figure 28b) and source location constrained at NEC (figure 29a,b and 26a). An exception was found on May 10, at the same time as SEC activity, when infrasonic transients showed shorter duration (about 2 seconds; figure 27b), larger peak-to-peak amplitude (figure 28b), and higher frequency (ranging between 3 and 4 Hz; figure 27c and 28c). Moreover, during the lava fountain at SEC infrasonic tremor was recorded causing a sharp RMS increase (figure 28a). We were able to locate only a few events related to the SEC activity because of the strong wind noise at ECPN and EPDN stations. Period II was initially characterised by the occurrence of infrasonic tremor, starting at 09:25 and marking the onset of the eruptive ac-

tivity of EF (figures 27d,e). This is the only available real time datum able to give us the exact timing of the eruption onset.

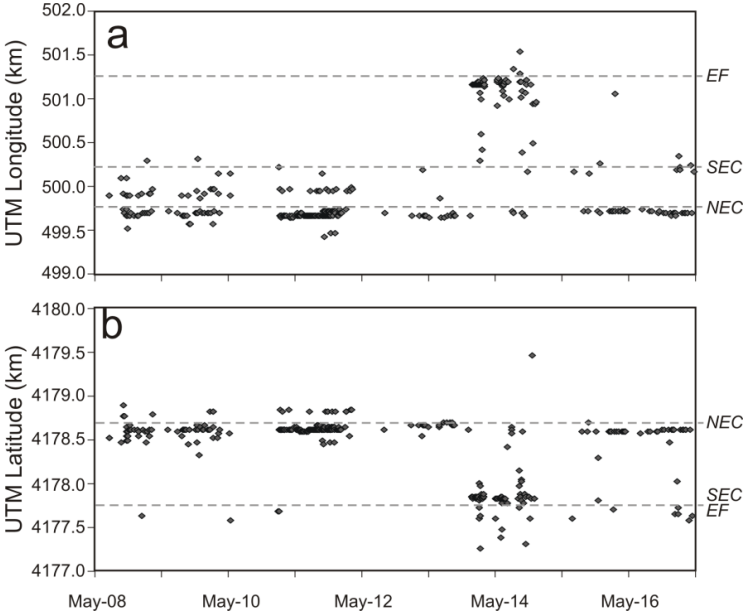

Figure 29: (a-b) Time variation of the source location of the infrasonic events.

The location was tentatively done on the basis of the first impulsive events following the continuous tremor signal. It is worth noting that during the first hours of the eruption, the spectral content of the infrasonic tremor gradually changed from about 1.0-3.5 Hz to 2.0-4.0 Hz (figure 27f), because of a change either in source location and/or in source parameters. The detected infrasonic events exhibited very short duration (about 1 second; figure 27b), frequencies mostly ranging between 2.5 and 4 Hz (figure 27c and 28c), and higher peak-to-peak amplitude (figure 28b). Moreover, on May 13-14, the infrasound source moved southeastward from NEC highlighting the activity at the lowermost tip of EF (figures 29a,b and 26a). During both periods I and II, three families of events with different features were detected: NEC, SEC and EF events (figures 27b,c). Due to the explosive activity characterising SEC and EF, and to the observed waveforms, the events of the second and third families can be modelled in terms of oscillations of Strombolian gas bubbles, as explained in section 6.2.2 modelled as cylinders with hemispherical heads before they burst. By the optimization process explained in section 6.2.4., the values of the three unknown parameters, radius, length of the bubble and initial overpressure were constrained. For measured data, two events for each family were take into account. In particular, an event with low amplitude and another with high amplitude (figure 30a and 30c). Both the investigated families showed fairly steady values of radius and length of the bubble, but very variable initial overpressure. For SEC events, a radius length of 2.9-3.3 m, a length 4.4-5.6 m and an initial overpressure of 48-221 kPa were obtained. On the other hand, EF events were fitted by using radius and length of the bubble respectively equal to 2.5-3.1 m and 2.8-3.4 m, with an initial overpressure of 72-421 kPa. These results are reasonable and in good agreement with previously obtained values at Mt. Etna (Vergniolle and Ripepe, 2008). Con-

versely, the source of long lasting (up to 10 s) NEC events cannot be explained by Strombolian bubble oscillations. A possible source of these signals is the coalescence of the very shallow part of a foam building up into the conduit, which produces large gas bubbles. In this case, the gas escapes through a tiny upper hole. The main difference with the former Strombolian bubble model is a lower overpressure, which changes the type of sound radiation.

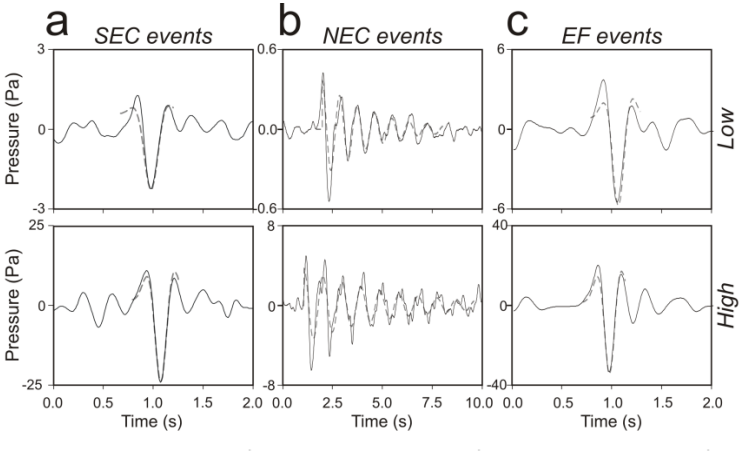

Figure 30: Comparison between the observed waveforms of the three families of infrasonic events (black) and the synthetic ones (dashed grey). Traces of NEC events are low-pass filtered at 1.5 Hz. "Low" and "High" indicate the waveforms of the events with low and high peak-to-peak amplitude, respectively.

The resulting acoustic signal can be modelled by the Helmholtz resonator introduced in section 6.2.3 Hence, NEC events were modelled by a Helmholtz resonator, by using the equation reported in section 6.2.3 and performing GA inversion (see section 6.2.4). Since the Helmholtz resonator is only able to model monochromatic damped oscillations, observed waveforms were filtered below 1.5 Hz (eliminating harmonics) considering events characterised by low and high amplitude (figure 30b). On the basis of results obtained analysing the infrasound recorded during September – November 2007 (Cannata et al., 2009b), the bubble radius at NEC was fixed at 6 m. Therefore, the obtained radius of the hole and length of the bubble were equal to 0.5 m and 34-40 m, respectively, with an initial overpressure of 1.8-22.7 kPa. Since the fact that other sources of damping are not considered in the model, the fit at the beginning of the oscillations was optimized (figure 30b). Moreover, the small mismatch observed at the very first beginning of the acoustic waveform is compatible with the finite time taken by the hole to reach its final size (Vergniolle and Caplan-Auerbach, 2004). Although the results of inversion for NEC events were acceptable, the different damping between synthetic and observed waveforms, together with the presence of harmonics in the signals, leads to a possible existence of other potential source mechanisms, allowing to model damped oscillations, such as the resonance of fluids (magma or gas) in a conduit (Garces and McNutt, 1997). Given that for NEC events the frequency value of a spectral peak is exactly twice the frequency value of the other spectral peak **(**figure 27c**)**, the conduit is to be assumed either open or closed at both ends (Garces and McNutt, 1997). We suggest that the part of the conduit of NEC generating infrasonic events was filled by gas and closed: the lower closed end was provided by the magma free surface, while the upper closed end by a narrowing of the conduit. This due to the fact that propagation of

infrasound in the atmosphere requires that the conduit is not completely closed. In any case, the observation that the conduit is plugged at the vent does not necessary imply that it is an acoustically closed boundary (Garces and McNutt, 1997). On the basis of this model, the lower spectral peak (1.1 Hz; figure 27c) can be interpreted as the fundamental mode. It is equal to the ratio between the speed of sound in gas and twice the length of the conduit. The speed of sound ranges between 708 m/s, considering a pure hot gas (Weill et al., 1992), and 340 m/s the speed of sound in air. Therefore, a length of the resonating portion of the conduit, roughly ranging between 150 and 320 m, can be reasonable. By a comparison between the two investigated periods, September-Novenber 2007 and May 2008, it is clear that the NEC events exhibit different features. While in the first period a strombolian bubble vibration model provided good results, in May 2008 the resonating conduit gave more reliable results. This change can be explained considering the different volcanic processes that led to different phenomena, the lava fountains in 2007 and the 2008-2009 eruption.

5.5 Clustering of infrasonic events as tool to detect and locate explosive activity at Mt. Etna volcano

The periods analyzed in sections 6.3 and 6.4 show how the active volcanoes generate infrasonic signals, whose investigation provides useful information for both monitoring purposes and the study of the dynamics of explosive phenomena. In this view, at Mt. Etna volcano, a pattern recognition system based on infrasonic waveform features has been developed. Firstly, by a parametric power spectrum method, in particular Sompi method, features able to characterize the infrasound events were used. As described in section 6.3, peak frequency and quality factor are a good waveform descriptors. Then, together with the peak-to-peak amplitude, these features set is used to classify waveforms. Before the classification, the definition of possible clusters in the feature space is needed. The goal of this process is to find a reasonable cluster partitioning of the feature space describing the infrasonic waveform and then the association with volcano activities. This process involves different techniques and constitutes the basis of an automatic system able to locate different kinds of infrasound events without the standard location algorithm described in sections 4.4 Since different kinds of activities are associated to distinct signal waveform features, this system is able to recognize different explosive regimes in the summit area of Mt. Etna. This leads to a waveform – source crater association. The following section will describe the first automatic event characterization applied on real time infrasound monitoring at active volcanoes (Montalto et al., 2010). It can be seen as a naturally extension of the sketch reported in figure 2 and described in section 6.1.

5.5.1 Discovering clusters using SOM

In this section infrasound signals recorded during the period September - November 2007, also described in section 6.3, are analyzed using unsupervised clustering approach. In order to investigate prospective similarities or differences among the waveform features, the frequency, the quality factor and the peak-to-peak amplitude, are plotted in the x-axis, y-axis and z-axis, respectively, obtaining the *feature space* (figure 31). This can be considered as an extension of the *feature plane* shown in figure 16 and described in section 6.3 The approach adopted in this section for clusters discovering is the Self- Organizing Map (SOM) (see section 3.4). SOM, is a neural network based on unsupervised learning useful in data visualization and exploration .

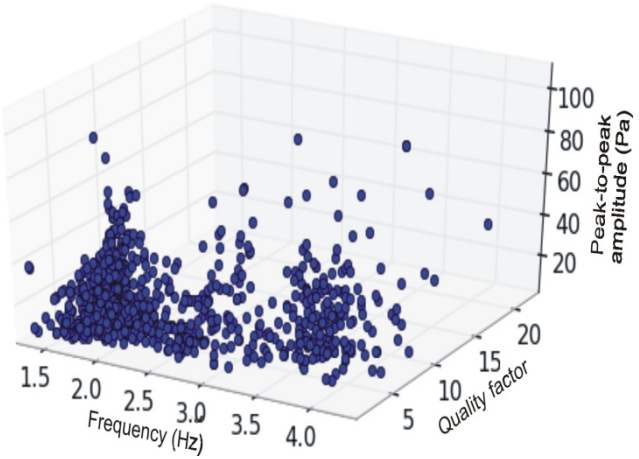

Figure 21: Feature space with frequency, quality factor and peak-to-peak amplitude of the infrasound events recorded at EBEL station during September - November 2007.

As mentioned in section 4.4 the fundamental of the SOM is the competition between the nodes in the output layer. For clustering aim, U-matrix is used for a visual inspection of SOM. It visualizes distances between neighboring map units, and thus shows the cluster structure of the map. In figure 32 the SOM U-matrix after training algorithm is shown. Each group of neurons constitutes a cluster. In the obtained U-matrix we can see three dark blue regions, corresponding to low values in the U-matrix, and hence to clusters in the data. By studying the final U-matrix map, and the underlying features plane of the map, a number of cluster can be identified by K-means algorithm. In section 3.2 the concept of cluster assessment was introduced; in the proposed approach, the best clustering structure of the SOM is obtained applying Davies-Bouldin index.

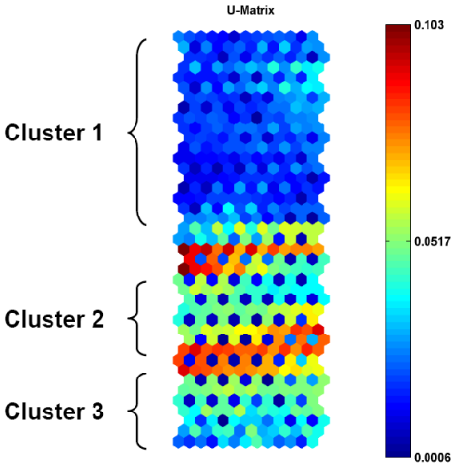

Figure 32: SOM U-Matrix after learning process. The blue dark regions indicate a possible clustering structure of the data.

As described in chapter 3, this index uses the within-cluster distance and the between-clusters distance. The Davies-Bouldin index is suitable for evaluation of k-means partitioning because it gives low values indicating good clustering results. In figure 33 the Davies-Bouldin index plot, in which the best clustering structure correspond to the number of three clusters, is shown. The best clustering structure of the obtained SOM is shown in figure 34 According to section 6.3.4, a cluster (called C1) is related to the degassing activity of the NEC, while the other two (called C2 and C3) to two different kinds of explosive activity of the SEC (figure 34).

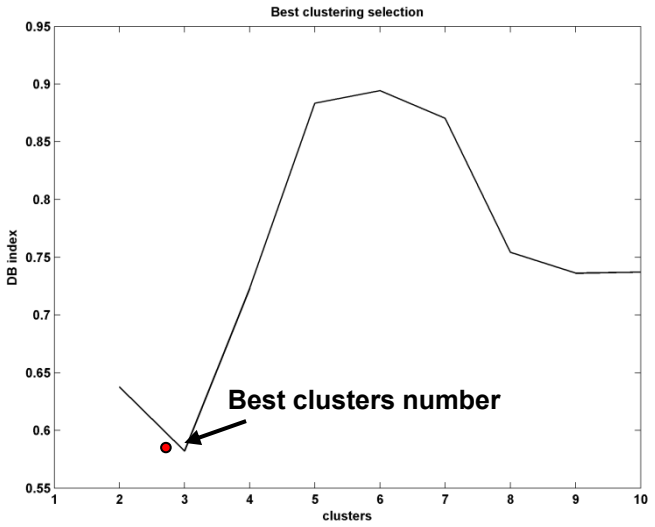

Figure 33: Best clustering structure computed using Davies-Bouldin index index (DB index).

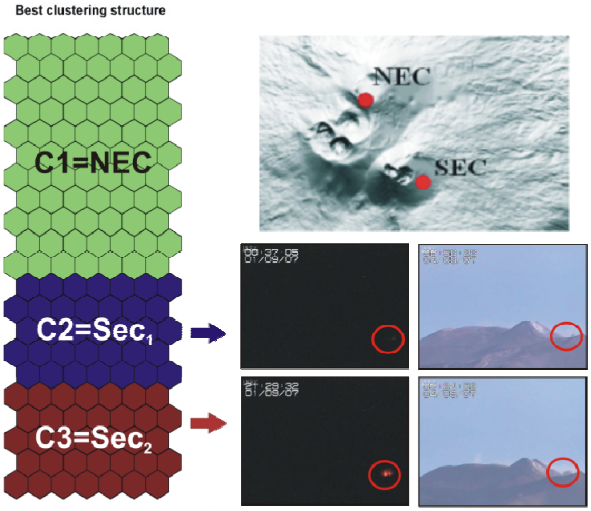

Figure 34: Best clustering structure of the SOM. Cluster 2 (C2) and Cluster 3 (C3) are associated with two different kinds of explosive events at SEC.

5.5.2 Real time infrasound signals classification system

In this section, a real time waveform classification is described. Using SOM a three cluster structure emerged by infrasound waveform features space. Although this kind of system can be used as a classifier, it does not provide information about outliers. To overcome this problem a clustering algorithm based on the concept of density, described in section 3.4, is applied. In particular, the proposed system is composed of two levels: 1) clustering using density (e.g. DBSCAN) and 2) classification using optimal hyperplane separators (e.g. SVM). The learning phase merges together results of clustering and classification analysis (figure 35). The techniques described in section 3.1.4 and 3.2.1, are applied on infrasound event features together with geophysical information used to "label" the recognised clusters. Using DBSCAN algorithm three clusters are recog-

nized (called cluster 1, 2 and 3) and other outlier points that can be considered as noise (figure 36). Points belonging to each cluster are related to infrasonic events that were located using semblance location method (see section 4.4.) (figure 37). As described in section 6.3, during September-November 2007, two infrasonic sources were found, NEC and SEC. In particular, a cluster was composed of events generated by NEC (cluster 1) and the other two by SEC.

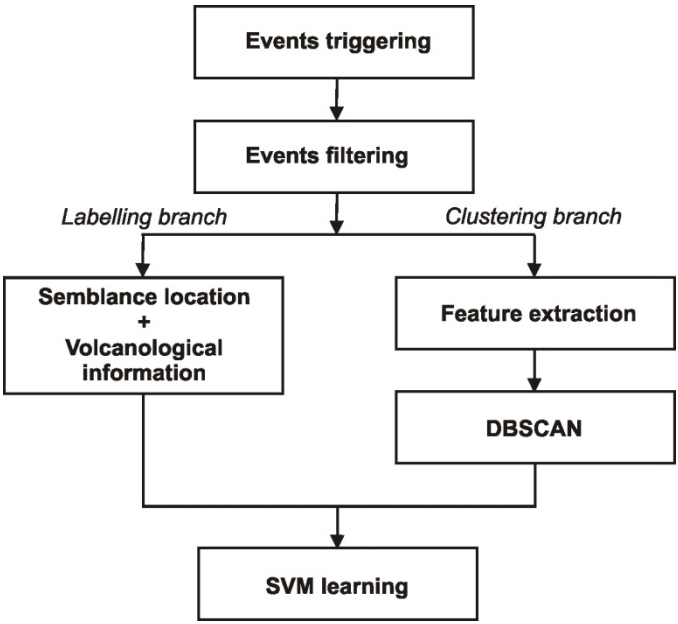

Figure 35: Scheme of the learning system.

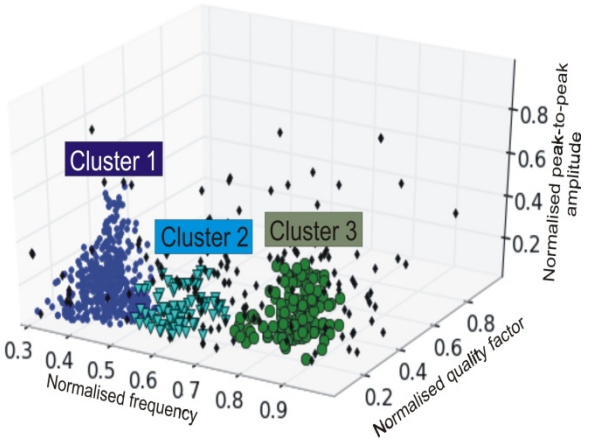

Figure 36: Clustering of the feature space reported in figure 31. The clusters are indicated with blue (cluster 1) and green dots (cluster 2) and light green triangles (cluster 3), the outliers with black diamonds.

Such last two clusters were related to different kinds of explosive activity at SEC. As reported in section 6.3.4 and 6.5.1, the events belonging to cluster 3 were coincident with "more visible" explosions, characterized by a relevant presence of ash, whereas the events of cluster 2 were hardly visible in the monitoring video-camera recordings (Cannata et al., 2009b). Features clustering together with labels provide the patterns for SVM learning process. As mentioned in section 3.3, optimization of parameters is a key step in model selection. In particular, C (regularization parameter) and σ (radial basis function kernel parameter) are key parameters in SVM learning because their values determine classification performance (Devos et al., 2009). As a consequence, model selection is applied with the aim of finding the best pair of parameters C and σ that minimizes the error rate estimated as the ratio between misclassified and hit patterns.

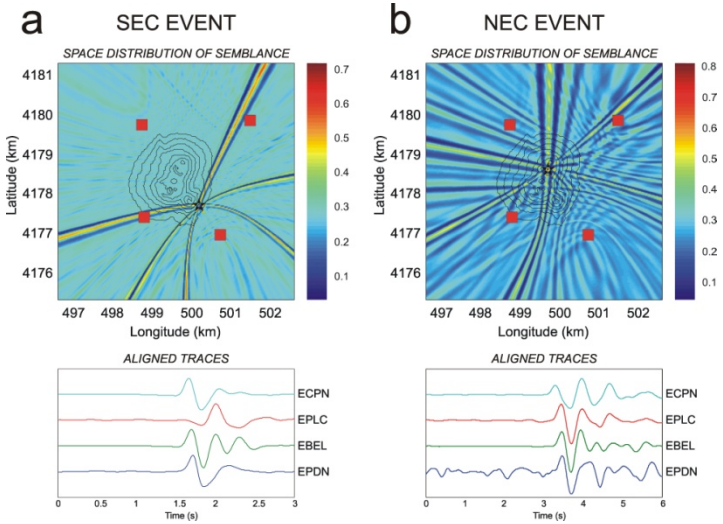

Figure 37: Examples of space distribution of semblance values, calculated by locating two infrasonic events at Mt. Etna (top plots), and corresponding infrasonic signals at four different stations shifted by the time delay that allows obtaining the maximum semblance (bottom plots). The red squares and stars in the top plots the indicate four station sites and the nodes with the maximum semblance value, respectively. The black lines in the top plots are the altitude contour lines from 3 to 3.3 km a.s.l.

These parameters can be chosen using a cross-validation (CV) approach (Hastie et al., 2002), which is, as described in section 3.3, a statistical method for learning algorithms evaluation and model selection. In particular, in K-fold CV the available dataset is partitioned into K subsets or "folds": K-1 folds are used for SVM learning purpose, and the remaining fold for model validation. All SVM training algorithms are computed using one-against-all method (see section 3.2.1). Since the used dataset is small, a simple exhaustive grid search can be performed (Hsu et al., 2007). C was systematically changed in the range [1 100] with a step of 10, σ in the range [0.1 10] with a step of 0.5, and a K-fold CV with K=10 was used.

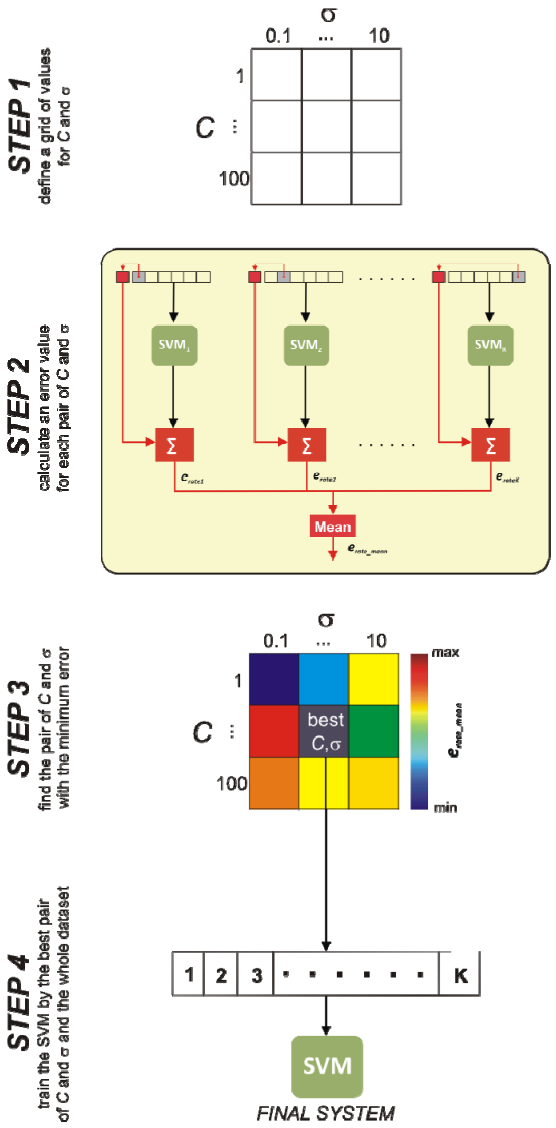

Figure 38: Best SVM model selection using K-Fold Cross-Validation (modified from figure 14 of section 3.3.).

The entire procedure can be summarized as follows (figure 38): 1) a grid value of C and σ is defined; 2) for each pair of C and σ values, a mean error rate is computed averaging the error rate values obtained by the K SVM models; 3) the pair of C and σ with the minimum error rate is selected; 4) such a pair is used to train the final SVM model with the whole dataset, comprising all the K folds. Here, the best parameter values were C=1 and σ=0.1, for which mean cross-validation error minimized to 0.6%. In order to verify the system, the trained SVM is tested by classifying new unknown infrasonic events and then assigning them to their source crater. The reliability is verified using events not analysed during the previous learning phase. To this end, a new test dataset of about 610 events, recorded during two months, August and December 2007, was used and labeled by semblance location algorithm (section 4.4) (figure 37). As aforementioned, the events belonging to cluster 2 and cluster 3 were labelled using information related to the intensity of the explosive activity (Cannata et al., 2009b). It is noteworthy that this kind of information often is not available, leading to a misclassification of the Cluster 2 and Cluster 3. The quality of classification is quantified using confusion matrix (table 1), where each column represents the instances in the predicted class (based on the SVM model), while each row represents the instances in the actual class (based on the previously attributed labels). Thus, the entries on the diagonal count the events in which prediction agrees with known labels, whereas the other entries the misclassified events. 63 elements were wrong assigned, providing an error rate of about 11.97%.

		PREDICTED		
		Cluster 1	Cluster 2	Cluster 3
ACTUAL	Cluster 1	**476**	9	6
	Cluster 2	9	**15**	8
	Cluster 3	8	33	**46**

Table 1: Confusion matrix calculated in the testing phase. Each column represents the instances in the predicted class (based on the SVM model), while each row represents the instances in the actual class (based on the previously attributed labels). Thus, the entries on the diagonal (bold numbers) count the events in which prediction agrees with known labels, whereas the other entries the misclassified events.

Misclassifications were mostly concentrated in the second and third classes that are related to the two different explosion activities of SEC crater. Indeed, such a distinction is qualitative and not clear-cut, hence many halfway events can be misclassified. If we do not take into account the distinction between clusters 2 and 3, and consider them as a single cluster, the error decreases to 5.25%.

Finally, the proposed system can be summarized as follows (figure 39): i) triggering procedure is performed on buffers of acquired signal; ii) then, if events are found, the system evaluates whether there is a sufficient number of stations for semblance location algorithm; iii) if the number of stations is not sufficient, alternative "single station" location is performed by extracting signal features and classifying them using the trained SVM. It is also worth noting that SVM classifier is also applied off-line on localizable events to evaluate its performance in distinguishing NEC events (cluster 1) from SEC events (clusters 2 and 3). In this case, events belonging to clusters 2 and 3 are simply considered SEC

events and then labelled based on the source vent, with no further distinction depending on the type of explosive activity. This task is carried out by comparing the results of the classifier with the location parameters provided by the semblance algorithm. By the inspection of the obtained error rate, a new clustering execution is necessary when classification of new signals is not aligned with that of infrasonic network classifier. This may be caused by the creation of a new active vent or by the changing activity of a preexisting vent; in such a case the system must be updated.

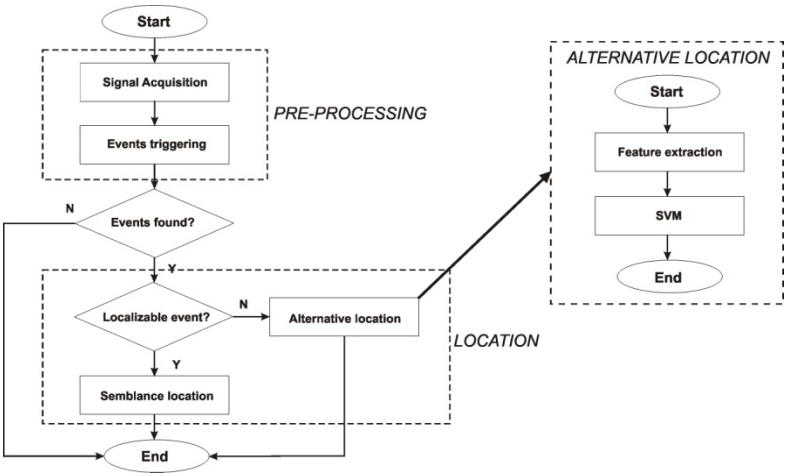

Figure 39: Flow chart of the proposed system.

Chapter 6

Insights into deep volcano dynamics using seismo-volcanic signals

A fundamental goal of volcano seismology is to understand the dynamics of active magmatic systems in order to assess eruptive behavior and the associated hazard. Imaging of magma conduits, quantification of magma transport, and investigation of long-period seismic sources, together with their temporal variations, are crucial for the comprehension of eruption-triggering mechanisms and its evolution over time. In this chapter seismo-volcanic signals recorded at Mt. Etna volcano during 2007-2008 will be analyzed in detail using time-frequency and nonlinear techniques. In particular, a novel technique based on multi stations coherence able to highlight periods of intense activity will be introduced. In the last part of the chapter an extensive analysis of the banded tremor phenomena, that occurred at Mt. Etna during the 2008-2009 eruption, will be analyzed. All the methods described in this chapter, provide the basic knowledge for volcano activity analysis and eruption forecasting at Mt. Etna.

6.1 Seismic signals on active volcanoes

In literature, on active volcanoes seismo-volcanic signals are routinely monitored, for surveillance and research purposes (e.g. Stephens and Chouet 2001; Patanè et al., 2008; Di Grazia et al., 2009; Varley et al., 2010). These seismo-volcanic signals, already introduced in section 1.2, including volcanic tremor and LP events, have origin in the dynamics of magmatic fluids (Chouet, 1996; Almendros et al., 2002a) and are considered precursory phenomena for eruptive activity (Chouet, 1996). In particular, as mentioned in section 1.2, volcanic tremor can be defined as a persistent seismic signal recorded on active volcanoes. Although the relation between tremor amplitude and eruptive activity is still not very clear, in many cases increases of tremor amplitude coincides with the onset of strombolian activity, lava fountains, dome building or effusive eruptions (e.g. Dvorak and Okamura, 1985; McNutt, 1986; Brandsdòttir and Einarsson, 1992; Patanè at al., 2007; Patanè et al., 2008; Di Grazia et al., 2009). However, in other cases no relationship between superficial activity and tremor amplitude can be identified. This suggests that temporal variations of volcanic tremor amplitude could also be a function of the flow rate of magma at large depths inside the crust (Ferrazzini and Aki, 1992; Konstantinou and Schlindwein, 2002). Focusing on the spectral content, volcanic tremor generally exhibits many frequency peaks related to either source or path/attenuation effects due to seismic wave propagation through heterogeneous volcanic structures. Temporal variations of the power spectrum are in general observed on active volcanoes and are interpreted as source effects (Gordeev et al., 1990; Patanè et al., 2008; Di Grazia et al., 2009). Since the frequency content evolution is one of the primary tools for investigating the nature of volcanic tremor, several methods have been developed. In particular, methods based on

the time-frequency transforms (e.g. STFT or CWT described in chapter 2) are widely applied on volcano monitoring systems.

Models related to the process of magma ascension from a deeper storage volume towards the surface, generating volcanic tremor, has been extensively studied. The quantitative study of the processes responsible of the generation of volcanic tremor requires the formulation of a system of partial differential equations describing the fluid flow and the elastic disturbance caused by the coupling between fluid and surrounding rock (Chouet and Julian, 1985; Konstantinou and Schlindwein, 2002).

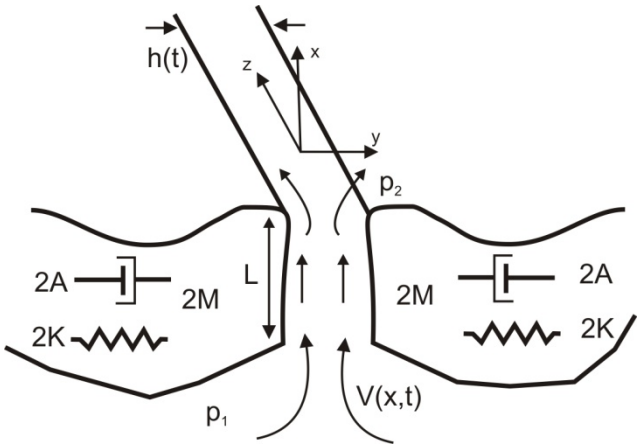

Figue 1: Lumped parameter model of the generation of volcanic tremor. Viscous incompressible fluid flows in the x direction from the upstream to downstream reservoir through a channel of length (L) with imperfectly elastic walls, modeled as movable but undeformable blocks of mass 2M, stiffness 2k and damping constant 2A (all measured per unit distance in the z direction). All motion occurs in the x-y plane and it is independent of z. The dynamic variables are the channel thickness h(t) and the fluid speed v(x,t) (from Julian, 1994).

As explained in Julian (1994), tremor generation process must necessarily be nonlinear. An important characteristic of time-invariant linear system is that its output can contain only frequencies that are present in its input signal. For this reason, this kind of system cannot oscillate spontaneously. Volcanic tremor exhibits a nonlinear behavior since it can be explained as an oscillatory response to a steady input (e.g. stress, fluid pressure, heat etc..). Julian (1994) proposed a simple lumped-parameter model that explains how tremor oscillations are excited by a nonlinear instability that arises when fluid flows through an irregular channel with deformable walls (figure 1). Further complications may arise if the fluid is considered biphasic, if the thickness of the conduit changes in space and/or in time, if there is a visco-elastic behavior.

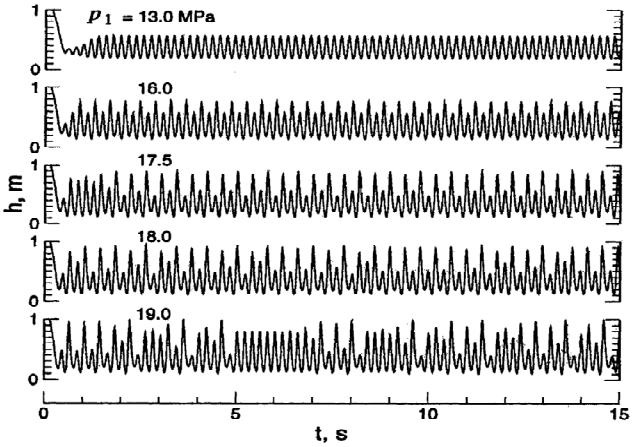

Figure 2: Synthetic seismograms of volcanic tremor (channel thickness versus time) generated for different values of the magma driving pressure p_1 depicted in the flow model shown in figure 1. Note the gradual transition from simple limit cycle, to limit cycle with one subharmonic up to chaotic behavior (from Julian, 1994).

In the light of it, a number of simplifying assumptions are usually made: (a) the fluid has one phase only, (b) the fluid has constant density, (c) the motion occurs in one or two dimensions, (c) the conduit behaves elastically, (d) conduit thickness change only as function of time (Konstantinou and Schlindwein, 2002).

Using the principles of mass and momentum conservation the lamped-parameter model of Julian (1994) derived a third-order system of nonlinear ordinary differential equations describing the flow through a constricted channel with elastic walls (figure 1). The model considers two reservoirs, filled with a single phase fluid at pressure p_1 and p_2 connected by a channel of length L and thickness h, through which the fluid can vary only in the x direction (figure 1), undeformable blocks of mass $2M$, stiffness $2k$ and damping constant $2A$. In particular, the channel thickness is a function of time and its variation is related to walls deformation along the y direction due to changes in the fluid pressure. The equations of motion that control the dynamics of the tremor model can be expressed using a third order system of ordinary differential equations (Julian, 1994):

$$\begin{cases} \rho \dot{v} + \dfrac{12\eta}{h^2} v = \dfrac{p_1 - p_2}{L} & (6.1) \\ \left[M + \dfrac{\rho L^3}{12h} \right] \ddot{h} + \left[A + \dfrac{L^3}{12h} \left(\dfrac{12\eta}{h^2} - \dfrac{\rho}{2} \dfrac{\dot{h}}{h} \right) \right] \dot{h} & \\ + k(h - h_0) = L \left[\dfrac{p_1 + p_2}{2} - \dfrac{pv^2}{2} \right] & (6.2) \end{cases}$$

where ρ is the fluid density, v is the flow speed averaged over the channel cross-section h and η is the viscosity. Julian (1994) demostrated numerically that synthetic tremor time series (channel thickness h versus time) generated for different values of the fluid driving pressure p_1, exhibit different types of behavior: from simple limit cycle to chaotic behavior (figure 2). Considering the previous system in a chaotic regimes, the phase space of the three state variable h, v and $\dot{h}$ of the system reveals sets of orbits that diverge from each other due to the high sensitivity to initial condition. The obtained geometrical object, already described in section 2.3.1, is a fractal object called strange attractor (figure 3).

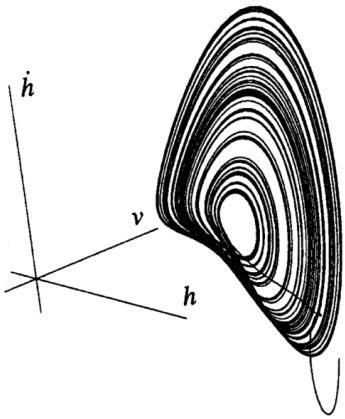

Figure 3: Phase space formed by plotting the triplet of values h, v, $\dot{h}$ for a driving pressure of p1 =19.0 MPa. (from Julian, 1994).

In particular, intermittency of particular seismo-volcanic events and the transition to tremor reflect behaviors characteristic of nonlinear systems (Stephens and Chouet, 2001). Evidence of chaotic behavior has been reported in the pattern of eruptions of hydrothermal systems at Old Faithful (Nicholl et al., 1994) and banded tremor episodes at Mt. Etna that will be described in this chapter.

The possibility of using LP signals to place quantitative constraints on the ascent rate of magma and on its pathway within the conduit is motivated by observations of rapidly increasing LP-event rate merging into the tremor before an eruption. Furthermore, the use of VLP and LP events to probe the state of the fluid and dynamic processes within a volcanic system has gained prominence in recent years (Neuberg et al., 2000; Chouet, 2003; Kumagai et al., 2003). In order to collect LP and VLP events at Mt. Etna, an automatic detection procedure, based on the trigger methods described in section 4.2, is used. In general, a dynamic threshold is computed as a multiple of the 5th percentile alculated on the squared RMS of the signal filtered in frequency bands of interest. This allows the recognition and counting of the different type of events, together with an evaluation of their energy content. Although LP swarm are observed before lava fountain and/or eruptions, the occurrence rate alone does not provide quantitative information about the activity state of the monitored volcanoes. For this reason, beyond the number of triggered seismo-volcanic events over time, other information related to them are needed. In particular their spectral characteristics, waveform morphology and source locations, are considered. A number of studies have shown evidences of apparently changing source depths of tremors. Thus, tremor source location could constitute the best candidate for mapping the extend and geometry of the underlying magma, conduits, or reservoirs and also for quantifying pressure transients caused by resonance

or movement of fluids along those conduits (Battaglia et al., 2005; Di Grazia et al., 2006). There have been previous attempts to estimate the location of volcanic tremor sources mainly based on recordings from a single or a number of multichannel seismic systems (Furumoto et al., 1990; Almendros et al., 2002b; Saccorotti et al., 2004). More recently, precise locations based on amplitudes, recorded at temporary or permanent short-period vertical or three-component broadband stations have been performed at Bromo (Gottschammer and Surono, 2000), Piton de la Fournaise (Battaglia and Aki, 2003), Mt. Etna (Di Grazia et al., 2006). In the next section several periods of intense volcano activity, such as the lava fountains that occurred in the periods September-November 2007 and May 2008, and the 2008-2009 eruption, will be analyzed in detail using the analysis techniques reported in the previous chapters.

6.2 Seismo-volcanic signals at Mt.Etna during 2007

Like many basaltic volcanoes, Mt. Etna typically erupts in effusive to weakly explosive styles (Mulargia et al., 1985), even though powerful explosive eruptions (sub-Plinian to Plinian events) have been recognized during the Quaternary (Del Carlo et al., 2004). As a result, lava flow propagation has typically been considered the main hazard at Etna and only recently its explosive activity has been taken into account as a serious volcanic risk for local populations and for aviation in the central Mediterranean region (Andronico et al., 2007, 2008b). This is because, in the last decades, explosive eruptions represented its most frequent activity, producing eruptive plumes and copious ash fallout on its flanks. Since the 1970s, more than 180 fire fountain episodes have occurred at summit craters (Behncke and Neri, 2003). During the 2001 and 2002–2003 eruptions, an exceptional and prolonged explosive activity was observed for the first time in the last century (Allard et al., 2006). These two highly explosive events were related to the arrival of undegassed, volatile-rich, fast-rising magma that rose from the deep portion of the feeding system and bypassed the central conduits (Andronico et al., 2008a; Patanè et al., 2003, 2006). After the 2004–2005 quiet summit effusive eruption and the 2006 summit eruptive phase, characterized by both effusive and explosive activity from the South East Crater (SEC), a new period of explosive activity started from this crater at the end of March 2007, producing four episodes of fire fountains in about 1.5 months. Thereafter, on 4–5 September 2007, one of the most powerful fire fountaining episodes (both in terms of duration, about 12 h, and erupted volume of lava and tephra, about 2–4 × 106 m3) originated from SEC, producing a plume up to 2 km high and dispersed deposits up to several tens of kilometers from the volcano (Andronico et al., 2008b). This was followed on

23–24 November by another energetic fire fountaining episode (with duration of about 6 hours).

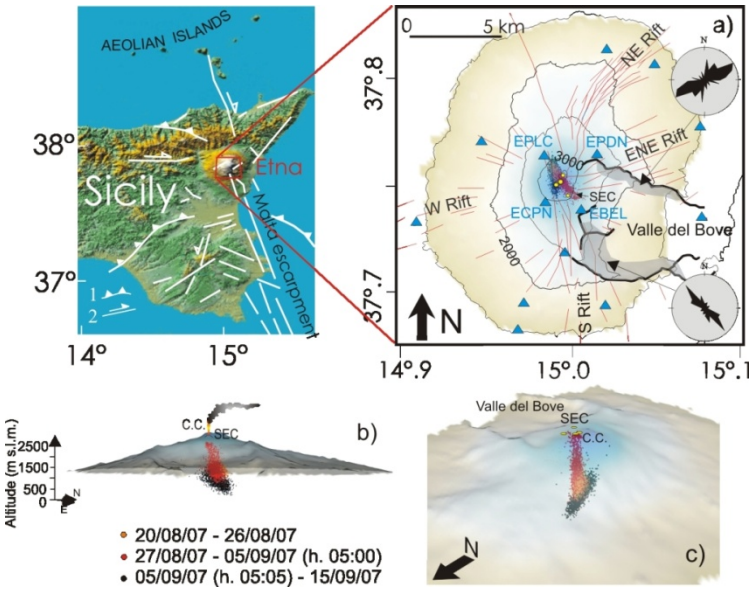

Figure 4: (top left) Structural map of eastern Sicily reporting the front of the Appenninic-Maghrebian chain and the main faults. (a) Map of the summit part of Mt. Etna volcano showing 3-D source centroids of volcanic tremor locations computed between 20 August and 15 September 2007. In the map, broadband seismic stations (light blue triangles) operating during the study period and used for tremor locations, the GPS stations used in this work (ECPN and EPDN are located at the same place as the homonymous seismic stations), historical eruptive fissures (red lines), and time evolution of tremor locations (orange, red, and black circles) are also reported. The concentric black curves represent elevation contours at 500-m intervals. Yellow dots indicate central craters (C.C.). The rose diagrams show the dike structures directions as appearing at the surface through erosion processes in the southern and northern walls of Valle de1 Bove. (b and c) 3-D images of the volcanic edifice reporting volcanic tremor locations.

Both explosive and effusive eruptive styles are believed to be largely controlled by the total volatile content and magma flow rate (Woods and Cardoso, 1997), which is modulated by processes within the volcanic conduit (Jaupart and Vergniolle, 1988). Models for the ascent of magma through shallow conduits have become increasingly sophisticated over the last two decades (Jaupart and Vergniolle, 1988; Sahagian, 2005). However, constraining the model behavior with observational data has proven difficult because the geometry of the shallow volcanic plumbing system is not generally well defined at almost all volcanoes worldwide, notwithstanding recent advances in the high-resolution seismic tomography studies (Chouet, 2003; Patanè et al., 2006).

In 2007, 14 seismic broadband stations were installed at elevations between 1100 and 3000 m a.s.l. and distances from the summit craters between 1.5 and 9 km (figure 4a), all equipped with Nanometrics TRILLIUM seismometers, with flat response within the 40–0.01 s period range. In this section quantitative observations of seismo-volcanic signals (tremor, LP and VLP events) recorded at Mt. Etna during a 7-month period are shown, focusing on the analysis of the two powerful lava fountain episodes taking place on 4–5 September and on 23–24 November 2007. In particular, the temporal evolution of the tremor and of LP-VLP activity in terms of source movement, change of the waveforms morphology, temporal evolution of the "dominant" resonance frequencies and the source quality factor (Q) for the LP events, will be studied using mainly the methods explained in chapter 4.

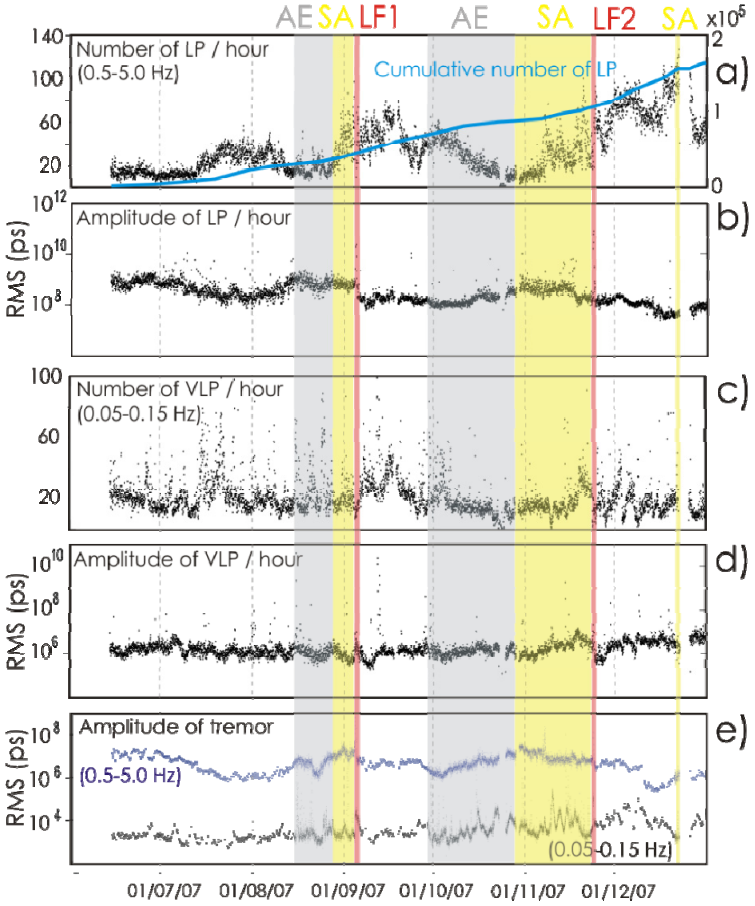

Figure 5: Temporal variation of the seismo-volcanic activity at ECPN station and GPS ground deformation in the period June–September 2007. (a and c) Number of LP and VLP events per hour and (b and d) related RMS values (energy content), (e) tremor amplitude computed in the LP and VLP bands.

6.2.1 Signal analysis

The wide variety of seismo-volcanic events at Mt. Etna requires a sophisticated trigger system able to detect the highest number of events when events swarm occurs. For this purpose the novel trigger method described in section 4.2 was for its ability to detect events that are very close to each other. In order to collect different kinds of signals, in particular LP and VLP events, the aforementioned procedure was applied on different frequency bands of interest. In this case, the 0.5-5 Hz frequency band is used for LP detection, while 0.03-0.2 Hz frequency for VLP detection. It is noteworthy that the LP detection frequency band allows the recognition of different types of events, as example ExQ, VT and Hybrid, together with an evaluation of their energy content. The graphs in figures 5a–5e show the details of tremor, LP, and VLP activity in the period 15 June to December 2007. The most relevant seismic feature (figures 5a–5e), recognizable before the two lava fountaining episodes from SEC, both preceded by discontinuous ash emission and strombolian activity, is the increase in the number of LP events (figure 5a). Also the amplitude of tremor in the LP band increases before the first eruptive episode at SEC (hereafter referred to as LF1), followed by a progressive decrease. By contrast, the second eruptive episode (hereafter referred to as LF2) occurred in a period of decreasing tremor amplitude, even though it was preceded by a period of increasing tremor amplitude. The VLP source during this period showed a low rate of occurrence (figure 5c). However, a temporary increase of the number of VLP events can be recognized in the second half of July before the first lava fountaining episode and after its end.

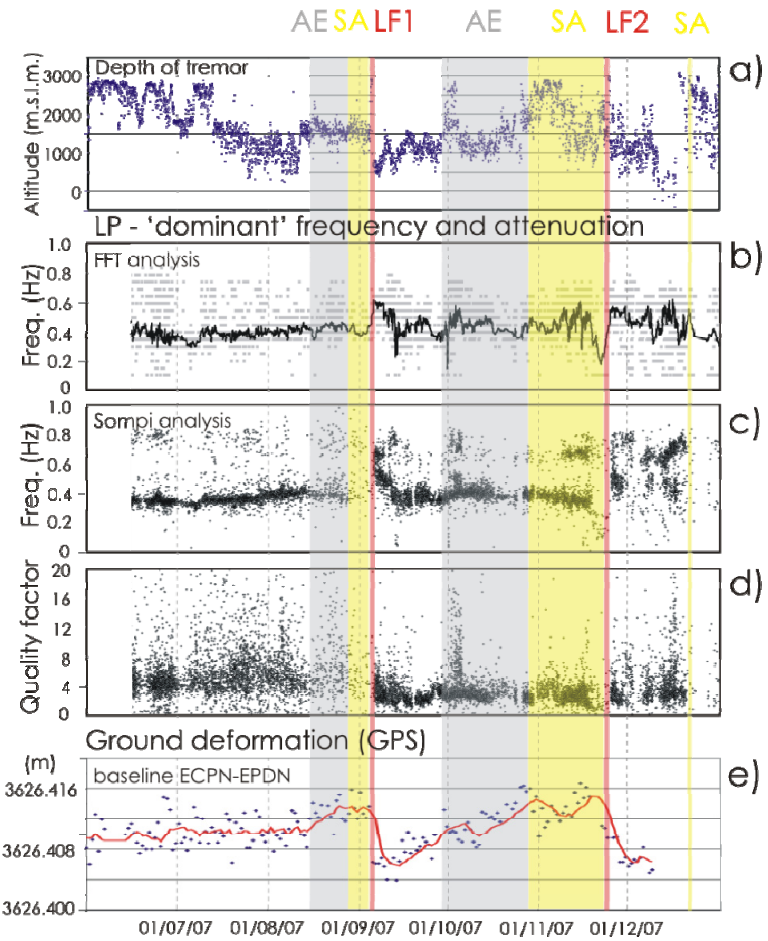

Figure 6: (a) tremor depth, (b–d) "dominant" frequency and quality factor of LP, and (e) GPS ground deformation measurements in the summit area (baseline between ECPN and EPDN GPS stations). The vertical red lines mark the two lava fountaining episodes of 4–5 September and 23– 24 November. The shadow gray area marks the period of discontinuous ash emission, whereas the yellow one marks the period of prevalent strombolian activity. The red line in (e) represents the moving average of original data considering groups of five measurements.

Afterward, another increase in the VLP rate is recorded about one week before the onset of the second lava fountaining episode. It is noteworthy that a low rate of VT seismicity was detected under the volcano during these months, similarly to the first half of 2007, which is in contrast with the progressively increasing occurrence rate of LP events. In the following sections, more detailed analyses are presented on LP and VLP sources, focusing on the two lava-fountaining episodes of 4–5 September and of 23–24 November. The tremor location procedure, normally applied at Etna on 1-h-long filtered signal windows (0.5–5 Hz) for surveillance purposes (figure 6a), has been reapplied on 5-min-long filtered signal windows (in both the frequency ranges 0.5–2.5 and 0.5–5.0 Hz) considering two wide periods encompassing the two lava fountaining episodes (shadow gray areas in figures 5 and 6). In addition, since also LPs and VLPs may be sensitive to factors that can change with time during a magmatic cycle (Chouet, 2003), their locations were also computed.

6.2.2 Tremor source location

In order to constrain the tremor source locations, the spatial distribution of tremor amplitudes was recorded by the distributed network shown in figure 4a. By using the location method described in section 4.4, precise locations based on 5-min-long filtered signal windows, were determined for tremor recorded from 20 August to 15 September for the first lava fountaining episode and during 15–30 November for the second episode. As aforementioned, tremor locations were retrieved considering two different frequency bands (0.5–2.5 Hz and 0.5–5.0 Hz) by using a grid-search approach (Battaglia et al., 2005; Gottschammer and Surono, 2000). In particular, to avoid unstable solutions, the location results were considered reliable only when (1) the goodness of the R2 fit is ~0.9 and

(2) at least 12 of the 14 stations are available. Even if the attenuation factor may not have a large influence on the source locations (Battaglia and Aki, 2003), several values of the parameter α ($0 \leq \alpha \leq 0.4$, step 0.01) that include the quality factor Q, are computed with the aim of improving the goodness of the fit. Following this procedure, the best fitting values (R2) were achieved with very low a values, mainly between 0 and 0.02, suggesting high values of Q. For example, considering $\alpha = 0.02$, c = 2.0 km/s, and f = 1 Hz or 2 Hz, Q values of 78 and 157 were obtained. These values are in agreement with recent attenuation studies on this volcano (De Gori et al., 2005; Martinez-Arevalo et al., 2005; Giampiccolo et al., 2007), considering an averaged Q value for body wave propagation in a large rock volume, that takes into account the station distances from the source (about 10 km). Finally, in order to assess the stability of the source location a Jackknife technique was employed (Efron, 1982). In Table 1, the 25th, 50th, and 75th percentile of the standard error for the whole computed Jackknife locations are reported for the period 20 August - 15 September 2007 which includes the first lava fountaining episode.

Table1: Standard Error, measured in kilometers, for Latitude, Longitude, and Depth of the Jackknife Estimation.

	25th percentile	**50th percentile**	**75th percentile**
Latitude	0.39	0.46	0.54
longitude	0.48	0.55	0.62
depth	0.65	0.77	0.88

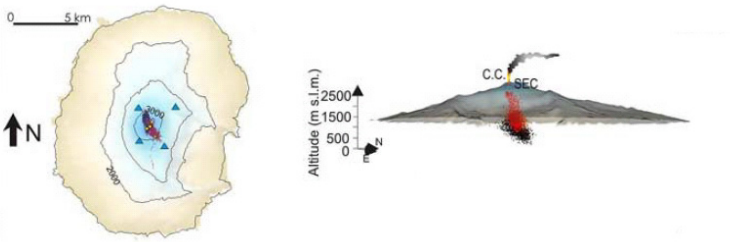

Figura 7: 3-D source centroids of volcanic tremor locations computed between October 2006 and December 2007.

Figure 7 depicts the 3-D source centroids of tremor locations computed for the period between 20 August and 15 September in the frequency range 0.5–5.0 Hz, also in order to take into account higher frequencies related to the very shallow tremor activity in proximity of the vents (Di Grazia et al., 2006). These locations reveal, for the first time, the geometry of the shallow central feeding system. The imaged conduit consists of two connected resonating dike-like bodies, extending from sea level to the surface. The shallower dike, crossing the central craters (orange and red dots in figures 4a–4c), shows a lateral dimension changing with depth. It is located between about 1.0 km a.s.l. and the surface. In proximity of the surface it presents a maximum horizontal extension of about 2.0 km while its deeper part shows a maximum horizontal extension of about 3.0 km. Retrieved inclination and azimuth of the dike are of 15° ± 10° and 135°± 5°, respectively, thus suggesting a resonating dike-like body striking NW–SE, slightly inclined from the vertical toward the SW. The deeper dike (black dots in figures 4a–4c), tilted to the north of 25° and mainly located below 1 km a.s.l., shows a lateral dimension of about 3 km and a vertical extension of about 0.5 km. It strikes in the NNW–SSE direction (black

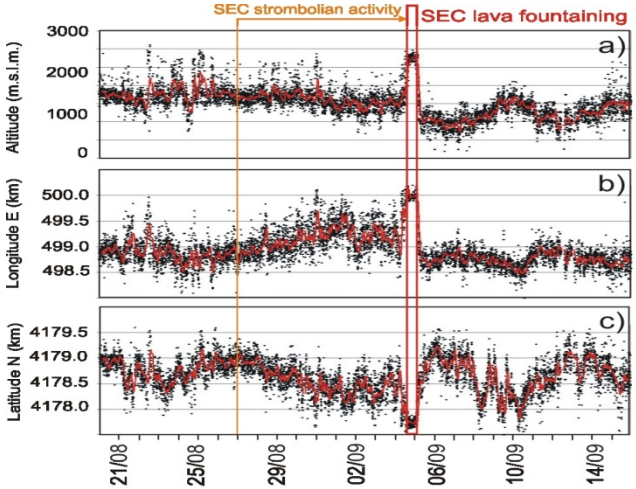

Figure 8: Temporal evolution between 20 August and 15 September of (a) altitude, (b) longitude, and (c) latitude of tremor sources. The red lines are the moving average of original data considering groups of 30 measurements. The vertical orange line marks the start of strombolian activity at SEC, while the empty red rectangle defines the lava fountaining period (for details see INGV-CT volcanological reports at http://ct.ingv.it).

dots in figures 4a–4c) and is slightly inclined (about 20°) from the vertical toward ENE. The stability of this shallow plumbing system geometry is confirmed considering: (1) 3-D source centroids of tremor locations computed during 15–30 November including the 23–24 November lava fountaining episode at SEC and (2) tremor locations calculated on the 1-hour-long windows of signals between October 2006 and December 2007, comprising the two lava fountaining episodes (figures 5 and 6). Notwithstanding the different time resolution, the locations reported in figure 4d, divided as a function of depth, show clearly the orientation of the two dike-like bodies at different depth (NNW–SSE the deeper and NW–SE the shallower). The temporal evolution of tremor sources during 20 Au-

gust to 15 September indicates a progressive migration toward the SEC, starting about 8 days before the onset of the lava fountaining (figures 8a–8c), whereas a clear shallowing of sources is observed only a few hours before the onset of the lava fountaining. After its end, the source centroids migrated deeper (below 1 km a.s.l.), clustering in a wide volume, NNW–SSE oriented, beneath the central craters (black dots in figures 4a–4c and figure 8c). Similar spatiotemporal results have also been obtained for the lava fountaining episode occurring on 23–24 November.

6.2.3 Waveform events classification

At Mt. Etna, LP signals are often accompanied by the VLP pulse or pulses with a peak frequency between 0.06 and 0.1 Hz. However, in some cases VLP signals occur alone, either as VLP tremor or a single VLP pulse not accompanied by an LP event (Saccorotti et al., 2007; Lokmer et al., 2007). The variability of the LP component associated with VLP events is evident in the seismogram reported in figure 9, which shows a small VLP pulse accompanying the LP event, and then a higher VLP pulse with a much weaker LP component. LP and VLP events often occur as swarms, also with many hundreds (tens for VLP) of earthquakes within a few hours. However, VLP events usually show an almost stable low rate of occurrence (figure 5c). It is well known that the waveform of a seismic event depends on different effects: source effects (location and geometrical-physical-chemical features of the structure that produces the signal), propagation effects (geometrical spreading, anelastic attenuation and scattering), site effects, and instrumental effects (e.g., Lay and Wallace, 1995). Therefore, two very similar waveforms imply that all these effects are the same. On the basis of such considerations and following Green and Neuberg's procedure reported in section 4.7

(Green and Neuberg, 2006), a waveform classification of the LP and VLP events occurring during the period 1 July to 31 December 2007, was performed using a cross-correlation analysis between all pairs of selected signals recorded at ECPN station. Nine hundred eighty LP events, characterized by high signal-to-noise ratio and uniformly distributed in time (about six events per day), were selected and filtered below 0.7 Hz. The correlation matrix was obtained considering 15-s-long windows that included the whole LP events and a threshold value of cross correlation coefficient equal to 0.8 was chosen.

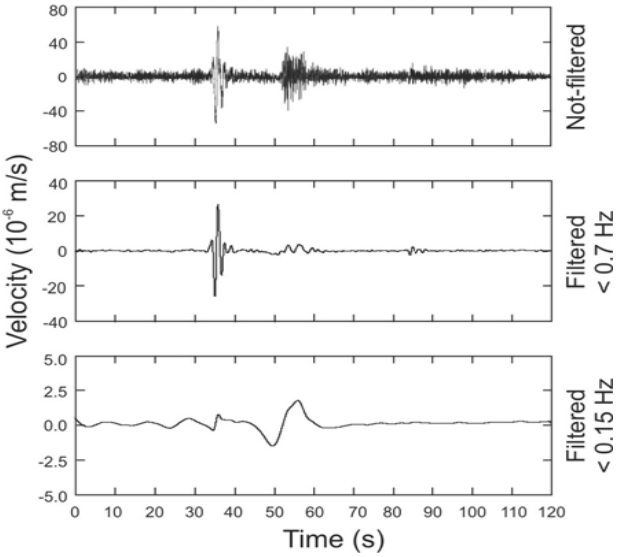

Figure 9: Velocity seismogram recorded at the vertical component of ECPN station on 7 September 2007. The low-pass filtered signals, below 0.7 Hz and 0.15 Hz, are also reported.

Considering only the families with more than 20 events, three main families of LP events (hereafter referred to as families 1, 2, and 3) were obtained. These families comprise about 90% of all the considered events suggesting the repetitive excitation of stationary sources in a nondestructive process. As shown in figure 10a, most of the events belong to the family 1 (frequencies ranging between 0.3 and 0.4 Hz), except for the events occurring after the first lava fountain episode (for about 10 days) and from the second one to the end of the studied period. During these two periods most of the events belong to the family 2 showing higher frequency content (about 0.5–0.6 Hz). On the other hand, the family 3 (frequency of about 0.3 Hz) is composed of events scattered in almost the whole period. Regarding the VLP activity, about 700 VLP events, characterized by high signal-to-noise ratio and uniformly distributed in time, were also selected and filtered below 0.15 Hz. Also for these events a cross-correlation threshold equal to 0.8 was used. Considering only the families with more than 20 events, four main families of VLP (hereafter referred to as families 1, 2, 3, and 4; figure 10a) were obtained. The average waveforms of the four families are shown in figure 10b. These families comprise about 85% of all the considered events suggesting also in this case the repetitive excitation of stationary sources in a nondestructive process.

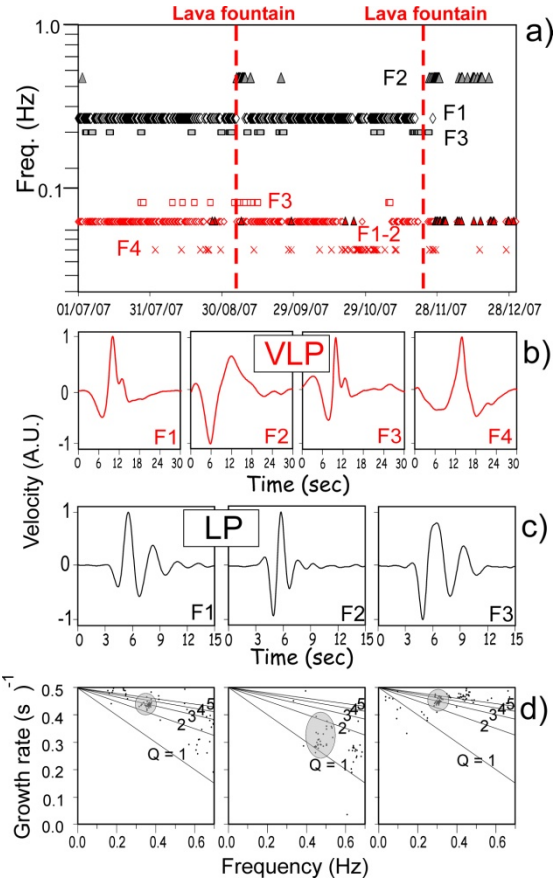

Figure 10: (a) Time distribution of the LP (families 1 (black diamonds), 2 (black triangles), and 3 (black squares)) and VLP (families 1 (red diamonds), 2 (red triangles), 3 (red squares), and 4 (red crosses) events as a function of their average frequency content, and RMS of the tremor signal calculated by 30-min-long time windows at the vertical component of ECPN station (black line). (b) Average waveforms of the four VLP families and (c) of the three LP families. (d) f-g diagrams of the average waveforms shown in (c). The black lines represent values of constant quality factor (Q). Clusters of points (encircled with gray ellipses) indicate a resolved dominant mode, scattered points represent noise.

6.2.4 Properties of the resonator system

It is known from simplified models of seismo-volcanic sources that the resonance frequency and damping of the system is strongly influenced by the nature of liquid and gas content (Chouet, 2003, and references therein). In order to study the temporal evolution of fluid-driven sources at Mt. Etna during the investigated period, the spectral features of about 13000 LPs were analyzed. Since the characteristic properties of a resonator system can be estimated by the spectral content of the radiated signals, two different spectral analyses on the selected LP events were performed. First, 20-s-long (2048 samples) windows were considered, whose onset coincided with onset of the LP events. Since most of the radiated energy was concentrated below 0.7 Hz, a low-pass filter below 0.7 Hz was applied. Then, the spectra of the vertical component of ECPN station was estimated using the Fast Fourier Transform (FFT) obtaining the highest peak frequency. Most of the calculated peak frequencies range between 0.3 and 0.7 Hz (figure 6g). The moving average over 25 samples (black line in figure 6g) highlights spectral time variations, most of which are related to the volcanic activity. In fact, the frequency values decreased before the lava fountain episodes occurring on 4–5 September and 23–24 November and then increased. The decrease was slight before the first episode and strong before the second one. In order to verify the aforementioned spectral variations and also to obtain information about the damping features of the LPs source, the Sompi analysis was applied (Chouet, 2003, and references therein). As explained in section 2.2.1, by this method, a signal is deconvolved into a linear combination of coherent oscillations with amplitudes decaying and additional noise. Again, a low-pass filter below 0.7 Hz was applied on the data obtaining frequency and quality factor for autoregressive (AR) orders ranging between 2 and 10. The

sharply monochromatic nature of the investigated signals justifies the choice of these low orders (Lesage, 2008). The results were very similar for all the used orders. As shown in figure 6c, the obtained frequency values (for AR order 2) confirm the results of the FFT analysis in figure 2b. The quality factor, mostly ranging between 2 and 8, showed an important variation after the first episode of lava fountain on 4–5 September (figure 6d), when the values decreased from about 5 to 2–3.

6.2.5 Events location

LP locations were performed by applying the semblance technique (Neidell and Tarner, 1971) described in section 4.4. This method was preferred to the radial semblance technique (Kawakatsu et al., 2000), used instead for the VLPs analysis, because the particle motion of the observed LPs was radial at only some summit stations. According to their uniform distribution in time and high signal-to-noise ratios, a subset of about 900 LPs were selected and located by using the five or six nearest stations to the summit area. Four-second-long windows of seismic data, low-pass filtered below 0.7 Hz, whose onset coincided with onset of the LP events, were used. For the locations a 3-D grid is adopted, with dimensions of 6x6 km and vertical extent of 3.25 km (from 0 km a.s.l. to the top of the volcano). The horizontal and vertical grid spacing is 125 m. A value of 1.7 km/s was chosen as seismic velocity because it allowed to obtain the maximum semblance value. This value is consistent with seismic velocity values reported in literature for this kind of study at Mt. Etna (e.g., Privitera et al., 2003; Gresta et al., 2004; Bean et al., 2008). Furthermore, the most recent high resolution velocity tomographies on this volcano suggest that for depth less than 1.0–1.5 km (Cocina et al., 2008), the used value is reliable and justified by the presence of intensely frac-

tured rocks and pyroclastic deposits in the shallow layers of the volcanic edifice. The results, summarized in figure 11, suggest shallow LP sources located below the summit craters. The LP source showed striking time variations and a deepening from 3 to 1 km a.s.l. after the two lava fountain episodes. In addition, the LP source gradually shifted northward from September to November. Concerning the VLP seismicity, about 400 VLP events occurring between July and October 2007 were located by the radial semblance method (Kawakatsu et al., 2000). Because of the low amplitude of these signals, the VLP source was located by using only the four stations nearest to the summit area. The lack of one of the closest stations (EPDN; figure 4) between November and December precluded the extension of the analysis to the period of the 23–24 November lava fountaining episode. Twenty-second-long windows of seismic signal, whose onset coincided with the onset of the VLP events, low-pass filtered below 0.15 Hz, were used. The 3-D grid is the same as the one used to locate the LP events. The VLP locations, shown in figure 11, also suggest for VLP seismicity shallow sources located just below the summit area. Unlike the LP locations, the VLP locations (figure 11) remain steady for the whole period. A slight deepening can be observed after the lava fountain episode occurring on 4–5 September. In order to estimate the error of the location, we followed the Almendros and Chouet method (Almendros and Chouet, 2003). It is noteworthy that in most cases, the obtained error region contained only the node of the grid characterized by the maximum semblance value. Therefore, if error bars are not reported, the error can be considered lower than the grid spacing. It is noteworthy that the used location methods do not take into account material heterogeneity and topography. The former can affect the location results of both semblance and radial semblance methods. Conversely, the latter mostly influences the locations obtained by radial semblance, that is based on

both the similarity of the waveform and the particle motion. However, results obtained during the large-scale passive seismological experiment (June–July 2008), aimed at complementing the permanent Etna monitoring system in the near-field, with the deployment of over 20 broadband stations in summit area, showed that the LP and VLP source locations obtained by only the permanent stations are quite reliable. For both LP and VLP sources, locations obtained using the dense network were only shifted by about 100–200 m. However, for seismovolcanic studies it is important to deploy as many stations as is feasible close to the source with the best azimuthal coverage possible as suggested by Neuberg and Pointer (2000), which allows partially minimizing the above mentioned effects.

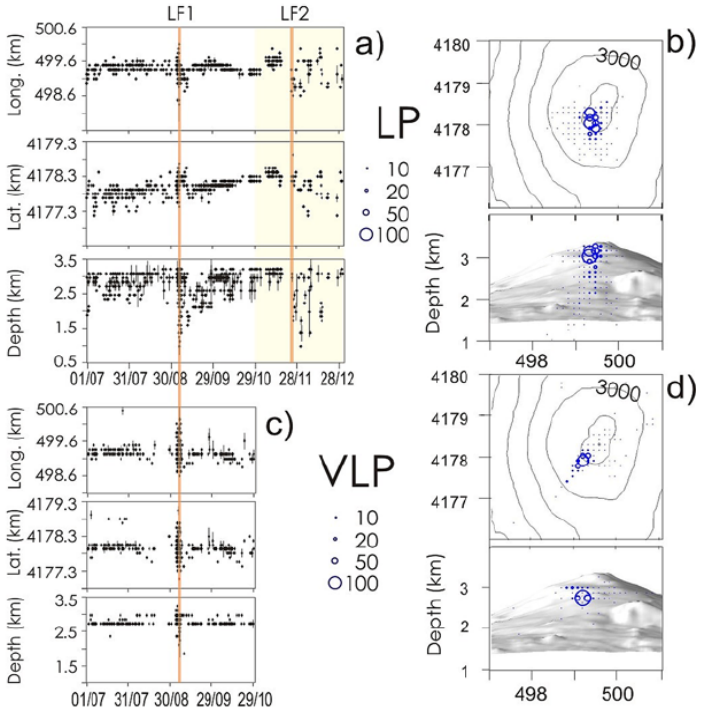

Figure 11: (a and c) Time variation of the source location of about 900 LP and 400 VLP events, occurring between 1 July and 31 December 2007 and between 1 July and 31 October 2007, respectively. The yellow rectangle indicates the time period when EPDN station did not operate. (b and d) Maps and W–E sections of summit area with the source locations of the LP (b) and VLP (Figure d) events (blue circles). The radii of the circles are proportional to the number of the locations in each grid node (see blue circles and numbers reported at center).

6.2.6 Volcanic processes

The geometry of the magma pathway feeding the eruptive activity at SEC was highlighted by precise volcanic tremor source locations obtained in long periods including two lava fountaining episodes. As described in section 6.2.2 the imaged plumbing system consists of two connected resonating dike-like bodies,NNW–SSE andNW–SE oriented, extending from sea level to the surface. The NW–SE trending source region has recently been supported by (1) the moment-tensor inversion of LPs sources, indicating a crack-like geometry (Lokmer et al., 2007) and (2) the dike propagation trends modeled by crustal deformation data (Bonaccorso and Davis, 2004; Patanè et al., 2005). Further evidence for NNW–SSE and NW–SE dike structures can be found at the surface, exposed by erosion nearby the summit craters. Their presence to depths of 500–700 m is displayed in a very impressive manner in the southern wall of the Valle del Bove (see rose diagram of dikes direction in figure 4a). Moreover, it was evident that the features of volcanic tremor, LP, and VLP events, accompanying eruptive activity changed and such variations can be explained by transport/discharge of gas-rich magma. In the medium-term, the clearest relationship between the uprising of magma, the progressive increase of the pressure in the conduits and the renewal of activity at SEC (INGV-CT volcanological reports at http://ct.ingv.it) can be recognized since 15 July by the increasing activity of LPs events. Afterward, since 15 August the onset of a discontinuous activity of ash emission, followed by strombolian activity at SEC (Andronico et al., 2008b) on 27 August, was accompanied by (1) the migration of tremor sources at shallow depth (figure 6a); (2) the progressive increase in the tremor amplitude (figure 5e); (3) the increase in the number of LPs and of their associated energy (figures 5a and 5b); and (4) by variations of ground deformation mea-

surements. In fact, ground deformation measured by GPS stations at the summit (in figure 6e the baseline ECPN-EPDN is shown) indicated an accelerating small dilatation of the summit area. A low rate of VT seismicity was, instead, detected under the volcano during these months, similarly to the first half of 2007, suggesting that magma flowed almost aseismically. These observations suggest that, since 15 August, the arrival of a small batch of undegassed magma (Nishimura, 2006) might have played a significant role in the re-activation of the SEC, leading to the 4–5 September lava fountaining episode. After this eruptive episode, the observed deflation of the edifice (figure 6e) and changes in tremor locations (deepening; figure 6a) can easily be explained by the gas-rich magma discharge during the paroxysm (Thompson et al., 2002; Kumagai, 2006). The cartoon in figure 12 illustrates the evolution of the eruptive activity at SEC, leading to this lava fountaining episode, between July and September 2007. Afterward, a new slow magma recharge affected the conduit, as testified by a similar but slightly different behavior of GPS ground deformation and variations in seismovolcanic parameters, which prepared the way for the 23–24 November lava fountaining episode. In the short term, the decrease and following increase of the "dominant" frequency of the LP events occurring before and after the two lava fountain episodes can be explained by variations of the resonator system. It is noteworthy that the first eruptive episode was also followed by a quality factor decrease. The resonator system, source of LPs, can be represented by a fluid-filled crack as suggested by recent studies based on the waveform inversion (Kumagai et al., 2003; Lokmer et al., 2007). Moreover, as suggested by the strong and frequent explosive activity involving discharge of high volumes of magma during the studied time period, the fluid can reasonably be considered a magma-gas mixture. Therefore, in the light of these assumptions, the aforementioned varia-

tions that followed the lava fountain episodes may be due to a decrease in the solid/fluid impedance contrast caused by either a decrease of the gas-volume fraction in the fluid or by an increase of pressure at constant temperature and gas-volume fraction (Kumagai, 2006). The observed eruptive activity supports the first interpretation that, in fact, is consistent with the gas/gas-rich magma discharge during the lava fountain episodes. Similarly, the decrease of the "dominant" frequency, observed before the lava fountain episodes, can be interpreted as the consequence of an increase of the gas-volume fraction in the fluid. This variation, therefore, can likely be linked to the fast uprise of gas-rich magma preceding the explosive activity. It is noteworthy that the interpretation of the quality factor variations implies that the attenuation due to intrinsic losses is negligible. Concerning the LP and VLP source locations, it is worth noting that the observed limited and stable spatial extension of the most active clusters of LP events can be recognized over the years (Saccorotti et al., 2007; Lokmer et al., 2008). This is indicative of the repetitive action of nondestructive sources in a restricted source zone where a shallow crack or a system of cracks probably exists. At Mt. Etna VLP events, similar to those observed in other active volcanoes (e.g., Kilauea, Hawaii), have dominant spectral peaks at periods of 10-15 s and can be associated with the transport of magma or gas slugs through cracks. As shown in figures 11b and 11d, the cluster of VLP lies directly beneath the main cluster of LP seismicity. This can be explained if VLP and LP oscillations originate in the same system, representing the volumetric deformation and LP oscillation of a shallow crack (or plexus of cracks), respectively

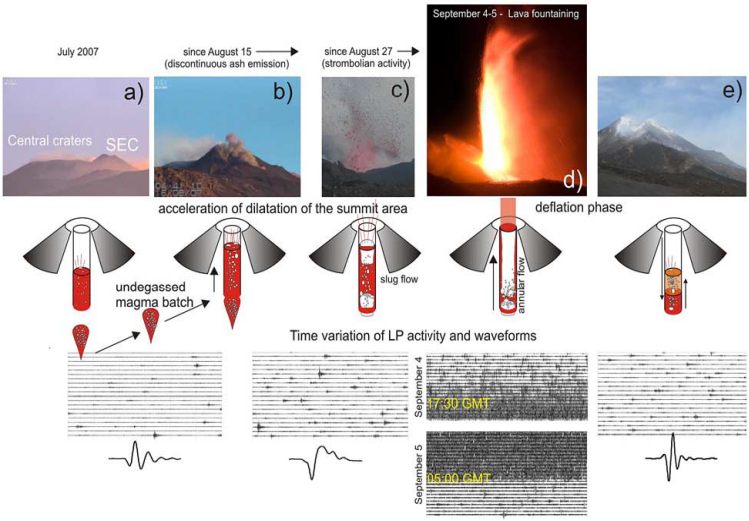

Figure 12: (a–e) Cartoon showing the evolution of eruptive activity at SEC between July and September 2007. Here the increase in the magma rising rate and volatile flux is considered the most probable trigger of the formation of the 4–5 September fire fountain through a progressive coalescence of bubbles in the conduit. In (b), in a first stage, since 15 August, a discontinuous activity of episodic ash puff was observed, mainly consisting of lithic material, indicating failure and collapses of the inner walls of the conduit (Andronico et al., 2008b). This emission gradually increased in frequency and intensity and was then replaced by the ejection of incandescent material. In (c), from 27 August, strombolian activity (formation and release of gas slugs) started, becoming more regular and stronger in the next days. In figure (d), the increasing gas volume fraction in the conduit modified the slug flow (strombolian activity) into an annular flow responsible for the 4–5 September lava fountain, driven by a long inner gas jet. In figure (e), after the eruptive episode, the observed fluctuation in the depth of tremor locations could suggest oscillation in the magma level in the conduit.

(Chouet, 2003). Conversely, the scattered sources of deeper LPs and volcanic tremors would represent the result of the dynamic interaction of volcanic fluids (magma degassing) with surrounding solid rocks in wider parts of conduit. In conclusion, our results confirm the feasibility of volcanic tremor and LPs location as an effective monitoring tool for tracking the temporal evolution of seismovolcanic sources and the ascent of small

magma gas-rich batches which could flow almost aseismically through the conduits. Moreover, the investigations of many seismic parameters, integrated with geodetic observations, may be useful to forecast eruptions that, like the summit effusive or explosive eruptions at Mt. Etna, apparently do not show clear precursor signals.

6.3 Seismo-volcanic signals at Mt.Etna during 2008

In this section, it is shown how volcanic tremor and LP events, together with infrasound signals treated in chapter 5, can represent important precursory phenomena of eruptive activity because of their strict relationship with eruptive mechanisms and with fluid flows through the volcano's feeding system. Important variations of these seismo-volcanic and infrasound signals, recorded at Mt. Etna volcano, occurred both in the medium- and short term before the eruption started on 13 May 2008. Several studies show how seismicity and ground deformation are the precursory phenomena most frequently observed before eruptions, as the Earth's crust is distorted by magma rising to the surface and fluids moving within rocks. In the considered period, the most significant changes were observed in the frequency content and location of LP events, as well as in volcanic tremor location that, similarly to what observed during the lava fountain episodes described in the previous sections, allowed to track the magma pathway feeding of the 2008 eruptive activity. The infrasound showed three different families of events linked to the activity of the three active vents: NEC, SEC crater and the eruptive fissure (hereafter referred to as EF). The seismic and infrasonic variations reported, corroborated by ground deformations variations, help to develop a quantitative prediction and early-warning system for effusive and/or explosive eruptions. In particular, the period 2008–2009 was characterized by both effusive and explosive activities. As described in section 5.4, after the lava fountain occurring on 10 May 2008, at SEC, a new eruption took place on 13 May from EF.

6.3.1 VT earthquakes, ground deformation and volcanic tremor

On the basis of the VT earthquakes, low-frequency seismic signals and deformation pattern, five different periods were distinguished during January–May 2008 (figures 15,16,19 and 20). At the beginning of 2008 (period I) volcanic activity renewal was evidenced by both the occurrence of deep earthquakes (about 10–20 km b.s.l.; Figure 15a) and the extension of GPS lines (green line EMGL-EMAL, in figures 13a and 15b). Deformation became more evident after mid-March (onset of period II) involving the lines located at higher altitude on the volcano (green line EPDN-EPLC, in Figures 13a and 15b).

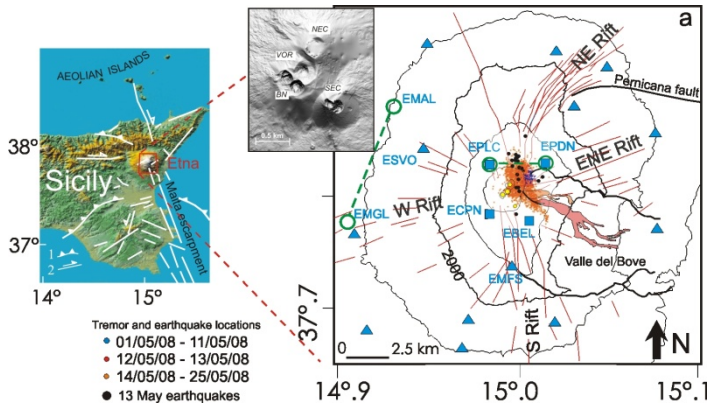

Figure 13: (top left) Structural map of eastern Sicily reporting the front of the chain (1) and the main faults (2). (a) Map of the summit part of Mt. Etna volcano showing 3D source centroids of volcanic tremor locations, filtered in the band 0.5–5 Hz and computed during the period 1–25 May 2008. Seismic stations (light blue triangles), seismic-infrasound stations (light blue squares), and baselines (green line and circles), whose measurements are shown in (b), are reported. The thick black line, located near the summit area, represents the eruptive fissure opened on 13 May 2008. Yellow and black dots indicate central craters and the earthquakes, occurring on 13 May 2008, respectively.

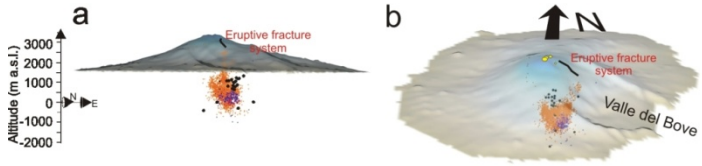

Figure 14: (a and b) 3D images of the volcanic edifice reporting volcanic tremor and earthquake locations, accompanying the eruption onset.

A modest increase in the number of earthquakes and in the strain release was observed (figure 15a) from early April to early May, when a strong swarm occurred near Pernicana Fault (an important volcano-tectonic structure in the north-eastern part of the volcano (e.g., Palano et al., 2009). This swarm marked the beginning of the period III. On 13 May (time boundary between period IV and V), hours before the beginning of the eruption, a further seismic swarm took place under the summit area (focal depths ranging between 1.5 b.s.l. and 1.5 km a.s.l.) and an intense deformation of about 0.9 m was measured, especially in the line at higher altitude, EPDN-EPLC (inset in figure 15b). Volcanic tremor locations are retrieved by following the approach described by Di Grazia et al. (2006) and Patane` et al. (2008), inverting the spatial distribution of tremor amplitude using the grid-search approach. Two different kinds of locations were performed: i) the volcanic tremor acquired during the whole 5 months period was located by using 1-hour-long moving windows (figure 15c); in order to obtain detailed information in the period 1-25 May (just before and during the first stage of the eruption), the tremor location technique was applied on 5-minute-long filtered signal windows. The 3D location of the volcanic tremor centroid for the period 1– 25 May (figures 13a,14b and 14c) constrains both the area and depth range of magma de-

gassing and highlights the magma pathway feeding the 2008 eruptive activity.

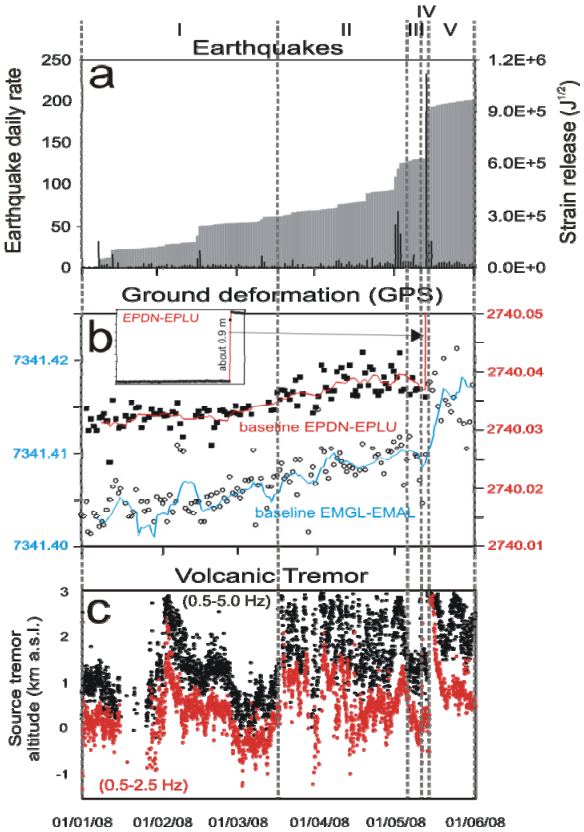

Figure 15: (a) Volcano-tectonic (VT) earthquake daily number (histogram) and cumulative strain release (grey area) during January–May 2008. (b) GPS measurements (baseline EMGL-EMAL and EPDN-EPLC in Figure 1a). The red and blue lines represent the moving average considering groups of five measurements. The inset in the left upper corner indicates the measurements of EPDN-EPLC baseline with a larger y-axis. (c) Altitude of the volcanic tremor source calculated by using 1-hour-long windows of the seismic signal filtered in the frequency band 0.5–2.5 Hz (red dots) and 0.5–5.0 Hz (black dots).

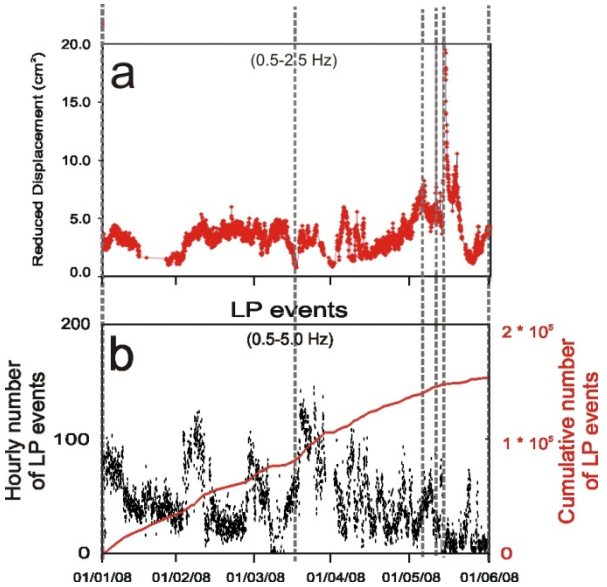

Figure 16: (a) Reduced displacement of the seismic signal recorded by EBEL station and filtered in the frequency band 0.5–2.5 Hz. (b) Hourly number of LP events detected in the frequency band 0.5–5.0 Hz (black dots) and their cumulative number (red line). The black vertical dashed lines and the top roman numbers indicate the time periods identified by VTearthquakes, low-frequency seismic signals and deformation pattern.

During the period January – mid- March (period I in Figure 15c) the volcanic tremor depth remained at 0– 1.5 km a.s.l. with the exception of a brief period (first half of February), characterized by a renewal of the explosive activity at SEC. Rapid changes in volcanic tremor depth began in mid-March (period II). In particular, volcanic tremor centroids activation at very shallow depth (up to 3 km a.s.l.) in the frequency range 0.5–5.0 Hz was observed. Also the deeper components of volcanic tremor better evidenced in the range 0.5–2.5 Hz (Figure 15c) shallowed from 0–0.5 km b.s.l to 1–1.5 km a.s.l.. From mid-March to the beginning of April, deep and shallow tremor sources alternated their dominance. From the second

part of April a deepening of location in the frequency range 0.5–2.5 Hz occurred. During these period, a regular increasing trend of the reduced displacement values occurred unlike the erratic variations previously noted (figure 16a). A further deepening occurred during 4–12 May (period III–IV; figure 15c). At the same time as the beginning of the eruption a shallowing of the tremor source was observed, followed by a deepening, evident in the frequency band 0.5–2.5 Hz (period V).

6.3.2 Long period events

During the period January–May 2008, over 100,000 LP events were recorded at Mt. Etna volcano (figure 16b). In figure 17 three examples of LP events at two stations (ECPN and EBEL) are shown. It is clear that the spectral content of these events is similar at the two considered stations, suggesting that the spectral peaks are due to source rather than to propagation and site effects. A subset of 7500 LP events characterized by a high signal to noise ratio at station ECPN was selected to carry out spectral analysis. For each LP event, a spectrum from the vertical component of station ECPN using 10.24 s windows were computed. Daily average spectra were calculated, normalized and visualized as a pseudo-spectrogram (figures 18 and 19a). Most of the radiated energy was concentrated in the band 0.4–4 Hz for almost the entire studied period. During the periods I-II the LP events were polychromatic. At least two different spectral peaks can be noted at frequencies ~0.7-1.5 and 3.5 Hz. In the first event of figure 17 (taking place on March 5) it is clear that these two spectral peaks of the

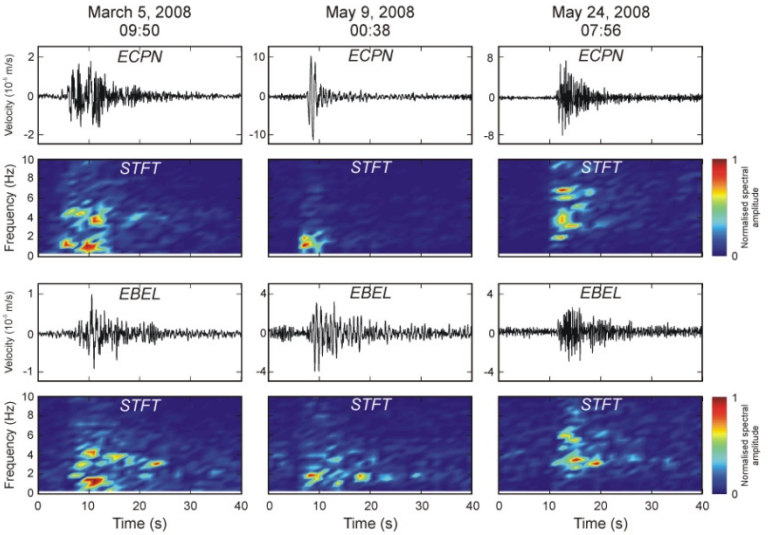

Figure 17: Examples of LP events recorded at the vertical component of ECPN and EBEL stations and their Short Time Fourier Transform (STFT). The STFT was calculated by 2.56-second-long moving windows overlapped by 1.28 s.

periods I and II are not due to two different kinds of LP events, but to the same type of polychromatic events. Assuming that the source of the LP events is represented by a resonating fluid-filled crack, as suggested by recent studies based on waveform inversion (e.g. Nakano et al., 2003; Lokmer et al., 2007), the spectral features of the LP signal depend on the size/geometry of the crack (Chouet, 1996; Kumagai and Chouet, 2000, 2001; Falsaperla et al., 2002) and on the physical-chemical features of the fluid within it (Kumagai and Chouet, 2000; Morrissey and Chouet, 2001). Therefore, on the basis of this, the two peaks could be related to two different resonating structures connected each other. It is also interesting to note that from March to the beginning of May (period II) a spectral peak gradually shifted from 0.7 to 1.5 Hz. Speculatively, the observed variations of the peak at 0.7-1.5 Hz could be due to a slow varia-

tion of the fluid characteristics inside the resonating structure. On 4 May the LP signal suddenly turned from polychromatic to monochromatic with almost the whole energy radiated at about 1.5 Hz (period III; figure 19a). Finally, during periods IV and V the LP events were again polychromatic with spectral content ranging from 1 to over 6 Hz (figure 17).

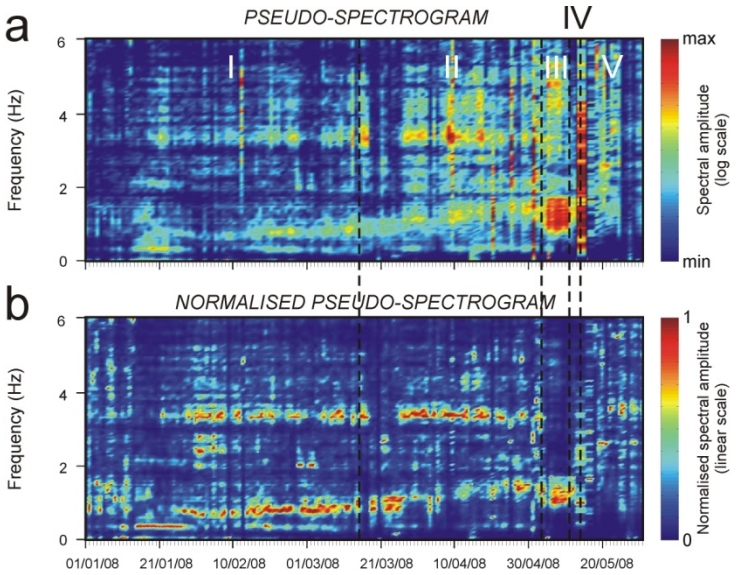

Figure 18: Pseudo-spectrograms obtained by using the daily average spectra (a) and the normalised ones (b) of the LP events recorded at the vertical component of ECPN station. The black vertical dashed lines in (a-b) and the top roman numbers indicate the time periods identified by VT earthquakes, low-frequency seismic signals and deformation pattern.

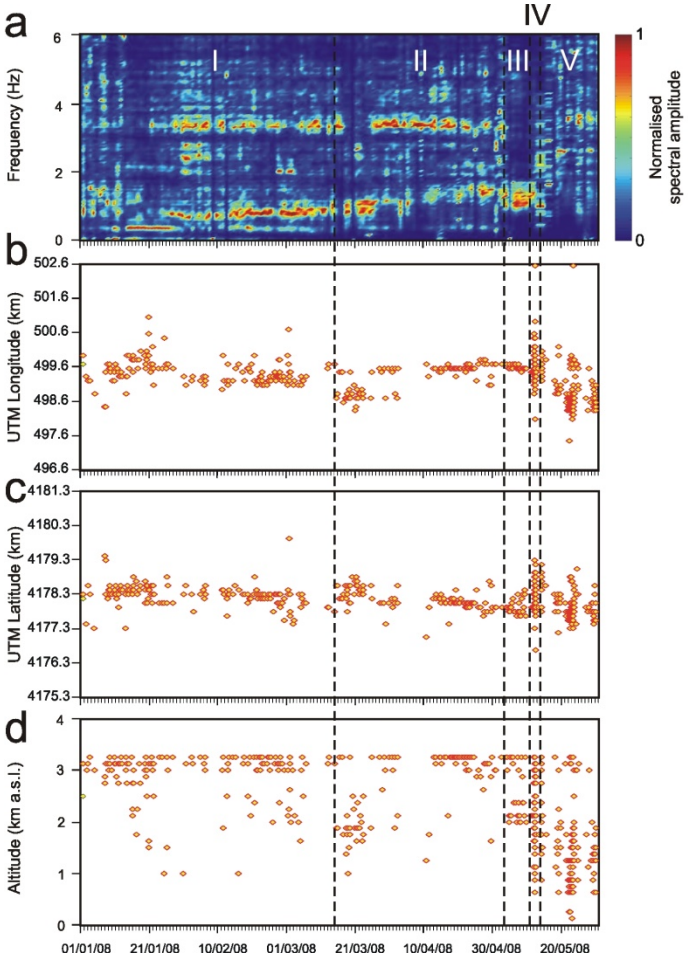

Figure 19: (a) Pseudo-spectrogram obtained by using the normalized daily average spectra of the LP events recorded at the vertical component of ECPN station. (b) Longitude, (c) latitude and (d) altitude of the source locations of 600 LP events.

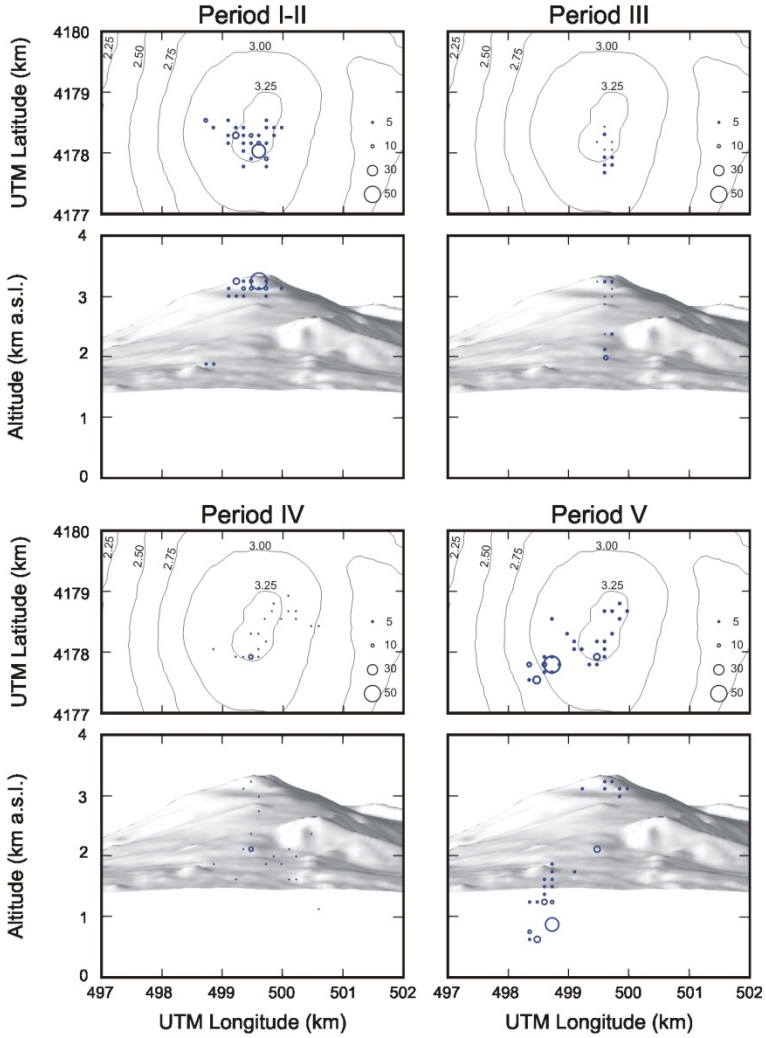

Figure 20: Map and section of Mt. Etna with the source locations of 600 LP events during the five periods. The radii of circles dots are proportional to the number of the locations in each grid node (see black circles and numbers reported in the lower right corner of the map).

A subset of 600 LP events with high signal to noise ratio at all the six stations nearest to the summit area (figure 13a) was selected to perform location analysis. LP events were located by following the semblance method (Neidell and Tarner, 1971) using 4-second-long windows of seismic signal, whose onset coincided with onset of the LP events, low pass filtered below 1 Hz. This frequency band was chosen because of the best performance of the location algorithm at low frequencies. The 3D grid was centered on the volcano edifice with dimensions of 6 × 6 × 3.25 km and node spacing of 125 m and a seismic velocity of 1.7 km/s (e.g., Patanè et al., 2008). The results show LP sources generally located below the summit craters (figures 19b–d). However, some source location changes were noted. From the beginning of January to 3 May (period I–II), the LP source remained stable below the Bocca Nuova crater at shallow depth (about 3 km a.s.l.). From 4 to 11 May (period III) the number of LP events located at greater depth (about 2 km a.s.l.) sharply increased. On 12 May (period IV), LP events northward shifted, roughly below NEC (figures 19 and 20).

6.3.3 Infrasound and LP events as precursor

As mentioned in section 5.4. three types of infrasonic events were found during May 2008, whose source locations are in good agreement with the position of the most active summit craters (figure 21a): “NEC events” lasting up to 10 seconds and characterized by dominant frequency generally between 1 and 2 Hz; “SEC events” showing duration of about 2 seconds, dominant frequency equal to 3–4 Hz and higher peak-to-peak amplitude than the NEC events; “EF events” exhibiting about 1 second duration, dominant frequencies mostly ranging between 2.5 and 4 Hz, and higher peak-to-peak amplitude than NEC and SEC events (Cannata et al., 2009a; Montalto et al., 2010) (figure 21b).

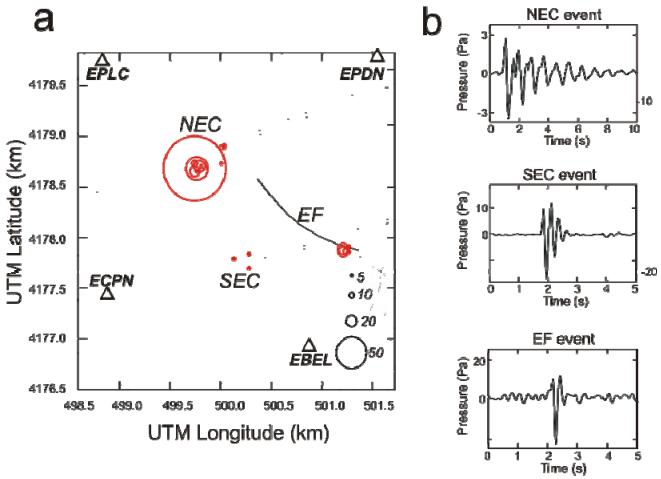

Figure 21: (a) Map of the summit area of Mt. Etna showing the site of the infrasonic sensors (triangles) and the source locations of infrasonic events (red circles). The radii of the red circles are proportional to the number of the locations in each grid node (black circles and numbers reported in the lower right corner of the map). (b) Infrasonic events recorded by EBEL station and related to the activity of NEC, SEC and EF.

The hourly number of infrasound events (figure 22b) and the variation of the amplitude of the whole infrasonic recordings (figure 22a) provide insights into the explosive activity. Generally the explosive activity is accompanied by increase in both hourly number of events and infrasonic RMS. Two exceptions can be noted in the event number series at the same time as the paroxysmal activity taking place on 10 and 13 May. The very high occurrence rate of events during the two paroxysmal episodes gave rise to a continuous signal and did not allow detecting single events.

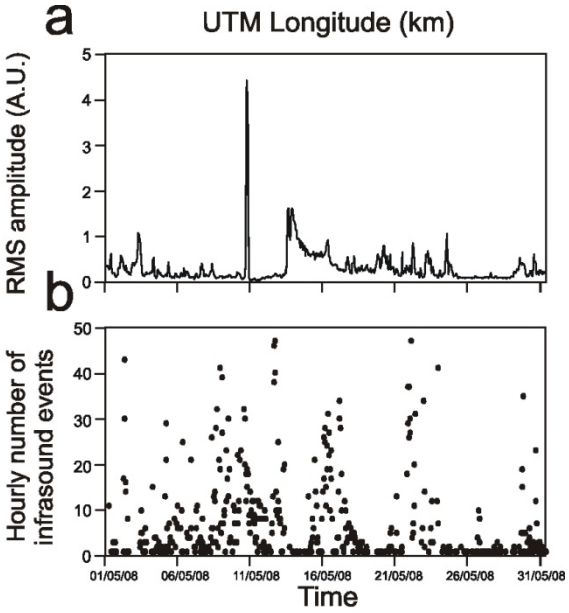

Figure 22: (a) Time variation of amplitude of the infrasonic signal, calculated as root mean square (RMS) of 1-hour-long moving windows of the recordings at EBEL. (b) Hourly number of infrasound events in the time period 1–31 May 2008.

Following the method described in the previous section, a pseudo-spectrogram was obtained for the infrasound events recorded during 8–14 May (figures 23b). A particular kind of NEC events, called long period infrasound (LPI) events, characterized by very low peak frequencies (0.3–0.5 Hz) and accompanied by strong seismic signature, was recorded just before the lava fountain at SEC and the beginning of the eruption at EF, taking place on 10 and 13 May, respectively (figures 23a and 23c). Finally, the dominant frequency of the NEC events decreased right after the end of the lava fountain at SEC (figure 23b). Focusing on LP and infrasound events recorded a few hours before the onset of the eruption, on 12 May (period IV), as aforementioned, LP events northward shifted, roughly below NEC (figures 19 and 20). At the same time the LPI events, generated by NEC, were recorded (figures 23b and 23c). Thus the shallow intrusion of the dike became evident. Finally, on 13 May (time boundary between period IVand V), a few hours before the beginning of the eruption a large number of phenomena highlighted the imminence of the eruption: pre-eruptive swarm and dramatic deformation of the upper part of the volcano took place, together with tremor amplitude increase and change in its source location, that clearly showed the eruptive fissure location (figure 13). Both the LP events and the infrasound showed that NEC played an important but still not clear role at the beginning of this eruption. This was confirmed by the epicenters of the earthquakes, occurring on 13 May (figure 13a), and by the dry fissures, opened on the same date (Neri, 2008), both located near the northern rim of NEC. A strict relationship was also highlighted between SEC and NEC by infrasound signals. In fact the lava fountain at SEC, taking place on 10 May, was followed by spectral changes in the NEC infrasound events (figure 23b). The proposed approach, based on the simultaneous observation of several parameters, is more powerful than a single precursor analysis.

The use of a dense geophysical permanent network – allowing a detailed space-time analysis (4D) – enabled to follow the volcano dynamics issuing two warnings (21 April and 3 May 2008) and to forecast the eruption a few hours before the onset.

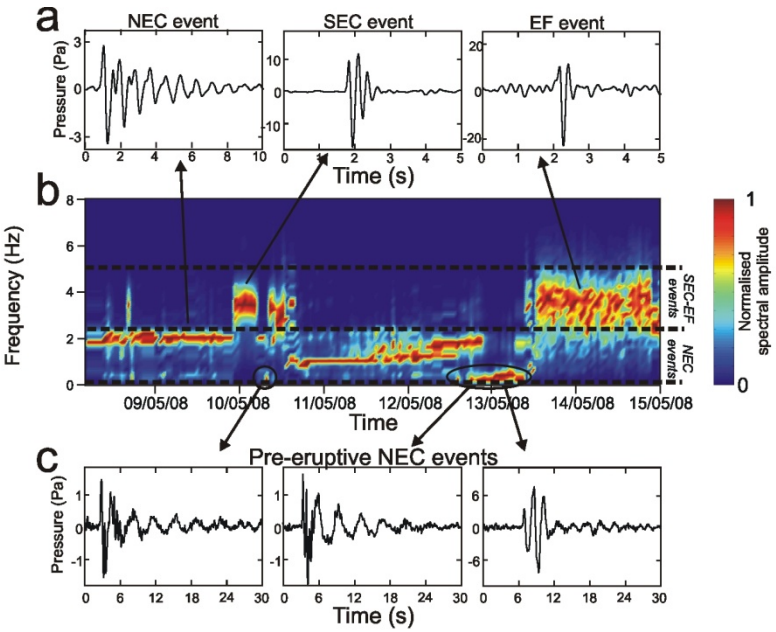

Figure 23: (a) Examples of waveforms of NEC, SEC and EF events recorded at EBEL station. (b) Pseudo spectrogram obtained by using the normalized hourly average spectra of the infrasound events recorded at EBEL. (c) Long period infrasound events, recorded by EBEL and characterized by dominant frequencies ranging between 0.3 and 0.5 Hz, occurring before the lava fountain at SEC and the beginning of the eruption at EF.

6.4 Discover lava fountain precursors using three component sensors

In this section the multi component analysis already described in section 4.6 is applied. The basic idea, also confirmed by the analysis shown in the previous section, is that seismic wavefield may strongly change before a critical volcanic event like a lava fountain or effusive eruption. To demonstrate this assumption, the three lava fountain episodes, previously described, were taken into account. The seismic wavefield investigation was performed using polarization method developed by Jurkevics (1988) and Benhama (1988) (see section 4.6) and applied on continuous three component signals recording on a reference summit station (figure 13). In order to discover SEC lava fountain precursors, EBEL station was chosen (figure 13). The analysis was performed on continuous seismic recording using a moving window of one minute with 50% of overlap, obtaining the time series of the three polarization parameters: azimuth, incidence and rectilinearity. Considering the lava fountain, that occurred on 4-5 September 2007, the temporal variations of the three parameters are shown in figure 24. Three variations appear in the azimuth time series starting from the second half of August together with an increase of tremor amplitude (figure 24a and 24b). As shown in figure 6a this pattern corresponds to the migration of tremor sources at shallow depth. The second pattern starts on 25 of August 2007, when the tremor source indicates a progressive migration toward SEC (figuree 8b and 8c). At the same time, a relevant variation of incidence angle occurs (figure 24c). In order to confirm the validity of polaritazion variations as precursor, other two lava fountain episodes, described in the previous section, were considered.

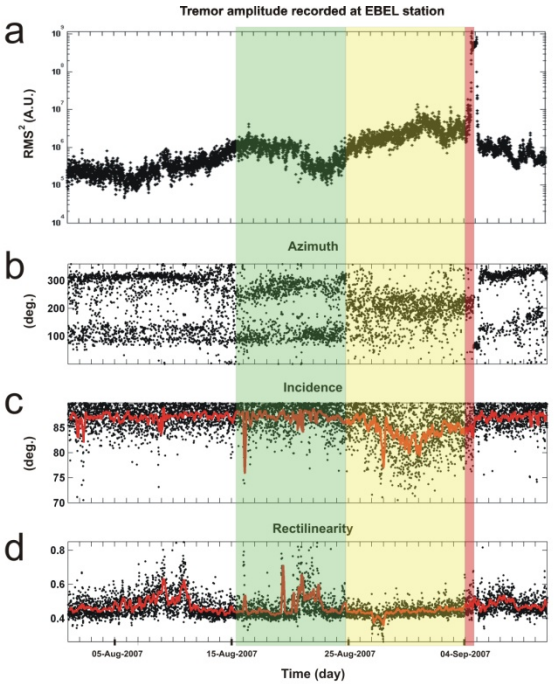

Figure 24: (a) Tremor amplitude during the period from 01-Aug-2007 to 10-Sep-2007. (b-d) Time series of azimuth, incidence and rectilinearity respectively. The green rectangle indicates the first anomaly while yellow and red rectangles indicate the second anomaly and the onset of the lava fountain respectively.

In figure 25 and 26 the variations of polarization parameters during the lava fountains on 23 November 2007 and on 10 May 2008 are shown, respectively. As displayed in figures 25b-c and 26b-c two strong variations of azimuth and incidence occurred before the onset of the two lava fountains. The comparison among the polarization parameters calculated during all the three considered lava fountains highlights that the wavefield variations may occur at different time scale. While on 4-5 September 2007 the polarization anomalies start about 15 day before the lava fountain, in the last two episodes (23 November 2007 and on 10 May

2008) the same pattern occurs only a few hours before the onset of the eruptions. During the considered periods the rectilinearity parameter does not show significant variations. The incidence changes before and during all the three fountains indicate a migration of the tremor source under SEC providing a reliable precursor parameter. The polarization analysis for the considered lava fountain periods reveals a similar trend of high values of incidence together with a clustered values of the azimuth. Several studies identified the dominant wavefield either as P waves (Ferrucci et al., 1990) or love/SH waves (Ereditato and Luongo, 1994; Wegler and Seidl, 1997) showing complicated overlapping patterns. Similar observations have also been reported on other volcanoes such as Arenal (Benoit and McNutt, 1997). The tremor wavefield observed during the considered lava fountain episodes turned out to be so complex that it is impossible to identify a clear wave type composition. This is not surprising, because, unlike the polarization analysis in earthquake seismology that can provide information about the wave types composing the wavefield and the seismic source location and mechanism (e.g., Alessandrini et al., 1994), in volcano seismology such an analysis cannot give these information because of the heterogeneities and rough topography of volcanoes (e.g., Neuberg and Pointer, 2000). However, this kind of analysis can be useful to detect even very small variations in seismic source location and/or mechanism. Moreover, this study showed that polarization parameters, together with the tremor amplitude and tremor source location, are an useful tool for the definition of eruption precursors.

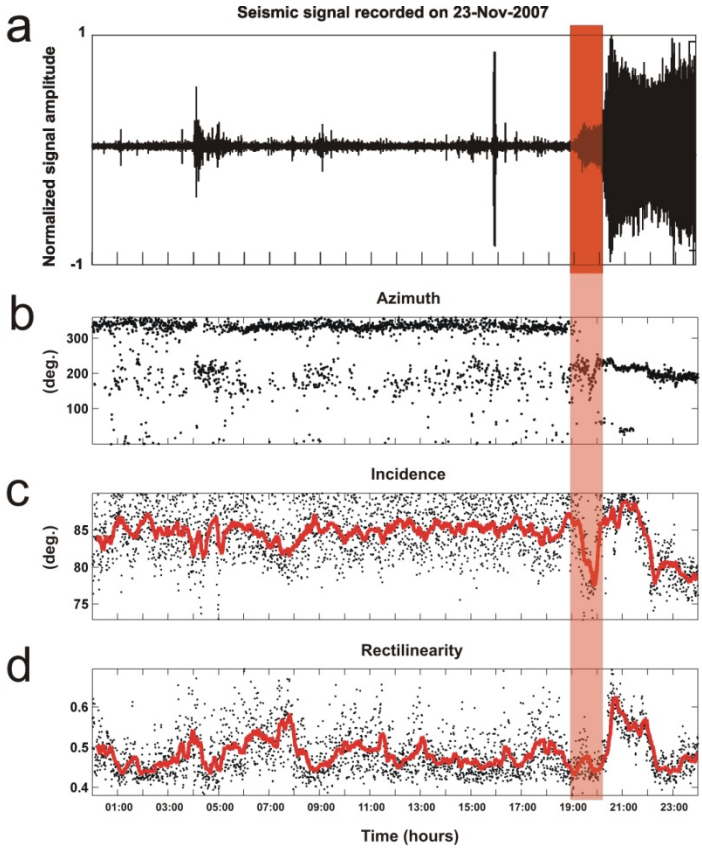

Figure 25: (a) Seismic signal recorded on 23 Nov 2007. (b-d) Time series of azimuth, incidence and rectilinearity respectively. Red rectangle indicates the incidence anomaly that occurred before the onset of the lava fountain.

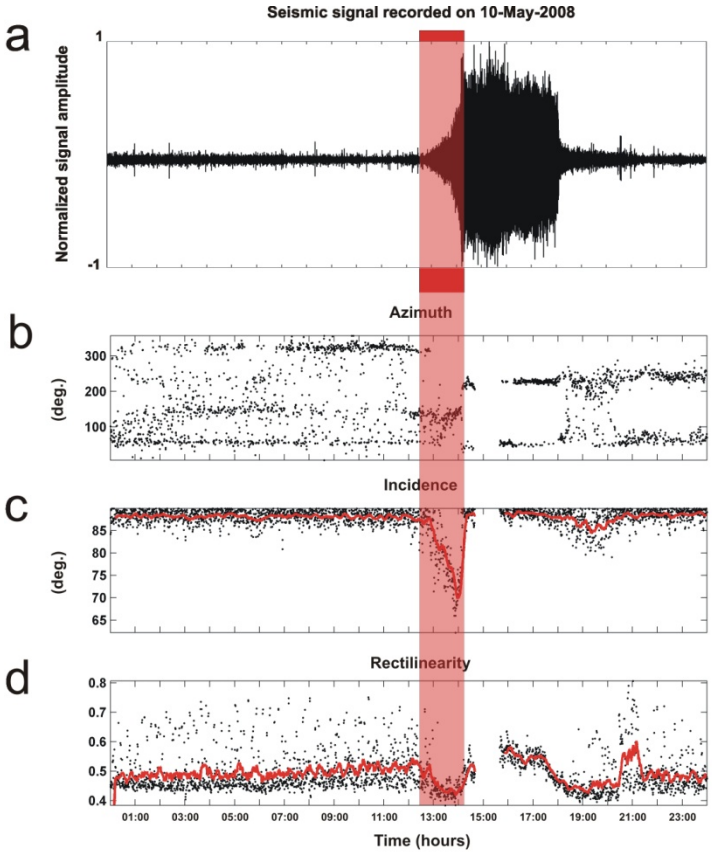

Figure 26: (a) Seismic signal recorded on 10 May 2008. (b-d) Time series of azimuth, incidence and rectilinearity respectively. Red rectangle indicates the incidence anomaly that occurred before the onset of the lava fountain.

6.5 Multi-stations coherence

The method introduced in section 4.3 allows highlighting the coherence among summit station signals over time. Although the source mechanism producing these coherence time changes is still not well known, there are evidences that summit stations coherence is related to volcano system recharge. Considering the three eruptive periods previously described, a full coherence analysis is here performed. For this purpose, the recorded signal on 2007-2008 time period were analyzed using the MVDR methods (section 4.3). The MVDR coherence is estimated considering a 10 minutes moving window without overlap and then a hourly averaged coherence value is calculated. The resulting coherogram shows how coherent the different frequency bands are among summit stations EBEL, EPDN, EPLC and ECPN as a function of time (figure 27). A first evidence of volcano system recharge is shown in figure 27 before the lava fountain that occurred on 4-5 September 2007.

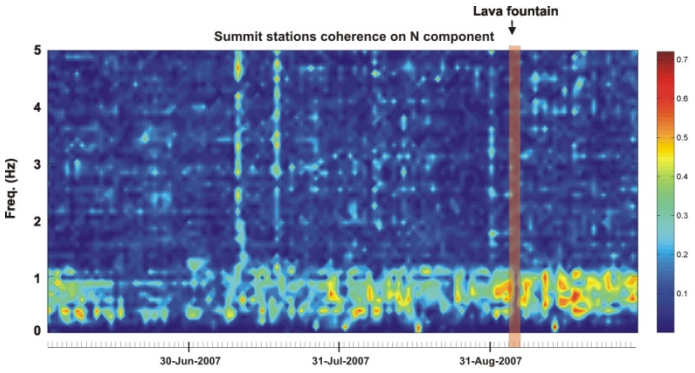

Figure 27: Summit stations coherence calculate at the N component during the time period June-September 2007. The red rectangle shows the lava fountain.

According to what reported in section 6.1.4 most of the energy, coherent at the summit stations, was concentrated near 0.7 Hz, showing a link with the LP source related to transport/discharge of gas-rich magma. This can highlight the recharge phase of the system before the onset of lava fountain and/or eruption. Other two clear evidences of this assumption are the high coherence episodes before the lava fountains of 23 November 2007 and 10 May 2008 (figures 28 and 29, respectively). In particular, the coherogram reported in figure 28 exhibits high coherence related to lava fountain of 4-5 September and a low coherence in the second half part of October when a new recharge phase starts in November leading to the fountain of 23-23 November. While the first episode is in agreement with the migration of tremor source under the SEC (figure 8), during the second episode this relationship is not so clear. The last episode, analyzed in this section, regards the summit stations coherence before the onset of the lava fountain that took place on 10 May 2008 shown in figure 29.

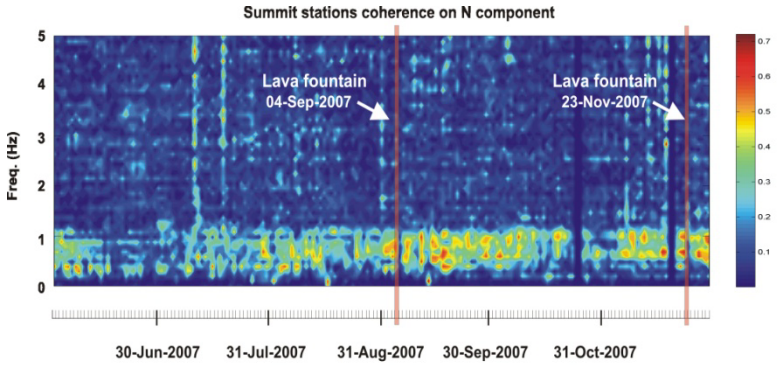

Figure 28: Summit stations coherence calculated at the N component during the time period June-September 2007. The red rectangles show the lava fountains.

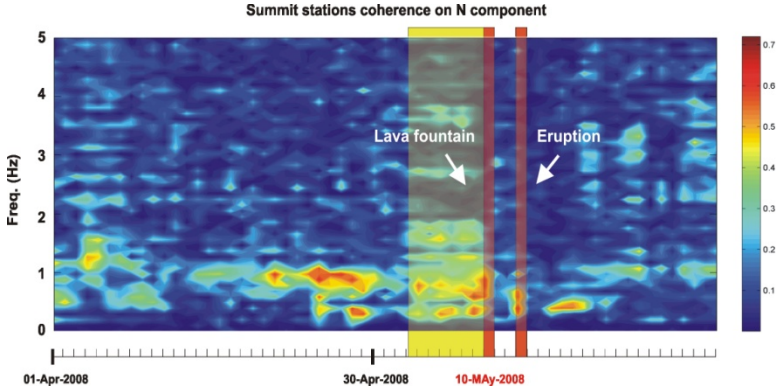

Figure 29: Summit stations coherence calculated at the N component during the time period April-May 2008. The red rectangles show the lava fountain on 10 May and the beginning of the eruption on 13 May. Yellow rectangle indicates the time period related to a deepening of LP and tremor source before the lava fountain.

In this last case, the summit station coherence indicates a system re-charge started at mid April when a progressive and regular increase of the reduce displacement of tremor was observed (figure 16a), confirming a gradual increase of energy of the volcanic system. Also, short-term changes occurred during the period 4–10 May, when the low frequency coherence (below 0.5 Hz) coincides with tremor and LP sources deepening (0–1.5 km a.s.l. and 2 km a.sl.) and LP spectral content changes (Figure 15c and 19).

6.6 Seismic and infrasonic coupling using cross wavelet analysis

A novel approach described in this section is used to discover coupling between seismo-volcanic and infrasonic signals. The analysis of a single signal (whether seismic or acoustic) sometimes is not sufficient to detect ongoing explosive activity. Indeed there are some cases when increases in tremor amplitude did not correspond to eruptive activity, such as during banded tremor activity (e.g. Cannata et al., 2010). Similarly, in some cases infrasound signal is so affected by weather-dependent effects, like wind noise, that could provide wrong information regarding the ongoing volcanic activity. Therefore, the joint analysis of infrasonic and seismic data turns out to be the best monitoring tool. Since the infrasonic signals are the clear evidences of open conduits on active volcano, the process that leads to infrasonic emission can generate low frequency seismic signals. Several studies have been performed on the physical relationship between these kinds of signals (e.g. Ripepe et al., 2001b). The cross-wavelet analysis computed on seismic and infrasonic RMS may reveal time periods of high coherence that can be related to volcano summit activity (e.g. Strombolian activity). At Mt. Etna, the high availability of infrasonic and seismic signals together with different kinds of volcanic regimes, permit the joint analysis of seismic and infrasonic signals in order to study their relations with the volcano activity. In several works (e.g. Grinsted et al., 2004), the coupling between different time series is performed using a multi resolution analysis like wavelet transform. In this section, cross-wavelet analysis (see section 2.1.6) will be applied on seismic and infrasonic RMS using a 1 hour moving window. In particular, two periods of intense Strombolian activity, that occurred before the two lava fountains of September and November 2007, will be analyzed. In figure 30 a clear episode of high seismic – infrasound coherence is

shown by the high coherence started on 29 August. It is in agreement with the SEC strombolian activity described, from an infrasound point of view, in section 5.3.4. It is noteworthy that this high coherence could be the evidence of the interaction between seismo-volcanic sources, whose wave-field change on 25 August is related to the migration of tremor sources at shallow depth (figures 8b-c), and the intense infrasonic activities at SEC. Less clear is the seismic-infrasonic relation during the lava fountain of November 2007 (figure 31). From a visual inspection of the signal buffer reported in figures 32 and 33, the high coherence is justified by the presence of infrasonic signals together with their seismic counterpart. In particular, these high coherence periods are related to main 4 episodes of intense infrasonic activity that took place at the end of November 2007 before the onset of lava fountain episode.

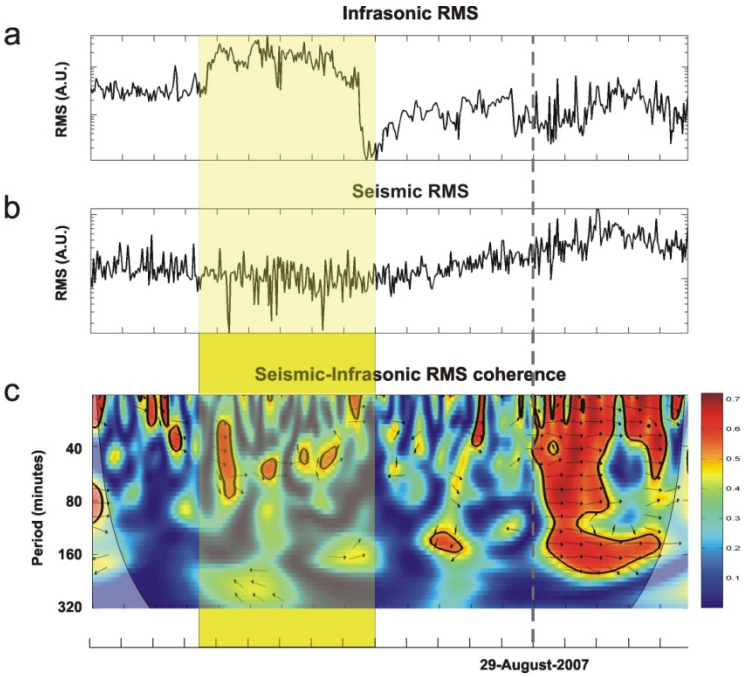

Figure 30: (a) RMS of the infrasonic signal recorded during the period 15 August 2007 – 03-September 2007. (b) RMS of the seismic signal recorded during the same time interval. (c) Wavelet coherence between infrasonic and seismic signal RMS. The vectors indicate the phase difference between the two RMS time series (a horizontal arrow pointing from left to right signifies in phase and an arrow pointing vertically upward means the first series lags the second one by 90°). The cone of influence (COI), where the edge effects might distort the picture, is shown as a lighter shade. The gray dashed lines indicate the onset of high signals coherence. The yellow rectangle indicates a period of high wind causing high infrasonic RMS due to noise.

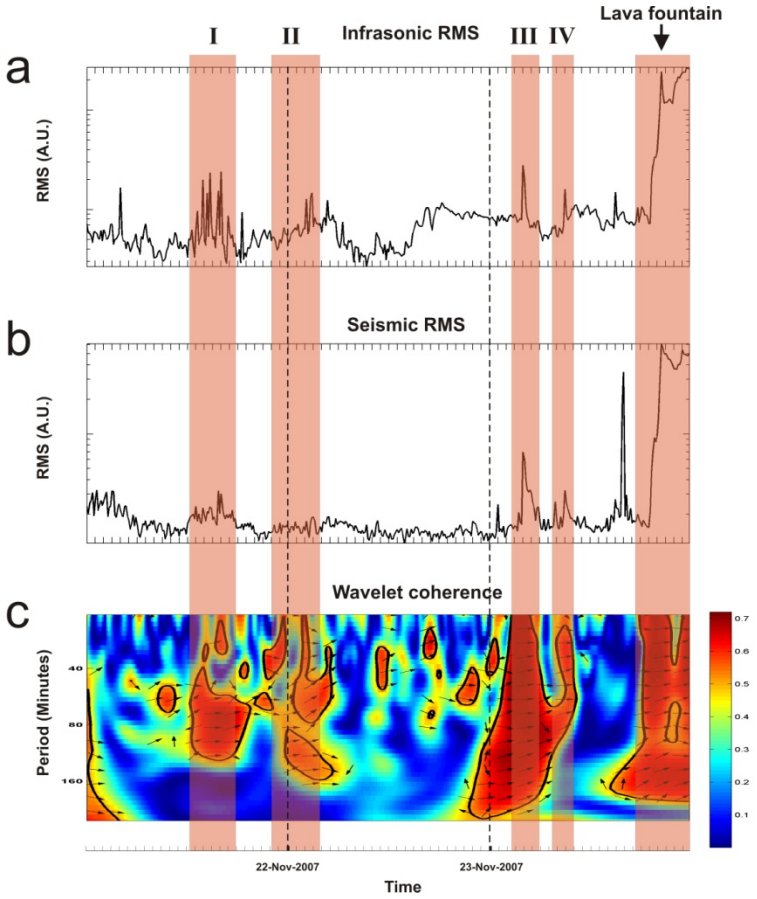

Figure 31: (a-b) RMS of infrasonic and seismic signals during the period 21-23 November 2007. (c) Wavelet coherogram of the two RMS time series. The vectors indicate the phase difference between the two RMS time series (see caption figure 30). The red rectangles with top roman numerals indicate the periods whose seismic and infrasound signals are shown in figures 32 and 33.The right red rectangle indicates the lava fountain period.

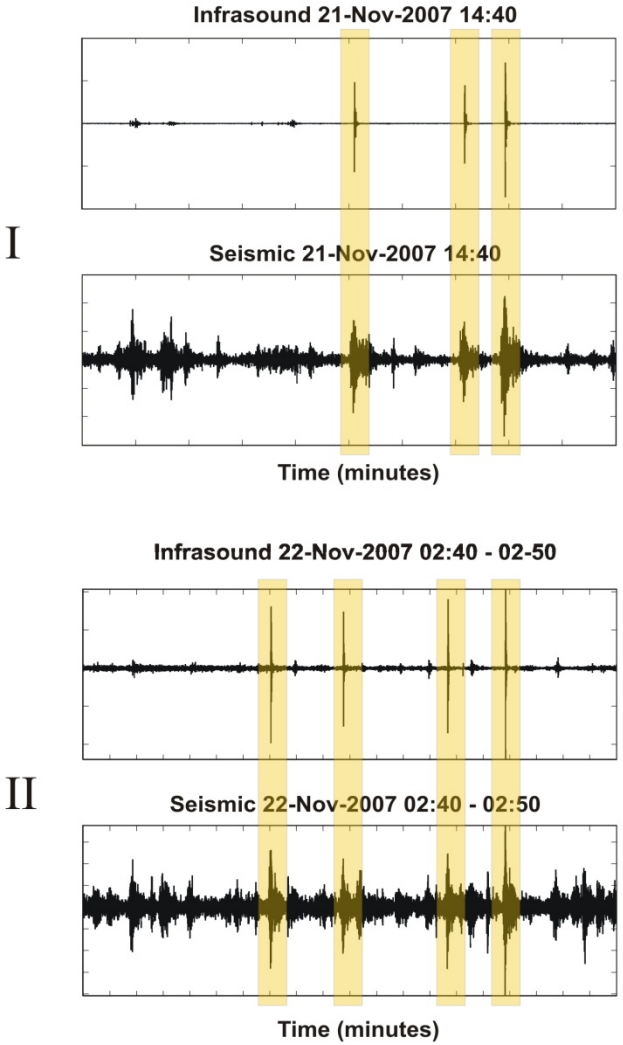

Figure 32: periods I and II shown in figure 31. The orange areas highlight both relevant seismic and infrasonic signals.

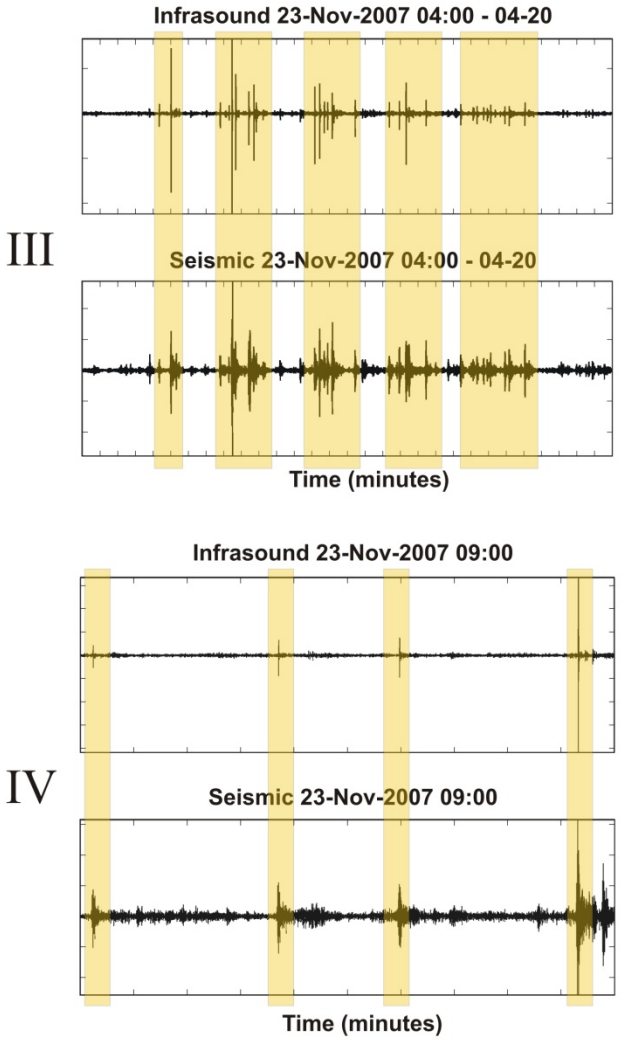

Figure 33: periods III and IV shown in figure 31. The orange areas highlight both relevant seismic and infrasonic signals.

6.7 Banded tremor phenomena at Mt. Etna during 2008

The literature reports the occurrence of a particular kind of volcanic tremor characterised by regular cyclic increases of amplitude in several volcanic and geothermal areas such as Nevado del Ruiz (Martinelli, 1990), Pinatubo (Mori et al., 1996), Soufriere Hills (Baptie and Thompson, 2003), Kilauea (Barker et al., 2003), Stromboli (Langer and Falsaperla, 1996), Etna (Gresta et al., 1996a), Pavlof, Manam and Poas (McNutt, 1992, 1994). Because of its peculiar seismic signature on the seismograph drum, forming evident stripes on seismograms, this kind of seismic signal is called "banded" tremor. It has largely been recorded during times of hydrothermal activity (McNutt, 1992) and its source process has recently been modelled using a two-phase hydrothermal instability flow model (Fujita, 2008). In this section banded tremor activity that occurred at Mt. Etna volcano between August-October 2008 during the 2008-2009 eruption was analyzed in detail. The banded tremor occurred in episodes lasting 25-30 minutes with intervals in between the episodes of about 25 minutes. Seismic signal analyses showed that the banded tremor was characterised by spectral contents, wavefields and source locations that differed from the "ordinary" volcanic tremor described in the previous sections. The infrasound recordings exhibited an intermittent infrasonic tremor alternating with the banded tremor episodes. Finally, nonlinear analyses suggested that banded tremor system can be considered chaotic, implying: i) sensitive dependence on initial conditions, suggesting not only that a banded tremor system requires particular conditions to generate, but also that slight variations of these conditions are able to greatly change the features of the banded tremor or even to stop it; ii) long-term unpredictability, that is, the impossibility to forecast the

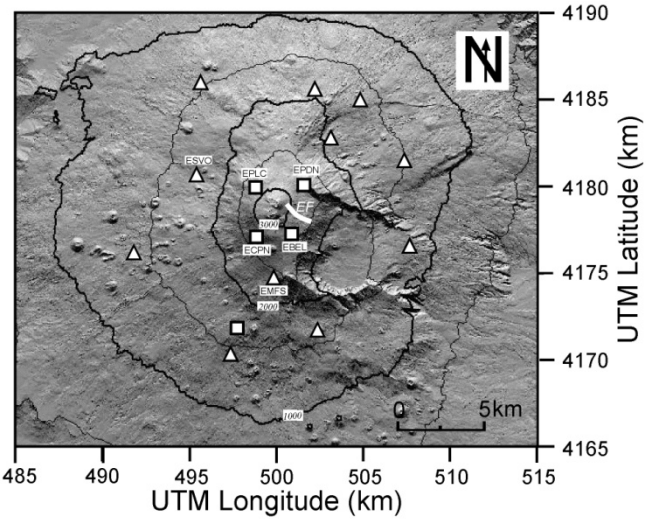

Figure 34: Digital elevation model of Mt. Etna with locations of the used stations equipped with seismometer (triangles), and with both seismometer and infrasonic sensor (squares). "EF" and the bold white line indicate location of the eruptive fissure that opened on 13 May 2008. The six named stations correspond to those used to locate the banded tremor source by the seismic signal envelope method.

long-term evolution of the banded tremor. On the basis of all these results and analogies with geyser models, a model of banded tremor that invokes alternating recharge-discharge phases is proposed. Banded tremor is due to "perturbations" in shallow aquifers, such as fluid movement and bubble growth or collapse due to hydrothermal boiling, triggered by the heat and hot fluid transfer from the underlying magma bodies. This heat-fluid transfer also causes an increasing pressure in the aquifer leading to fluid-discharge. During this process the seismic radiation decreases and, if the fluid-discharge is well coupled with the atmosphere, acoustic signals are generated.

6.7.1 Banded tremor characteristics

Station EBEL (figure 34) recorded the banded tremor best. To characterize the tremor, a long time series is constructed for all three components of EBEL by subdividing the continuous time series into non-overlapping 1-minute-long windows. An average spectrum was calculated for each window by averaging two spectra computed on partially overlapped, roughly 40-second-long portions of window, and these average spectra were used both to obtain multi-day-long spectrograms and to calculate the overall spectral amplitude (OSA; for details of OSA calculation see Alparone et al., 2007) (figures 35 and 36). In order to emphasize the banded tremor episodes, the OSA was computed in the frequency band 12-20 Hz, which generally lacks energy contributions from the "ordinary" tremor source (<10 Hz) and is quite unaffected by seismic noise due to wind and rainfall (>20 Hz). In order to define the onset and end times of the single episodes of banded tremor, and thus their duration and the intervals between them, the following method was used. The OSA time series of the vertical component of EBEL station, calculated as above described, was smoothed by means of a moving average over 5 minutes. Then, the smoothed series was divided into 400-minute-long windows overlapped by 399 minutes, and an amplitude threshold was fixed for each window equal to 40-*th* percentile. As explained in section 4.2, for a given time series, the p-th percentile can be defined as the value such that at most (100*p)% of the measurements are less than this value and 100*(1-p)% are greater. Whenever the smoothed OSA time series exceeds the threshold value, the onset time of an episode is declared. Similarly, every time the smoothed OSA time series falls below the threshold value, the end time of an episode is declared.

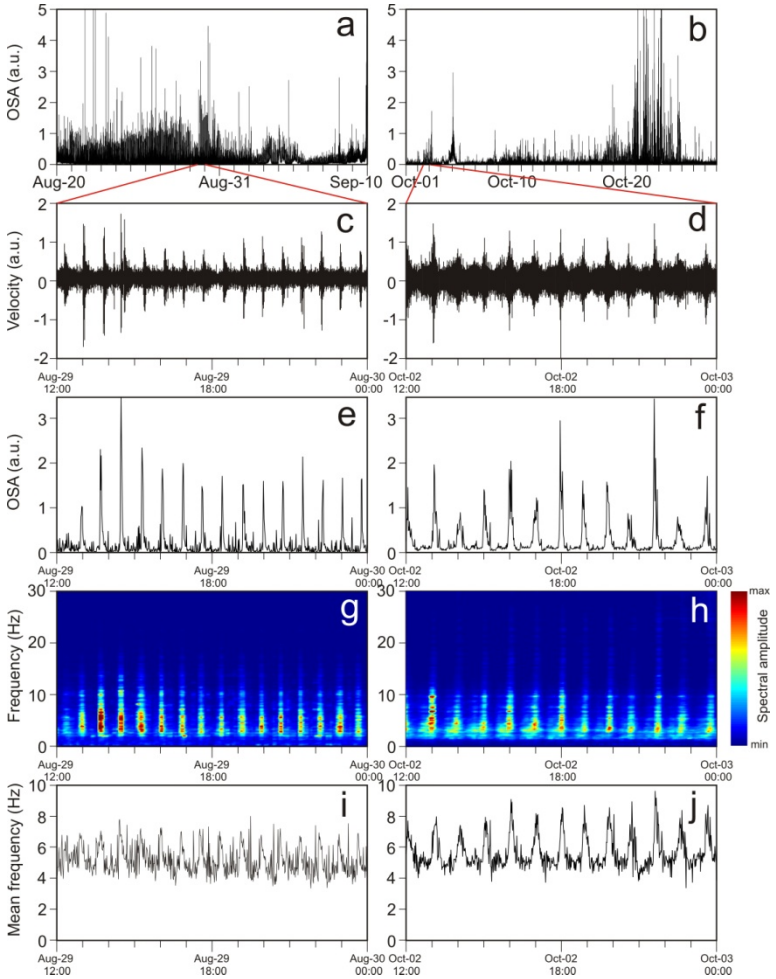

Figure 35: Overall spectral amplitude (OSA) of the seismic signal recorded at the vertical component of station EBEL during (a) 20 August–9 September and (b) 1–27 October 2008. Seismic signal recorded on the vertical component of EBEL in the interval (c) 1200–2400 on 29 August and (d) 1200–2400 on 2 October, and corresponding (e, f) OSA, (g, h) spectrograms and (i, j) mean frequency. All times reported are in UTC.

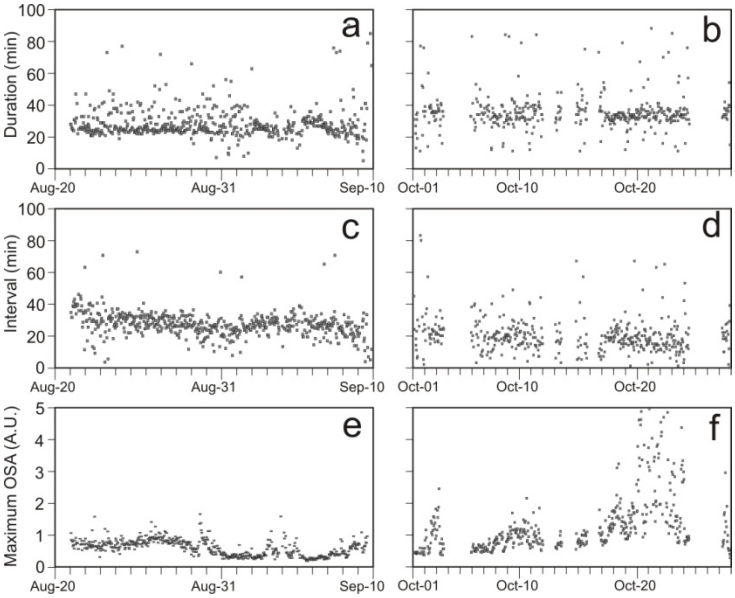

Figure 36: (a, b) Durations of the banded tremor episodes; (c, d) length of the intervals between the end of one episode and the start of another; (e, f) maximum OSA values reached during all the banded tremor episodes. (a, c, e) and (b, d, f) refer to the periods 20 August–9 September and 1–27 October 2008, respectively.

In the light of it, the first studied period, 20 August – 9 September 2008, was characterised by ~620 clear episodes of banded tremor with fairly steady duration for the entire period and equal to ~25 minutes (figure 36a). The interval between the end of an episode and the onset of the following one was also quite steady and roughly equal to the time duration of the episodes (figure 36c). There was a high degree of variability in the maximum values of OSA for different episodes (figure 36e). During the second period, 1-27 October 2008, ~650 episodes of banded tremor occurred with average episode duration of ~30 minutes and intervals between the end of an episode and the onset of the following one roughly

equal to 25 minutes (figures 36b and 36d). The maximum values of OSA were very variable but generally higher than the values of the first studied period (figure 36e and 36f).

6.7.2 Spectral and polarization analysis

The spectral representation of the banded tremor activity was obtained by the method described in section 6.7.1 taking into account periods characterised by both the most energetic banded tremor episodes and very low seismic noise due to wind and rainfall. They were averaged and compared to the spectra calculated during intervals in between the episodes (figure 37). The spectra for banded tremor were broader than those for "ordinary" tremor activity. In fact, the radiated energy at frequencies above 5 Hz sharply increased during the banded tremor episodes, as also shown by the mean frequency plotted in figure 35i and 35j (computed using the method described in Carniel et al., 2005). Moreover, a slight difference can be seen between the spectra of the two banded tremor periods: the spectrum of the second period is characterised by greater energy at high frequency (>20 Hz) than the spectrum of the first period. The higher and broader frequency content of the banded tremor is a distinctive feature of such cyclic banded tremor episodes. Indeed, unlike such banded tremor episodes, the repetitive increases of volcanic tremor, sometimes taking place at Mt. Etna at the same time as strombolian activity and lava fountaining occur, are accompanied by a decrease in the dominant frequency and by a narrowing of the spectra (Falsaperla et al., 2005; Cannata et al., 2008). The polarization analysis was performed using the method described in section 4.6 based on the calculation of the covariance matrix for the three components of the seismic signal.

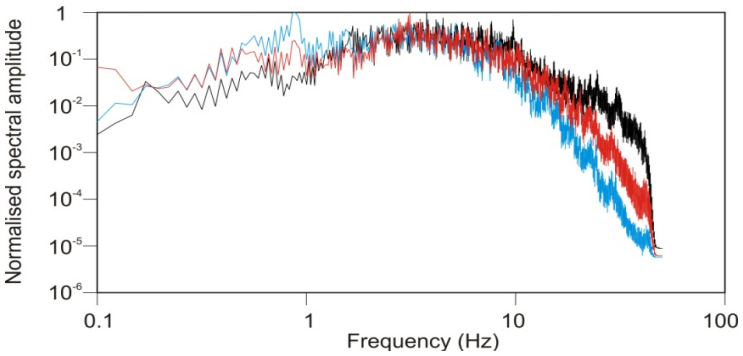

Figure 37: Spectra obtained by averaging the spectra calculated on 40.96 second-long seismic windows recorded during the most energetic banded tremor episodes in the periods 20 August–9 September (dark gray line) and 1–27 October 2008 (black line) and during "ordinary" volcanic tremor (light gray line).

Two different frequency bands were analysed: 0.5-5.0 Hz, characterised by both "ordinary" and banded tremor; 12-20 Hz, with only banded tremor. The multi-day-long tremor time series at station EBEL was divided into windows of 2 second with 50% overlap for the band 0.5-5.0 Hz and 0.5 second for 12-20 Hz. In figures 38 and 39 the time variation of the polarization parameters during the periods 12:00-24:00 on 24 August and 12:00-24:00 on 2 October is reported. These two intervals were chosen because of the high signal to noise ratio at all the three components of the seismic signal at station EBEL. The frequency band 0.5-5.0 Hz is characterised by azimuth values ranging from 80° to 110°, incidence above 80° and rectilinearity coefficient between 0.6 and 0.9. In particular variations in the polarization parameters took place at the same time as the occurrence of the banded tremor: specifically, rectilinearity coefficients decrease, while the azimuth slightly increases during the banded tremor episodes.

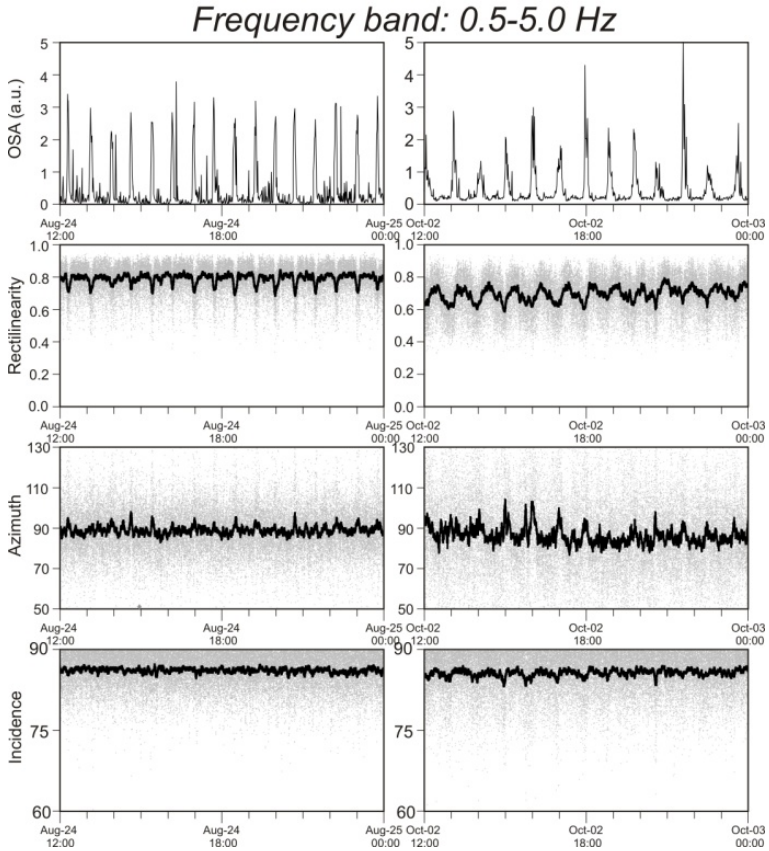

Figura 38: OSA (black lines in the top plots) calculated in the frequency band 12–20 Hz, polarization parameters (light gray dots) and their moving average over 200 samples (thick black lines) in two frequency bands 0.5–5.0 Hz of signal recorded at EBEL during the periods 1200–2400 on 24 August and 1200–2400 on 2 October. The incidence angle is calculated with respect to the vertical direction. The polarization parameters (gray dots) were calculated by using windows of 2 and 0.5 seconds for 0.5–5 Hz.

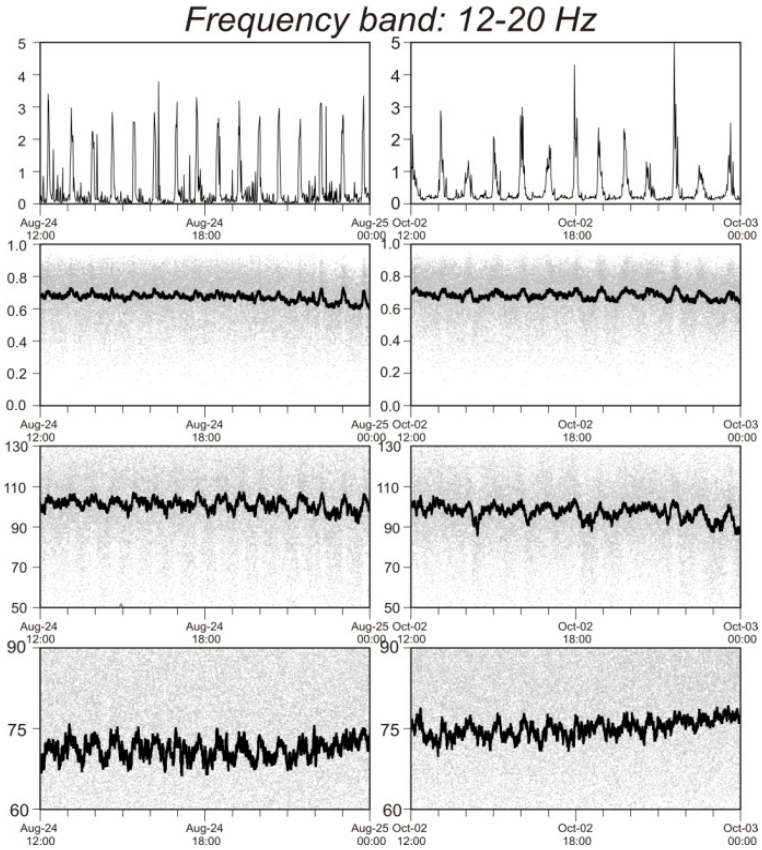

Figura 39: OSA (black lines in the top plots) calculated in the frequency band 12–20 Hz, polarization parameters (light gray dots) and their moving average over 200 samples (thick black lines) in two frequency bands 12–20 Hz of signal recorded at EBEL during the periods 1200–2400 on 24 August and 1200–2400 on 2 October. The incidence angle is calculated with respect to the vertical direction. The polarization parameters (gray dots) were calculated by using windows of 2 and 0.5 seconds for 12–20 Hz.

Variations in incidence angles are less clear, but slight decreases can be seen in the incidence time series of 2 October. The frequency band 12-20 Hz shows azimuth of 90-110°, lower values of incidence than the other band, ranging from 70° to 80° and rectilinearity above 0.6. Also in this case variations can be noted at the same time as the banded tremor episodes occurred. Similarly to the variations observed in the other frequency band, azimuth values slightly increase, while, unlike the results of the other frequency band, both incidence and rectilinearity increase during banded tremor episodes. The different patterns observed in the two analysed frequency bands can be explained as follows. The band 0.5-5.0 Hz is characterised by both continuous "ordinary" tremor and cyclic occurrence of banded tremor. Therefore, during the periods in between the banded tremor episodes, a wavefield features of the "ordinary" tremor was observed, whereas, during the banded tremor episodes, the "coexistence" between the two wavefields giving rise to variations of the polarization parameters occurred. In particular, because of the "mixture" of seismic waves coming from different sources out-of-phase with each other, the wavefield becomes more chaotic and the rectilinearity coefficient decreases. On the other hand, the band 12-20 Hz is only characterised by banded tremor and obviously background noise, and thus during the episodes of banded tremor the rectilinearity increases because of both the lack of "ordinary" tremor and the less chaotic wavefield of banded tremor than the background noise wavefield. Finally, on the basis of such data, it is not possible to identify the exact wave types constituting the wavefields of "ordinary" and banded tremor.

6.7.3 Tremor source location

Unlike location method used to localize ordinary volcanic tremor (see section 4.5), the banded tremor was localized using methods based on cross-correlation of seismic signal envelopes at different stations (Obara, 2002; Obara and Hirose, 2006). This is justified by the fact that, unlike "ordinary" volcanic tremor, the banded tremor was well recorded only by the nearest stations to the summit area and showed significant and rapid amplitude variations, making it particularly amenable to location via envelope cross-correlation. In this section, source location of both tremor signals, ordinary and banded, are explained. In particular, ordinary volcanic tremor is localized using the approach explained in section 4.5 also used to highlight the geometry of the shallow volcanic plumbing system in section 6.2 and 6.3 For this purpose, signals recorded by 16 stations, belonging to the broadband permanent seismic network and located at distances ranging between 1.5 and 9 km from the centre of the summit area were used considering a 3D grid of 6x6x6 km^3 volume with a spacing between nodes of 250 m. For the tremor source localization here reported, the goodness of the linear regression fit R^2 (details are reported in section 4.5) were achieved with very low α values (equation 4.8), mainly between 0 and 0.02, suggesting high values of ray-path-averaged quality factor Q (equations 4.7. and 4.8). To avoid unstable solutions, a result is accepted only when: i) the goodness of the R^2 fit is ≥ 0.9, and ii) at least 13 stations are available. Three different frequency bands, 1-5, 5-10 and 10-15 Hz, were analysed. The first one comprises both continuous "ordinary" tremor and cyclic occurrence of banded tremor. In this case the tremor sources were located in a volume between the eruptive fissure and the SEC (see figure 34) at altitude

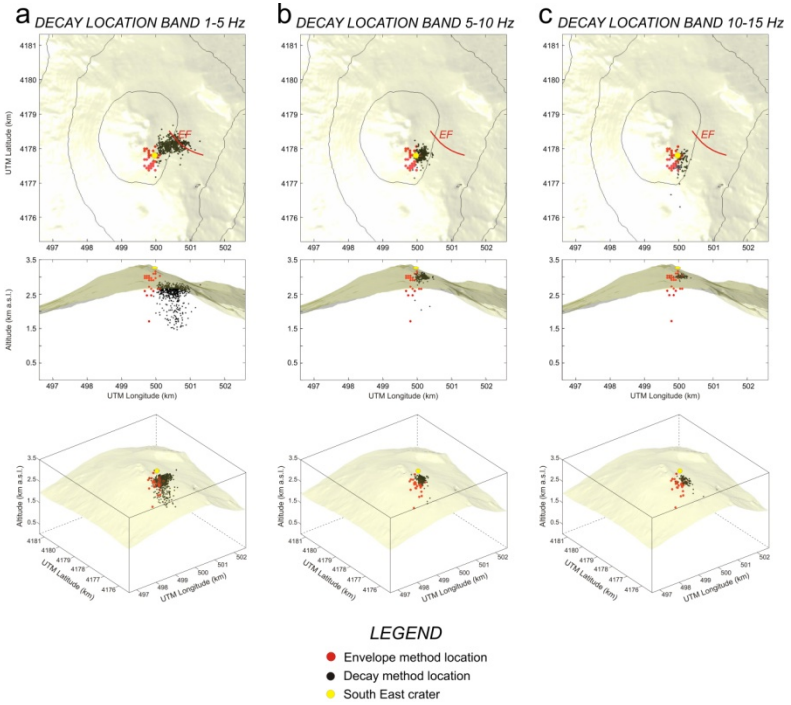

Figure 40: Source locations of tremor obtained by amplitude decay in the frequency bands 1–5 (a), 5–10 (b) and 10–15 (c) Hz on 29 August and 2–3 October, and by the comparison of the seismic signal envelopes during 27 August–3 September and 2–3 October 2008 (see key for details).

of 1.0-2.8 km above sea level (a.s.l.; black dots in figure 40a). It is worth noting that time variations of the source location, consisting of shallowing and westward shifts, were observed at the same time as the occurrence of banded tremor episodes (figure 41). In figure 41 a gradual shallowing of the ordinary tremor source is also evident, which could be related to either a real tremor source shift or the decrease of the noise level during the nocturnal hours. In fact, large variations in noise amplitudes during the daytime, especially evident at the stations located at low alti-

tude, can generate apparent changes in the depth of the tremor source. The seismic signal filtered in the bands 5-10 and especially 10-15 Hz contained a lower contribution of "ordinary" volcanic tremor to advantage of banded tremor than in the band 1-5 Hz. In these cases the source remained fairly stable and was located below SEC at very shallow depth (~3 km a.s.l.; black dots in figures 40b and 40c). Since for the band 10-15 Hz very few tremor locations showed R^2 values greater than 0.9, a minimum R^2 value of 0.85 for that band was fixed. Such low quality of tremor location in this frequency band can be related to the shallowness of the source of the banded tremor and then to the low tremor amplitude at the stations farthest from the summit area, linked to the strong cultural and environmental noise at high frequency at these stations. The method based on the comparison of the seismic signal envelopes was similar to the technique developed to locate the source of the deep non-volcanic tremor in Japan (Obara, 2002; Obara and Hirose, 2006). As a first step, we selected 30 tremor episodes for both investigated periods that were characterised by high seismic energy of banded tremor at the six stations nearest to the summit area (see stations with labels of name in figure 34) and lacked long period (LP) events and explosion-quakes.

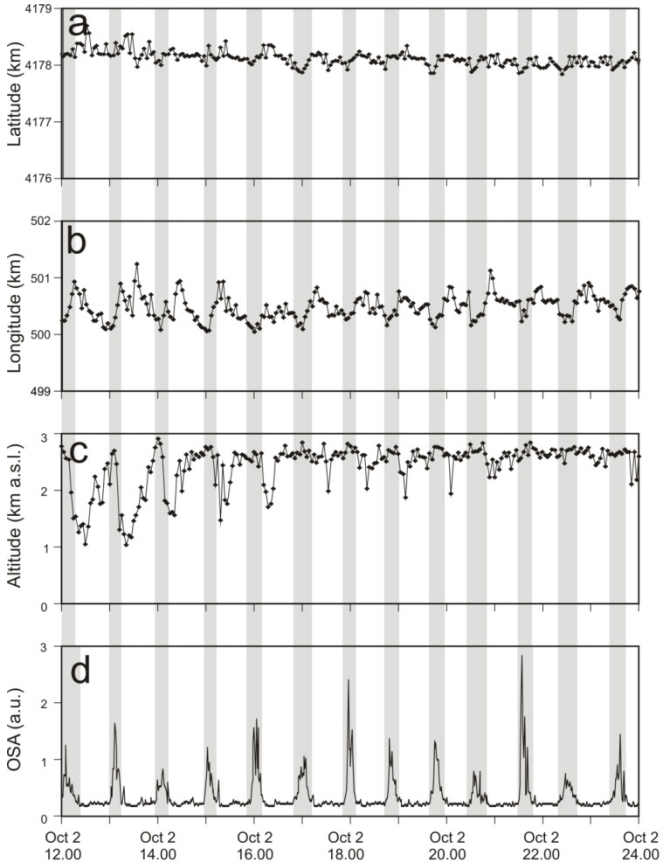

Figure 41: (a, b, c) Time variations of the source location of the tremor filtered in the frequency range 1–5 Hz and (d) OSA time series during the interval 12:00–24:00 on 2 October 2008. The gray areas indicate the time spans with banded tremor episodes.

In fact, the higher amplitude of these transients relative to the tremor generate peaks in the RMS series of all the considered stations, strongly affecting the following time lag calculation. In order to emphasize the banded tremor contribution, the vertical component of the seismic signal recorded during these selected episodes was filtered in the frequency band 12-20 Hz.

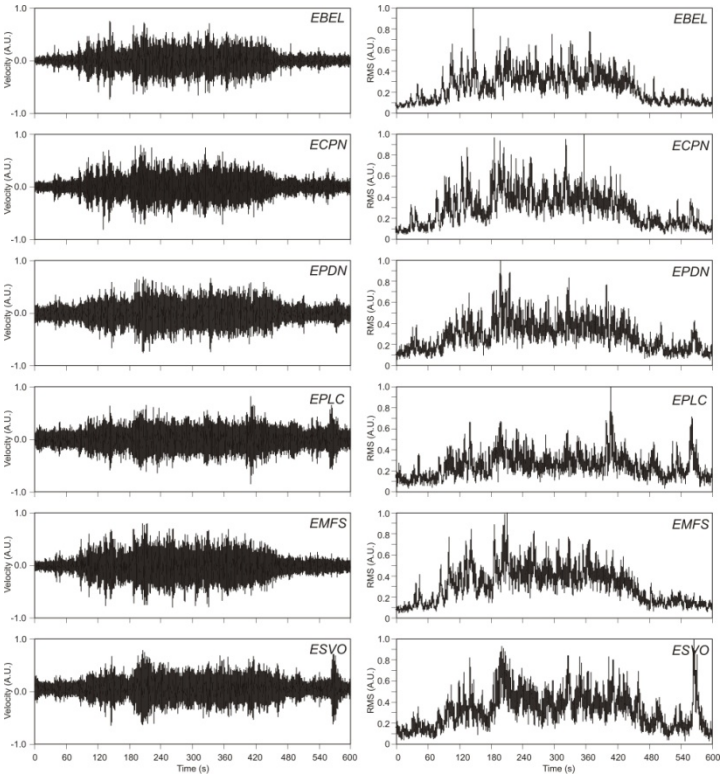

Figure 42: Example of seismic signals and corresponding RMS amplitude time series at the six station used to locate the source of the banded tremor by cross correlation of seismic signal envelopes.

The root mean square (RMS) envelope of the filtered signal was calculated for 0.5-second-long moving windows shifted every 0.01 s (one sample) for all six stations (figure 42). Then a cross-correlation analysis between 10-minute-long RMS time series at all the station pairs, systematically changing the lag between the series, was performed. A time lag Δt_{obs} between station pairs that produced maximum cross correlation coefficients is evaluated. Then, the location of the tremor episodes is computed using a three-dimensional grid of assumed source positions. The grid was centred underneath the craters, had horizontal dimensions of 6 x 6 km, a vertical extent of 3.25 km (from 0 km a.s.l. to the top of the volcano), and an even node spacing of 62.5m. A set of theoretical time lags between the station pairs (Δt_{theor}) was calculated for each node, considering a homogeneous velocity model equal to 1.4 km/s, that was chosen because it allowed minimizing the difference between observed and theoretical time lags. The source location was determined by searching for the node that minimized the difference between observed and theoretical time lags. The location results, consistent with the location obtained by the standard method in the frequency bands 5-10 and 10-15 Hz, showed that the banded tremor sources were shallow and located near to the SEC (red dots in figure 40). It is noteworthy that there is not any significant variations between the first (20 August – 9 September) and second (1-27 October) periods. Very shallow sources of banded tremor were also inferred by Fujita (2008) at Miyakejima volcano.

6.7.4 Comparison between seismic and infrasonic OSA patterns

In order to understand whether the banded tremor source has a connection with the atmosphere, the infrasound signal recorded by EBEL station (figure 34) during the two investigated periods was analysed. This station, located at a distance of about 1.5 km from the centre of the summit area, worked well and showed the best signal to noise ratio during the studied period. The OSA of the infrasonic signal was calculated by the method described in section 6.7.1 In order to exclude the contribution of the infrasonic events of the NEC, generally characterised by spectral content below 2 Hz (Cannata et al., 2009a,b), the frequency band 3-6 Hz was chosen to calculate the OSA series. In order to investigate the relation between the infrasonic and seismic OSA time series, the method proposed in section 6.6 was applied. The mother wavelets used for the analysis is the Morlet wavelet, since it provides a good balance between time and frequency localization as well as information about phase (Grinsted et al., 2004). During the first time interval (20 August – 9 September 2008) there was no significant relation between the infrasonic and seismic time series, whereas an initial portion of the second interval (08:00 on 2 October – 05:00 on 3 October; all times reported in this paper are in UTC), characterised by fairly high OSA values (figure 36f), showed a meaningful relation for periods of about 50-60 minutes (figure 43). This period roughly corresponds to the sum of the duration of a single episode and the time interval between the end of an episode and the onset of the following one. It is worth noting that the phase analysis mainly exhibited a phase difference of about 180° between the two time series, highlighting that increases in the seismic amplitude corresponded

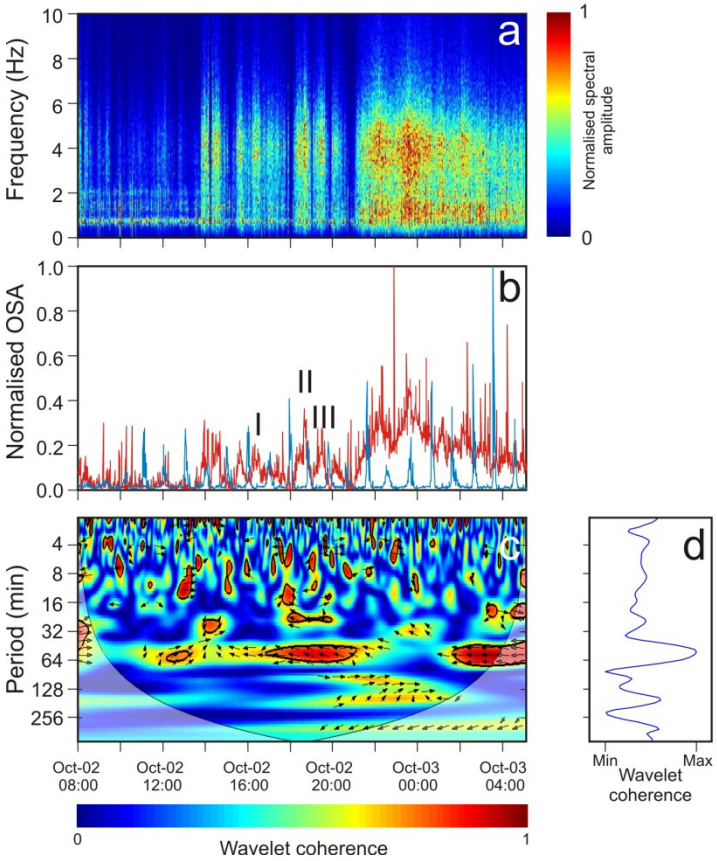

Figure 43: (a) Short Time Fourier Transform (STFT) of the infrasound signal recorded by EBEL station in the period 0800 on 2 October–0500 on 3 October 2008. (b) Normalized OSA values calculated for the seismic (blue line) and infrasonic (red line) signals. (c) Wavelet Transform Coherence (WTC) between the OSA values reported in (b). The thick contour shows the 95% confidence interval and the lighter shade indicates the cone of influence, or the region of the wavelet spectrum affected significantly by edge effects. The relative phase relations are shown with arrows, with in-phase pointing right, anti-phase pointing left, and seismic OSA leading infrasonic OSA by 90° pointing straight down. (d) Stacking of the columns of coherence values reported in (c). The roman numbers (I, II, III) reported in (a) and (b) indicate the amplitude increases of infrasound signal shown in figure 44.

to decreases in the infrasonic amplitude and vice versa. The increases in the infrasonic amplitude were not due to the occurrence of discrete events but to a weak continuous signal (weak infrasonic tremor) in the 3-5 Hz band that lasted for several minutes (figure 44).

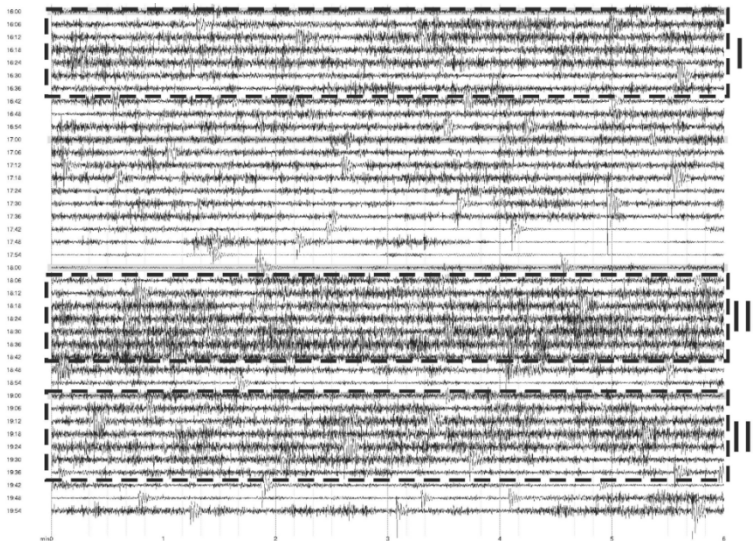

Figure 44: Raw infrasonic signal recorded on 02 October 2008. (I, II, III) indicate the amplitude increases of infrasound signal shown in figure 43b.

6.7.5 Nonlinear analysis of banded tremor

As stated by Kostantinou and Lin (2004), in order to better understand the source mechanisms of seismic signals in volcanic areas, such as volcanic and banded tremor, the assumption that the underlying mechanism requires a linear oscillator that is set into resonance by a sudden sustained disturbance should be reconsidered. Shaw (1992) and Julian (1994) suggested that a nonlinear process of some kind may be involved in tremor generation. Indeed, the attraction of nonlinear models of volcanic tremor is that the harmonic frequencies are not proportional to a geometric length scale as they are in the linear case, which may explain why tremor frequencies are similar at volcanoes of vastly different size (Hagerty and Benites, 2003). Moreover, such nonlinear models are able to produce a large range of complex behaviours for relatively small changes in some control parameters (Hagerty and Benites, 2003). This issue also implies considering new methods of analysis based on the discipline of nonlinear dynamics. Such methods allow studying systems with many degrees of freedom n, not known a priori, which cannot be observed directly. In these cases sets of differential equations are unavailable but only one system parameter is accessible (Faybishenko, 2002). As inferred by Fujita (2008), the banded tremor system is ruled by many parameters that cannot directly be observed and measured. In view of all these considerations, nonlinear time series analysis technique was applied in order to better understand the underlying physical process of the banded tremor. Application of these methods to the geophysical sciences demonstrated that nonlinear models are useful tools for understanding complex phenomena such as seismic signals in volcanic areas and their chaotic behaviour (e.g., Kostantinou and Lin, 2004).

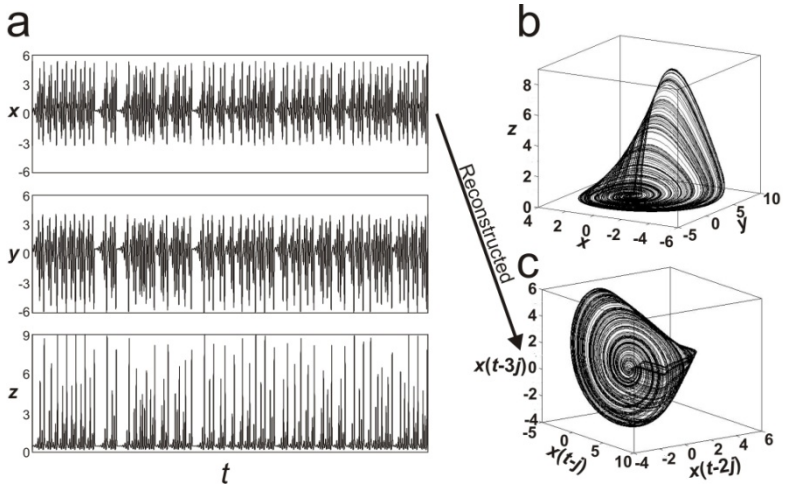

Figure 45: (a) Evolution in time of the state variables x, y and z of the Rossler attractor, (b) Rossler attractor and (c) reconstructed attractor calculated from x state variable. j in (c) is referred to as the delay time.

Classical linear analysis methods based on Fourier transform and linear correlations implicitly assume that the data come from linear systems. This means that the intrinsic dynamics of the system is governed by the linear paradigm: small causes lead to small effects (e.g., Kantz and Schreiber, 1997). From an analytical point of view, small errors in determining initial conditions result in a small error in the prediction of the future behaviour. This behaviour is lost if we consider systems with nonlinear relation among state variables, where small errors in the measurements of initial conditions lead to entirely different outcomes. This phenomenon is called sensitive dependence on initial conditions (e.g., Gao et al., 2007). In this section the nonlinear time series analysis techniques reported in section 2.3 will be applied on a two-day-long window of OSA time series figure 46a. Thus, the single oscillations were not investigated but rather the “macro-dynamics” of the banded tremor activ-

ity was taken into account. The phase space was reconstructed using Cao method (Cao, 1997). An example of phase space reconstruction considering only one state variable is reported in figure 45 where, a synthetic example using Rossler attractor is shown. The values of both parameters $E1(m)$ (equation 2.54) and $E2(m)$ (equation 2.55) versus the embedding dimension m are shown in figure 47 where the kink in the plot suggests a minimum embedding dimension of 4. Both quantities are computed by using a time delay $j = 15$ which is the first minimum in the mutual information function. As aforementioned, the delay time is chosen such that the two time series values x_t and x_{t+j} are dynamically independent and their estimation is needed to reconstruct the phase space. After the reconstructed phase space is defined, the nonlinear nature of the OSA time series was investigated using the surrogate data analysis method (section 2.3.2).

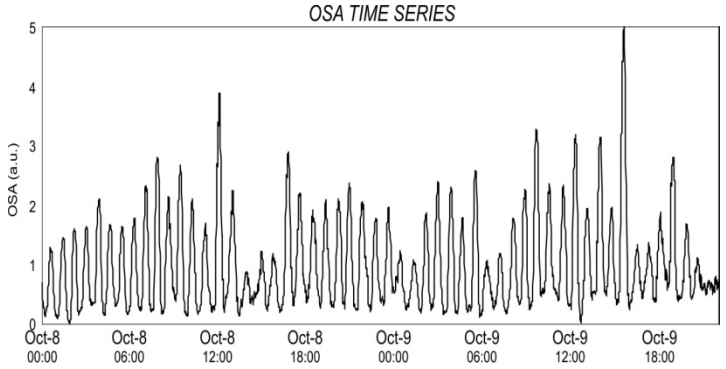

Figure 46: OSA time series window, considered in the nonlinear analysis.

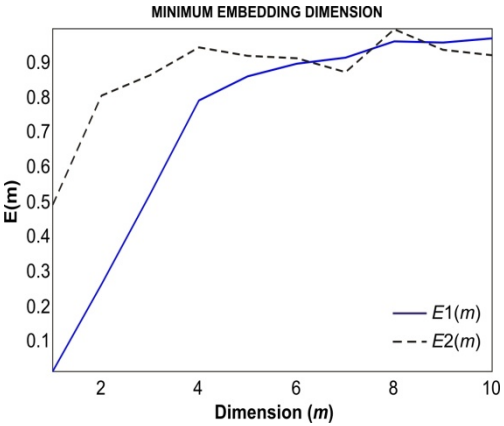

Figure 47: Minimum embedding dimension computed by using Cao's method.

In order to apply this technique 99 surrogate time series are generated using *random phase surrogate approach* that preserves the signal distribution and amplitude spectrum of the original one. As reported in section 2.3.3 a null hypothesis is that the original time series is generated by a Gaussian linear stochastic process (Kanty and Schreiber, 2004) and it is rejected if the associate statistic test is not conform with the null hypothesis. In the light of it, DVV method was applied on both the original and the 99 surrogate time series. When the time series exhibit some kinds of structure and the embedding dimension and time lag are correctly determined, similar delay vectors (in term of Euclidean distance) have similar targets (Kaplan, 1994). As explained in section 2.3.7, in DVV methods the target variance (equation 2.70) conveys information regarding the predictability of the time series. In the *DVV scatter diagram* plotting reported in section 2.3.7, the original time series is judged to be linear if the surrogate and original time series are similar to each other leading to a scatter diagram that coincides with the bisector line. Conversely, when the DVV scatter diagram shows a deviation from the

bisector line, the original time series can be judged nonlinear. The result of DVV analysis, computed on banded tremor OSA time series, is shown in figure 48, where the deviation from bisector line stresses the nonlinear nature of the analyzed series. Once that the nonlinear nature is confirmed, other parameters such as fractal dimension and largest Lyapunov exponent are computed. The selected periods showed values of correlation dimension computed using Takens' estimator (Takens, 1981) of 3.5, an embedding dimension of 4 and a positive Lyapunov exponent, estimated by the slope of the linear segment of prediction error (figure 49), of 0.04.

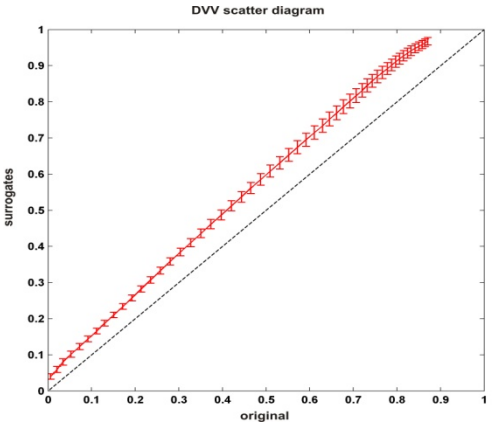

Figure 48: DVV scatter diagram obtained by plotting the target variance of the original banded tremor OSA time series against the mean of the target variance of the 99 surrogate data.

In particular, the embedding dimension *m* is lower than other periods when the banded tremor did not occur. These results can be interpreted as an indication that banded tremor generation is not controlled by a stochastic process, and then it can be described by only a few degrees of freedom. For representation purposes, only three variables are selected for phase space plot shown in figure 50**.** The attractor derived by OSA series of the banded tremor exhibits the characteristics described for a generic strange attractor. Briefly, it is characterised by the following features: i) orbits do not intersect or overlap, suggesting that the system does not return to a previous state and implying a chaotic behaviour; ii) orbits move within a bounded region of the phase space due to dissipation of energy in the system; iii) orbits that are initially close diverge exponentially from each other due to sensitivity to initial conditions.

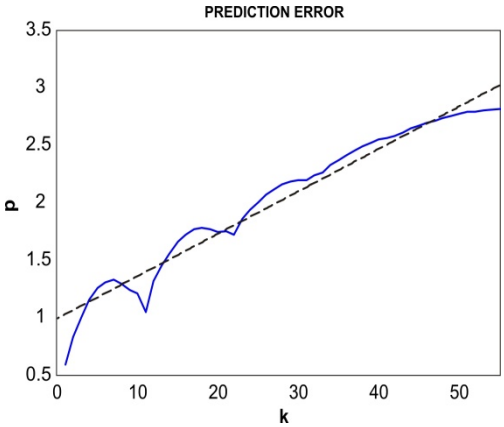

Figure 49: prediction error for the considered time series. The black dashed line indicates the regression line.

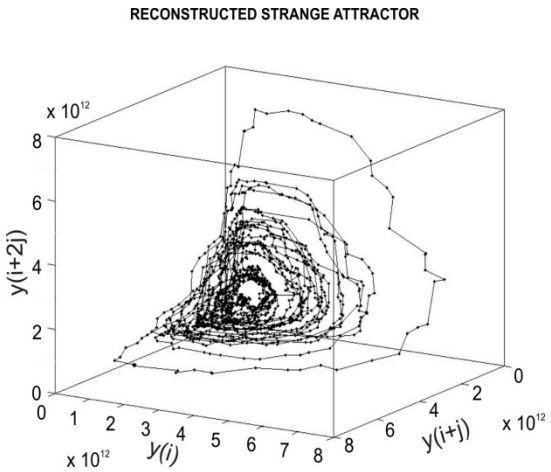

Figure 50: 3D phase portrait of the strange attractor, obtained for the OSA time series window shown in figure 46. y(i) indicates the OSA time series reported and *j* is referred to as the delay time.

6.7.6 Banded tremor qualitative model

In light of all the analyses shown in the previous sections, the following model, consisting in alternating recharge-discharge phases, can be proposed for the studied banded tremor activity (figure 51). The banded tremor episodes are likely due to "perturbations" in shallow aquifers, such as fluid movement and bubble growth or collapse due to hydrothermal boiling, triggered by the heat and hot fluid transfer from the underlying magma bodies. The presence of magma below the summit area is suggested by ground deformation data (Aloisi et al., 2009) and volcanic tremor source locations (Di Grazia et al., 2009), indicating that the 2008-2009 eruption was fed by an intrusion following the path of the central conduit in the first part of the intrusion (below 1.5-2.0 km a.s.l.) and then breaking off towards the east in the last shallow part. The perturbations

of the shallow aquifers can cause resonance and oscillations of fluid-filled cracks. The heat transfer also causes an increasing pressure in the aquifer, that leads to fluid-discharge. During this process, the increased fraction of steam increases the acoustic impedance between the aquifer and the surrounding rocks, thus causing a drastic decrease of the seismic radiation. On the other hand, if these "eruptions" are well coupled with the atmosphere, acoustic signals are produced, otherwise no acoustic signal can be detected. Phenomena of time-coupling between infrasound tremor and gas emission have been noted at different volcanoes, including Tungurahua (Ruiz and Arenallo, 2008), Kilauea (Fee and Garces, 2008) and Sakurajima (Morrissey et al., 2008). Since an increases in infrasound activity was detected only during a short time span of the investigated periods, a time modification of the source, such as a slight depth change, can be inferred. Other phenomena that can prevent the acoustic emission in the atmosphere are self-sealing and clogging of fractures because of circulation of hydrothermal fluids, common processes in fumarolic systems (e.g., Harris and Maciejewski, 2000). Once the level of hot fluids within the aquifer has sufficiently decreased, the discharge stops. Since the banded tremor activity maintains its features for long periods (tens of days), it is reasonable to assume a phenomenon of supply of fluids from shallower or deeper levels. Unfortunately, because of the lack of meteorological data acquired in the summit area of the volcano, an eventual relations between rainfall or atmospheric temperature/pressure and the onset or end of the banded tremor cannot be investigated. On the basis of this banded tremor source model, it is possible to infer that there were no direct links between the banded tremor activity and the eruption at EF (figure 51). Another interesting observation was the different

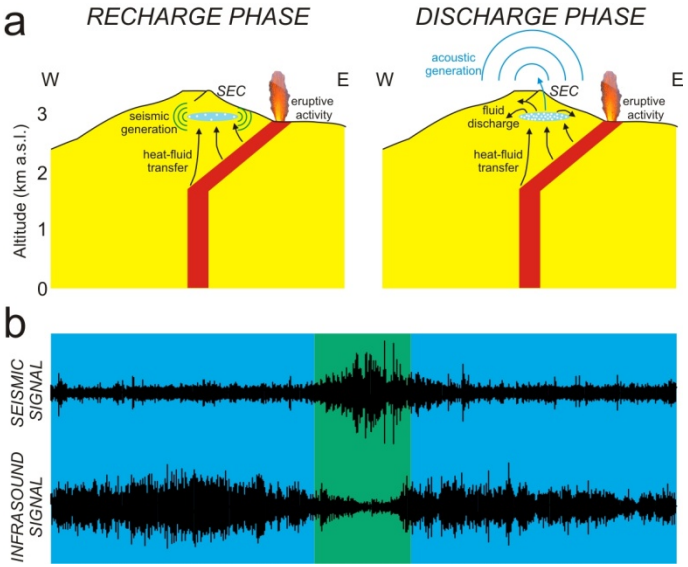

Figure 51: (a) Cartoon showing the proposed model of generation of banded tremor during alternating phases of recharge and discharge (see text for details). (b) Examples of seismic and infrasound signals during phases of discharge (blue area) and recharge (green area).

behaviour of banded tremor during the two analysed periods in terms of duration of the episodes, average amplitude of OSA and spectral content of the radiated seismic signal (figures 36,37). In particular, the second period (October 2008) was characterised by longer episode duration, higher average amplitude and greater energy at high frequency than the first period (August-September 2008). The first two changes can be connected to each other. Indeed, similarly to geysers, if the time to resaturate the system with fluids increases, eruptions become less frequent and larger (Ingebritsen and Rojstaczer, 1996). A larger eruption could reasonably imply more energetic seismic radiation. Further, on the basis of the aforementioned tremor source model, the different spectral content

during the two analysed periods could be due to either different size/geometry of the resonating cracks or physical–chemical features of the fluid within it. For instance, considering a crack containing bubbly water and assume that geometry, size and fluid chemical composition remain steady, a simple increase in temperature and/or pressure is enough to generate seismic energy with higher frequency (e.g., Kumagai and Chouet, 2000). The nonlinear analysis performed on OSA time series in section 6.7.5 showed that banded tremor has a chaotic behaviour. Since it was shown that both mass flow rate and eruption interval data of a geyser have a chaotic behaviour (Ingebritsen and Rojstaczer, 1996; Nicholl et al., 1994), the close similarity between banded tremor and geyser systems is further supported. The chaotic behaviour firstly implies a sensitive dependence on initial conditions. Therefore, this means that not only does banded tremor require particular conditions to generate, but also that slight variations of these conditions are able to greatly change the features of the banded tremor or even to stop it. Some of the conditions/factors controlling the system generating banded tremor and its features are system geometry, quantity of water and heating rate (Fujita, 2008). Rock properties, such as permeability and porosity, have also been found to strongly affect geyser systems (Ingebritsen and Rojstaczer, 1993; 1996), and then presumably also greatly the features of the banded tremor. Even very small variations in any of these factors can modify the system and consequently the characteristics of the banded tremor or to stop it. Such sensitivity is testified for geysers by many external events able to modulate their activity, such as earthquakes (Husen et al., al., 2004) and precipitations (Hurwitz et al., 2008). In addition to the sensitive dependence on initial conditions, which Lorenz has called “butterfly effect”, there are several other features that must be present in systems that exhibit chaotic behaviour (Faybishenko, 2002), and thus also in

banded tremor systems: i) the system is dissipative and the motion irreversible, as in systems with friction or those exchanging energy with external media; ii) intrinsic properties of the systems, not random external factors, are the cause of chaotic behaviour; iii) the chaotic nature also implies the severely limited predictability of future behaviour, regardless of how much data is collected.

Chapter 7

Conclusions

This thesis presents a study of different types of seismic and infrasonic signals recorded at Mt. Etna and their relation to different kind of volcano activity. The study of seismic and infrasound signals using the techniques described in the first 4 chapters, turned out to be a very powerful tool to investigate the volcano dynamics. The infrasound signals can be helpful to investigate the volcanic processes occurring in the vents (e.g. Ripepe et al., 1996; 2001a), that can be considered as the shallowest parts of the volcano plumbing systems. As shown for Mt. Etna, the study of infrasound, reported in chapter 5, allows to discriminate different kinds of source processes, such as strombolian bubble (Vergniolle and Brandeis, 1994), Helmholtz resonator (Vergniolle and Caplan-Auerbach, 2004) or resonance of fluids in a conduit (Garces and McNutt, 1997).

The LP and VLP events analysis at Mt. Etna allows to investigate the portions of plumbing systems characterised by fluid movements (e.g. Chouet, 1996a; Almendros et al., 2002). Moreover, the analysis of these signals can reveal time variations of the composition of magmatic fluids filling the resonant structures inside volcanoes (e.g. Kumagai, 2006; Patanè et al., 2008). In particular, the extensive application of time-frequency analysis highlighted time variations of frequency and quality factor of seismo-volcanic events observed before and after the three lava fountains analyzed in chapter 6. Such variations were interpreted as fast

uprise and discharge of gas-rich magma. An important result regards the variations of the polarization parameters before the onset of the lava fountains. As explained in chapter 6, polarizations parameters are related to changes in wavefield due to tremor source changes (e.g. in its location and/or in its physical characteristics) and provide a very clear precursor before the onset of lava fountain. Another novel technique reported in this study is the multi channel coherence. In particular, the coherence among summit stations showed possible recharge phenomena of the magmatic system, while the coherence analysis between seismic and infrasound signals turned out to be a suitable approach for summit volcano activity detection. In this last case, a multi-scale approach using wavelet transform was applied.

All results presented in this thesis have shown, for the first time at Mt. Etna, how the seismo-volcanic together with infrasound signals are a useful tool for real-time volcano monitoring. These signals, integrated with geodetic observations, may be useful to forecast eruptions that, like the summit effusive or explosive eruptions, apparently do not show clear precursor signals. While detection of waveform variations of LP and VLP events turned out to be very effective to follow movements of batches of gas-rich magma inside the volcano, the infrasound signals allowed locating explosive activity in space and time and estimating its intensity. For this purpose, the infrasound monitoring system described in chapter 5 is routinely applied to track Mt. Etna summit activity. Moreover, a novel approach based on pattern recognition techniques (e.g. density clustering approach and SVM classification) is able to localize different kinds of signals using only one reference station. This method is very useful to monitor explosive activity at Mt. Etna especially during the winter season when because of the bad weather conditions most of the infrasonic sensors do not operate and then the standard location

algorithm cannot be applied. All the studies here reported show how volcanic activity is an high nonstationary process and, in some cases, may evolve in a chaotic manner. One of the best example is the banded tremor phenomenon treated in chapter 6, that reveals an hypothetical geyser-like system located near the summit area. The dynamics of this process shows that a hydrothermal system can modulate the tremor signal recorded using the seismic stations. This system, similarly to volcanic tremor processes, exhibits high sensitivity to initial and boundary conditions, leading to a chaos theory interpretation of the underlying generating system.

References

Abarbanel, H.D.I., Brown, R., Sidorowich, J.J. and Tsimring, L. Sh. (1993), The analysis of observed chaotic data in physical system, Rev. Mod. Phys., 65, 1331.

Abarbanel, H.D.I., (1996), Analysis of observed chaotic data, Springer, New York.

Aki, K., Fehler, M., and Das, S. (1977), Source mechanism of volcanic tremors: Fluid driven crack models and their application to the 1963 Kilauea eruption, J. Volcanol. Geotherm. Res. 2, 259–287.

Aldridge, M., (2006), Clustering an overview, in "Lecture Notes in Data Mining", Berry M.W., and Browne, M. eds., pp. 99-107, World Scientific.

Alessandrini, B., Cattaneo, M., Demartin, M., Gasperini, M., Lanza, V., 1994. A simple P-wave polarization analysis: Its application to earthquake location. Ann. Geophys. 5, pp. 883–897.

Allard, P., B. Behncke, S. D'Amico, M. Neri, and S. Gambino (2006), Mount Etna 1993–2005: Anatomy of an evolving eruptive cycle, Earth Sci. Rev., 78, 85–114, doi:10.1016/ j.earscirev.2006.04.002.

Allen, M. R. and Smith, L. A. (1996), Monte Carlo SSA: Detecting irregular oscillations in the presence of coloured noise, J. Clim., 9, pp. 3373–3404.

Almendros, J., B. Chouet, P. Dawson, and T. Bond (2002a), Identifying elements of the plumbing system beneath Kilauea Volcano, Hawaii, from the source locations of verylong-period signals, Geophys. J. Int., 148, 303 –312, doi:10.1046/j.1365-246X.2002.01629.x.

Almendros, J. B., B. Chouet, P. Dawson, and C. Huber (2002b), Mapping the sources of the seismic wavefield at Kilauea volcano, Hawaii, using data recorded on multiple seismic antennas, Bull. Seismol. Soc. Am., 92, 2333–2351, doi:10.1785/0120020037.

Almendros, J. and Chouet, B. (2003), Performance of the radial semblance method for the location of very long-period volcanic signals, Bull. Seismol. Soc. Am. 93, 1890–1903.

Aloisi, M., A. Bonaccorso, F. Cannavò, S. Gambino, M. Mattia, G. Puglisi, and E. Boschi (2009), A new dyke intrusion style for the Mount Etna May 2008 eruption modelled through continuous tilt and GPS data, *Terra Nova*, *21*, 316–321.

Alparone, S., Cannata, A., Gresta, S. (2007). Time variation of spectral and wavefield features of volcanic tremor at Mt. Etna (January–June 1999). J. Volcanol. Geotherm. Res. doi:10.1016/j.jvolgeores.2006.12.012.

Anderberg, M. R. (1973), Cluster Analysis for Applications, Academic Press, Inc., New York, NY.

Andronico, D., Cristaldi, A., Lo Castro, D., Scollo, S., and Taddeucci J. (2007), The 24 November 2006 paroxysm at south-east crater, Mt. Etna, paper presented at XXIV General Assembly, Int. Union of Geodesy and Geophys., Perugia, Italy.

Andronico, D., Scollo, S., Caruso, S., and Cristaldi, A. (2008a), The 2002–03 Etna explosive activity: Tephra dispersal and features of the deposits, J. Geophys. Res., 113, B04209, doi:10.1029/2007JB005126.

Andronico, D., Cristaldi, A., and Scollo, S. (2008b), The 4–5 September 2007 lava fountain at South–East Crater of Mt Etna, Italy, J. Volcanol. Geotherm. Res., 173, 325–328, doi:10.1016/ j.jvolgeores.2008.02.004.

Arrowsmith, S., Revelle, D., Edwards, W., and Brown, P. (2008), Global detection of infrasonic signals from three large bolides, Earth Moon Planet 102, 357–363.

Assink, J.D., Evers, L.G.,Holleman, I., and Paulssen, H. (2008), Characterization of infrasound from lightning, Geophys. Res. Lett. 35, L15802, doi:10.1029/2008GL034193.

Baeza-Yates, R. A. (1992), Introduction to data structures and algorithms related to information retrieval, In Information Retrieval: Data Structures and Algorithms, W. B. Frakes and R. Baeza-Yates, Eds., Prentice-Hall, Inc., Upper Saddle River, NJ, pp. 13–27.

Bame, D.A. and M.C. Fehler (1986), Observations of long-period earthquakes hydraulic fracturing, Geophys. Res. Lett., 13, pp. 149-152.

Baptie, B., and G. Thompson (2003), Post-collapse banded tremor at the Soufriere Hills volcano, Monserrat, West Indies, Geophys. Res. Abstr., *5*, 13276.

Barker, S.R., D.R. Sherrod, M. Lisowski, C. Heliker, J.S. Nakata (2003), Correlation between lava-pond drainback, seismicity and ground deformation at Pu'u O'o, U.S. Geol. Surv. Prof. Pap., 1676, pp. 53-62.

Bartosch T., and Seidl, D. (1999), Spectrogram analysis of selected tremor signals using short-time Fourier transform and continuous wavelet transform. Ann. Geofis, 42, pp. 497–506.

Battaglia, J., and K. Aki (2003), Location of seismic events and eruptive fissures on the Piton de la Fournaise volcano using seismic amplitudes, J. Geophys. Res., 108, doi:10.1029/2002 JB002193.

Battaglia, J., K. Aki, and V. Ferrazzini (2005), Location of tremor sources and estimation of lava output using tremor source amplitude on the Piton de la Fournaise volcano: 1. Location of tremor sources, J. Volcanol. Geotherm. Res., 147, pp. 268–290, doi:10.1016/j.jvolgeores.2005.04.005.

Bean, C., I. Lokmer, and G. O'Brien (2008), Influence of nearsurface volcanic structure on long-period seismic signals and on moment tensor inversions: Simulated examples from Mount Etna, J. Geophys. Res., 113, B08308, doi:10.1029/2007JB00 5468.

Behncke, B. and Neri, M. (2003), Cycles and trends in the recent eruptive behaviour of Mount Etna (Italy), Can. J. Earth Sci. 40, pp. 1405–1411.

Belousov, A.I., Verzakov, S.A., Von Frese, J. (2002), Applicational aspects of support vector machines, J. Chemom., 16, pp. 482–489.

Benítez, C., Ramírez, J., Segura, J.C., Ibáñez, J.M., Almendros, J., García-Yeguas, A., and Cortés, G. (2007), Continuous HMM-based seismic event classification at deception Island, Antarctica, IEEE Transactions on Geoscience and Remote Sensing, 45, pp. 138-146, doi: 10.1109/TGRS.2006.882264.

Benesty, J., Chen, J., Huang, Y. (2005), A generalized MVDR spectrum, IEEE Signal Processing Lett, 12, pp. 827–830.

Benhama, A., Cliet, C., and Dubeseet, M. (1988), Study and application of spatial directional filtering in three component recordings, Geophysical Prospecting, 36, pp. 591-613.

Benoit, J., McNutt, S.R., 1997. New constraints on the source processes of volcanic tremor at Arenal volcano, Costa Rica, using broadband seismic data. Geophys. Res. Lett. 24, pp. 449-452.

Berge, P., Pomeau, Y., and Vidal, C. (1984), Order within Chaos: Towards a Deterministic Approach to Turbolence. Hermann.

Berkhin P.(2002), Survey Of Clustering Data Mining Techniques. Accrue Software: San Jose, CA.

Bertagnini, A., Coltelli, M., Landi, P., Pompilio, M., and Rosi, M. (1999), Violent explosions yield new insights into dynamics of Stromboli volcano, EOS 80, pp. 633–636.

Bonaccorso, A., and P. M. Davis (2004), Modeling of ground deformation associated with recent lateral eruptions: Mechanics of magma ascent and intermediate storage at Mt. Etna, in Mt. Etna: Volcano Laboratory, Geophys. Monogr. Ser., vol. 143, edited by A. Bonaccorso et al., pp. 293–306, AGU, Washington, D. C.

Brandsdòttir, B., Einarsson, P. (1992), Volcanic tremor and low-frequency earthquakes in Iceland, In: Gasparini, P., Scarpa, R., Aki, K. (Eds.), Volcano Seismology. IAVCEI Proc. Volcanol. 2, pp. 212-222.

Buckingham, M.J. and Garces, M.A. (1996), A canonical model of volcano acoustics, J. Geophys. Res. 101, 8129–8151.

Burges, C. J. C. (1998), A tutorial on support vector machines for pattern recognition, Data Mining and Knowledge Discovery, 2:121–167.

Cannata, A., Catania, A., Alparone, S., and Gresta, S. (2008), Volcanic tremor at Mt. Etna: Inferences on magma dynamics during effusive and explosive activity, J. Volcanol. Geotherm. Res., doi:10.1016/j.jvolgeores.2007.11.027.

Cannata, A., Montalto, P., Privitera, E., Russo, G., and Gresta, S. (2009a), Tracking eruptive phenomena by infrasound: May 13, 2008 eruption at Mt. Etna, Geophys. Res. Lett., doi:10.1029/2008GL036738.

Cannata, A., Montalto, P., Privitera, E., and Russo, G. (2009b), Characterization and location of infrasonic sources in active volcanoes: Mt. Etna, September-November 2007, J. Geophys. Res. 114, B08308, doi:10.1029/2008JB006007.

Cannata, A., Hellweg, M., Di Grazia, G., Ford, S., Alparone, S., Gresta, S., Montalto, P., and Patanè`, D. (2009c), Long-period and very long-period events at Mt. Etna volcano: Characteristics, variability and causality, and implications for their sources. J. Volcanol. Geothherm. Res., doi:10.1016/j.jvolgeores.2009.09.007.

Cannata, A., Giudice, G., Gurrieri, S., Montalto, P., Alparone, S., Di Grazia, G., Favara, R., Gresta, S. (2010). Relationship between soil CO2 flux and volcanic tremor at Mt. Etna: implications for magma dynamics. Environmental Earth Science doi:10.1007/s12665-009-0359-z.

Cannata, A., Di Grazia, G., Montalto, P., Ferrari, F., Nunnari, G., Patanè, D., and Privitera, E. (2010), New insights into 27 banded tremor from the 2008–2009 Mount Etna eruption, J. Geophys. Res., 115, doi:10.1029/2009JB007120.

Cao, L. (1997), Practical method for determining the minimum embedding dimension of a scalar time series, Physica D., 110, pp. 43-50.

Capon, J. (1969), High-resolution frequency-wavenumber spectrum analysis, Proceedings of the IEEE, 57, pp. 1408-1418.

Carniel, R., E. Del Pin, R. Budai, and P. Pascolo (2005), Identifying timescales and possible precursors of the awake to asleep transition in EOG time series, Chaos Solit. Fract., 23, pp. 1259-1266.

Casdagli, M. (1991), Chaos and deterministic versus stochastic non-linear modeling. J. R. Stat. Soc. B 54, pp. 303–328.

Caviness, J.N., Adler, C.H., Sabbagh, M.N., Connor, D.J., Hernandez, J.L., Lagerlund, T.D. (2003), Abnormal corticomuscular coherence is associated with the small amplitude cortical myoclonus in Parkinson's disease, Mov Disord.,18, pp. 1157-62.

Chatfield, C. (1989), The Analysis of Time Series: An Introduction. 4th Ed. Chapman and Hall, 241 pp.

Chouet, B.A., Julian, B.R. (1985), Dynamic of an expanding fluid-filled crack. J. Geophys. Res. 90, pp. 11187-11198.

Chouet, B. (1996a), Long-Period volcano seismicity: Its source and use in eruption forecasting, Nature, 380, 309–316, doi: 10.1038/380309a0.

Chouet, B. (1996b), New methods and future trends in seismological volcano monitoring, In "Monitoring and mitigation of volcano hazards" (Scarpa, Tilling Eds.), Springer, New York, pp. 23–97.

Chouet, B. (2003), Volcano seismology, Pure Appl. Geophys., 160, pp. 739–788, doi:10.1007/PL00012556.

Cocina, O., G. Barberi, and D. Patanè (2008), The Mt Etna 2001 – 2003 eruptive period: The seismological point of view, paper presented at General Assembly, Int. Assoc. of Volcanol. and Chem. of the Earth's Int., Reykjavik.

Corsaro, R.A. (2008), Rapporto settimanale sull'attivita` eruttiva dell'Etna (11–17 febbraio 2008) (in Italian), volcanological report, Ist. Naz. di Geofis. e Vulcanol., Catania, Italy, (available at http://www.ct.ingv.it/Report/WKRVGREP20080217.pdf).

Cosentino M., Lombardo G., and Privitera, E. (1989), A model for internal dynamical processes on Mt. Etna, Geophys. J., 97, pp. 367–379, DOI: 10.1111/j.1365-246X.1989.tb00508.x.

Cristianini, N., Shawe-Taylor, J. (2000), An Introduction to Support Vector Machines, Cambridge University Press, Cambridge.

Cristofolini, R., S. Gresta, S. Imposa, and G. Patanè (1988), Feeding mechanism of eruptive activity at Mt. Etna based on seismological and petrological data, in Modelling of Volcanic Process, edited by C. Y. King and R. Scarpa, pp. 73– 93, Springer, Berlin.

Daubechies, I., (1990), The wavelet transform time-frequency localization and signal analysis. IEEE Trans. Inform. Theory, 36**,** pp. 961–1004.

Daubechies, I., (1992), Ten Lectures on Wavelets. Society for Industrial and Applied Mathematics, 357 pp.

Davies, D.L., Bouldin, D.W., (1979), IEEE Transaction on Pattern Analysis and Machine Intelligence PAMI-1.

Dawson, P.B., Chouet, B.A., Okubo, P.G., Villasen, O.R., Benz, H.M. (1999), Threedimensional Velocity Structure of Kilauea Caldera, Hawaii. Geophys. Res. Lett., 26, pp. 2805-2808.

De Angelis, S. and McNutt, S.R. (2007), Observations of volcanic tremor during the January–February 2005 eruption of Mt. Veniaminof, Alaska, Bull. Volcanol. 69, pp. 927–940.

De Gori, P., C. Chiarabba, and D. Patanè (2005), Qp structure of Mt. Etna: Constraints for the physics of the plumbing system, J. Geophys. Res., 110, doi:10.1029/2003JB002875.

Del Carlo, P., L. Vezzosi, and M. Coltelli (2004), Last 100 ka tephrostratigraphic record of Mount Etna, in Mt. Etna: Volcano Laboratory, Geophys. Monogr. Ser., vol. 143, edited by A. Bonaccorso et al., pp. 77–89, AGU, Washington, D. C.

Del Pezzo, E., Esposito, A., Giudicepietro, F., Marinaro, M., Martini, M., and Scarpetta S. (2003), Discrimination of earthquakes and under water explosions using neural networks, Bull. Seismol. Soc. Amer., 93, pp. 215-223.

Devos O., Ruckebusch C., Durand A., Duponchel L., Huvenne J. P., (2009), Support vector machines (SVM) in near infrared (NIR) spectroscopy: Focus on parameters optimization and model interpretation, . Phys. Chem. B, Vol. 113, pp 6031 – 6040.

Diday, E., and Simon, J. C. (1976), Clustering analysis, In Digital Pattern Recognition, K. S. Fu, Ed. Springer-Verlag, Secaucus, NJ, pp. 47–94.

Di Grazia, G., S. Falsaperla, and H. Langer (2006), Volcanic tremor location during the 2004 Mount Etna lava effusion, Geophys. Res. Lett., 33, L04304, doi:10.1029/2005GL025177.

Di Grazia, G., Cannata, A., Montalto, P., Patanè , D., Privitera, E., Zuccarello, L., and Boschi, E. (2009), A new approach to volcano monitoring based on 4D analyses of seismo-volcanic and acoustic signals: the 2008 Mt. Etna eruption, Geophys. Res. Lett. 36, doi:10.1029/2009GL039567.

Drazin, P. G. (1994), Nonlinear Systems, Cambridge University Press, New York.

Dubes, R., Jain, A.K., (1976), Clustering techniques: the user's dilemma. Pattern Recognition 8, pp. 247-260.

Dubes, R. C. (1993), Cluster analysis and related issues. In Handbook of Pattern Recognition & Computer Vision, C. H. Chen, L. F. Pau, and P. S. P. Wang, Eds., World Scientific Publishing Co., Inc., River Edge, NJ, pp. 3–32.

Duda, R.O. and Hart P. E. (1973), Pattern Classification and Scene Analysis, New Yourk: John Wiley & Sons.

Dunham, M. (2003), Data Mining: Introductory and Advanced Topics, Prentice Hall, Upper Saddle River, NJ.

Dvorak, J.J., Okamura, A.T. (1985), Variations in tilt rate and harmonic tremor amplitude during the January-August 1983 East Rift eruptions of Kilauea volcano, Hawaii. J. Volcanol. Geotherm. Res. 25, pp. 249-258.

Eckmann, J.P., and Ruelle, D. (1992), Fundamental limitations for estimating dimensions and Lyapunov exponents in dynamical systems, Physica D, 56, pp. 185–187.

Efron, B. (1982), The Jackknife, the Bootstrap and Other Resampling, Soc. for Ind. and Appl. Math, Philadelphia, Pa.

Ereditato, D., Luongo, G. (1994), Volcanic tremor wavefield during quiescent and eruptive activity at Mt. Etna (Sicily), J. Volcanol. Geotherm. Res. 61, pp. 239-251.

Evers, L.G., and Haak, H.W. (2005), The detectability of infrasound in The Netherlands from the Italian volcano Mt. Etna, J. Atmosph. Sol. Terr. Phys. 67, pp. 259–268.

Falsaperla, S., E. Privitera, B. Chouet, and P. Dawson (2002), Analysis of long-period events recorded at Mt. Etna (Italy) in 1992, and their relationship to eruptive activity. J. Volcanol. Geotherm. Res., 114, pp. 419-440.

Falsaperla, S., S. Alparone, S. D'Amico, G. Di Grazia, F. Ferrari, H. Langer, T. Sgroi, and S. Spampinato (2005), Volcanic tremor at Mt. Etna, Italy, preceding and accompanying the eruption of July–August, 2001, Pageoph, 162, pp. 1–22.

Farge, M. (1992), Wavelet transforms and their applications to turbulence, Annu. Rev. Fluid Mech., 24, pp. 395–457.

Faybishenko, B. (2002), Chaotic dynamics in flow through unsaturated fractured media, Advances in Water Resources, 25, pp. 793–816.

Fee, D., and M. Garces (2008), Infrasonic observations of explosions and degassing at Kilauea summit, American Geophysical Union, Fall Meeting 2008, V34A-02.

Fell, J. , Roschke, J., and Schäffner, C. (1996), Surrogate data analysis of sleep electroencephalograms reveals for nonlinearity, Biol. Cybern., 75, pp. 85–92.

Ferrazzini, V., Aki, K. (1992), Preliminary results from a field experiment on volcanic events at Kilauea using an array of digital seismograph. In: Gasparini, P., Scarpa, R., Aki, K. (Eds.), Volcano Seismology. IAVCEI Proc. Volcanol. 3, pp. 168-189.

Ferrick, M.G., Qamar, A., and Lawrence, W.F. (1982), Source mechanism of volcanic tremor, J. Geophys. Res., 87, pp. 8675–8683.

Ferrucci, F., Godano, C., Pino, N.A. (1990), Approach to the volcanic tremor by covariance analysis: application to the 1989 eruption of Mt Etna (Sicily), Geophys. Res. Lett., 17, pp. 2425-2428.

Finch, R.H. (1949). Volcanic tremor (Part I). Bull. Seis. Soc. Am., 39, pp. 73-78.

Firstov, P.P. and Kravchenko, N.M. (1996), Estimation of theamount of explosive gas released in volcanic eruptions using air waves, Volcanol. Seismol. 17, 547–560.

Francis, P.W., Wadge, G., Mouginis-Mark, P.J. (1996), Satellite monitoring of volcanoes, In Monitoring and mitigation of volcano hazards (Scarpa, Tilling Eds.), pp. 253-296.

Fraser, A. M. and H. L. Swinney (1986), Independent Coordinates for Strange Attractors from Mutual Information, Phys. Rev. A, 87, pp. 1134-1140.

Fu, K. S. and Lu, S. Y. (1977), A clustering procedure for syntactic patterns, IEEE Trans. Syst. Man Cybern., 7, pp. 734–742.

Fujita, E. (2008), Banded tremor at Miyakejima volcano, Japan: implication for two-phase flow instability. J. Geophys. Res., 113, doi:10.1029/2006JB004829.

Fukao, Y. & Suda, N. (1989), Core modes of the Earth's free oscillations and structure of the inner core, Geophys. Res. Lett., 16, pp. 401-404.

Fukunaga K., Introduction to statistical pattern recognition (2nd ed), Academic Press, Boston 1990.

Furumoto, M., K. Takahiri, H. Inoue, I. Yamada, K. Yamaoka, A. Ikami, and Y. Fukao (1990), Twin sources of high-frequency volcanic tremor of Izu-Oshima volcano, Japan, Geophys. Res. Lett., 17, pp. 25–27, doi:10.1029/GL017i001p00025.

Gao, J., Y. Cao, W. Tung, and J. Hu (2007), Multiscale Analysis of Complex Time Series: Integration of Chaos and Random Fractal Theory, and Beyond, Wiley.

Garces, M.A. and McNutt, S.R. (1997), Theory of the airborne sound field generated in a resonant magma conduit, J. Volcanol. Geotherm. Res., 78, pp. 155–178.

Garces, M., Harris, A., Hetzer, C., Johnson, J., Rowland, S., Marchetti, E., and Okubo, P. (2003), Infrasonic tremor observed at Kilauea Volcano, Hawaii, Geophys. Res. Lett., 30, doi: 10.1029/2003GL018038.

Gautama, T., Mandic, D. & Van Hulle, M. (2003), Signal nonlinearity in fMRI: a comparison between BOLD and MION, IEEE Trans. Med. Imaging, 22, pp. 636–644, doi:10.1109/TMI.2003.812248.

Gautama, T., Mandic, D.P., and Van Hulle, M. M. (2004), The delay vector variance method for detecting determinism and nonlinearity in time series, Physica D, 190, pp. 167-176.

Ge, Z., (2007), Significance tests for the wavelet power and the wavelet power spectrum, Annales Geophyisicae, 25, pp. 2259–2269.

Ge. Z., (2008), Significance tests for the wavelet cross spectrum and wavelet linear coherence, Annales Geophysicae, 26, 12, pp. 3819-3829.

Geller, R. J., and C. S. Mueller (1980), Four similar earthquakes in central California, Geophys. Res. Lett., 7, 821-824, doi:10.1029/ GL007i010p00821.

Gershenfeld, N. (2006) The nature of mathematical modelling. (Cambridge, UK: Cambridge University Press), 6th printing, ISBN 0-521-57095–6.

Ghoshray, S. and Yen, K.K. (1995), More efficient genetic algorithm for solving optimization problems. Proc. 1995 IEEE Internat. Conf. on Systems for the 21st Century, pp. 4515–4520.

Giampiccolo, E., S. D'Amico, D. Patane`, and S. Gresta (2007), Attenuation and source parameters of shallow microearthquakes at Mt. Etna Volcano, Italy, Bull. Seismol. Soc. Am., 97, pp. 184–197, doi:10.1785/0120050252.

Gilman, D. L., F. J. Fuglister, and J. M. Mitchell Jr. (1963), On thepower spectrum of “red noise.” J. Atmos. Sci., 20**,** pp. 182–184.

Goedeev, E.I., Saltykov, V.A., Synitsin, V.I., Chebrov, V.N. (1990), Temporal and spatial characteristics of volcanic tremor wavefields, J. Volcanol. Geotherm. Res., 40, pp. 89-101.

Gonzalez, R.C., Thomas, M.G. (1978), Syntactic Pattern Recognition: an Introduction, Addison Wesley, Reading, MA.

Gordeev, E.I. (1993), Modelling of volcanic tremor as explosive point sources in a singled-layer, elastic half-space, J. Geophys. Res. 98, pp. 19687–19703.

Gottschammer, E., and I. Surono (2000), Locating tremor and shock sources recorded at Bromo volcano, J. Volcanol. Geotherm. Res., 101, pp. 199-209, doi:10.1016/S0377-0273(00)00171-2.

Govindan, R.B., Narayanan, K., Gopinathan, M.S. (1998), On the evidence of deterministic chaos in ECG: surrogate and predictability analysis, Chaos*,* 8, pp. 495–502.

Green, D., and J. Neuberg (2006), Waveform classification of volcanic lowfrequency earthquake swarms and its implication at Soufrière Hills Volcano, Monserrat, J. Volcanol. Geotherm. Res., 153, pp. 51–63, doi:10.1016/j.jvolgeores.2005.08.003.

Gresta, S., Montalto, A., Patanè, G. (1991), Volcanic tremor at Mt. Etna (January 1984–March 1985), its relationship to the eruptive activity and modelling of the summit feeding system. Bull. Volcanol., 53, pp. 309–320.

Gresta, S., E. Privitera, A. Leotta, and P. Gasperini (1996a), Analysis of the intermittent volcanic tremor observed at Mt. Etna, Sicily during March-May 1987, Ann. Geophys., 39, pp. 421-428.

Gresta, S., Ripepe, M., Marchetti, E., D'Amico, S., Coltelli, M., Harris, A.J.L., and Privitera, E. (2004), Seismoacoustic measurements during the July–August 2001 eruption at Mt. Etna volcano, Italy, J. Volcanol. Geotherm. Res. 137, pp. 219–230.

Grinsted, A., J. C. Moore, and S. Jevrejeva (2004), Application of the cross wavelet transform and wavelet coherence to geophysical time series, Nonlinear Proc. Geophys., 11, pp. 561–566.

Guilbert, J., Harjadi, P., Purbawinata, M., Jammes, S., Le Pichon, A., and Feignier, B. (2005), Monitoring of Indonesian volcanoes with infrasound: Preliminary results, 2005 Infrasound Technology Workshop, Tahiti.

Hagerty, M., and Benites, R. (2003), Tornillos beneath Tongariro Volcano, New Zealand, J. Volcanol. Geotherm. Res. 125, doi: 10.1016/S0377-0273(03)00094-5.

Hagerty, M.T., Schwartz, S.Y., Garces, M.A., and Protti, M. (2000), Analysis of seismic and acoustic observations at Arenal Volcano, Costa Rica, 1995–1997, J. Volcanol. Geotherm. Res. 101, pp. 27–65.

Harris, A.J.L., Blanke, S., Rothery, D.A., and Stevens, N.F. (1997), A chronology of the 1991 to 1993 Mount Etna eruption using advanced very high resolution radiometer data: Implications for real-time thermal volcano monitoring, J. Geophys. Res. 102, pp. 7985–8003.

Harris, A.J.L., and A.J.H. Maciejewski (2000), Thermal surveys of the Vulcano Fossa fumarole field 1994-1999: evidence for fumarole migration and sealing, J. Volcanol. Geotherm. Res., 102, pp. 119-147.

Hastie, T., Tibshirani, R. & Friedman, J., 2002. The Elements of Statistical Learning. 533 pp., Springer, New York.

Hedlin, M.A.H., Garces, M., Bass, H., Hayward, C., Herrin, G., Olson, J., and Wilson, C. (2002), Listening to the secret sounds of Earth's atmosphere, EOS 83, pp. 564–565.

Hou, S. Li, Y. (2010), Detecting nonlinearity from a continuous dynamic system based on the delay vector variance method and its application to gear fault identification, Nonlinear Dynamics, 60, pp. 141-148, doi: 10.1007/s11071-009-9586-9.

Hsu C. W., Lin C.J. (2002), A comparison of methods for multi-class support vector machines, IEEE Trans. On Neural Networks, vol. 13, pp. 415-425.

Hsu, C.W., Chang C.C. & Lin, C.J. (2007), A practical guide to support vector classification, http://www.csie.ntu.edu.tw//~cjlin/papers/guide/guide.pdf.

Hurwitz, S., A. Kumar, R. Taylor, and H. Heasler (2008), Climate-induced variations of geyser periodicity in Yellowstone National Park, USA, Geology, 36, pp. 451–454.

Husen, S., R. Taylor, R.B. Smith, and H. Healser (2004), Changes in geyser eruption behaviour and remotely triggered seismicity in Yellowstone National Park produced by the 2002 M 7.9 Denali fault earthquake, Alaska, Geology, 32, pp. 537–40.

Hwanjo Y., Jiong Y., Jiawei H., (2003), Classifying large data sets using SVMs with hierarchical clusters, Proceedings of the ninth ACM SIGKDD international conference on Knowledge discovery and data mining, August 24-27, 2003, Washington, D.C.

Ibanez, J.M., Carmona, E., Almendros, J., Saccorotti, G., Del Pezzo, E., Abril, M., Ortiz, R. (2003), The 1998-1999 seismic series at Deception Island volcano, Antarctica. J. Volcanol. Geotherm. Res., 128, pp. 65-88.

Ichino, M., and Yaguchi, H. (1994), Generalized Minkowski metrics for mixed feature-type data analysis, IEEE Trans. Syst. Man Cybern., 24, pp. 698–708.

Ingebritsen, S.E., and Rojstaczer S.A. (1993), Controls on geyser periodicity, Science, 262, pp. 889– 892.

Ingebritsen, S.E., and S.A. Rojstaczer (1996), Geyser periodicity and the response of geysers to small strains in the Earth, J. Geophys. Res., 101, pp. 21891–21907.

Jain, A. K., and Dubes, R. C. (1988), Algorithms for Clustering Data, Prentice-Hall advanced reference series, Prentice-Hall, Inc., Upper Saddle River, NJ.

Jain, A.K., Murty, M. N.. and Flynn, P.J. (1999), Data clustering: a review, ACM Computing Surveys (CSUR), 31, pp. 264-323.

Jain, A.K., Duin, P.W., and Mao J. (2000), Statistical pattern recognition: a review, IEEE Transactions on Pattern Analysis and Machine Intelligence, 22, pp. 4-37.

Jaupart, C., and S. Vergniolle (1988), Laboratory models of Hawaiian and Strombolian eruptions, Nature, 331, pp. 58–600, doi:10.1038/331058a0.

Jenkins, G. M., and D. G. Watts, (1968), Spectral Analysis and Its Applications. Holden-Day, 525 pp.

Jevrejeva, S., Moore, J. C., and Grinsted, A. (2003), Influence of the Arctic Oscillation and El Nin˜o-Southern Oscillation (ENSO) on ice conditions in the Baltic Sea: The wavelet approach, J. Geophys. Res., 108, 4677, doi:10.1029/2003JD003417.

Johnson, J. B., J. M. Lees, and E. I. Gordeev (1998), Degassing explosions at Karymsky Volcano, Kamchatka, Geophys. Res. Lett., 25, pp. 3999– 4002, doi:10.1029/1998GL900102.

Johnson, J.B. and Lees, J.M. (2000), Plugs and chugs: Seismic and acoustic observations of degassing explosions at Karymsky, Russia and Sangay, Ecuador, J. Volcanol. Geotherm. Res. 101, pp. 67–82.

Johnson, J.B. (2005), Source location variability and volcanic vent mapping with a small-aperture infrasound array at Stromboli Volcano, Italy, Bull. Volcanol. 67, pp. 1–14.

Johnson, J.B., Aster, R.C. (2005), Relative partitioning of acoustic and seismic energy during Strombolian eruptions, J. Volcanol. Geotherm. Res., 148, pp. 334-354.

Johnston, M.J.S., Mueller, R.J., Dvorak, J. (1981), Volcano-magnetic observations during eruptions, May-August 1980, US Geol. Surv. Prof. Pap., 1250, pp. 183-189.

Jones, K.R., Johnson, J., Aster, R., Kyle, P.R., and McIntosh, W.C. (2008), Infrasonic tracking of large bubble bursts and ash venting at Erebus volcano, Antarctica, J. Volcanol. Geotherm. Res., doi:10.1016/j.jvolgeores.2008.02.001.

Joswig, M. (1990), Pattern recognition for earthquake detection, Bull. Seism. Soc. Am., 80**, pp.** 170–186.

Julian, B.R. (1994), Volcanic tremor: nonlinear excitation by fluid flow, J. Geophys. Res. 99, pp. 11859–11877.

Jurkevics, A. (1988), Polarization analysis of three-component array data. Bull. Seism. Soc. Am., 78, pp. 1725-1743.

Kaneshima, S., Kawakatsu, H., Matsubayashi, H., Sudo, Y., Tsutsui, T., Ohminato, T., Ito, H., Uhira, K., Yamasato, H., Oikawa, J., Takeo, M., Iidaka, T. (1996), Mechanism of phreatic eruptions at Aso Volcano inferred from near-field broadband seismic observations. Science, 273, pp. 642-645.

Kantz, H., and Schreiber, T. (1997), Nonlinear Time Series Analysis. Cambridge University Press,Cambridge , pp. 350.

Kaplan, D. (1994), Exceptional events as evidence for determinism, Physica D, 73, pp. 38–48. doi:10.1016/0167-2789(94)90224-0.

Kaplan, D. (1997), Nonlinearity and nonstationarity: the use of surrogate data in interpreting fluctuations, In Frontiers of blood pressure and heart rate analysis (Di Rienzo, M., Mancia, G., Parati, G., Pedotti, A., and Zanchetti, A., eds), pp. 15–28. Amsterdam, The Netherlands: IOS Press.

Kaufman L., and Rousseeuw, P.J. (1990), Finding Groups in Data: An Introduction to Cluster Analysis, Wiley, New York.

Kawakatsu, H., T. Ohminato, and H. Ito (1994), 10s-period volcanic tremors observed over a wide area in southwestern Japan, Geophys. Res. Lett., 21(18), pp. 1963–1966, doi:10.1029/ 94GL01683.

Kawakatsu, H., Kaneshima, S., Matsubayashi, H., Ohminato, T., Sudo, Y., Tsutsui, T., Uhira, K., Yamasato, H., Ito, H., and Legrand, D. (2000), Aso94: Aso seismic observation with broadband instruments, J. Volcanol. Geotherm. Res., 101, pp. 129–154, doi:10.1016/S0377-0273(00)00166-9.

Kawakatsu, H., and M. Yamamoto (2007), Volcano Seismology , Schubert, G. (ed.) In Treatise on Geophysics, 4, pp. 389-420, Oxford: Elsevier.

Kay, S. M. (1981), Modern spectral estimation, theory and application, Academic Press.

Kecman, V., (2001), Learning and soft computing. Support vector machines, Neural networks, and Fuzzy logic models. The MIT press, Cambridge.

Kennel, M.B., R. Brown, and H.D.I. Abarbanel (1992), Determining embedding dimension for phase-space reconstruction using a geometrical construction. Physical Review A, 45, pp. 3403-3411.

Knuth, D. (1973), The Art of Computer Programming, Addison-Wesley, Reading, MA.

Kohonen, T. (1989), Self-Organization and Associative Memory, Springer.

Konstantinou, K. I. and Schlindwein, V. (2002), Nature, Wavefield Properties and Source Mechanism of Volcanic Tremor: A Review, J. Volc. Geotherm. Res. 93, pp. 4835-4849.

Konstantinou, K.I., and C.H. Lin (2004), Nonlinear time series analysis of volcanic tremor events recorded at Sangay volcano, Ecuador, Pure Appl. Geophys., *161*, pp. 145-163.

Kumagai, H., Chouet, B. (1999), The complex frequencies of long-period seismic events as probes of fluid composition beneath volcanoes. Geophys. J. Int., 138, F7-F12.

Kumagai, H., and B. Chouet (2000), Acoustic properties of a crack containing magmatic or hydrothermal fluids. J. Geophys. Res., 105, pp. 25493-25512.

Kumagai, H., and B. Chouet (2001), The dependence of acoustic properties of a crack on the resonance mode and geometry. *Geophys. Res. Lett.*, *28*, pp. 3325-3328.

Kumagai, H., K. Miyakawa, H. Negishi, I. Hiroshi, K. Obara, and D. Suetsugu (2003), Magmatic dike resonances inferred from very-long-period seismic signals, Science, 299, pp. 2058–2061, doi:10.1126/science.1081195.

Kumagai, H. (2006), Temporal evolution of a magmatic dike system inferred from the complex frequencies of very long-period seismic signals, J. Geophys. Res. 111, B06201, doi:10.1029/ 2005JB003881.

Kumazawa, M., Y. Imanishi, Y. Fukao, M. Furumoto, and A. Yamamoto (1990), A theory of spectral analysis based on the characteristic property of a linear dynamic system, Geophys. J. Int., 101, pp. 613–630, doi:10.1111/j.1365-246X.1990.tb05574.x.

Kunhimangalam, R., Joseph, P.K., Sujith, O.K. (2008), Nonlinear analysis of EEG signals: Surrogate data analysis, IRBM, 29, pp. 239-244, doi: 10.1016/j.rbmret.2007.09.006.

Labat, D. (2005), Recent advances in wavelet analyses: Part 1. A review of concepts, Journal of Hydrology, 314, 1-4, pp. 275-288, DOI: 10.1016/j.jhydrol.2005.04.003.

Lacoss, R.T. (1971), Data adaptative spectral analysis methods, Geophysics , 36, pp. 661–675.

Lahr, J., Page, R.A., Chouet, B.A., Stephens, C.D., Harlow, D.H. (1994), Seismic evolution of the 1989–90 eruption sequence of Redoubt Volcano, Alaska. J. Volcanol. Geotherm. Res., 62, 69-94.

Langer, H., and S. Falsaperla (1996), Long-term Observation of Volcanic Tremor on Stromboli Volcano (Italy): A Synopsis, Pageoph, 147, pp. 57-82.

Langer, H., Falsaperla, S., Masotti, M., Campanini, R., Spampinato, S.& Messina, A. (2009), Synopsis of supervised and unsupervised pattern classification techniques applied to volcanic tremor data at Mt Etna, Italy. Geophys. J. Int., doi: 10.1111/j.1365-246X.2009.04179.x.

Lay, T., and T. C. Wallace (1995), Modern Global Seismology, 521 pp., Academic, San Diego, Calif.

Lesage, P., Glangeaud, F., Mars, J. (2002), Applications of autoregressive and time-frequency analysis to the study of volcanic tremor and LP events, J. Volcanol. Geotherm. Res., 114, pp. 391-417.

Lesage, P. (2008), Automatic estimation of optimal autoregressive filters for the analysis of volcanic seismic activity, Nat. Hazards Earth Syst. Sci., 8, pp. 369–376.

Lighthill, J., Waves in Fluids, (Cambridge University Press 1978) 504 pp.

Likas, A., Vlassis, N., and Verbeek, J. (2003), The global k-means algorithm, Pattern Recognition, 36, pp. 451-461.

Linde, A.T., Agustsson, K., Sacks, I.S., Stefansson, R. (1993), Mechanism of the Hekla Iceland 1991 eruption from continuous borehole strain monitoring. Nature, 365, pp. 737-741.

Liu, P. C. (1994), Wavelet spectrum analysis and ocean wind waves. Wavelets in Geophysics, E. Foufoula-Georgiou and P. Kumar, Eds., Academic Press, pp. 151–166.

Lokmer, I., C. J. Bean, G. Saccorotti, and D. Patane` (2007), Moment-tensor inversion of LP events recorded on Etna in 2004 using constraints obtained from wave simulation tests, Geophys. Res. Lett., 34, L22316, doi:10.1029/2007GL031902.

Lokmer, I., G. Saccorotti, B. Di Lieto, and C. J. Bean (2008), Temporal evolution of long-period seismicity at Etna volcano, Italy, and its relationships with the 2004–2005 eruption, Earth Planet. Sci. Lett., 266, pp. 205– 220, doi:10.1016/j.epsl.2007.11.017.

Mandic, D.P., Chen, M., Gautama, T., Van Hulle, M.M., and Constantinides, A. (2008), On the characterization of the deterministic/stochastic and linear/nonlinear nature of time series, Proceedings of Royal Society.

Mao, J. And Jain, A. K. (1996), A self-organizing network for hyperellipsoidal clustering (HEC), *IEEE Trans. Neural Netw., 7*, pp. 16–29.

Maraun, D. and J. Kurths, 2004, Cross wavelet analysis: significance testing and pitfalls. Nonlinear processing in Geophysics, vol. 11, pp. 505-514.

Marchetti, E., Ripepe, M., Harris, A.J.L., and Delle Donne, D. (2009), Tracing the differences between Vulcanian and Strombolian explosions using infrasonic and thermal radiation energy, Earth Planet. Sci. Lett., doi:10.1016/j.epsl.2009.01.004.

Marple, S. L. (1987), Digital spectral analysis with applications, Prentice Hall, Englewood Cliffs.

Mars, J., Lacoume, J.-L., Mari, J.-L., and Glangeaud, F. (2004), Traitement du signal pour géologues et géophysiciens – Vol. 3, Techniques avancées, Technip.

Martinelli, B. (1990), Analysis of seismic patterns observed at Nevado del Ruiz volcano, Colombia, during August-September 1985, J. Volcanol. Geotherm. Res., 41, pp. 297-314.

Martinez-Arevalo, C., D. Patane`, A. Rietbrock, and J. M. Ibanez (2005), The intrusive process leading to the Mt. Etna 2001 flank eruption: Constraints from 3-D attenuation tomography, Geophys. Res. Lett., 32, doi:10.1029/ 2005GL023736.

Martini, M. (1996), Chemical Characters of the Gaseous Phase in Different Stages of Volcanism: Precursors and Volcanic Activity. In "Monitoring and mitigation of volcano hazards" (Scarpa, Tilling Eds.), pp. 199-219.

Masotti, M., Campanini, R., Mazzacurati, L., Falsaperla, S., Langer, H., and Spampinato, S. (2008), TREMOrEC: a software utility for automatic classification of volcanic tremor, Geochemistry Geophysics Geosystems, 9(1), Q04007.

Matcharashvili, T., Chelidze, T., Javakhishvili, Z., (2000), Nonlinear analysis of magnitude and interevent time interval sequences for earthquakes of Caucasian region. Nonlinear Process. Geophys., 7, pp. 9–19.

Matoza, R.S., Hedlin, M., and Garces, M. (2007), An infrasound array study of Mount St. Helens, J. Volcanol. Geotherm. Res. 160, pp. 249–262.

Matoza, R.S., Garces, M.A., Chouet, B., D'Auria, L., Hedlin, H., De Grooth-Hedlin, C., and Waite, G.P. (2009), The source of infrasound associated with long-period events at Mount St. Helens, J. Geophys. Res. 114, doi:10.1029/2008JB006128.

McGuire, W.J. (1992), Monitoring active volcanoes: procedures and prospects, Proceedings of the Geologists' Association, 103, pp. 303-320, ISSN 0016-7878, doi: 10.1016/S0016-7878(08)80128-9.

McNutt, S.R. (1986). Observations and analysis of B-type earthquakes, explosions and volcanic tremor at Pavlof volcano, Alaska. Bull. Seismol. Soc. Am. 76, pp. 153-175.

McNutt, S.R. (1992), Volcanic tremor, Encyclopedia od Earth System Science (Academic Press, San Diego, CA), 4, pp. 417-425.

McNutt, S.R. (1994), Volcanic tremor from around the world: 1992 update. *Acta Vulcanol.*, *5*, pp. 197–200.

McNutt, S.R. (1996), Seismic monitoring and eruption forecasting of volcanoes: a review of the state of the art and case histories, In Monitoring and mitigation of volcano hazards (Scarpa, Tilling Eds.), pp. 99-146.

McNutt, S.R., Rymer, H., Stix, J. (2000), Synthesis of Volcano Monitoring, In Encyclopaedia of volcanoes (Sigurdsson et al., Eds.), pp. 1165-1183.

McNutt, S.R. (2005), Volcanic Seismology. Annual Review of Earth and Planetary Sciences, 32, pp. 461-491.

McQueen, J. (1967), Some methods for classification and analysis of multivariate observations, In Proceedings of the Fifth Berkeley Symposium on Mathematical Statistics and Probability, pp. 281–297.

Mika, S., Ratsch, G., Weston, J., Scholkopf, B. Mullers, K.R. (1999), Fisher discriminant analysis with kernels, IEEE International Workshop on Neural Networks for Signal Processing IX, Madison, USA, August, pp. 41–48.

Miller, A.D., Foulger, G.R., Julian, B.R. (1998), Non-double-couple earthquakes 2. Observations. Rev. of Geophys., 36, pp. 551-568.

Minakami, T. (1974), Seismology of volcanoes in Japan. In Developments in Solid Earth Geophysics. Physical Volcanology (Civetta, Gasparini, Luongo, Rapolla Eds.), 6, pp. 1-27, Amsterdam, Elsevier.

Mitchell, M. (1996), An Introduction to Genetic Algorithms, MIT Press, Cambridge, 205 pp.

Mitschke, F., and Dämmig, M. (1993), Chaos versus noise in experimental data, Int. J. Bifurcation Chaos, 3, pp. 693–701.

Modha, D. S., and Spangler W. S. (2002), Feature weighting in k-means clustering, Machine Learning, 50.

Montalto, P., Cannata, A., Privitera, E., Gresta, S., Nunnari, G. and Patanè, D. (2010), Towards an automatic monitoring system for infrasonic events at Mt. Etna: strategies for source location and modelling. Pure and Applied Geophysics, doi: 10.1007/s00024-010-0051-y.

Moran, S.C. (2003), Multiple seismogenic processes for high-frequency earthquakes at Katmai National Park, Alaska: Evidence from stress tensor inversions of fault-plane solutions, Bull. Seism. Soc. Am., 93, pp. 94–108.

Moran, S.C., Matoza, R.S., Garces, M.A., Hedlin, H., Bowers, D., Scott, W.E., Sherrod, D.R., and Vallance, J.W. (2008), Seismic and acoustic recordings of an unusually large rockfall at Mount St. Helens, Washington, Geophys. Res. Lett. 35, doi: 10.1029/2008GL035176.

Mori, J., White, R.A., Harlow, D.H., Ohkubo, P., Power, J.A., Hoblitt, R.P., Laguerta, E.P., Lanuza, A., and Bautista, B.C. (1996), Volcanic earthquakes following the 1991 climatic eruption of Mount Pinatubo: Strong seismicity during a waning eruption, in Fire and Mud, edited by C. Newhall and R. Punongbayan, pp. 339-350.

Morrissey, M.M., and B. Chouet (2001), Trends in long-period seismicity related to magmatic fluid compositions. J. Volcanol. Geotherm. Res., 108, pp. 265-281.

Morrissey, M., M. Garces, K. Ishihara, and M. Iguchi (2008), Analysis of infrasonic and seismic events related to the 1998 Vulcanian eruption at Sakurajima. J. Volcanol. Geotherm. Res., 175, pp. 315-324.

Mulargia, F., S. Tinti, and E. Boschi (1985), A statistical analysis of flanks eruptions on Etna volcano, J. Volcanol. Geotherm. Res., 23, pp. 263 -272, doi:10.1016/0377-0273(85)90037-X.

Murase, T. and McBirney, A.R. (1973), Properties of some common igneous rocks and their melts at high temperatures, Geol. Soc. Am. Bull. 84, pp. 3563–3592.

Nakahara, H. (2004), Correlation distance of waveforms for closely located events—I. Implication of the heterogeneous structure around the source region of the 1995 Hyogo-Ken Nanbu, Japan, earthquake (Mw = 6.9), Geophys. J. Int., 157, pp. 1255-1268, doi:10.1111/j.1365-246X.2004.02278.x.

Nakano, M., Kumagai, H., Chouet, B.A. (2003), Source mechanism of long-period events at Kusatsu-Shirane Volcano, Japan, inferred from waveform inversion of the effective excitation functions. J. Volcanol. Geotherm. Res., 122, pp. 149-164.

Nawab, S. and Quatieri, T. (1988), Short-time Fourier transform, in Advanced Topics in Signal Processing, Lim, J.S., Oppenheim, A.V. Eds, Prentice Hall, New Jersey.

Neidell, N. and Taner, M.T. (1971), Semblance and other coherency measures for multichannel data, Geophysics 36, pp. 482–497.

Neri, M. (2008), Eruzione dell'Etna, 28/05/2008—Fratture non eruttive sul fianco settentrionale del Cratere di Nord-Est (in Italian), volcanological report, Ist. Naz. di Geofis. e Vulcanol., Catania, Italy, (Available at http://www.ct.ingv.it/Report/ RPTVGSTR20080528.pdf).

Neuberg, J., Luckett, R., Ripepe, M., Braun, T. (1994), Highlights from a seismic broadband array on Stromboli volcano. Geophys. Res. Lett., 21, pp. 749-752.

Neuberg, J. and Pointer, T. (2000), Effects of volcano-topography on seismic broadband waveforms, Geophys. J. Int. 143, pp. 239-248.

Neuberg, J., Luckett, R., Baptie, B., Olsen, K. (2000), Models of tremor and low frequency earthquake swarms on Montserrat. J. Volcanol. Geotherm. Res., 101, pp. 83-104.

Neuberg, J., Tuffen, H., Collier, L., Green, D., Powell, TW., Dingwell, D. (2006), The trigger mechanism of low-frequency earthquakes on Montserrat, Journal of Volcanology and Geothermal Research, 153, pp. 37-50. doi:10.1016/j.jvolgeores.2005.08.008.

Nicholl, M. J., S. W. Wheatcraft, S. W. Tyler, and B. Berkowitz (1994), Is Old Faithful a strange attractor?, J. Geophys. Res., 99, pp. 4495–4503.

Nishimura, T., Hamaguchi, H. and Ueki, S. (1995), Source mechanisms of volcanic tremor and low-frequency earthquakes associated with the 1988–89 eruptive activity of Mt Tokachi, Hokkaido, Japan. Geophys. J. Int., 121, pp. 444–458.

Noble, W.S. (2004), Support vector machine applications in computational biology. Kernel Methods in Computational Biology, MIT Press, Cambridge, MA.

Obara, K. (2002), Nonvolcanic deep tremor associated with subduction in southwest Japan. Science, *296*, pp. 1679– 1681.

Obara, K., and H. Hirose (2006), Non-volcanic deep low-frequency tremors accompanying slow slips in the southwest Japan subduction zone, Tectonophysics, 417, pp. 33–51.

Oehler K.L. and Gray R.M. (1995), Combining Image Compression and Classification Using Vector Quantization, IEEE Trans. Patter Analysis and Machine Intelligence, vol. 17, no. 5, pp. 461-473.

Ohminato, T., B. Chouet, P. Dawson, Kedar, S. (1998), Waveform inversion of very long period impulsive signals associated with magmatic injection beneath Kilauea Volcano, Hawaii. J. Geophys. Res., 103, 23839-23862.

Oshima, H. and Maekawa, T. (2001), Excitation process of infrasonic waves associated with Merapi-type pyroclastic flow as revealed by a new recording system, Geophys. Res. Lett. 28, pp. 1099–1102.

Palano, M., Puglisi, G., Gresta, S. (2008), Ground deformation patterns at Mt. Etna from 1993 to 2000 from joint use of InSAR and GPS techniques. J. Volcanol. Geotherm. Res., 169, pp. 99-120.

Palano, M., Gresta, S., and Puglisi, G. (2009), Time-dependent deformation of the eastern flank of Mt. Etna: After-slip or viscoelastic relaxation?, Tectonophysics, 473, pp. 300-311, doi:10.1016/j.tecto.2009.02.047.

Parlitz, U. (1998), Nonlinear Time-Series Analysis, in *Nonlinear* Modeling - Advanced Black-Box Techniques, edited by J.A.K. Suykens and J. Vandewalle, pp. 209-239, Kluwer Academic Publishers.

Patanè, D., De Gori, P., Chiarabba, C., and Bonaccorso, A. (2003), Magma ascent and the pressurization of Mt. Etna's volcanic system, Science, 299, pp. 2061-2063, doi:10.1126/science .1080653.

Patanè, D., Mattia, M., and Aloisi, M. (2005), Shallow intrusive processes during 2002–2004 and current volcanic activity on Mt. Etna, Geophys. Res. Lett., 32, doi:10.1029/ 2004GL021773.

Patanè, D., G. Barberi, O. Cocina, P. De Gori, and C. Chiarabba (2006), Time-resolved seismic tomography detects magma intrusions at Mount Etna, Science, 313, pp. 821-823, doi:10.1126/science.1127724.

Patanè, D., Mattia, M., Di Grazia, G., Cannavò, F., Giampiccolo, E., Musumeci, C., Montalto, P., Boschi, E. (2007). Insights into the dynamic processes of the 2007 Stromboli eruption and possible meteorological influences on the magmatic system. Geophys. Res. Lett., 34, L22309, doi:10.1029/2007GL031730.

Patanè , D., Di Grazia, G., Cannata, A., Montalto, P., and Boschi, E. (2008), The shallow magma pathway geometry at Mt. Etna volcano, Geochem. Geophys. Geosyst. 9, doi:10.1029/ 2008GC002131.

Pavlidis T. (1977), Structural Pattern Recognition, Springer Verlag, Berlin.

Pena, J., Lozano, J., and Larranaga, P. (1999), An empirical comparison of four initialization methods for the k-means algorithm, Pattern Recognition Letters, 20, pp. 1027-1040.

Peltier, A., Bachèlery, P., and Staudacher, T. (2009), Magma transport and storage at Piton de La Fournaise (La Réunion) between 1972 and 2007: A review of geophysical and geochemical data, J. Volcanol. Geotherm. Res. 148, pp. 93–108.

Power, J.P., Lahr, J.C., Page, R.A., Chouet, B.A., Stephens, D.H., Harlow, T.L., Murray T.L., and Davies, J.N. (1994), Seismic evolution of the 1989–1990 eruption sequence of Redoubt Volcano, Alaska, J. Volcanol. Geotherm. Res., 62, pp. 69–94.

Priestley, M.B. (1981), Spectral analysis and time series. New York, NY: Academic Press.

Privitera, E., T. Sgroi, and S. Gresta (2003), Statistical analysis of intermittent volcanic tremor associated with the September 1989 summit explosive eruptions at Mount Etna, Sicily, J. Volcanol. Geotherm. Res., 120, pp. 235–247, doi:10.1016/S0377-0273(02)00400-6.

Prokoph, A., and Patterson, R.T. (2004), Application of wavelet and discontinuity analysis to trace temperature changes: Eastern Ontario as a case study. Atmosphere Ocean, 42, pp 201-212.

Ripepe, M. and Marchetti, E. (2002), Array tracking of infrasonic sources at Stromboli volcano, Geophys. Res. Lett. 29, 2076, doi: 10.1029/2002GL015452.

Ripepe, M., Poggi, P., Braun, T., and Gordeev, E. (1996), Infrasonic waves and volcanic tremor at Stromboli, Geophys. Res. Lett. 23, pp. 181–184.

Ripepe, M., Ciliberto, S., and Della Schiava, M. (2001a), Time constraint for modelling source dynamics of volcanic explosions at Stromboli, J. Geophys. Res. 106, pp. 8713–8727.

Ripepe, M., Coltelli, M., Privitera, E., Gresta, S., Moretti, M., and Piccinini, D. (2001b), Seismic and infrasonic evidences for an impulsive source of the shallow volcanic tremor at Mt. Etna, Italy, Geophys. Res. Lett. 28, pp. 1071–1074.

Ripepe, M., Harris, A.J.L., and Carniel, R. (2002), Thermal, seismic and infrasonic evidences of variable degassing rates at Stromboli volcano, J. Volcanol. Geotherm. Res. 118, pp. 285-297.

Ritter, H., Schulten, K., (1986), Kohonen's Self-Organizing Maps: Exploring their Computational Capabilities, Biol. Cybernetics Vol 54, 1986, pp. 99-106.

Rowe, C.A., Aster, R.C., Kyle, P.R., Dibble, R.R., and Schlue, J.W. (2000), Seismic and acoustic observations at Mount Erebus Volcano, Ross Island, Antarctica, 1994–1998, J. Volcanol. Geotherm. Res. 101, pp. 105–128.

Ruiz, M.C., Lees, J.M., and Johnson, J.B. (2006), Source constraints of Tungurahua volcano explosion events, Bull. Volcanol. 68, pp. 480-490.

Ruiz, M.C., and S.R. Arenallo (2008), Characteristics and distribution of infrasound signals at Tungurahua volcano, Ecuador, American Geophysical Union, Fall Meeting 2008, V51E-2089.

Rymer, H. (1996), Microgravity monitoring. In "Monitoring and mitigation of volcano hazards" (Scarpa, Tilling Eds.), pp. 169-197.

Saab, R., McKeown, M.J., Myers, L.J., Abu-Gharbieh, R., (2005), A Wavelet Based Approach for the Detection of Coupling in EEG Signals. Neural Eng. Conf. Proc. pp. 616–620.

Saccorotti, G., L. Zuccarello, E. Del Pezzo, J. Ibanez, and S. Gresta (2004), Quantitative analysis of the tremor wavefield at Etna volcano, Italy, J. Volcanol. Geotherm. Res., 136, pp. 223–245, doi:10.1016/j.jvolgeores.2004.04.003.

Saccorotti, G., I. Lokmer, C. J. Bean, G. Di Grazia, and D. Patanè (2007), Analysis of sustained long-period activity at Etna Volcano, Italy, J. Volcanol. Geotherm. Res., 160, pp. 340–354, doi:10.1016/j.jvolgeores.2006.10.008.

Sahagian, D. (2005), Volcanic eruption mechanisms: Insights from intercomparison of models of conduit processes, J. Volcanol. Geotherm. Res., 143, pp. 1-15, doi:10.1016/j.jvolgeores. 2004.12.006.

Sahetapy-Engel, S.T., Harris, A.J.L., and Marchetti, E. (2008), Thermal, seismic and infrasound observations of persistent explosive activity and conduit dynamics at Santiaguito lava dome, Guatemala, J. Volcanol. Geotherm. Res. 173, pp. 1–14.

Sanchez, J.J., McNutt, S.R., Power, J.A., Wyss, M. (2004), Spatial variations in the frequency-magnitude distribution of earthquakes at Mount Pinatubo volcano. Bull. Seis. Soc. Am., 94, pp. 430–38.

Scarpa, R., and Gasparini, P. (1996), A review of volcano geophysics and volcano-monitoring methods, In "Monitoring and Mitigation of Volcano Hazards" (Scarpa - Tilling eds.), pp. 3-22.

Scarpetta, S., Giudicepietro, F., Ezin, E., Petrosino, S., Del Pezzo, E., Martini, M., and Marinaro, M. (2005), Automatic classification of seismic signals at Mt. Vesuvius volcano, Italy, using neural network, Bull. Seism. Soc. Amer., 95, pp. 185-196.

Schick, R., (1988), Volcanic tremor-source mechanism and correlation with eruptive activity, Natural Hazard, 1, pp. 125-144.

Schick, R., (1992), Volcanic tremor: seismic signals of (almost) unknown origin. In: Gasparini P, Scarpa R, Aki K (eds) Volcanic seismology. Springer, Berlin Heidelberg New York, pp 157-167.

Schreiber, T. (1997), Detecting and analysing nonstationarity in a time series using nonlinear cross prediction, Phhys. Rev. Lett. 78, 843.

Schreiber T., and Schmitz A. (1997), On the discrimination power of measures for nonlinearity in a time series, Phys. Rev. E, 55, pp. 5443-5447.

Schreiber, T. (1998), Constrained randomization of time series data. Physical Review Letters,80, 2105.

Schreiber, T. and Schmitz, A. (2000), Surrogate time series, Physica D, 142, pp. 346–382. doi:10.1016/S0167-2789(00)00043-9.

Seidl D., Schick R., Riuscetti M. (1981), Volcanic tremors at Etna: a model for hydraulic origin. Bull. Volcanol., 44, pp. 43-56.

Seidl, D. and Hellweg, M. (2003), Parameterization of multichromatic tornillo signals observed at Galeras Volcano (Colombia), J. Volcanol. Geotherm. Res. 125, pp. 171–189.

Shaw, H.R. (1992), Nonlinear Dynamics and Magmatic Periodicity; Fractal Intermittency and Chaotic Crises, Int. Geol. Congr., 510.

Sherrod, D.R., Scott, W.E., and Stauffer, P.H. (2008), A volcano rekindled; the renewed eruption of Mount St. Helens, 2004-2006, U.S. Geological Survey Professional Paper 1750, 856 pp.

Spampinato, L., C. Oppenheimer, S. Calvari, A. Cannata, and P. Montalto (2008), Lava lake surface characterization by thermal imaging: Erta 'Ale volcano (Ethiopia), Geochem. Geophys. Geosyst., 9, Q12008, doi:10.1029/2008GC002164.

Sprott, J. C. (2003). Chaos and time-series analysis. Oxford: Oxford University Press.

Stam, C.J., Pijn, J.P.M., Pritchard, W.S. (1998), Reliable detection of nonlinearity in experimental time series with strong periodic components, Physica D, 112, pp. 361-380, doi: 10.1016/S0167-2789(97)00183-8.

Stephens, C.D., Chouet, B. (2001), Evolution of the December 14, 1989 precursory long-period event swarm at Redoubt Volcano, Alaska. J. Volcanol. Geotherm. Res., 109, pp. 133-148.

Stoica, P., and Moses, R. (1997), Introduction to Spectral Analysis. Prentice Hall, Upper Saddle River, NJ.

Stoica, P., Jakobsson, A., and Li, J. (1998), Matched-filter bank interpretation of some spectral estimators, Signal Process., 66, pp. 45–59.

Takens, F. (1981), Detecting strange attractors in turbulence, in Dynamical Systems and Turbulence, edited by D.A. Rand and L.S. Young, pp. 365– 381, Lecture Notes in Mathematics vol. 898, Springer, Berlin.

Theiler, J. (1990),Estimating fractal dimension, Journal of the Optical Society of America A, 7, 1055.

Temkin, S., Elements of Acoustics (Wiley and Sons 1981) 515 pp.

Theiler, J., Eubank, S., Longtin, A., Galdrikian, B. & Farmer, J. (1992), Testing for nonlinearity in time series: the method of surrogate data, Physica D, 58, pp. 77-94, doi:10.1016/0167-2789(92)90102-S.

Theiler J., and Prichard, D. (1996), Constrained-realization Monte-Carlo method for hypothesis testing, Physica D, 94, pp. 221-235.

Thompson, G., S. R. McNutt, and G. Tytgat (2002), Three distinct regimes of volcanic tremor associated with eruptions of

Shishaldin volcano, Alaska, April 1999, Bull. Volcanol. 64, 535-547, doi:10.1007/s00445-002-0228-z.

Tilling, R.I. (2008), The critical role of volcano monitoring in risk reduction, Adv. Geosci. 14, pp. 3-11.

Timmer, J. (2000), What can be inferred from surrogate data testing?, Phys. Rev. Lett., 85, 2647, doi:10.1103/PhysRevLett.85.2647.

Torrence, C., and G. P. Compo (1998), A practical guide to wavelet analysis, Bull. Am. Meteorol. Soc., 79, pp. 61–78, doi:10.1175/1520-0477(1998)079<0061:APGTWA>2.0.CO;2.

Torrence, C. and Webster, P. (1999), Interdecadal Changes in the ESNO-Monsoon System, J. Clim., 12, pp. 2679–2690.

Uhira, K., Takeo, M. (1994), The source of explosive eruptions of Sakuajima volcano, Japan. J. Geophys. Res., 99, pp. 17775-17789.

Ultsch, A., (1993), Self organized features planes for monitoring and knowledge acquisition of a chemical process, Proceedings of the International Conference on Artificial Neural Networks, pp. 864-867. Springer-Verlag. London.

Ultsch, A. (2000), The neuro-data-mine, In H. Bothe and R. Rojas, editors, Proceeding of the ICS Symposia on Neural Computation (NC'2000) May, 23-26, 2000 in Berlin, Germany. Philipps-University of Marburg, Dep. Of Computer Science, ICSC Academic Press.

Van der Laat, R. (1996). Ground-Deformation Methods and Results. In "Monitoring and mitigation of volcano hazards" (Scarpa, Tilling Eds.), pp. 147-168.

Vapnik V.N. (1995), The Nature of Statistical Learning Theory, Springer Verlag, New York.

Vapnik V.N. (1998), Statistical Learning Theory, John Wiley & Sons, New York.

Varley, N., Arámbula-Mendoza, R., Reyes-Dávila, G., Stevenson, J., and Harwood, J. (2010), Long-period seismicity during magma movement at Volcán de Colima, Bull. Volcanol., doi: 10.1007/s00445-010-0390-7.

Vergniolle, S., and Brandeis, G. (1994), Origin of the sound generated by Strombolian explosions, Geophys. Res. Lett. 21, pp. 1959–1962.

Vergniolle, S., Brandeis, G., and Mareschal, J.C. (1996), Strombolian explosions: Eruption dynamics determined from acoustic measurements, J. Geophys. Res. 101, pp. 20449–20466.

Vergniolle, S., and Brandeis, G. (1996), Strombolian explosions: A large bubble breaking at the surface of a lava column as a source of sound, J. Geophys. Res. 101, pp. 20433–20448.

Vergniolle, S. (2003), Listening to volcanoes as a tool to understand eruption dynamics: Etna (Italy), Shishaldin (Alaska), paper presented at IUGG XXIII General Assembly State of the Planet: Frontiers and Challenges, Sapporo, Japan.

Vergniolle, S. and Caplan-Auerbach, J. (2004), Acoustic measurements of the 1999 basaltic eruption of Shishaldin volcano, Alaska: 2) Precursor to the Subplinian activity, J. Volcanol. Geotherm. Res. 137, pp. 135–151.

Vergniolle, S., Boichu, M., and Caplan-Auerbach, J. (2004), Acoustic measurements of the 1999 basaltic eruption of Shishaldin volcano, Alaska: 1) Origin of Strombolian activity, J. Volcanol. Geotherm. Res. 137, pp. 109–134.

Vergniolle, S. (2008), From sound waves to bubbling within a magma reservoir: Comparison between eruptions at Etna (2001, Italy) and Kilauea (Hawai'i), in Fluid Motions in Volcanic Conduits: A Source of Seismic and Acoustic Signals, edited by S. J. Lane and J. S. Gilbert, Geol. Soc. Spec. Publ., 307, pp. 125– 146.

Vergniolle, S. and Ripepe, M. (2008), From Strombolian explosions to fire fountains at Etna Volcano (Italy): What do we learn from acoustic measurements? Geol. Soc., London, Special Publications 307, pp. 103–124.

Vesanto, J., Alhoniemi, E., (2000), Clustering of the self-organizing map. IEEE Transactions on Neural Networks, 11 (3), pp. 586-600.

Vesanto, J. (2000), Using SOM in Data Mining, Licentiate's thesis, Helsinki University of Technology.

Waite, G.P., Smith, R.B. (2004). Seismotectonics and stress field of the Yellowstone volcanic plateau from earthquake firstmotions and other indicators. J. Geophys. Res. 109, 10.1029/2003JB002675.

Wassermann, J., 2009. Volcano Seismology. In: Bormann, P. (Ed.), New manual of seismological observatory practice. IASPEI 42 pp. doi:10.2312/GFZ.NMSOP_r1_ch13.

Wegler, U., Seidl, D., 1997. Kinematic parameters of the tremor wavefield at Mt. Etna (Sicily). Geophys. Res. Lett. 24, pp. 759-762.

Weill, A., Brandeis, G., Vergniolle, S., Baudin, F., BilBille, J., Fevre, J.F., Pirron, B., and Hill, X. (1992), Acoustic sounder measurements of the vertical velocity of volcanic jets at Stromboli volcano, Geophys. Res. Lett. 19, pp. 2357-2360.

Weston J., Watkins C. (1999), Multi-class support vector machines, presented at the Proc. ESANN99, M. Verleysen, Ed., Brussels, Belgium.

Wilson, L., and J. W. Head (1981), Ascent and eruption of basaltic magma on the Earth and Moon, J. Geophys. Res., 86, pp. 2971-3001, doi:10.1029/JB086iB04p02971.

Wilson, D. R. And Martinez, T. R. (1997), Improved heterogeneous distance functions, J. Artif. Intell. Res., 6, pp. 1-34.

Withers, M. (1997), An automated local/regional seismic event detection and location system using waveform correlation. PhD thesis.

Withers, M., Aster, R., Young, C., Beiriger, J., Harris, M., Moore, S., and Trujillo, J. (1998), A comparison of select trigger algorithms for automated global seismic phase and event detection, Bull. Seism. Soc. Am. 88, pp. 95-106.

Woods, A.W., and S. S. S. Cardoso (1997), Bubble-melt separation as a trigger for basaltic volcanic eruptions, Nature, 385, 518-520, doi:10.1038/385518a0.

Wu, K., and Yang, M. (2002), Alternative c-means clustering algorithms, Pattern Recognition, 35, pp. 2267-2278.

Wu, W., Xiong, H., and Shekhar, S. (2004), Clustering and Information Retrieval, Kluwer Academic Publishers, Norwel, MA.

Xie Q.B., Laszlo C.A. and Ward R.K., (1993), Vector Quantization Technique for Nonparametric Classifier Design, IEEE Trans. Patter Analysis and Machine Intelligence, vol. 15, pp. 1326-1330.

Yamamoto, M., H. Kawakatsu, S. Kaneshima, T. Mori, T. Tsutsui, Y. Sudo, and Y. Morita (1999), Detection of a crack-like conduit beneath the active crater at Aso Volcano Japan, Geophys. Res. Lett., 26(24), pp. 3677–3680, doi:10.1029/1999GL005395.

Zhang, K. (1995), Algorithms for the constrained editing distance between ordered labeled trees and related problems, Pattern Recogn, 28, pp. 463–474.

Zobin, V.M. (2003), Introduction to volcanic seismology. Developments in Volcanology, 6, Amsterdam, Elsevier. 290 pp.

Appendix

Software

All software used in this thesis include:

Crosswavelet and wavelet coherence softwares provided by A. Grinsted (2004) (http://www.pol.ac.uk/home/research/waveletcoherence/)

The OpenTSTOOL software package provided by C. Merkwirth et al. (2002) (http://www.physik3.gwdg.de/tstool/);

Delay Vector Variance Matlab Toolbox provided by P. Mandic (2008) (http://www.commsp.ee.ic.ac.uk/~mandic/dvv.htm)

SOM toolbox for Matlab provided by J. Vesanto (2000) (http://www.cis.hut.fi/somtoolbox/)